NATIONAL ADVISORY COMMITTEE FOR AERONAUTICS

TECHNICAL NOTE 3916

SYSTEMATIC TWO-DIMENSIONAL CASCADE TESTS OF NACA 65-SERIES COMPRESSOR BLADES AT LOW SPEEDS

By L. Joseph Herrig, James C. Emery,
and John R. Erwin

Langley Aeronautical Laboratory
Langley Field, Va.

Washington
February 1957

NATIONAL ADVISORY COMMITTEE FOR AERONAUTICS

TECHNICAL NOTE 3916

SYSTEMATIC TWO-DIMENSIONAL CASCADE TESTS OF NACA 65-SERIES COMPRESSOR BLADES AT LOW SPEEDS[1]

By L. Joseph Herrig, James C. Emery, and John R. Erwin

SUMMARY

The performance of NACA 65-series compressor blade sections in cascade has been investigated systematically in a low-speed cascade tunnel. Porous test-section side walls and, for high-pressure-rise conditions, porous flexible end walls were employed to establish conditions closely simulating two-dimensional flow. Blade sections of cambers from c_{l_o} of 0 to c_{l_o} of 2.7 were tested over the usable angle-of-attack range for various combinations of inlet angle β_1 of 30°, 45°, 60°, and 70°, and solidity σ of 0.50, 0.75, 1.00, 1.25, and 1.50. Design points were chosen on the basis of optimum high-speed operation. A sufficient number of combinations were tested to permit interpolation and extrapolation of the data to all conditions within the usual range of application.

The results of this investigation indicate a continuous variation of blade-section performance as the major cascade parameters, blade camber, inlet angle, and solidity were varied over the test range. Summary curves of the results have been prepared to enable compressor designers to select the proper blade camber and angle of attack when the compressor velocity diagram and desired solidity have been determined.

At a few test conditions, an upper limit to the camber that could perform satisfactorily was found. These results provide information as to the maximum value of the loading parameter, expressed as the product of solidity and section lift coefficient based on the vector mean velocity, that can be used effectively in compressor design. Analysis of the trends indicated that the common practice of employing a constant maximum value of the loading parameter for all inlet angles and solidities fails to define the observed performance of the compressor blades studied in this investigation.

---

[1] Supersedes declassified NACA Research Memorandum L51G31 by L. Joseph Herrig, James C. Emery, and John R. Erwin, 1951.

An index that the positive and negative limits of useful angle-of-attack range occurred when the section drag coefficient reached twice the minimum value was used to estimate the operating range of the compressor blade sections studied. A broad operating range for these sections was observed, except for conditions of highest pressure rise across the cascade corresponding to high cambers at high inlet angles. These conditions are not typical of usual design practice and no difficulty should ordinarily be encountered in employing these blade sections. In general, the observed performance of NACA 65-series compressor blades in cascade is considered to be very satisfactory.

INTRODUCTION

The design of an axial-flow compressor of high performance involves three-dimensional high-speed flow of compressible viscous gases through successive rows of closely spaced blades. No adequate theoretical solution for this complete problem has yet appeared nor considering the complexity of the problem does it seem likely that complete relationships will be established for some time. Various aspects of the problem have been treated theoretically, and the results of those studies are quite useful in design calculations. All such studies, however, have been based on idealized flow, neglecting effects of one or more such physical realities as compressibility, finite blade spacing, and viscosity. Consideration of viscosity effects has been particularly difficult. It appears, therefore, that in spite of advances in theoretical methods, theory must be supplemented by experimental data for some time to come.

Some of the information required can be obtained only by experiment in single-stage and multistage compressors. Much of the information, however, can be obtained more easily by isolating the effects of each parameter for detailed measurement. The effects of inlet angle, blade shape, angle of attack and solidity on the turning angle and drag produced can be studied by tests of compressor blades in two-dimensional cascade tunnels. Cascade tests can provide many basic data concerning the performance of compressors under widely varying conditions of operation with relative ease, rapidity, and low cost. A number of successful high-speed axial-flow compressors have been designed using low-speed cascade data directly. A more refined procedure, however, would use cascade data, not as the final answer, but as a broad base from which to work out the three-dimensional relations.

A large number of two-dimensional cascade tests have been run in this and other countries during the last 15 years. It is believed that, although the cascade configurations were geometrically two-dimensional, in no case except that of the porous-wall cascade of reference 1 was the flow two-dimensional. This situation is ordinarily accepted on the grounds that the flow in the compressor is also subject to three-dimensional end effects. That similar end conditions would exist in stationary cascades and rotating blade rows seems unlikely. As discussed in reference 1, there is evidence, however, that the flow through typical axial compressor blades is more nearly like that in aerodynamically two-dimensional cascades than like that in cascades which are only geometrically two-dimensional. Excellent correlation between porous-wall cascade and rotor-blade pressure-distribution and turning-angle values is shown for the design conditions of the compressor investigation reported in reference 2. The proper basic approach to the compressor design problem, therefore, would seem to be to separate the two-dimensional effects from the three-dimensional. This should also aid in the evaluation of the separate effects of tip clearance and secondary flow in axial compressors. Therefore, a systematic series of low-speed cascade tests of the NACA 65-series compressor blade sections were made using the porous-wall technique to insure two-dimensionality of the flow. Test results and preliminary analysis are presented in this paper.

SYMBOLS

a	mean-line loading designation
b	blade height or span, feet
c	blade chord, feet
C_d	section drag coefficient
C_F	resultant-force coefficient
C_l	section lift coefficient
C_{l_o}	camber, expressed as design lift coefficient of isolated airfoil
C_N	section normal-force coefficient
C_{N_M}	section normal-force coefficient obtained by calculation of momentum and pressure changes across blade row
C_{N_P}	section normal-force coefficient obtained by integration of blade-surface pressure distribution
C_w	wake momentum difference coefficient

F	force on blades, pounds
F_M	force on blades due to momentum change through blade row, pounds
F_p	force on blades due to pressure change through blade row, pounds
F_w	force on blades due to momentum difference in wake, pounds
g	tangential spacing between blades, feet
L/D	lift-drag ratio
P	total pressure, pounds per square foot
p	static pressure, pounds per square foot
q	dynamic pressure, pounds per square foot
$\Delta p/q_1$	nondimensional static-pressure-rise parameter
R	Reynolds number based on blade chord
S	pressure coefficient $\left(\frac{P - p_l}{q_1}\right)$
U	rotor blade rotational speed, feet per second
V	flow velocity, feet per second
W	flow velocity relative to blades, feet per second
x	chordwise distance from blade leading edge, feet
y	perpendicular distance from blade chord line, feet
α	angle between flow direction and blade chord, degrees
β	angle between flow direction and axis, degrees
θ	flow turning angle, degrees $(\beta_2 - \beta_1)$
γ	angle between resultant-force direction and tangential direction, degrees

ρ	mass density of flow, slugs per cubic foot
σ	solidity, chord of blades divided by tangential spacing

Subscripts:

a	component in axial direction
d	design, when used with angles
l	local
m	referred to vector-mean velocity, W_m
u	component in tangential direction
s	flow outside wake
1	upstream of blade row
2	downstream of blade row

APPARATUS, TEST PROGRAM, AND PROCEDURE

Description of Test Equipment

The test facility used in this investigation was the Langley 5-inch low-speed, porous-wall cascade tunnel described in reference 1 and shown in figures 1 and 2. During the course of this program some further improvements were required to establish proper testing conditions at higher pressure rise conditions. In particular, there was sufficient boundary-layer buildup behind the slot on the convex flexible end wall with high pressure rise cascades to cause separation and destroy simulation of the infinite cascade even though the blade flow was not separated. This was corrected by replacing the end wall with a porous flexible wall and suction chamber. In addition the large difference in flow length from the entrance cone to the side-wall slots between the tunnel ends at the higher inlet air angles gave quite different boundary-layer thickness along the length of the side-wall slots and made uniform flow entering the test section difficult to obtain. This condition was improved by making the changeable side plates porous and drawing a small amount of air through them. The concave flexible end wall was made porous to provide a further control of flow conditions through the test section.

The porous material found to be most satisfactory is commercial woven monel filter cloth. This is available in various meshes in widths up to 36 inches and can be calendered at the factory to reduce porosity and improve surface smoothness. The combination found most suitable for the present work was a twill Dutch double weave of 30 by 250 mesh with warp wire diameter of 0.010 inch and fill wire diameter of 0.008 inch. The original thickness of about 0.026 inch was reduced to 0.018 inch by calendering. The resulting material has the porosity characteristics shown in figure 3. The primary advantages of this material over others tried previously are its uniformity, flexibility, strength, surface smoothness, and relatively low cost.

Description of Airfoils

The blade family used in this investigation is formed by combining a basic thickness form with cambered mean lines. The basic thickness form used is the NACA 65(216)-010 thickness form with the ordinates increased by 0.0015 times the chordwise stations to provide slightly increased thickness toward the trailing edge. This thickness form has been designated the 65-010 blower blade section in references 3 and 4. It was not derived for 10-percent thickness but was scaled down from the NACA 65,2-016 airfoil given on page 80 of reference 5. As discussed in reference 5, the scaling procedure gives the best results when it is restricted to maximum thickness changes of a few percent. Since the start of the program the NACA 65-010 basic thickness has been derived and is given on page 82 of reference 5. These basic thickness forms differ slightly but are considered to be interchangeable within the accuracy of the results reported herein. Ordinates for both the scaled and derived thickness forms are given in table I.

The basic mean line used is the $a = 1.0$ mean line given on page 97 of reference 5. The amount of camber is expressed in reference 5 as design lift coefficient c_{l_o} for the isolated airfoil, and that system has been retained. Ordinates and slopes for the $a = 1.0$ mean line are given in table II for $c_{l_o} = 1.0$. Both ordinates and slopes are scaled directly to obtain other cambers. Cambered blade sections are obtained by applying the thickness perpendicular to the mean line at stations laid out along the chord line. The blade sections tested are shown in figure 4. In the designation the camber is given by the first number after the dash in tenths of c_{l_o}. For example, the NACA 65-810 and NACA 65-(12)10 blade sections are cambered for $c_{l_o} = 0.8$ and $c_{l_o} = 1.2$, respectively.

Test Program and Procedure

Test program.- The test program was planned to provide sufficient information to satisfy any conventional vector diagram of the type shown in figure 5. Tests of seven-blade cascades were run with various combinations of inlet air angle β_1 of 30°, 45°, 60°, and 70°, solidity σ of 0.5, 0.75, 1.0, 1.25, and 1.5, and cambers from C_{l_o} of 0 to 2.7 over the useful angle-of-attack range. The most complete test series were run at solidities of 1.0 and 1.5; sufficient tests were made at the other solidities to guide interpolation and extrapolation. The combinations of β, σ, and blade section which were tested are tabulated in table III. The camber range covered at solidities of 1.0 and 1.5 was determined by one of two limitations. At the higher inlet angles progressively higher cambers were used until the limit loading had been reached, that is, until the design condition coincided with stall; at lower inlet angles, however, design turning angle exceeded inlet angle before the limit loading had been reached and the tests were terminated there. Limit conditions were attained at $\beta = 70^\circ$, $\sigma = 1.0$, 1.25, and 1.5, and $\beta = 60^\circ$, $\sigma = 1.0$ and 1.5.

Test procedure.- It was shown in reference 1 that two-dimensional flow can be achieved by controlling the removal of boundary-layer air through porous test-section side walls so that the downstream static pressure equals the ideal value, corresponding to the turning angle, corrected for the blocking effect of the wake. This criterion was accordingly used in these tests. In addition, the flexible end wall shapes and suction flow quantities were adjusted to obtain uniform upstream flow direction and wall static pressures, criteria of two-dimensional flow simulating an infinite cascade. This procedure necessitated an approximate measurement of turning angle and wake size and an estimate of the correct pressure rise before the final settings could be made. Initially this required some cut-and-try procedure but after the initial tests at each β - σ combination a chart similar to figure 5 of reference 1 could be drawn to assist in estimating the pressure rise. An experienced operator could make the required estimates and settings very quickly using this procedure. Spot calculations of the correct pressure rises were made after completion of tests to check the accuracy of the values used.

Tests were made at each cascade combination shown in table III over a range of angles of attack at intervals of 2° to 3°. In general, the tests covered the interval from negative to positive stall, where stall was determined by a large increase in wake size. The principal exceptions occurred for low cambered blades where negative stall would have occurred at negative turning. It was found that the small wall boundary-layer buildup for negative turnings and hence negative pressure rises would have required a less porous material than that normally used, to avoid excess air removal while maintaining sufficient suction pressure differential to avoid local reverse flow through the porous material. It was not deemed worthwhile to change the porous material to obtain data in this relatively uninteresting range. For the NACA 65-010 section at $\beta = 30^\circ$, however, the difficulty persisted well above 0° turning, and this combination was tested with both porous and solid walls.

The tests were entirely within a speed range considered incompressible. The bulk of the tests at solidities of 1.0 and 1.5 were run at an entering velocity of 95 feet per second. For the usual 5-inch blade chord, the Reynolds number was 245,000. Some information near the design point was obtained at higher effective Reynolds number for most cascade combinations by adding roughness to the blade leading edges in the form of $\frac{1}{4}$-inch-wide strips of masking tape draped around the leading edges from wall to wall. In addition, some tests near design were run at a speed of 135 feet per second and Reynolds number of 346,000 with and without roughness. Two cascade combinations were run at design over a range of Reynolds numbers from 160,000 to 470,000 to assist in estimating performance at Reynolds numbers other than the usual test value. In order to provide further information on scale effects, two cascade combinations were tested through the α range with leading-edge roughness at the standard Reynolds number and in the smooth condition at a Reynolds number of 445,000. For solidities of 0.5 and 0.75 the tunnel could not accommodate seven blades of 5-inch chord; the blade chord was reduced to 2.5 inches and the Reynolds number to approximately 200,000 for those tests. Tests with roughness were made near the design point for solidities below 1.0, but Reynolds numbers higher than 200,000 could not be obtained with the existing equipment.

Test measurements.- Blade pressure distribution was measured at the midspan position of the central airfoil at each angle of attack. In addition, surveys of wake total-pressure loss and turning angle were made downstream of the cascade. The total-pressure surveys were made with a nonintegrating multitube rake approximately 1 chord downstream of the blade trailing edges. Turning angle surveys were made by the "null method" with a claw type yaw head; since the yaw device was mounted on a track at the rear of the tunnel the distance from the blades varied from about 1 to 3 chords in the flow direction depending upon the inlet- and turning-angle combination. Flow discharge angle readings were taken at a number of points downstream of several blade passages along the tunnel center line. These readings were averaged to obtain the final value. Since the angle readings in the wake deviated several degrees from the average reading, and the direction of the deviation varied consistently with the direction of the total pressure gradient, the accuracy of readings in the wake was questioned. Therefore, the values obtained when the wake readings were included and excluded in the averaging process were compared for a number of tests.

The resulting turning-angle curves compared very well, but there was considerably less scatter when only the readings outside the wake were used to obtain the turning-angle value. This latter procedure has been adopted as the standard method of measuring the flow discharge direction. Upstream conditions were measured in the same manner as in reference 1.

Calculations.- Pressure distribution and wake-survey data were recorded and force values calculated nondimensionally as coefficients based numerically on the upstream dynamic pressure q_1. This choice was dictated partly by convenience in reducing the data (standardization of q_1 permits use of manometer scales which give nondimensional values directly) and partly by the belief that information based on entering flow is most convenient for design use, particularly when critical speed is important.

All forces due to pressure and momentum changes across the blade row were summed to obtain the resultant blade force coefficient C_{F_1}. In this process the wake total-pressure deficit was converted to an integrated momentum difference by the method given for the drag calculation in the appendix of reference 5. This wake momentum difference, expressed nondimensionally, is designated the wake coefficient C_{W_1}; it represents the momentum difference between the wake and the stream outside the wake, and is based on q_1 numerically. The wake coefficient is not considered to be a true drag coefficient, but is used merely for convenience in assessing the contribution of the wake in the summation of forces.

The resultant-force coefficient was resolved into components perpendicular and parallel to the vector mean velocity W_m (see fig. 5) to obtain the lift coefficient c_{l_1} and the drag coefficient c_{d_1}, respectively. The mean velocity was calculated as the vector average of the velocities far upstream and far downstream. The velocity far downstream was obtained from measurements just behind the blades by using a momentum-weighted average of the velocity just behind the blades. This rather detailed method was found necessary to give consistent drag values. Since the resultant force is very nearly perpendicular to the mean velocity, the value of the component parallel to the mean velocity is quite sensitive to mean-velocity direction. Attempts at using the downstream velocity outside the wake for averaging rather than the momentum-average velocity gave very erratic drag results indicating that mean velocity directions obtained in that manner were not reliable. In addition to the lift and drag, the blade normal-force coefficient $c_{N_{M_1}}$ was obtained by computing the component of the resultant-force coefficient perpendicular to the blade chord line. This normal-force coefficient was compared with the normal-force coefficient $c_{N_{P_1}}$ obtained by integration of the blade surface pressure distribution as a check on the accuracy of individual tests. A detailed derivation of the method of calculating the force coefficients is given in the appendix.

Accuracy of results.- In general the turning-angle values measured are believed to be accurate within $\pm\frac{1}{2}^{\circ}$ near the design values. The correlation procedure used is believed to have improved further the accuracy of the design values in the final results. For tests far from design, that is, near positive or negative stall, the accuracy was reduced somewhat. In addition, at an inlet angle of 70° with sections of zero camber, satisfactory measurements were very difficult to obtain and the accuracy was reduced.

As noted in the section describing calculation methods, the blade normal-force coefficient $c_{N_{M_1}}$ calculated from pressure-rise and momentum considerations was compared with the normal-force coefficient $c_{N_{P_1}}$ obtained from the pressure distribution as a check on the over-all accuracy of individual tests. Since these values would be affected by error in turning-angle, surface pressure or wake-survey readings, or by failure to achieve two-dimensionality of the flow, this comparison is a check on the over-all acceptability of the results. A difference of 5 percent between the two normal-force coefficients was set as the outside limit for acceptance of individual tests for lift coefficients above 0.2; below lift coefficients of 0.2 a direct numerical comparison was made using a limit of plus or minus 0.01. The agreement was well within the 5-percent limit for most of the tests as originally run, and only a few conditions had to be repeated. The accuracy of the lift coefficients is directly comparable to that of the normal-force coefficients. The accuracy of wake-coefficient and drag-coefficient values will be discussed later under Reynolds number effects.

PRESENTATION OF RESULTS

Detailed blade-performance data for all cascade combinations tested are presented in the form of surface-pressure distributions and blade-section-characteristic plots in figures 6 to 84. The representative pressure distributions presented have been selected to illustrate the variation through the angle-of-attack range for each combination. The section characteristics presented through the angle-of-attack range are turning angle, lift coefficient, wake coefficient, drag coefficient, and lift-drag ratio. The effects of changes in Reynolds number and blade-surface condition on section characteristics are given in figure 85.

Trends of section operating range, in terms of angle-of-attack range, with camber for the four inlet angles tested are presented in figure 86. Variation of ideal and actual dynamic-pressure ratio across the cascade with turning angle and inlet angle is presented in figure 87. Figure 88 gives the relation between inlet dynamic pressure and mean dynamic pressure for convenience in converting coefficients from one reference velocity to the other. Limit loading information is summarized in figure 89. Comparison of the present porous-wall-cascade turning-angle data with those of the solid-wall cascade of reference 3 is made in figure 90 for a typical inlet angle and solidity combination.

The information which is most useful for choosing the blade sections to fulfill compressor design vector diagrams is summarized in figures 91 to 111. The variation of turning angle with angle of attack for the blade sections tested is presented for one combination of inlet angle and solidity in each of the figures 91 to 106. Trends of the slopes of the turning-angle, angle-of-attack curves near design are given in figure 107. Figures 108 to 111 are design and correlation charts; the variation of design turning angle and design angle of attack with the parameters, camber, inlet angle, and solidity, is presented for several combinations of the parameters so that interpolation to the conditions of a design velocity diagram is relatively easy.

DISCUSSION

Design Conditions

The values and shape of the blade-surface-pressure distribution are important criteria for predicting the conditions of best operation at high Mach numbers. Velocity peaks occurring on either surface in low-speed tests would be accentuated at high speeds, and supersonic velocities with attendant shock losses would occur at relatively low entering Mach numbers. The selection of the angle of attack designated as "design" for each combination of inlet angle, solidity, and camber is based on the premise that the blade section will be required to operate at Mach numbers near the critical value. The trend of pressure-distribution shape over the angle-of-attack range was examined for each cascade combination, and the angle for which no velocity peaks occurred on either surface was selected as being optimum from the standpoint of high-speed usage. In general, the design angle so selected is near the middle of the low-drag range thus indicating efficient section operation for angles a few degrees higher or lower than the design condition. The design-angle-of-attack choices are indicated by an arrow on the blade-section-characteristic plots of figures 6 to 84. The design angles are also shown by cross bars on the turning-angle summary curves in figures 91 to 106.

Correlation of the design angles of attack and design turning angles over the range of camber, solidity, and inlet angle is given by figures 108 to 111 in a manner convenient for design use. The correlation is excellent; smooth curves result when any two of the three parameters are used as independent variables.

The section-characteristic curves of figures 6 to 84 indicate that, in general, the design points chosen do not give maximum lift-to-drag ratios for low- and medium-speed operation. For designs which will not operate near critical speed, therefore, higher efficiency could be obtained by using angles of attack several degrees higher than the design points presented. This procedure must be used with caution at the higher camber and inlet-angle combinations, however, since the section operating range becomes quite narrow for combinations of highest camber and inlet angle corresponding to the highest values of $\Delta p/q_1$. It is recommended that the individual pressure distributions and section-characteristic curves be examined before departure from the specified design points is made.

Reynolds Number Effects

Pressure distribution and boundary layers.- For many of the tests at angles of attack near and below design, there is evidence that a region of laminar separation of the boundary-layer flow occurred on the convex blade surface; this separated boundary layer then became turbulent and reattached to the blade surface as a relatively thick turbulent boundary layer. The mechanism of such a flow sequence is described for the isolated airfoil in reference 6. The laminar separation is indicated by a relatively flat region in the pressure distribution and the turbulent reattachment is characterized by a rapid pressure recovery just downstream of the separated region. This flow pattern can be seen clearly in many of the figures but it is particularly evident in figures 42(a), 42(c), 56(b) to 56(d), and 66(a) to 66(e). For some tests, it appears that laminar separation occurred on the concave surface as well. This is noticeable in figures 42(b), 42(d), 42(e), 66(c), and 66(d).

The extent of laminar boundary-layer flow which occurs on an airfoil surface is affected by Reynolds number, stream turbulence level, airfoil surface condition, and surface pressure gradient. Increases in Reynolds number, stream turbulence, and surface roughness would promote earlier transition. Qualitatively a gradient of decreasing surface pressure would be required to maintain laminar flow if the Reynolds number, stream turbulence, surface roughness, or the combination of these, which might be referred to as "effective Reynolds number," were high enough to favor transition. At the turbulence level of the 5-inch cascade tunnel, however, laminar flow and laminar separation on the convex surface persisted to Reynolds numbers up to 245,000 even when the surface pressure gradient was slightly unfavorable. The addition of leading-edge roughness, as described in the "Testing Methods" section reduced the extent of the laminar separation region, but did not eliminate it in some cases. In view of the thick boundary layer which results from laminar separation and reattachment, it appears that the minimum final boundary-layer thickness and section drag coefficient would result if the Reynolds number and turbulence values were such as to cause transition before laminar separation occurred. Use of leading-edge roughness to reduce an extended laminar separation region would probably result in a thinner final boundary layer than that for the smooth blade at the same Reynolds number but would probably result in a thicker boundary layer than that for the smooth blade at high Reynolds number. A thick turbulent boundary layer would be expected to promote turbulent separation near the trailing edge of compressor blades which produce a significant pressure rise.

Wake coefficient and drag coefficient.- As noted previously, the wake coefficient c_{w_1} expresses the momentum difference between the wake flow and the downstream flow outside the wake in a manner convenient for use in summing blade forces. The wake coefficient is, of course, directly dependent upon boundary-layer thickness and shape, and changes in the boundary layer with changes in effective Reynolds number are reflected in the wake-coefficient values. Furthermore, if the effective Reynolds number is near the condition where laminar separation may or may not occur, the change in surface pressure gradient with change in angle of attack would control the presence and extent of laminar separation on either blade surface. Obviously erratic variations in the value of the wake coefficients would result under those circumstances. The blade-section-characteristic curves of figures 6 to 84 show that in most cases the wake-coefficient values were irregular as the angle of attack was varied in the region near design at the usual test Reynolds number of 245,000. With higher Reynolds number and/or leading-edge roughness the rapid local pressure recovery associated with boundary-layer reattachment was less evident in the surface pressure distributions and the wake coefficient usually was reduced. For a few cases, notably those of figures 34(g), 35(g), 68(g), and 84(g), leading-edge roughness increased the wake coefficient, however; in those cases the roughness apparently produced a more severe turbulent boundary layer than laminar separation and reattachment did.

The trend of drag coefficient c_{d_1}, defined as the component of resultant force parallel to the mean velocity, was similar to that of wake coefficient. The drag curves were quite irregular near design angle of attack and the values measured varied as much as 30 percent with Reynolds number and roughness. Obviously the values of both drag coefficient and lift-drag ratio near design are not sufficiently reliable to use directly in a design analysis. These values should be of some use for comparison purposes, however. The large drag rise associated with positive and negative stall should be relatively insensitive to Reynolds number effects, because the pressure gradients on the critical surfaces are then unfavorable to laminar flow, and so should be useful for determining effective operating range.

The trend of drag coefficient with Reynolds number near the design condition for the NACA 65-(12)10 blade section at β of 60°, σ of 1.0, and β of 45°, σ of 1.5 shown in figure 85(a) serves to indicate the magnitude of the Reynolds number effect. Increasing the stream turbulence by the use of a $\frac{1}{2}$-inch-mesh screen upstream of the test section lowered the drag coefficients at low Reynolds number, and reduced the Reynolds number at which the drag coefficients become essentially constant with Reynolds number. The comparison of C_d values through the angle-of-attack range for the same cascade combinations at two Reynolds numbers in figures 85(b) and 85(c) gives some further indication of Reynolds number effect. For R of 445,000, the drag coefficients are lower and the curves are smoother than for R of 245,000. The addition of leading-edge roughness in figure 85(b) smoothed the drag curve but did not give the same decrease in drag that the high R did. There appears to be some effect on the angle of attack at which the drag rises rapidly in figure 85(c) but since the effect was not the same in figure 85(b) no conclusions can be drawn.

<u>Turning angle and lift</u>.- Figure 85(a) shows that the effect of Reynolds number on turning angle near design α is almost insignificant for R between 220,000 and 470,000. This is borne out by the fact that throughout figures 6 to 84 changes in θ with Reynolds number and roughness were, in general, within the limits of measuring accuracy. Below R of 220,000 a decrease of design turning angle can be expected. There appears to be some R effect on turning angle near stall in figure 85(c), but again the effect has not been definitely established. It can be concluded that the design turning angles presented are correct for R above 220,000, but that the effect of R near stall is unknown.

Laminar separation had no appreciable effect on the measured lift. The lift-coefficient values for a given test agreed well at low and high Reynolds numbers and with and without roughness. The normal-force coefficients obtained by integration of the pressure distributions also changed very little with changes in Reynolds number and roughness.

Operating Range

In order to estimate the useful operating range of the various sections at the several solidity and inlet angle conditions tested, Howell's index of twice the minimum drag (ref. 7) was used to select the upper and lower limits of angle of attack. As discussed previously in the section concerning Reynolds number effects, the accuracy of the measured values of drag coefficient near design angle of attack suffered due to laminar-flow separation. The minimum value of drag coefficient could not be determined exactly and an approximate value was used to determine the operating range. For most of the test configurations, the drag coefficient changed rapidly with angle of attack near the ends of the useful range, so an error in the value of minimum drag used would have only a small effect on the operating range value. Some scatter in the results was evident, however.

No significant effect of solidity was observed. Most values at constant camber and inlet angle fell within the scatter of the points. A tendency for the range to increase slightly as the solidity was increased was detectable at $\beta = 45^\circ$, but this was not evident for other inlet angles. The results plotted in figure 86 indicate that the major determinant of operating range is inlet angle. As the inlet angle is increased, the usable range of angle of attack is decreased, with greater changes indicated for angles above design than for angles lower than design. The camber of the section affects the operating range in the following manner for angles of attack above design: at an inlet angle of 30°, the range increased with increasing camber; at inlet angles of 45°, 60°, and 70°, the opposite trend occurred. For values of α less than design, little change in range with camber was indicated for $\beta = 30^\circ$; at higher inlet angles, the range decreased as the section camber increased.

With high entering velocities, the section operating range would be reduced due to a more rapid increase of drag at angles of attack well above or below design. Further, the comparison between sections of different camber, at constant inlet angle and solidity, would be altered as the flow velocities relative to the blade surfaces exceed the local velocity of sound.

Pressure Rise

The ideal, nondimensional pressure rise $\Delta p/q_1$ across a two-dimensional cascade is specified when the inlet angle and turning angle are known, since the ratio of the flow areas determines the pressure rise. Since the mass flow is constant, the actual pressure rise is less than the ideal because of the "blocking" effect of the wake on the downstream flow area. For given inlet and turning angles, the blocking effect would be more severe for higher solidity, since the unaffected flow area is reduced. For incompressible flow the nondimensional pressure rise is equal to one minus the dynamic-pressure ratio, that is, $\frac{\Delta p}{q_1} = 1 - \frac{q_2}{q_1}$. The actual dynamic-pressure ratio becomes higher than the ideal because of the wake blocking effect. The ideal dynamic-pressure ratios, and the actual ratios at design turning angles for two solidities, are summarized in figure 87 for the range of inlet and turning angles tested. The dynamic-pressure ratios for individual tests are given by the short bars at the 100-percent points of the pressure-distribution plots. Wake blocking effects would be changed by the same Reynolds number and roughness factors which change the wake coefficient; however, the percentage change in dynamic-pressure ratio would be small.

Limit Loading

Information on the maximum loading which can be achieved in a compressor blade row is important in the design of high performance axial-flow compressors. As noted previously, the high pressure rise associated with large turning at high inlet angles promotes turbulent separation so that at inlet angles of 60° and 70° the stall angle of attack moved progressively closer to the design angle with increasing section camber. The limit turning is reached when the maximum turning is no greater than design turning. The practical limit would be somewhat lower to give a reasonable operating range.

Approximate limit turning was reached at β of 60°, σ of 1.0 and 1.5, and at β of 70°, σ of 1.0, 1.25, and 1.5. Information from those tests is given in terms of a commonly used loading parameter, σC_{l_m}, in figure 89. Both the actual test values of the parameter, and the ideal values calculated using the test inlet and turning angles are presented. Note that the lift coefficient is here based, numerically, on the mean velocity, to conform to the usual form of the parameter.

Arbitrarily chosen constant values of σC_{l_m} have often been used as maximum allowable values in design analyses. The fallacy of using any constant value as a limit is clearly shown in figure 89; the true limiting value increases with increasing solidity and decreases with increasing inlet angle. Since no limits were reached for inlet angles of 45° and 30°, it is clear that the limitation has very little significance there except, perhaps, at very low solidities. The phenomenon is not yet well enough understood to permit the choice of a parameter which could define the over-all limitation as a single value.

Comparison with Solid-Wall Cascade Data

The comparison between pressure-distribution and turning-angle data for a solid-wall cascade tunnel and for the present porous-wall cascade tunnel is given in reference 1 for the NACA 65-(12)10 blade section at β_1 of 60° and σ of 1.0. The comparison has been extended in figure 90 to include turning-angle data for all the cambers reported for β_1 of 60° and σ of 1.0 in reference 3. The turning-angle curves compare fairly well for cambers up to C_{l_o} of 0.8, but beyond that the data of reference 3 deviate significantly from the present results. Comparisons at other conditions would show similar trends.

Relationships Between Turning Angle and Angle of Attack

Summaries of the relationships between turning angle and angle of attack through the camber range are given for each inlet angle and solidity in figures 91 to 106. The variations are quite consistent for most of the range. Some inconsistency in the shape of the curves at stall is a result of reduced accuracy of measurement there. For combinations giving moderate pressure rises there are straight-line relationships for considerable portions of the curves. For the highest pressure rises, however, there are no definite straight-line relationships. The variation of the slopes near design is given in figure 107 to assist in estimating relationships at conditions other than those tested. These slopes are average slopes for the camber range, and do not apply for the highest cambers. They must be used with particular caution for inlet angles near 70°, since very narrow straight-line regions are prevalent there.

SUMMARY OF RESULTS

The systematic investigation of NACA 65-series compressor blade sections in a low-speed cascade tunnel has provided design data for all conditions within the usual range of application. The results of this investigation indicate a continuous variation of blade-section performance as the major cascade parameters, blade camber, inlet angle, and solidity are varied over the useful range. Summary curves have been prepared to facilitate selection of blade sections and settings for compressor-design velocity diagrams for optimum high-speed operation.

Upper limits for the loading parameter σC_{l_m} have been established for some conditions, and the invalidity of using a constant value of the parameter has been shown.

The variation of the useful section operating range with camber, inlet angle, and solidity has been shown. The operating range was found to be broad except for the highest pressure-rise conditions.

Langley Aeronautical Laboratory,
National Advisory Committee for Aeronautics,
Langley Field, Va., July 18, 1951.

APPENDIX

CALCULATION OF BLADE FORCE COEFFICIENTS

The two-dimensional resultant force on a blade in cascade is the vector sum of all the pressure and momentum forces exerted by the fluid. At any appreciable distance behind the blade row the static pressure is constant along a line parallel to the blade row, since any prior pressure gradients would have been converted to momentum changes. Assuming a pressure force acting in the upstream direction to be positive:

$$F_p = \left(p_2 - p_1\right)bg \tag{1}$$

Sum momentum forces in the axial and tangential directions. Assume axial momentum forces positive if the force on the blade is in the upstream direction, and tangential momentum forces positive if the tangential velocity change is in the usual direction shown in figure 5. The axial momentum force then is

$$F_{M_a} = \int_g \rho_2 V_{a_{2_l}}\left(V_{a_{2_l}} - V_{a_1}\right)b\ dg \tag{2}$$

and the tangential momentum force is

$$F_{M_u} = \int_g \rho_2 V_{a_{2_l}}\left(W_{u_1} - W_{u_{2_l}}\right)b\ dg \tag{3}$$

Since momentum values in the wake can be obtained most easily as differences between the wake values and the downstream value outside the wake, it is convenient to rewrite equations (2) and (3)

$$F_{M_a} = \rho_1 V_{a_1}\left(V_{a_{2_s}} - V_{a_1}\right)bg + \int_g \rho_2 V_{a_{2_l}}\left(V_{a_{2_l}} - V_{a_{2_s}}\right)b\ dg \tag{4}$$

$$F_{M_u} = \rho_1 V_{a_1}\left(W_{u_1} - W_{u_{2_s}}\right)bg + \int_g \rho_2 V_{a_{2_l}}\left(W_{u_{2_s}} - W_{u_{2_l}}\right)b\ dg \tag{5}$$

But the wake momentum force, as calculated from wake surveys, is

$$F_w = \int_g \rho_2 V_{a_2}\left(W_{2_s} - W_{2_l}\right) b\ dg \tag{6}$$

If, now, the flow direction in the wake can be assumed to be the same as the average downstream flow direction, the wake force can be resolved into components in the axial and tangential directions. Using the same sign convention as before

$$F_{w_a} = -F_w \cos\beta_2 = \int_g \rho_2 V_{a_{2_l}}\left(V_{a_{2_l}} - V_{a_{2_s}}\right) b\ dg \tag{7}$$

$$F_{w_u} = F_w \sin\beta_2 = \int_g \rho_2 V_{a_{2_l}}\left(W_{u_{2_s}} - W_{u_{2_l}}\right) b\ dg \tag{8}$$

These are the integral terms in equations (4) and (5). Substituting equation (7) in equation (4) and equation (8) in equation (5), the axial and tangential force components become

$$F_a = F_p + F_{M_a} = \left(p_2 - p_1\right) bg + \rho_1 V_{a_1}\left(V_{a_{2_s}} - V_{a_1}\right) bg - F_w \cos\beta_2$$

$$F_u = F_{M_u} = \rho_1 V_{a_1}\left(W_{u_1} - W_{u_{2_s}}\right) bg + F_w \sin\beta_2$$

For convenience use coefficients based on q_1

$$C_{F_{a_1}} = \frac{F_a}{\frac{1}{2}\rho_1 W_1{}^2 bc} = \frac{1}{\sigma}\left[\frac{\Delta p}{q_1} + \frac{2V_{a_1}\left(V_{a_{2_s}} - V_{a_1}\right)}{W_1{}^2}\right] - C_{w_1} \cos\beta_2$$

$$C_{F_{u_1}} = \frac{F_u}{\frac{1}{2}\rho_1 W_1{}^2 bc} = \frac{1}{\sigma}\left[\frac{2V_{a_1}\left(W_{u_1} - W_{u_{2_s}}\right)}{W_1{}^2}\right] + C_{w_1} \sin\beta_2$$

The resultant-force coefficient is given by

$$C_{F_1} = \sqrt{C_{F_{a_1}}{}^2 + C_{F_{u_1}}{}^2}$$

If γ is used to denote the angle between the resultant force and the tangential direction

$$\gamma = \tan^{-1} \frac{C_{F_{a_1}}}{C_{F_{u_1}}}$$

The lift coefficient C_{l_1} and drag coefficient C_{d_1} are the components of C_{F_1} perpendicular and parallel to the vector mean velocity, W_m, respectively, where W_m is the vector average of the velocities far upstream and far downstream. The upstream velocity can be easily measured. The velocity far downstream is obtained by proper averaging of the velocities just behind the blades. Since the axial area controls the axial velocity, conservation of mass determines the axial component of the velocity far downstream. Since there are no physical boundaries in the tangential direction to support pressure gradients, conservation of momentum controls the tangential component far downstream. The discussion up to this point applies to compressible as well as incompressible flow.

For compressible flow the effect of wake mixing on pressures and densities makes accurate determination of the axial velocity far downstream rather tedious. In the incompressible, two-dimensional case the downstream axial component is V_{a_1}, and the downstream tangential component is the momentum-weighted average of W_{u_2}. This tangential component can be obtained by adding to the tangential momentum of the discharge free stream the integrated tangential momentum of the wake. The integrated tangential momentum of the wake can be determined from the tangential component of the wake coefficient. Having the correct velocity far downstream, the vector mean-velocity direction W_m can be easily obtained. The direction of W_m should be determined accurately since C_{F_1} is very nearly perpendicular to W_m, and the value of the drag component C_{d_1} is sensitive to small changes in the direction of W_m.

REFERENCES

1. Erwin, John R., and Emery, James C.: Effect of Tunnel Configuration and Testing Technique on Cascade Performance. NACA Rep. 1016, 1951. (Supersedes NACA TN 2028.)

2. Westphal, Willard R., and Godwin, William R.: Comparison of NACA 65-Series Compressor-Blade Pressure Distributions and Performance in a Rotor and in Cascade. NACA TN 3806, 1956. (Supersedes NACA RM L51H20.)

3. Bogdonoff, Seymour M., and Bogdonoff, Harriet E.: Blade Design Data for Axial-Flow Fans and Compressors. NACA WR L-635, 1945. (Formerly NACA ACR L5F07a.)

4. Bogdonoff, Seymour M., and Hess, Eugene E.: Axial-Flow Fan and Compressor Blade Design Data at 52.5° Stagger and Further Verification of Cascade Data by Rotor Tests. NACA TN 1271, 1947.

5. Abbott, Ira H., von Doenhoff, Albert E., and Stivers, Louis S., Jr.: Summary of Airfoil Data. NACA Rep. 824, 1945. (Supersedes NACA WR L-560.)

6. Bursnall, William J., and Loftin, Laurence K., Jr.: Experimental Investigation of Localized Regions of Laminar-Boundary-Layer Separation. NACA TN 2338, 1951.

7. Howell, A. R.: Design of Axial Compressors. Lectures on the Development of the British Gas Turbine Jet Unit Published in War Emergency Issue No. 12 of the Institution of Mechanical Engineers. A.S.M.E. Reprint, Jan. 1947, pp. 452-462.

TABLE I

ORDINATES FOR NACA 65-010 BASIC THICKNESS FORMS

[Stations and ordinates in percent of chord]

Station, x	Ordinates, ±y	
	65(216)-010 airfoil combined with y = 0.0015x	Derived 65-010 airfoil
0	0	0
.5	.752	.772
.75	.890	.932
1.25	1.124	1.169
2.5	1.571	1.574
5.0	2.222	2.177
7.5	2.709	2.647
10	3.111	3.040
15	3.746	3.666
20	4.218	4.143
25	4.570	4.503
30	4.824	4.760
35	4.982	4.924
40	5.057	4.996
45	5.029	4.963
50	4.870	4.812
55	4.570	4.530
60	4.151	4.146
65	3.627	3.682
70	3.038	3.156
75	2.451	2.584
80	1.847	1.987
85	1.251	1.385
90	.749	.810
95	.354	.306
100	.150	0
L.E. radius	.666	.687

TABLE II

ORDINATES FOR THE NACA a = 1.0 MEAN LINE

[Stations and ordinates in percent of chord]

c_{l_o} = 1.0		
Station, x	Ordinate, y	Slope, dy/dx
0	0	-------
.5	.250	0.42120
.75	.350	.38875
1.25	.535	.34770
2.5	.930	.29155
5.0	1.580	.23430
7.5	2.120	.19995
10	2.585	.17485
15	3.365	.13805
20	3.980	.11030
25	4.475	.08745
30	4.860	.06745
35	5.150	.04925
40	5.355	.03225
45	5.475	.01595
50	5.515	0
55	5.475	-.01595
60	5.355	-.03225
65	5.150	-.04925
70	4.860	-.06745
75	4.475	-.08745
80	3.980	-.11030
85	3.365	-.13805
90	2.585	-.17485
95	1.580	-.23430
100	0	-------

TABLE III

CASCADE COMBINATIONS TESTED

σ	β (deg)			
	30	45	60	70
0.50		65-410 65-(12)10 65-(18)10	65-410 65-(12)10 65-(18)10	
.75		65-410 65-(12)10 65-(18)10	65-410 65-(12)10 65-(18)10	
1.00	65-010 65-410 65-810 65-(12)10 65-(15)10 65-(18)10	65-010 65-410 65-810 65-(12)10 65-(15)10 65-(18)10 65-(21)10 65-(24)10 65-(27)10	65-010 65-410 65-810 65-(12)10 65-(15)10 65-(18)10 65-(21)10	65-010 65-410 65-810 65-(12)10 [a]65-(15)10
1.25	65-410 65-(12)10 65-(18)10	65-410 65-(12)10 65-(18)10	65-410 65-(12)10 65-(18)10	65-410 65-810 65-(12)10 65-(15)10
1.50	65-010 65-410 65-810 65-(12)10 65-(15)10 65-(18)10	65-010 65-410 65-810 65-(12)10 65-(15)10 65-(18)10 65-(21)10 65-(24)10	65-010 65-410 65-810 65-(12)10 65-(15)10 65-(18)10 65-(21)10 65-(24)10	65-010 65-410 65-810 65-(12)10 65-(15)10

[a] No design point was obtained for this combination.

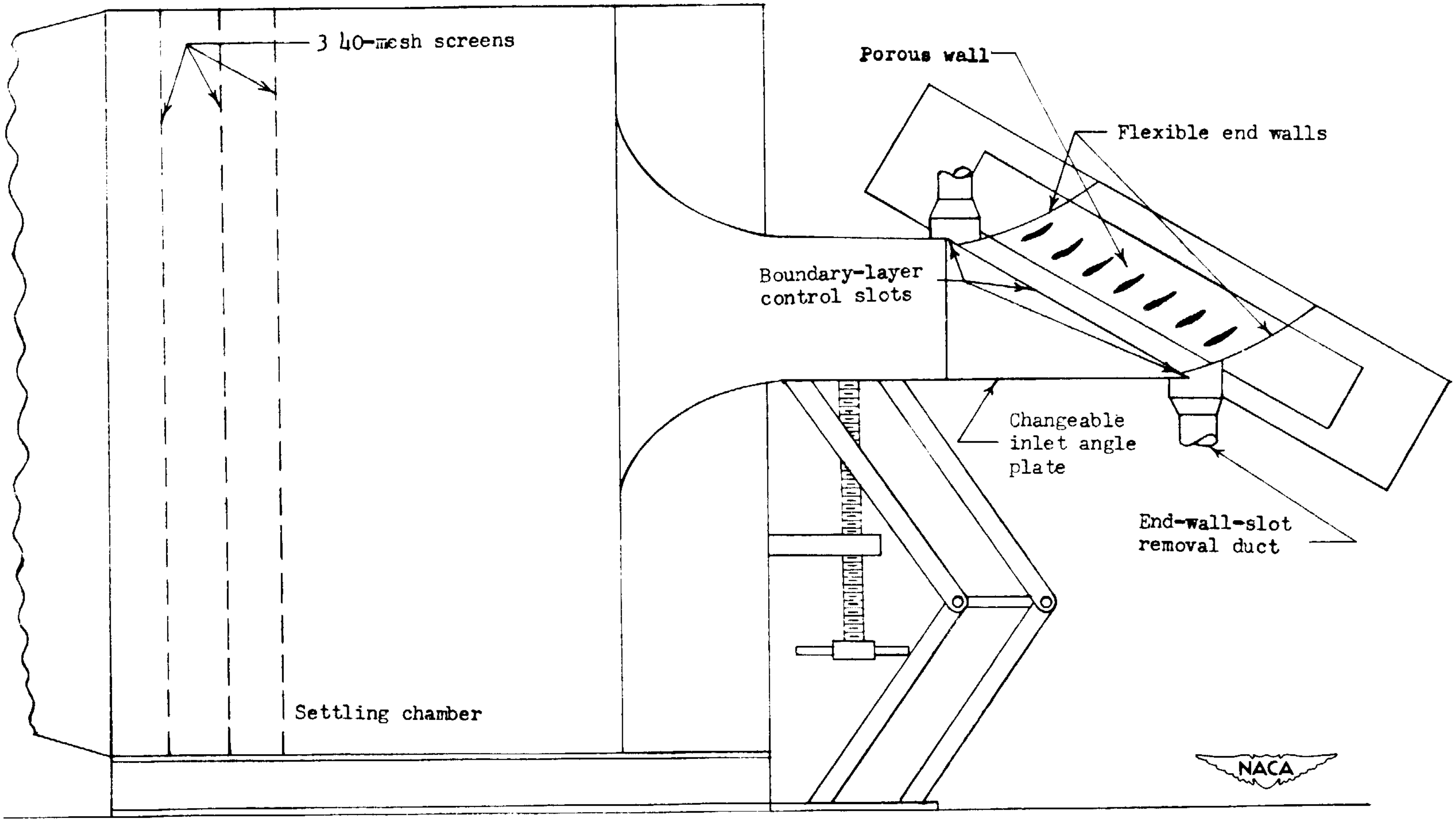

Figure 1.- Vertical cross section of two-dimensional low-speed cascade tunnel.

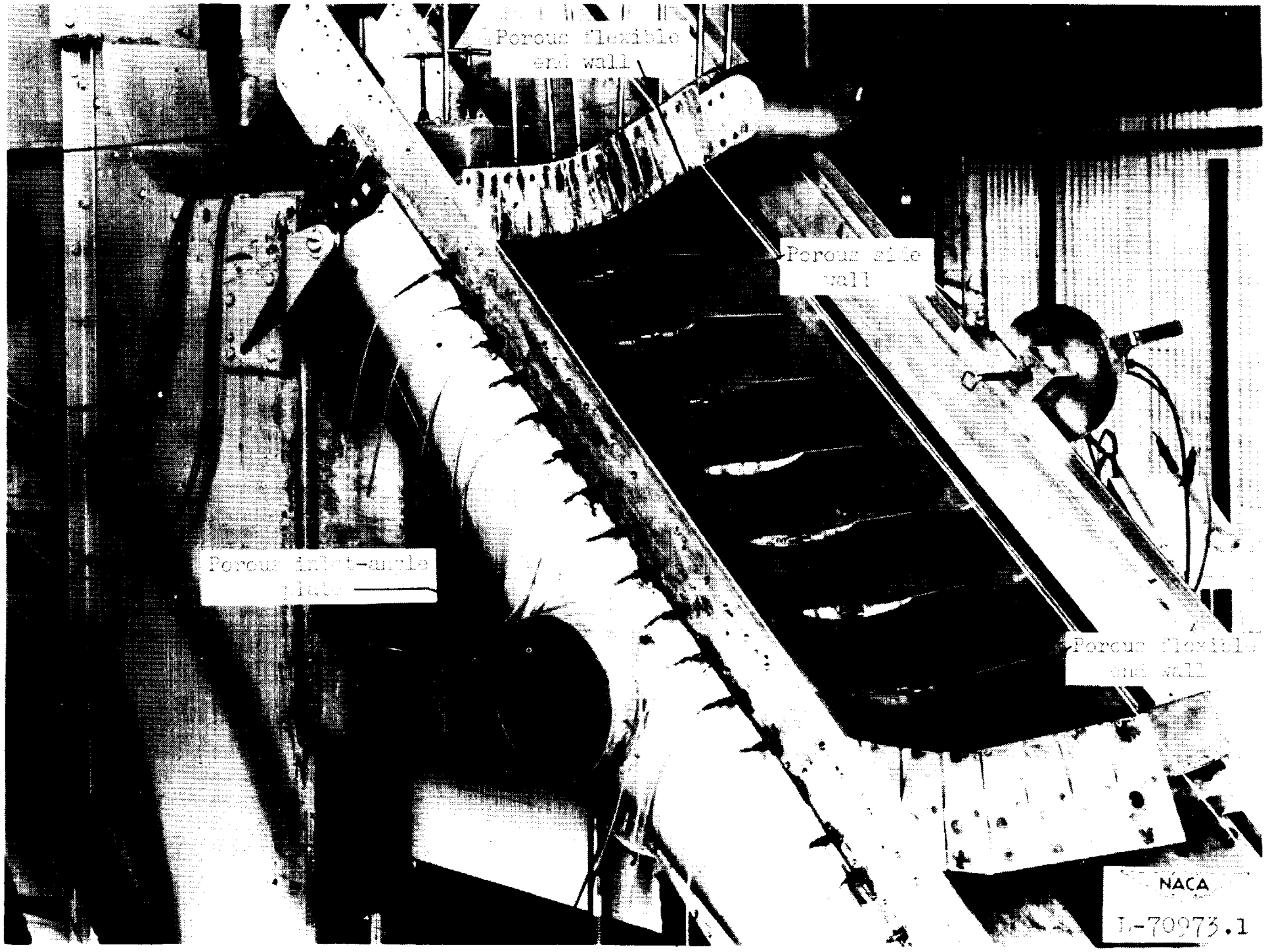

Figure 2.- Photograph of Langley 5-inch cascade tunnel with portions of one side removed to show porous surfaces.

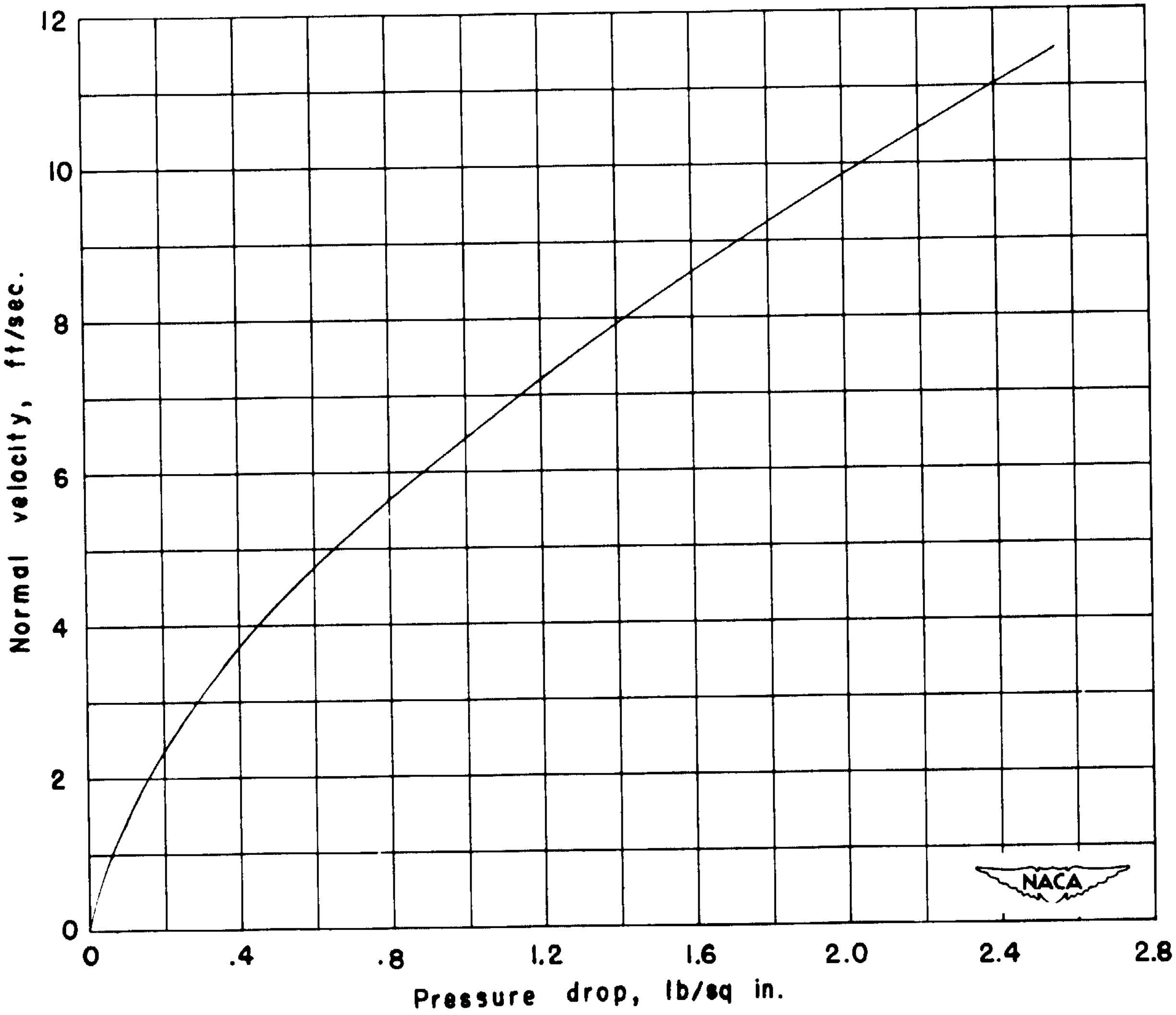

Figure 3.- Porosity characteristics of the calendered monel filter cloth used in this investigation.

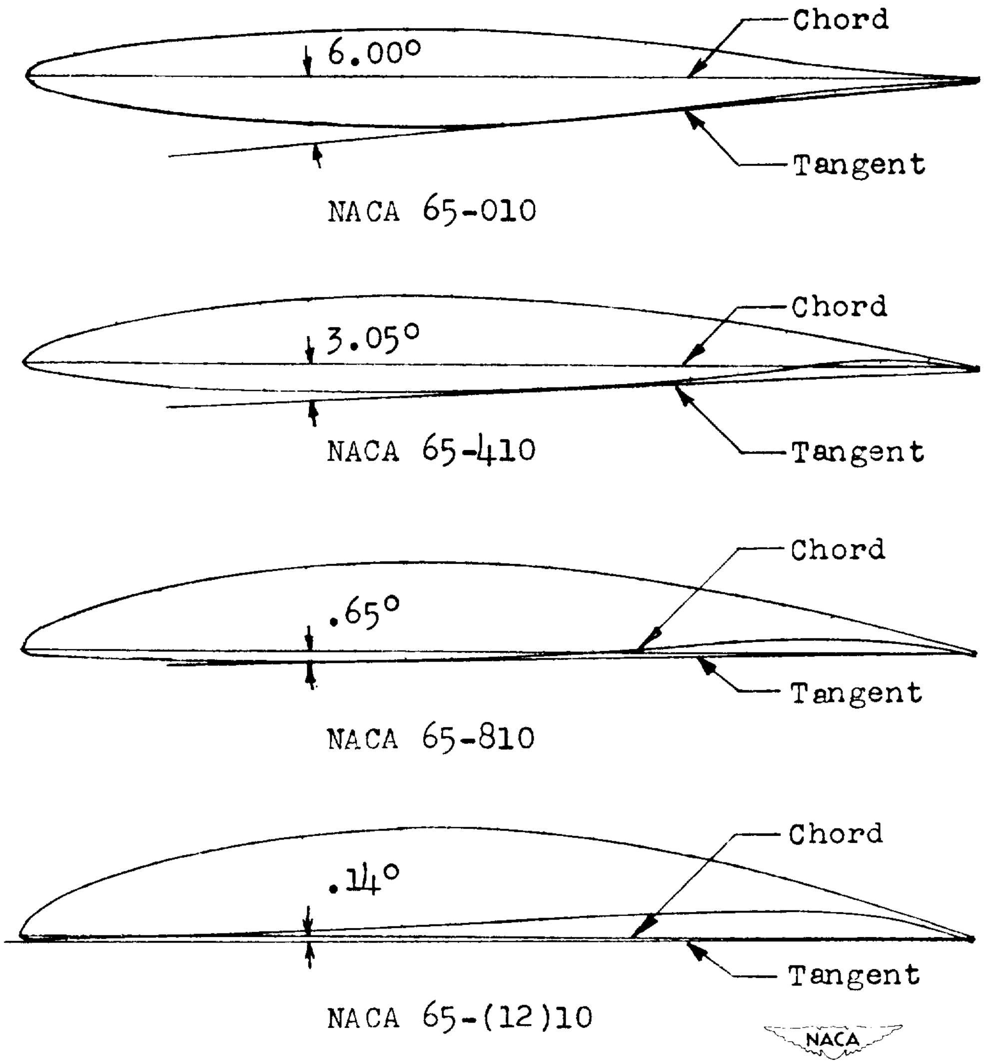

(a) Lower cambered sections. Angle between chord line and tangent to lower surface as shown for the various sections.

Figure 4.- Blade sections tested in this investigation.

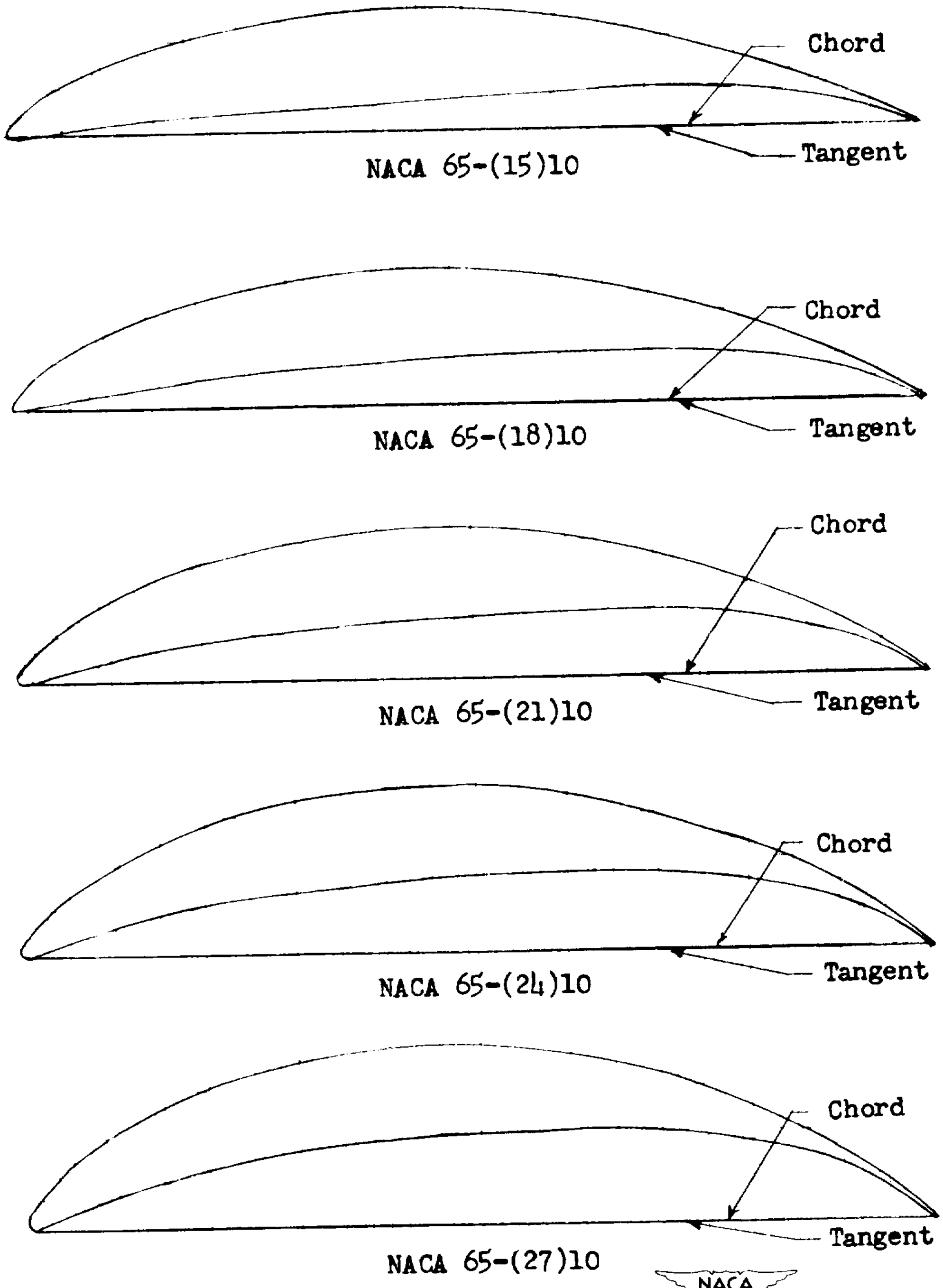

(b) Higher cambered sections. Chord line and tangent line coincident.

Figure 4.- Concluded.

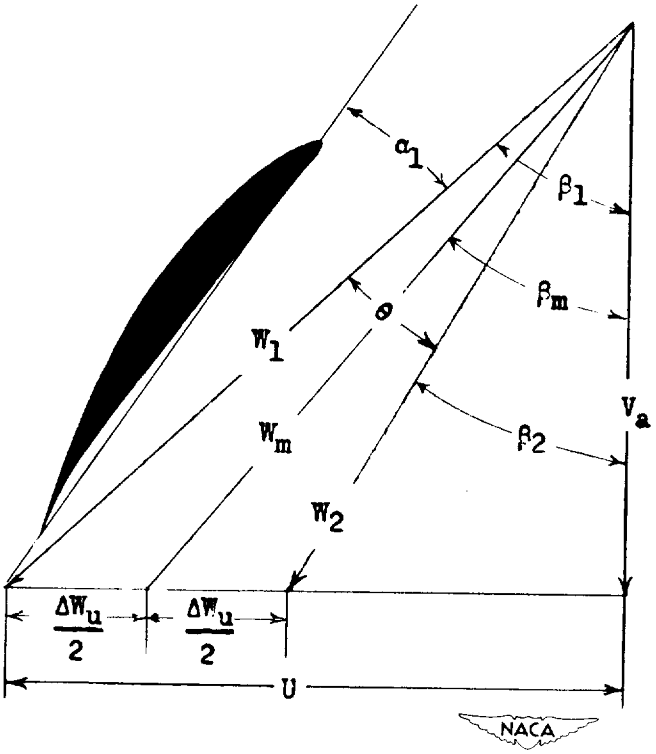

Figure 5.- Typical vector diagram for a compressor rotor.

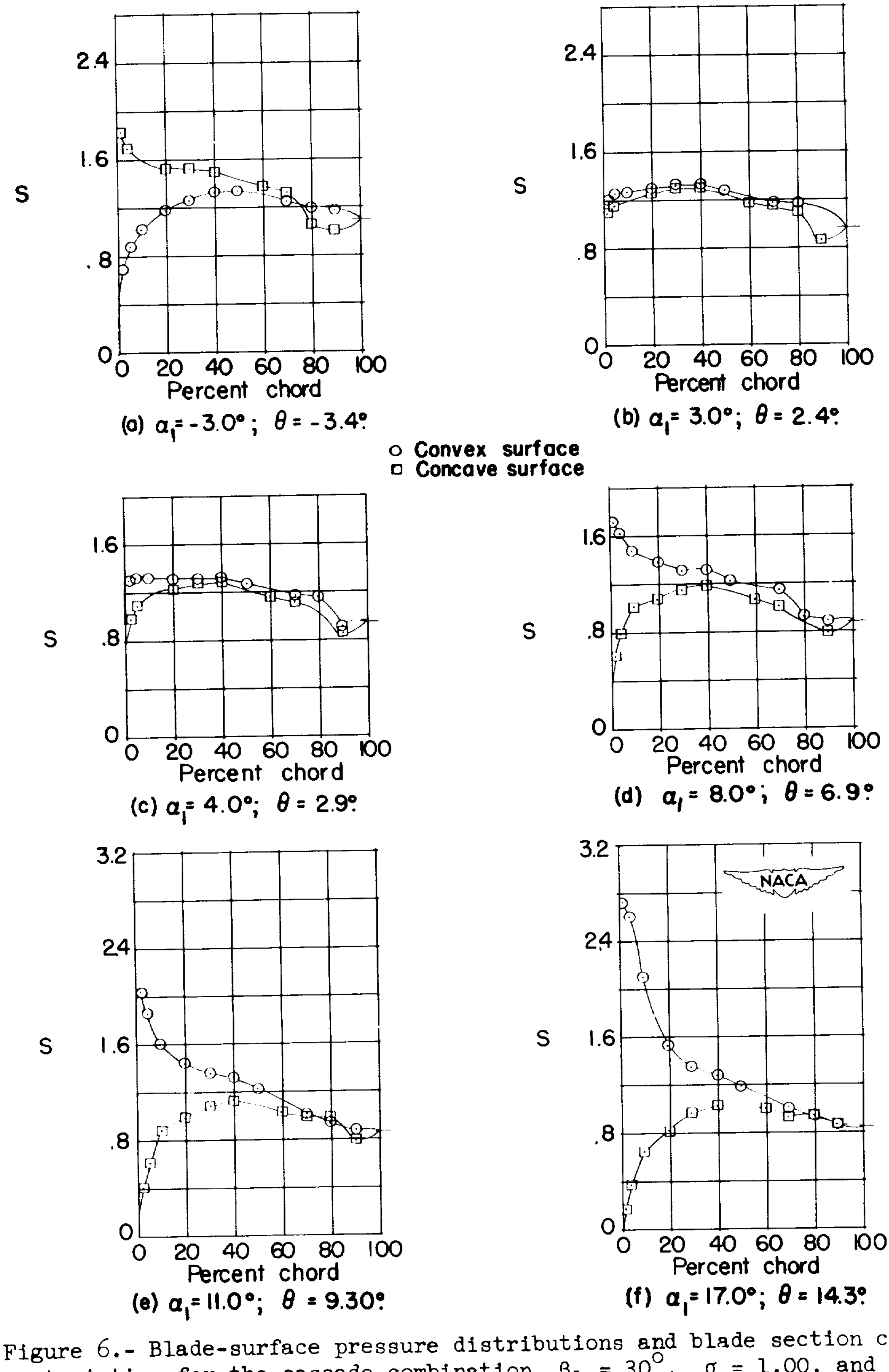

(a) $\alpha_1 = -3.0°$; $\theta = -3.4°$

(b) $\alpha_1 = 3.0°$; $\theta = 2.4°$

(c) $\alpha_1 = 4.0°$; $\theta = 2.9°$

(d) $\alpha_1 = 8.0°$; $\theta = 6.9°$

(e) $\alpha_1 = 11.0°$; $\theta = 9.30°$

(f) $\alpha_1 = 17.0°$; $\theta = 14.3°$

Figure 6.- Blade-surface pressure distributions and blade section characteristics for the cascade combination, $\beta_1 = 30^{\circ}$, $\sigma = 1.00$, and blade section, NACA 65-010.

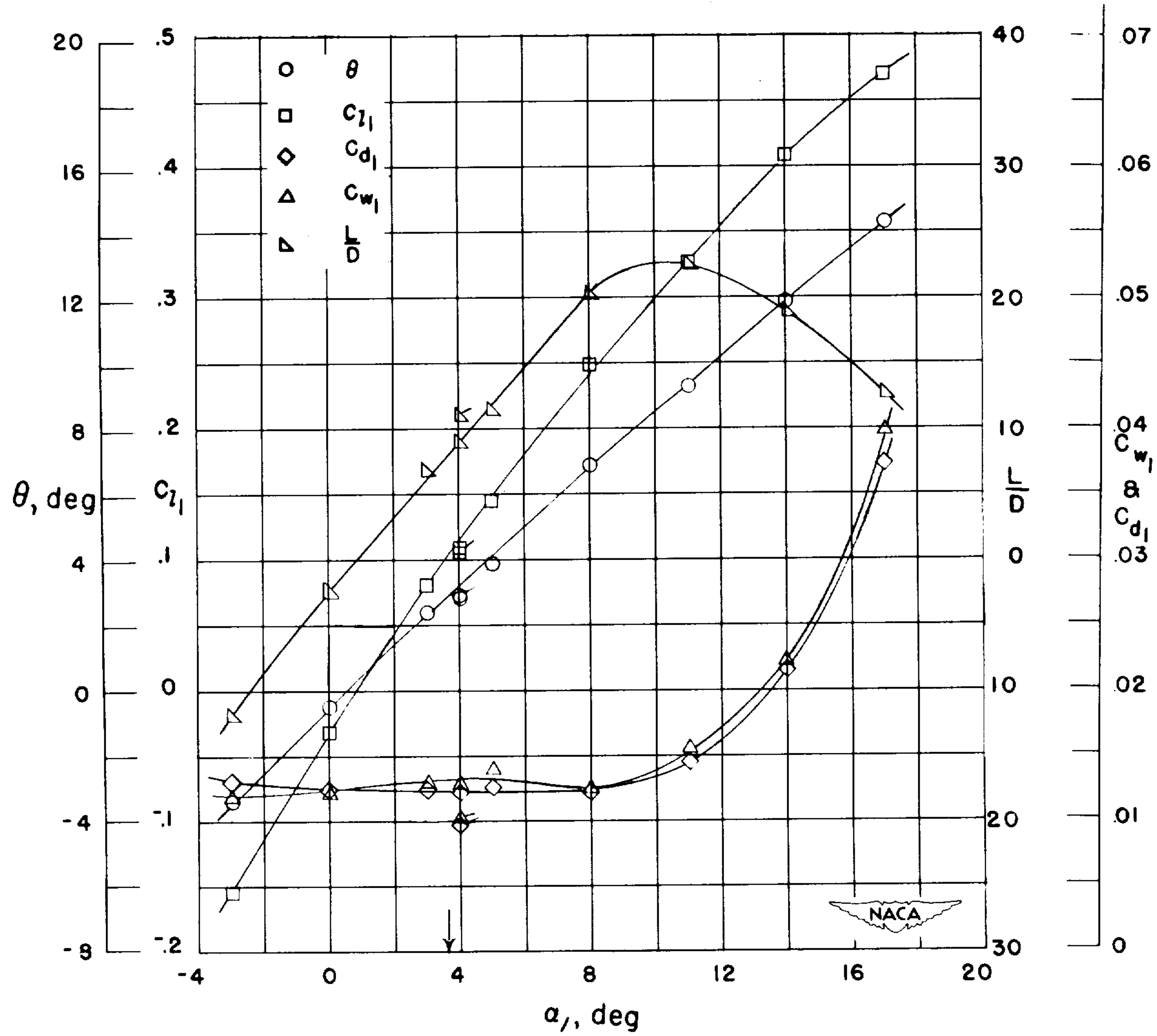

(g) Section characteristics; arrow shows design angle of attack; flagged symbol indicates leading-edge roughness.

Figure 6.- Concluded.

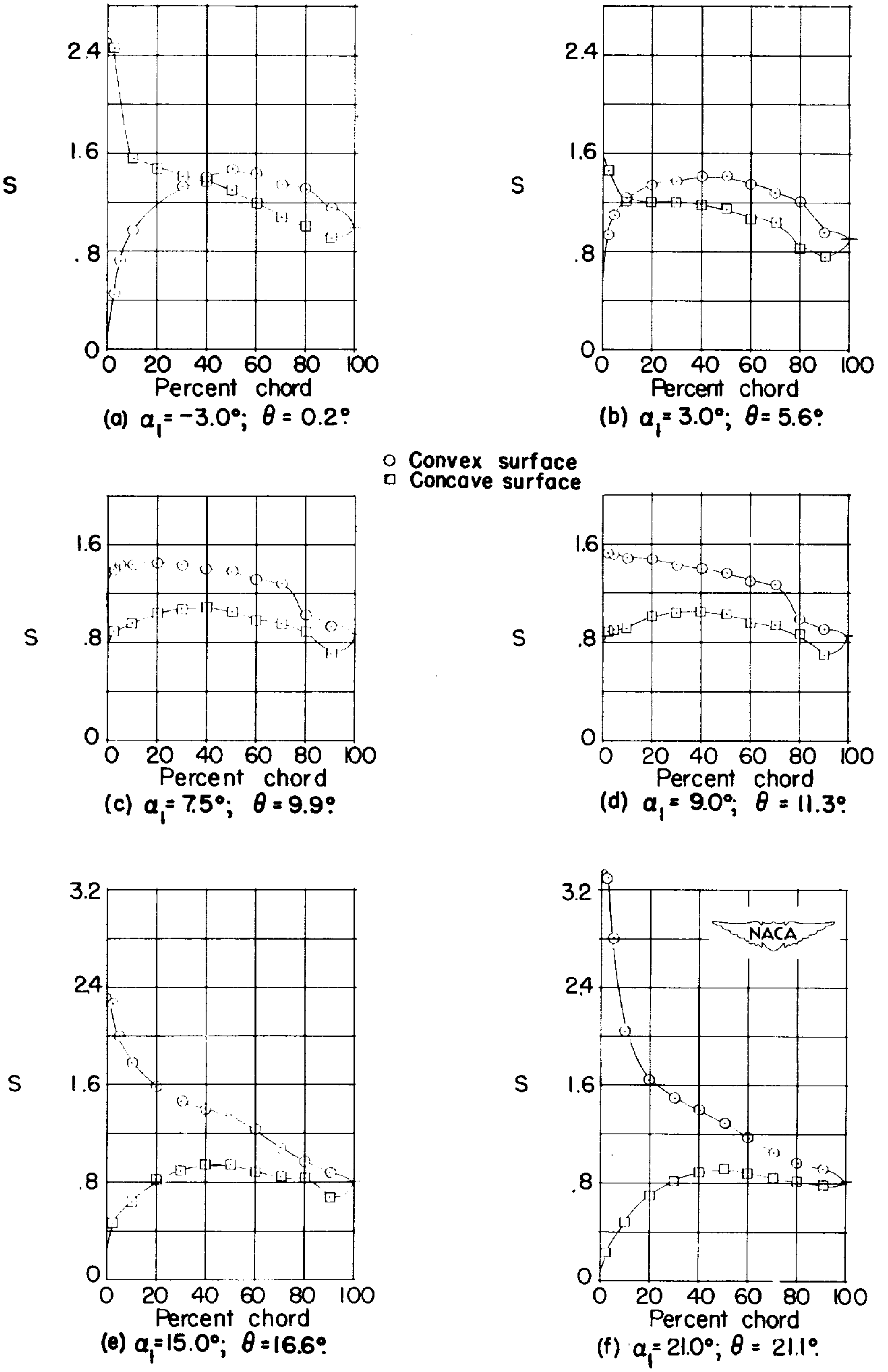

Figure 7.- Blade-surface pressure distributions and blade section characteristics for the cascade combination, $\beta_1 = 30^{\circ}$, $\sigma = 1.00$, and blade section, NACA 65-410.

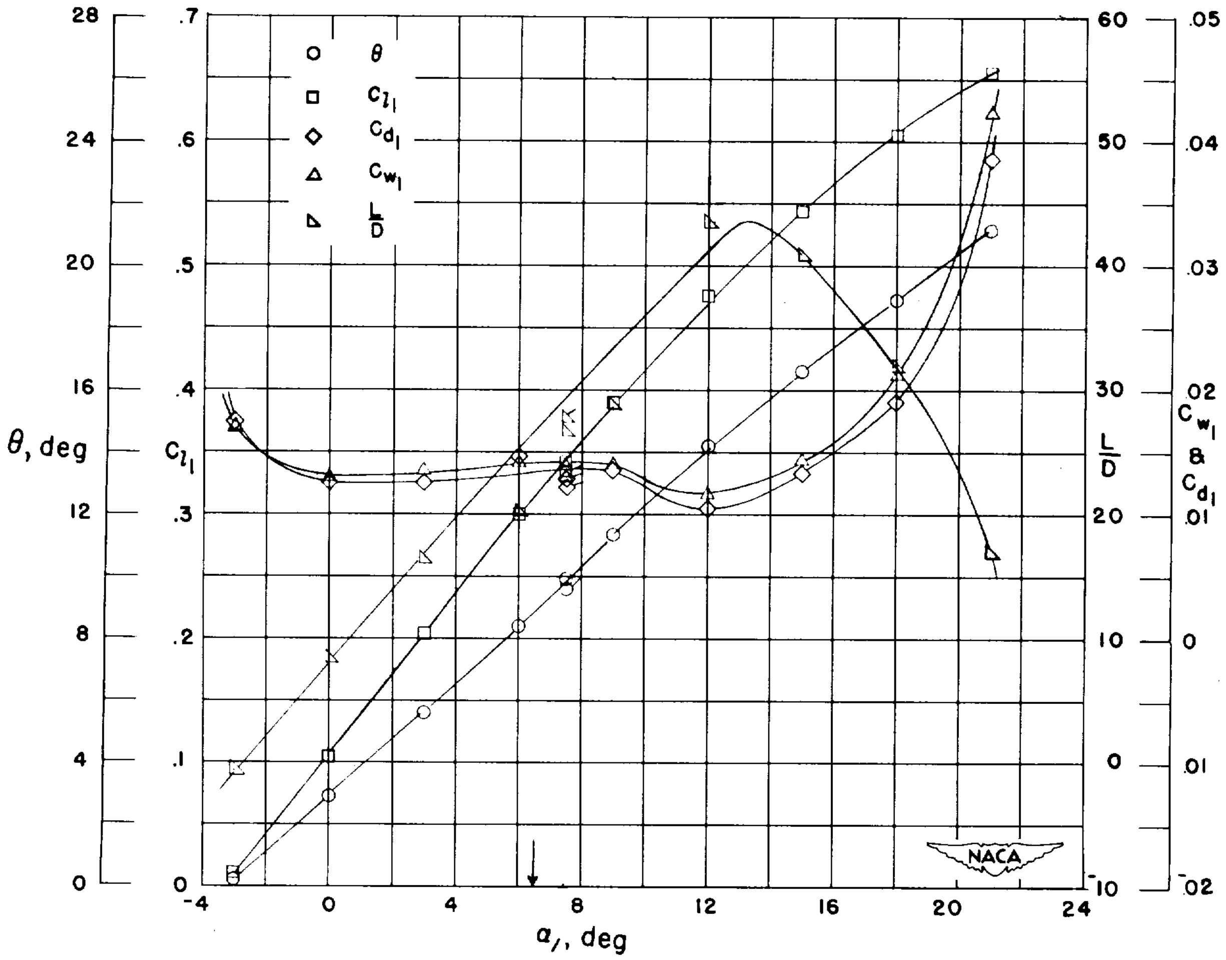

(g) Section characteristics; arrow shows design angle of attack; flagged symbol indicates leading-edge roughness.

Figure 7.- Concluded.

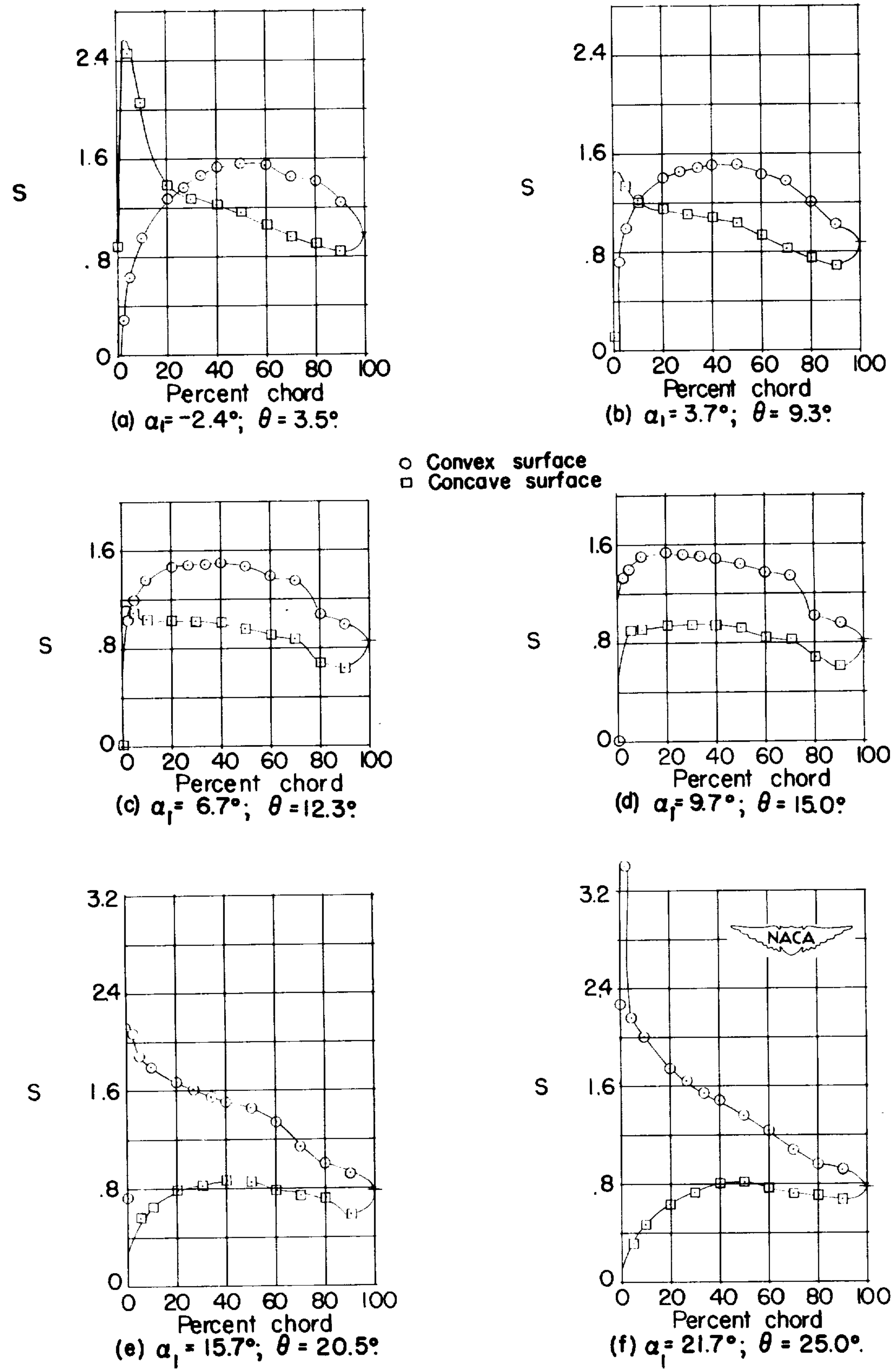

(a) $\alpha_1 = -2.4°$; $\theta = 3.5°$

(b) $\alpha_1 = 3.7°$; $\theta = 9.3°$

(c) $\alpha_1 = 6.7°$; $\theta = 12.3°$

(d) $\alpha_1 = 9.7°$; $\theta = 15.0°$

(e) $\alpha_1 = 15.7°$; $\theta = 20.5°$

(f) $\alpha_1 = 21.7°$; $\theta = 25.0°$

Figure 8.- Blade-surface pressure distributions and blade section characteristics for the cascade combination, $\beta_1 = 30°$, $\sigma = 1.00$, and blade section, NACA 65-810.

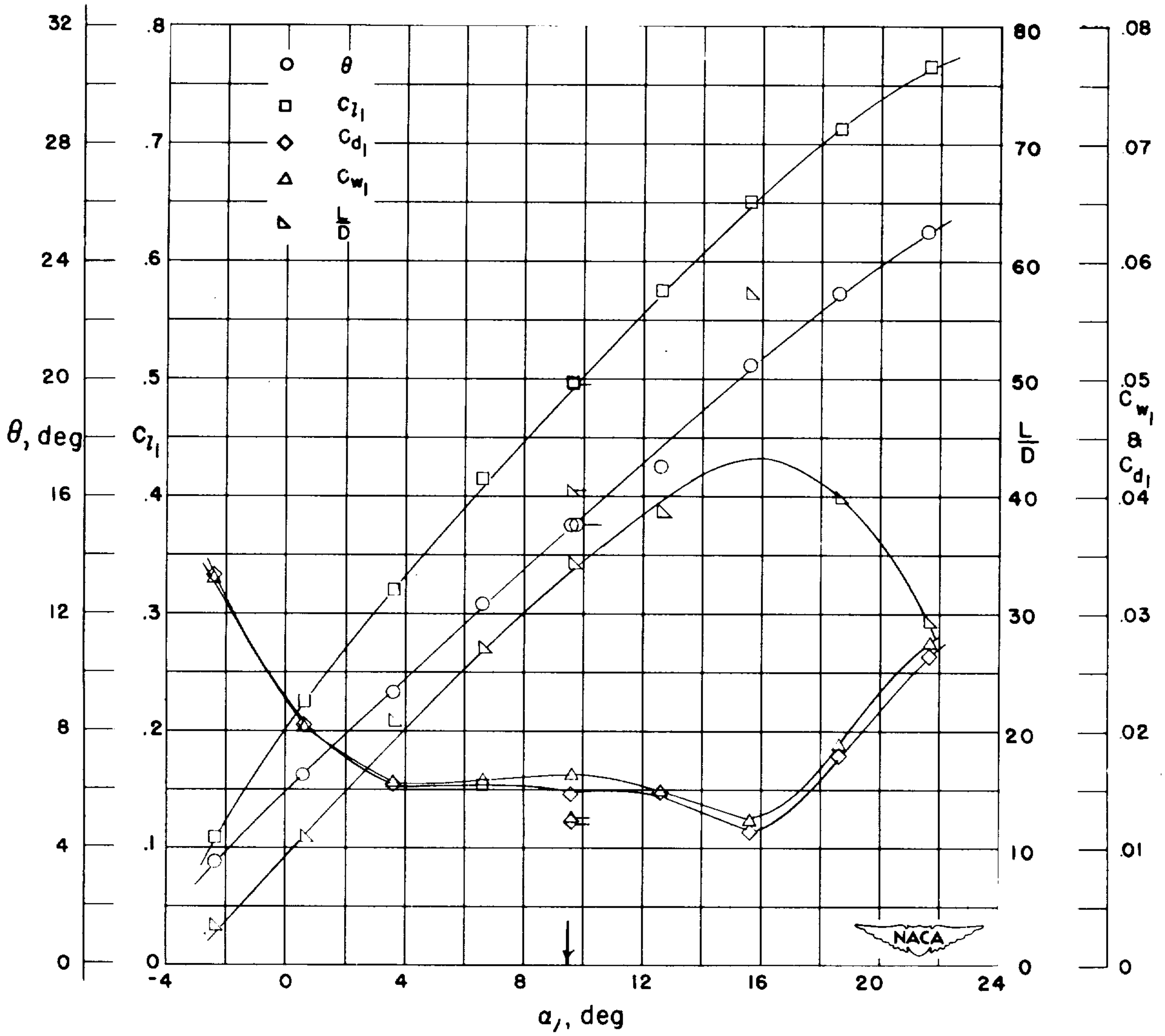

(g) Section characteristics; arrow shows design angle of attack; flagged symbol indicates leading-edge roughness.

Figure 8.- Concluded.

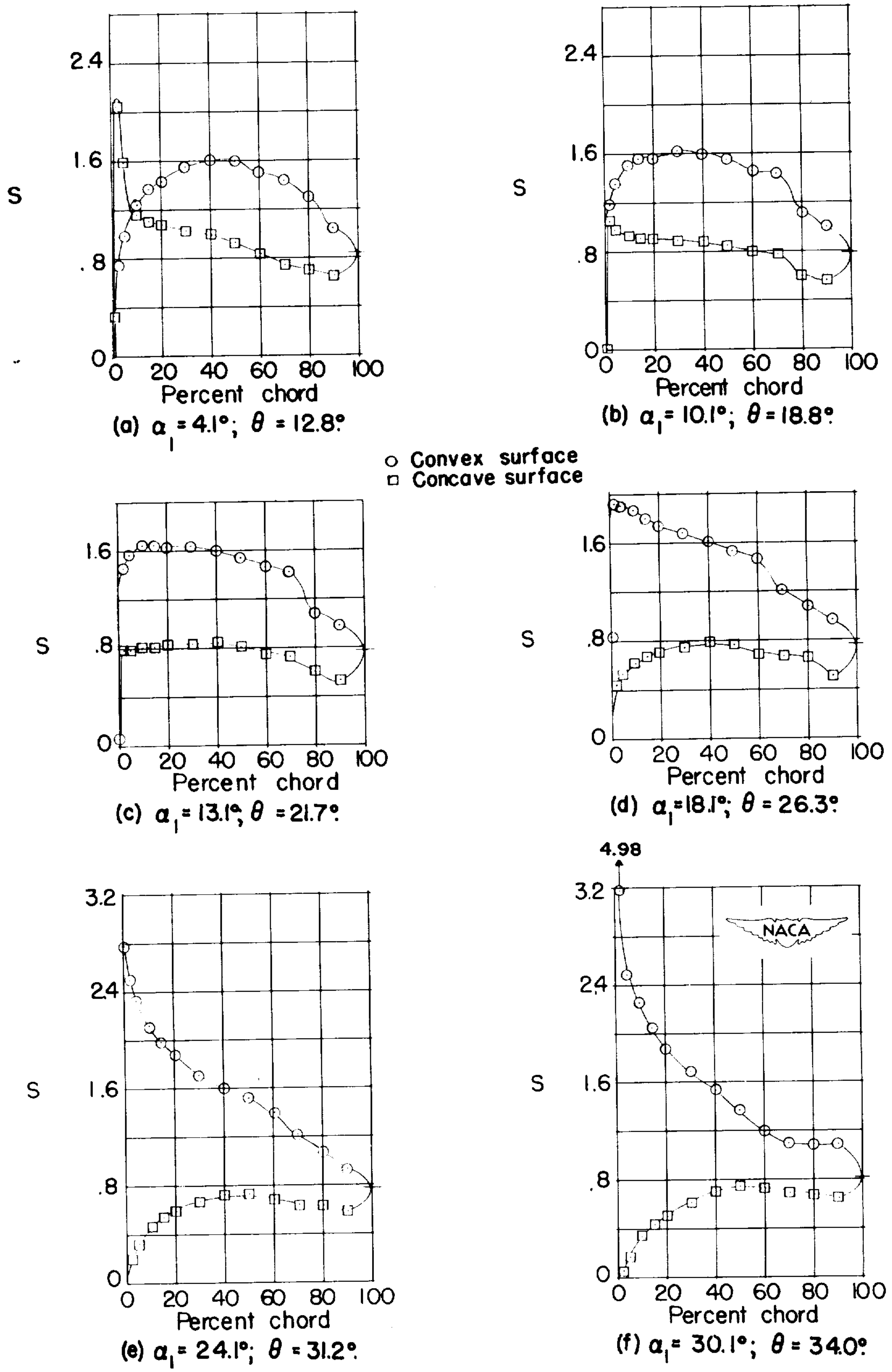

(a) $\alpha_1 = 4.1^\circ$; $\theta = 12.8^\circ$

(b) $\alpha_1 = 10.1^\circ$; $\theta = 18.8^\circ$

(c) $\alpha_1 = 13.1^\circ$; $\theta = 21.7^\circ$

(d) $\alpha_1 = 18.1^\circ$; $\theta = 26.3^\circ$

(e) $\alpha_1 = 24.1^\circ$; $\theta = 31.2^\circ$

(f) $\alpha_1 = 30.1^\circ$; $\theta = 34.0^\circ$

Figure 9.- Blade-surface pressure distributions and blade section characteristics for the cascade combination, $\beta_1 = 30^\circ$, $\sigma = 1.00$, and blade section, NACA 65-(12)10.

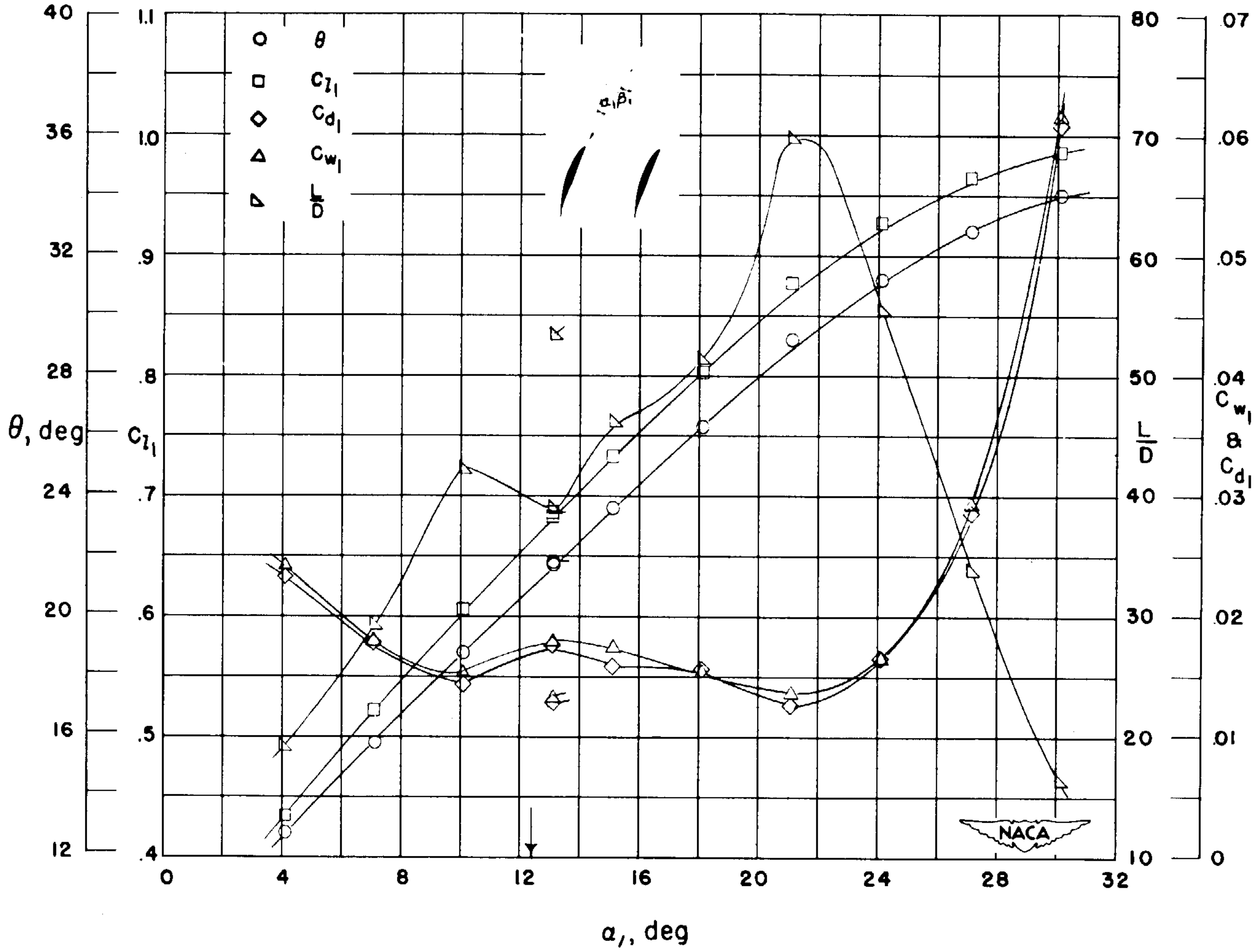

(g) Section characteristics; arrow shows design angle of attack, flagged symbol indicates leading-edge roughness.

Figure 9.- Concluded.

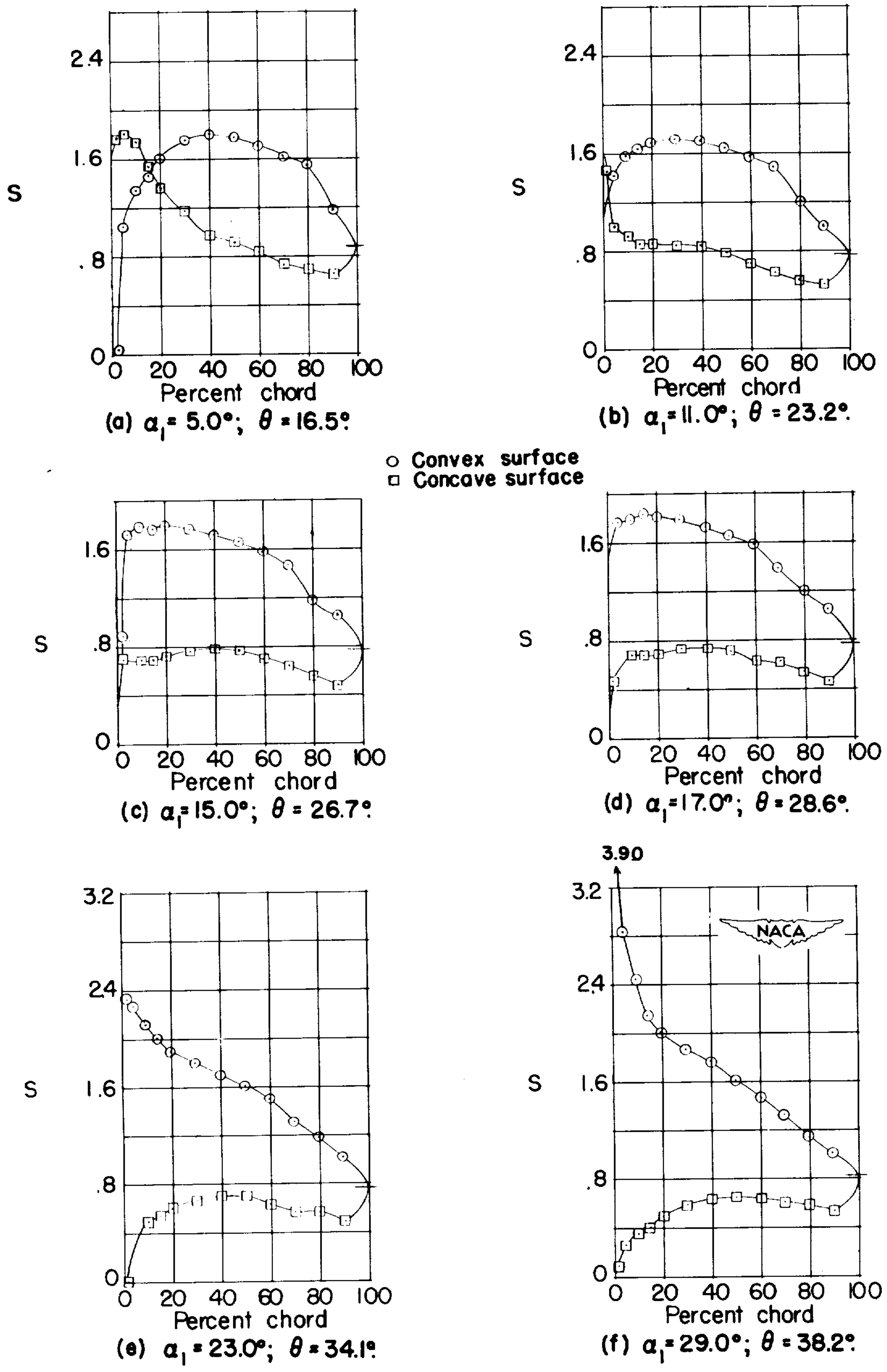

(a) $\alpha_1 = 5.0°$; $\theta = 16.5°$.

(b) $\alpha_1 = 11.0°$; $\theta = 23.2°$.

(c) $\alpha_1 = 15.0°$; $\theta = 26.7°$.

(d) $\alpha_1 = 17.0°$; $\theta = 28.6°$.

(e) $\alpha_1 = 23.0°$; $\theta = 34.1°$.

(f) $\alpha_1 = 29.0°$; $\theta = 38.2°$.

Figure 10.- Blade-surface pressure distributions and blade section characteristics for the cascade combination, $\beta_1 = 30°$, $\sigma = 1.00$, and blade section, NACA 65-(15)10.

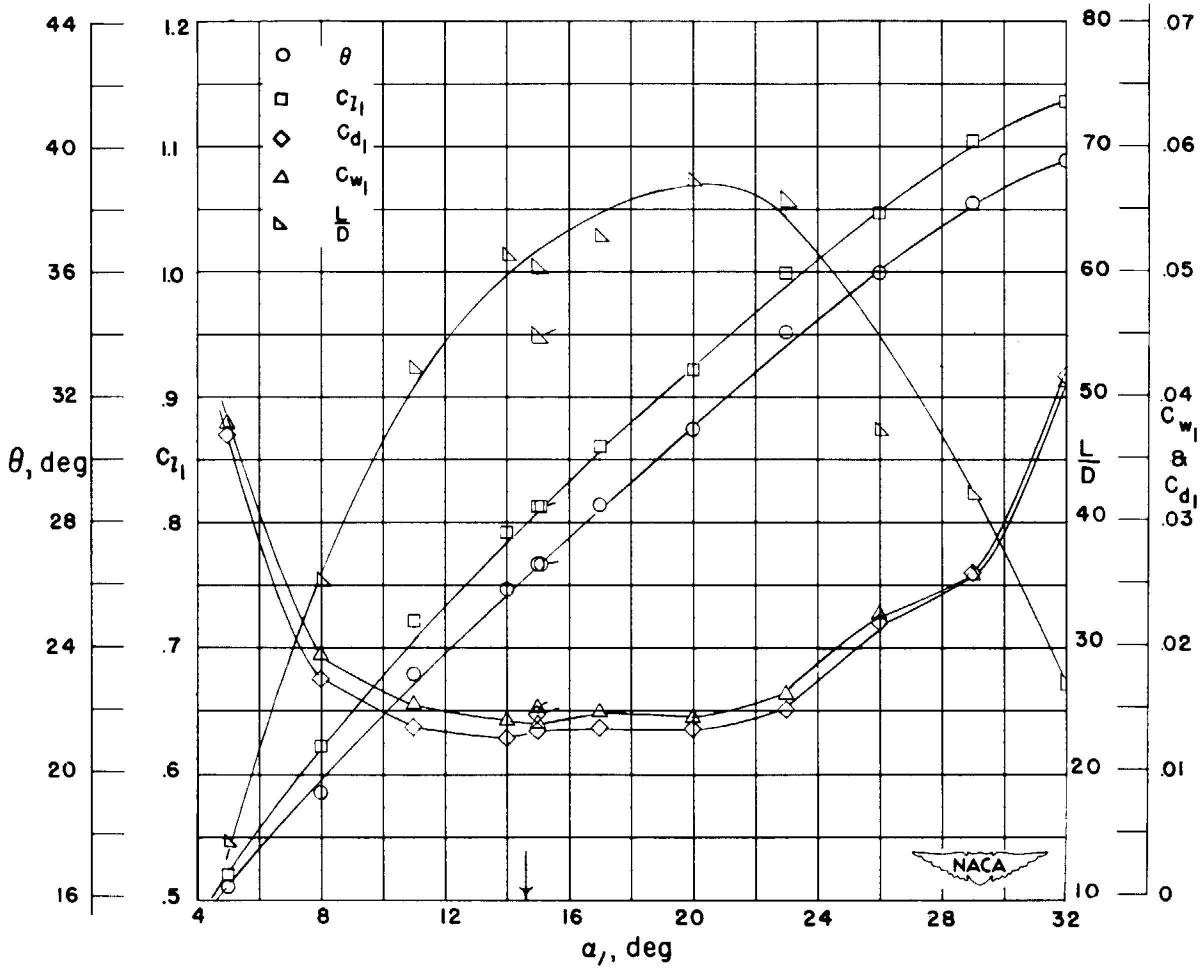

(g) Section characteristics; arrow shows design angle of attack; flagged symbol indicates leading-edge roughness.

Figure 10.- Concluded.

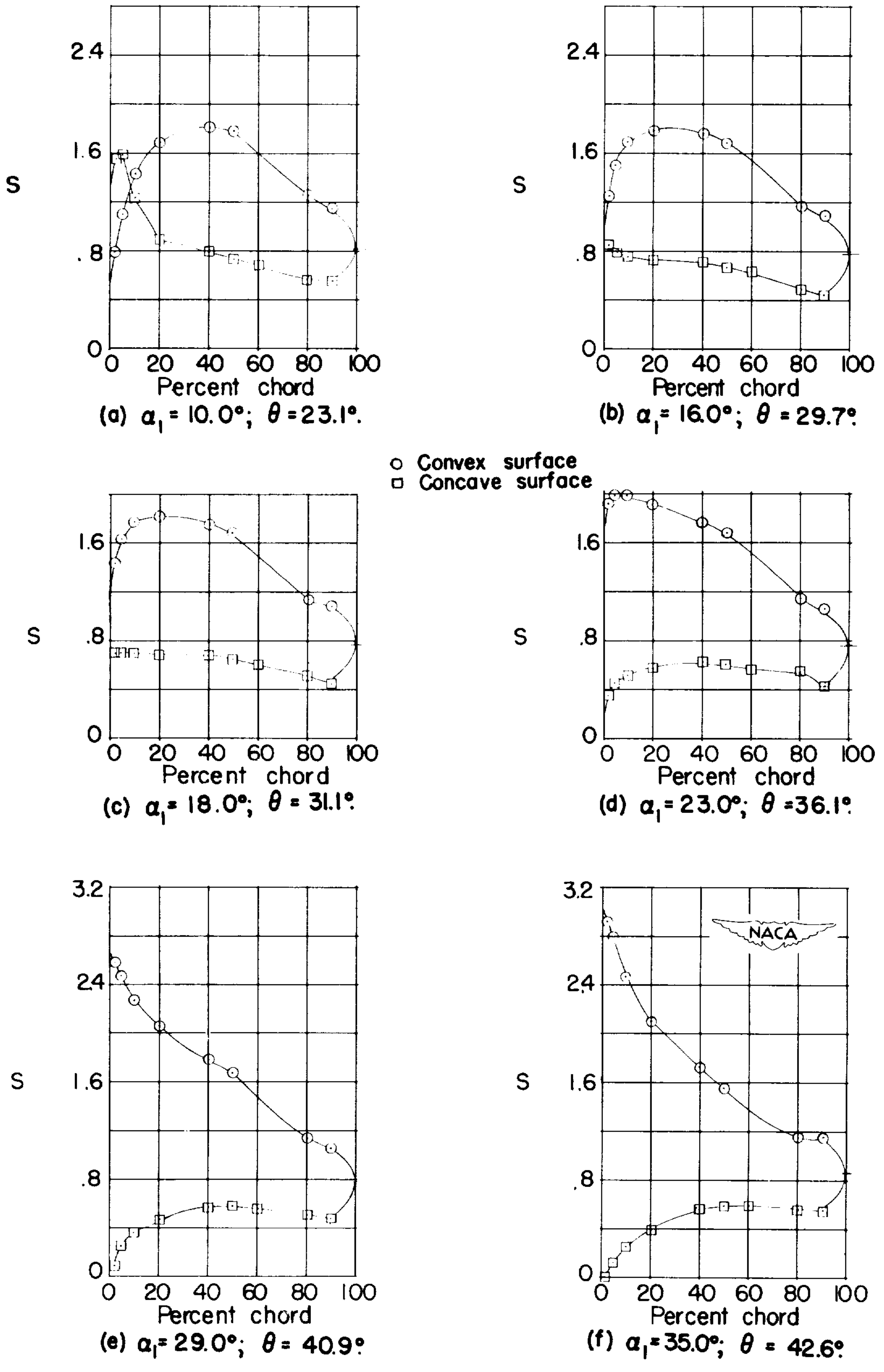

(a) $\alpha_1 = 10.0°$; $\theta = 23.1°$.

(b) $\alpha_1 = 16.0°$; $\theta = 29.7°$.

(c) $\alpha_1 = 18.0°$; $\theta = 31.1°$.

(d) $\alpha_1 = 23.0°$; $\theta = 36.1°$.

(e) $\alpha_1 = 29.0°$; $\theta = 40.9°$.

(f) $\alpha_1 = 35.0°$; $\theta = 42.6°$.

Figure 11.- Blade-surface pressure distributions and blade section characteristics for the cascade combination, $\beta_1 = 30^{\circ}$, $\sigma = 1.00$, and blade section, NACA 65-(18)10.

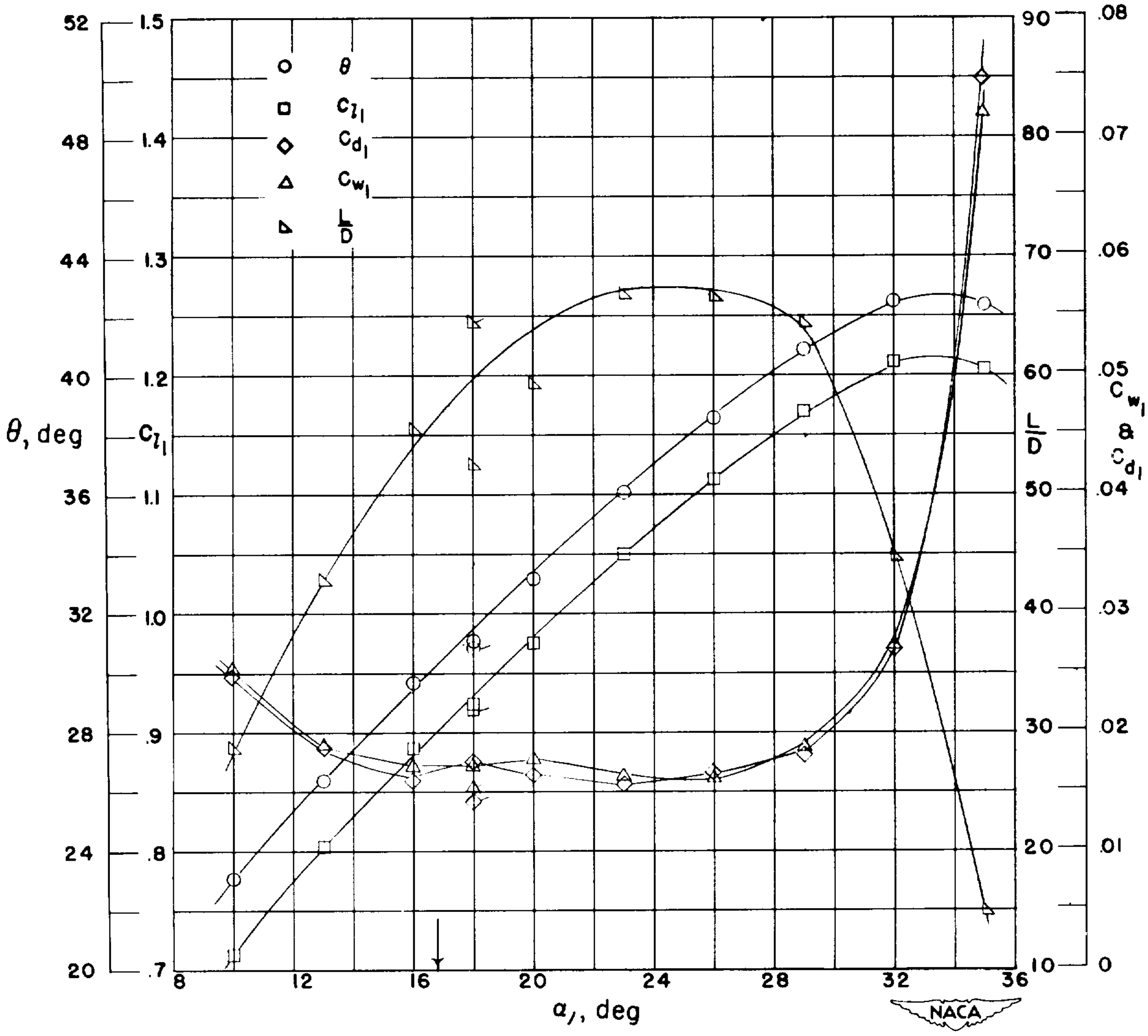

(g) Section characteristics; arrow shows design angle of attack, flagged symbol indicates leading-edge roughness.

Figure 11.- Concluded.

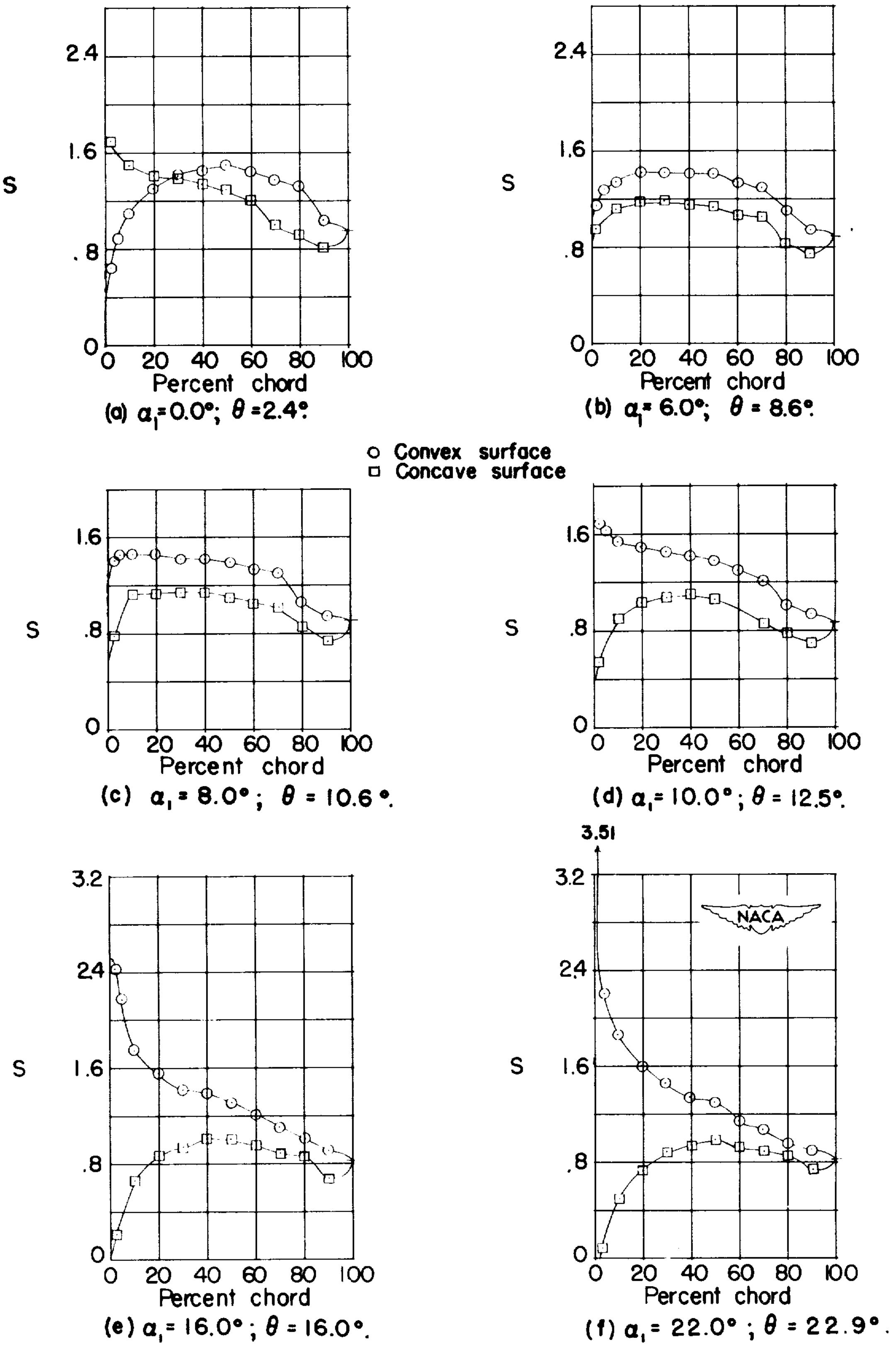

(a) $\alpha_1 = 0.0°$; $\theta = 2.4°$.

(b) $\alpha_1 = 6.0°$; $\theta = 8.6°$.

(c) $\alpha_1 = 8.0°$; $\theta = 10.6°$.

(d) $\alpha_1 = 10.0°$; $\theta = 12.5°$.

(e) $\alpha_1 = 16.0°$; $\theta = 16.0°$.

(f) $\alpha_1 = 22.0°$; $\theta = 22.9°$.

Figure 12.- Blade-surface pressure distributions and blade section characteristics for the cascade combination, $\beta_1 = 30°$, $\sigma = 1.25$, and blade section, NACA 65-410.

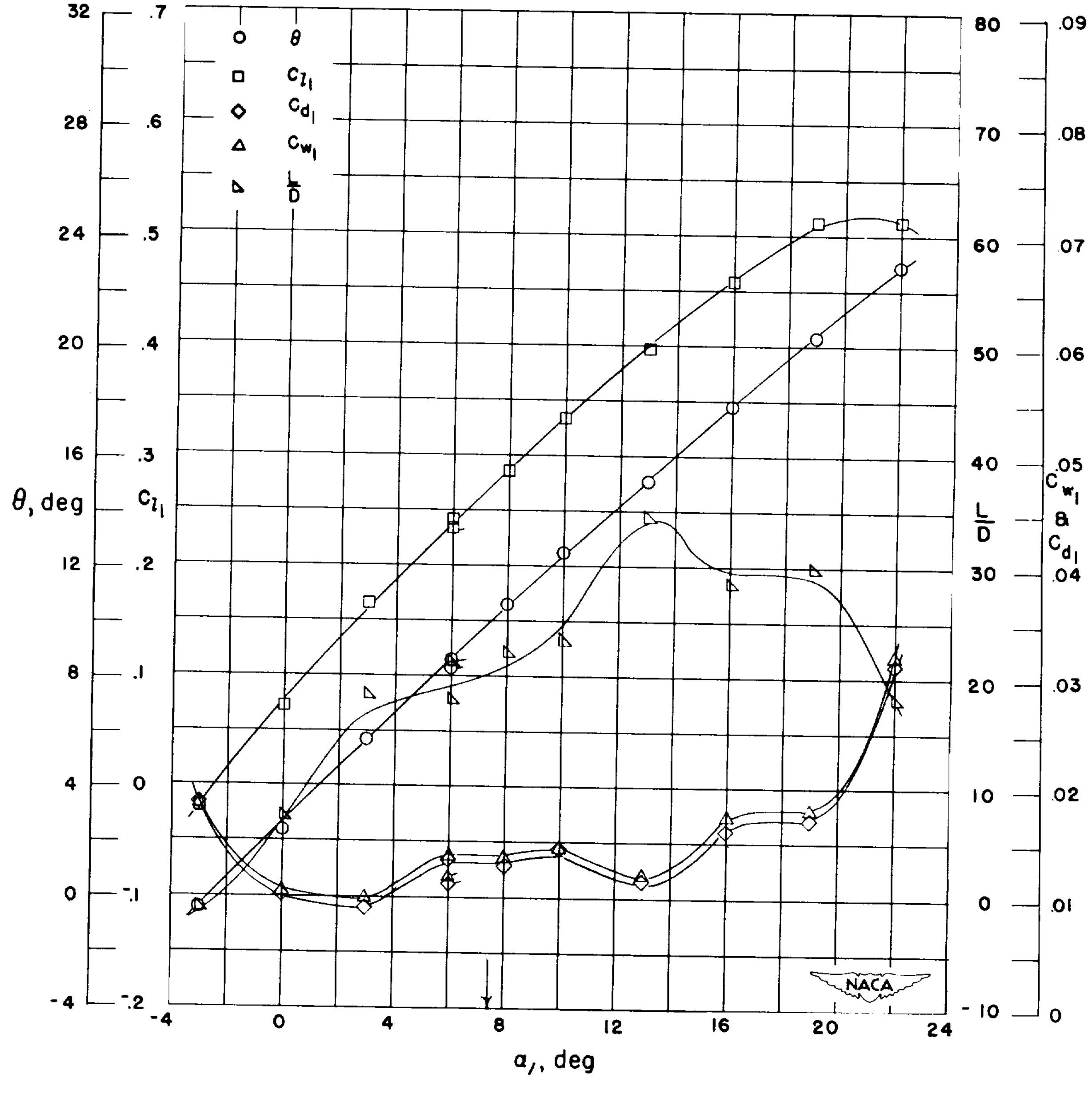

(g) Section characteristics; arrow shows design angle of attack; flagged symbol indicates leading-edge roughness.

Figure 12.- Concluded.

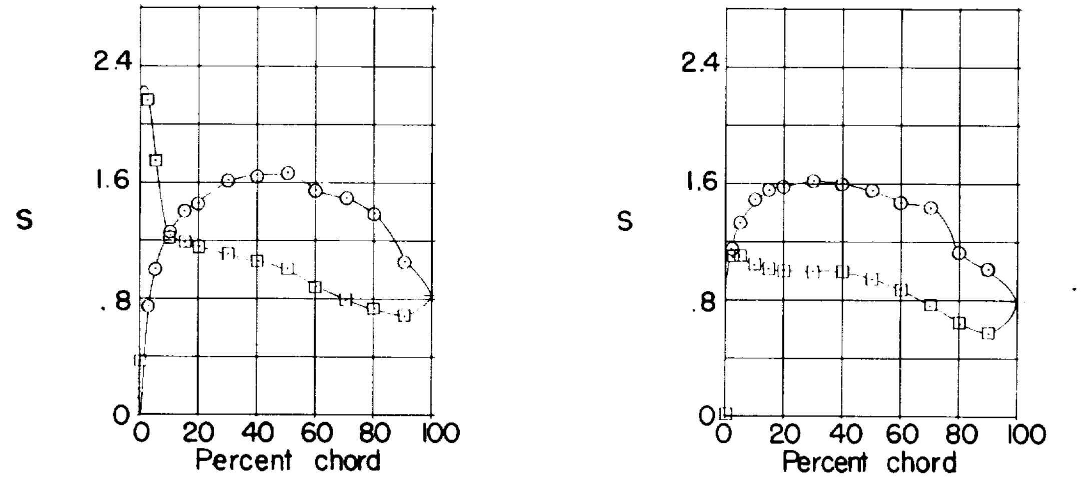

(a) $\alpha_1 = 4.1°$; $\theta = 13.9°$.

(b) $\alpha_1 = 10.1°$; $\theta = 19.9°$.

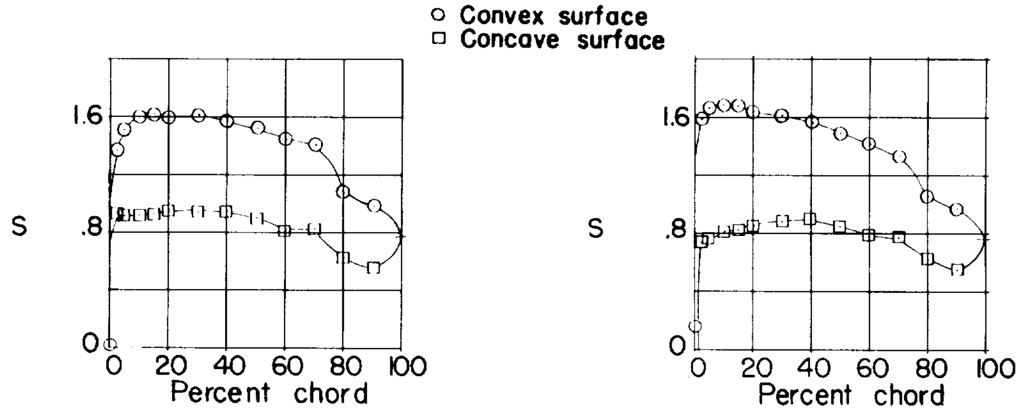

(c) $\alpha_1 = 13.1°$; $\theta = 22.7°$.

(d) $\alpha_1 = 15.1°$; $\theta = 24.5°$.

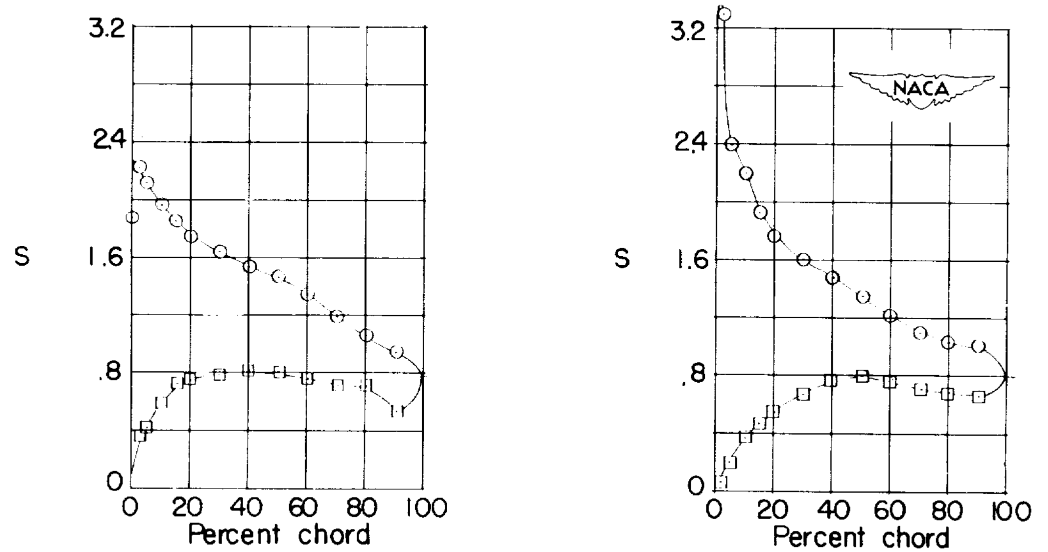

(e) $\alpha_1 = 23.1°$; $\theta = 31.9°$.

(f) $\alpha_1 = 32.1°$; $\theta = 38.3°$.

Figure 13.- Blade-surface pressure distributions and blade section characteristics for the cascade combination, $\beta_1 = 30^{\circ}$, $\sigma = 1.25$, and blade section, NACA 65-(12)10.

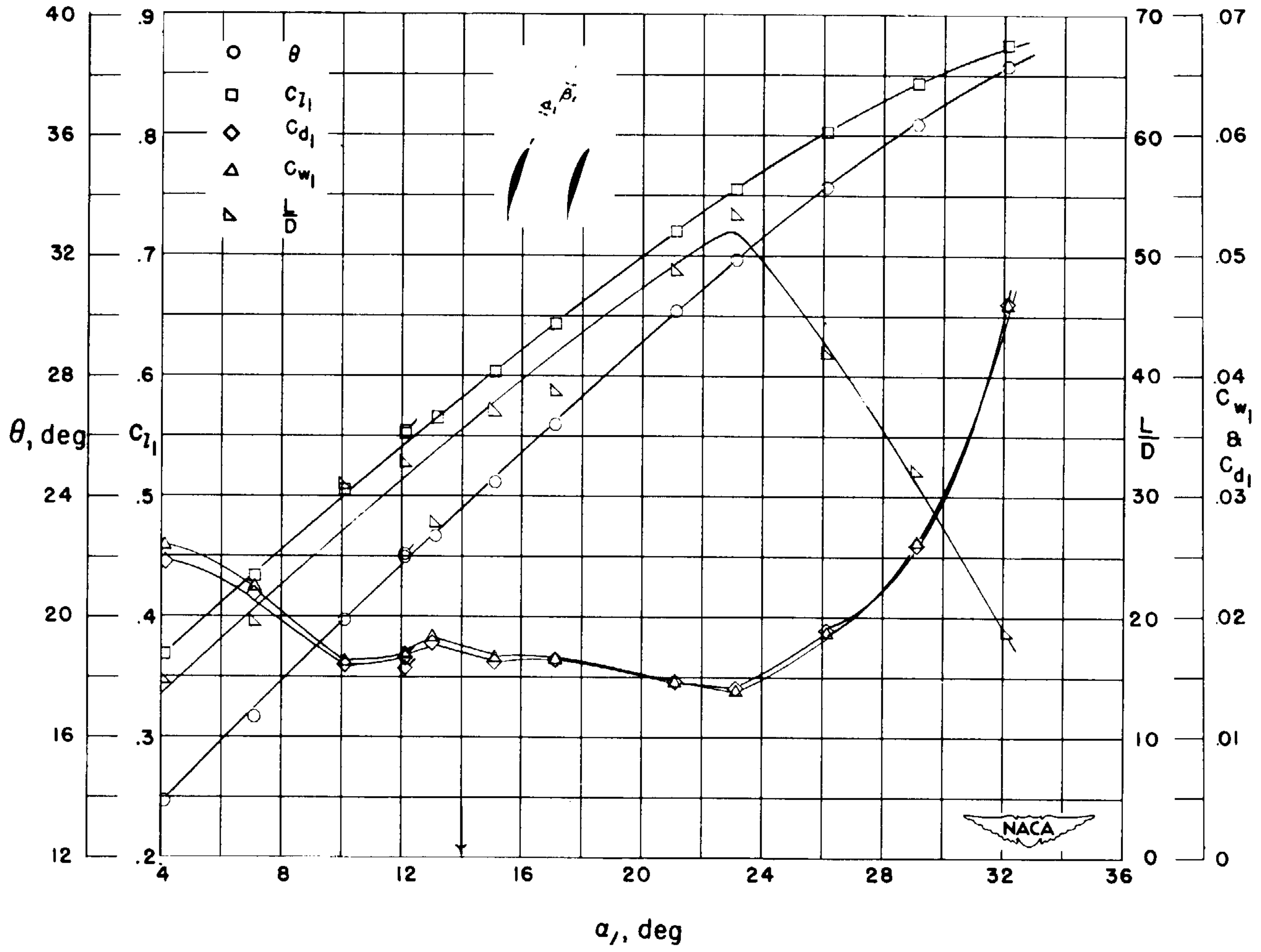

(g) Section characteristics; arrow shows design angle of attack; flagged symbol indicates leading-edge roughness

Figure 13.- Concluded.

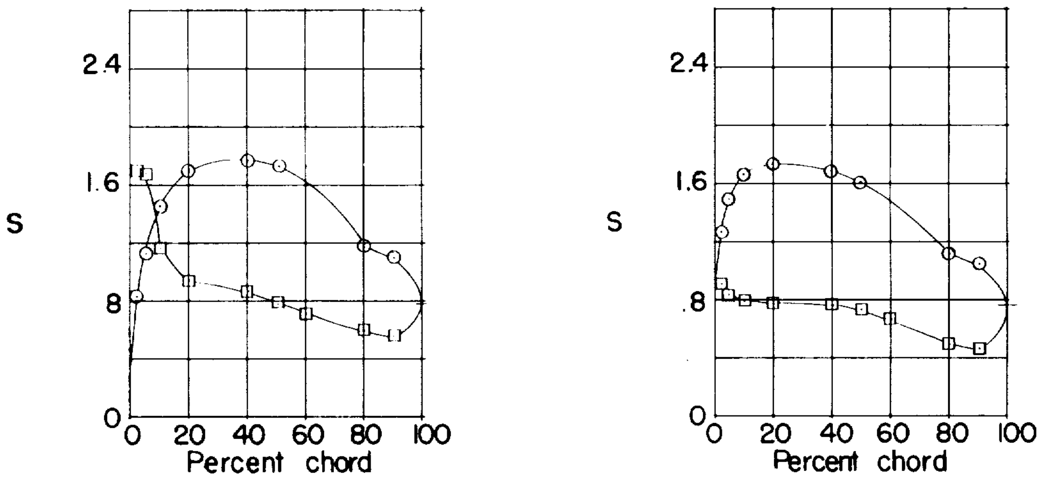

(a) α_1 = 11.0° ; θ = 25.2°.

(b) α_1 = 17.0° ; θ = 31.9°.

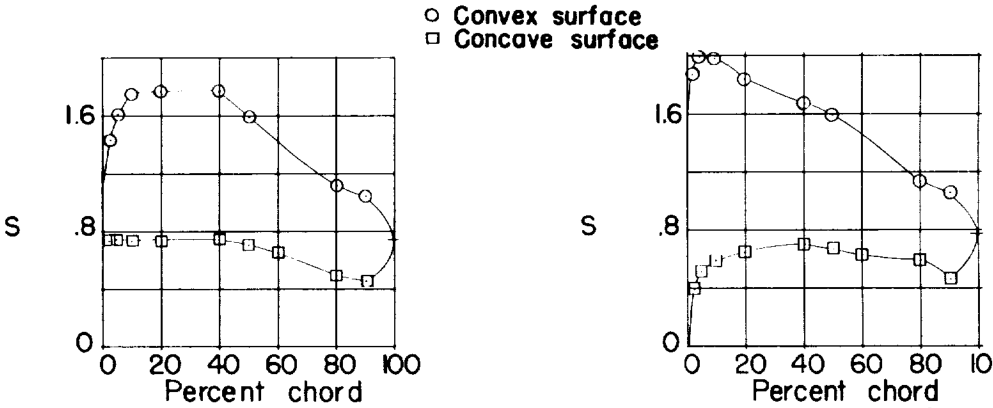

(c) α_1 = 19.0° ; θ = 33.8°.

(d) α_1 = 24.0° ; θ = 38.6°.

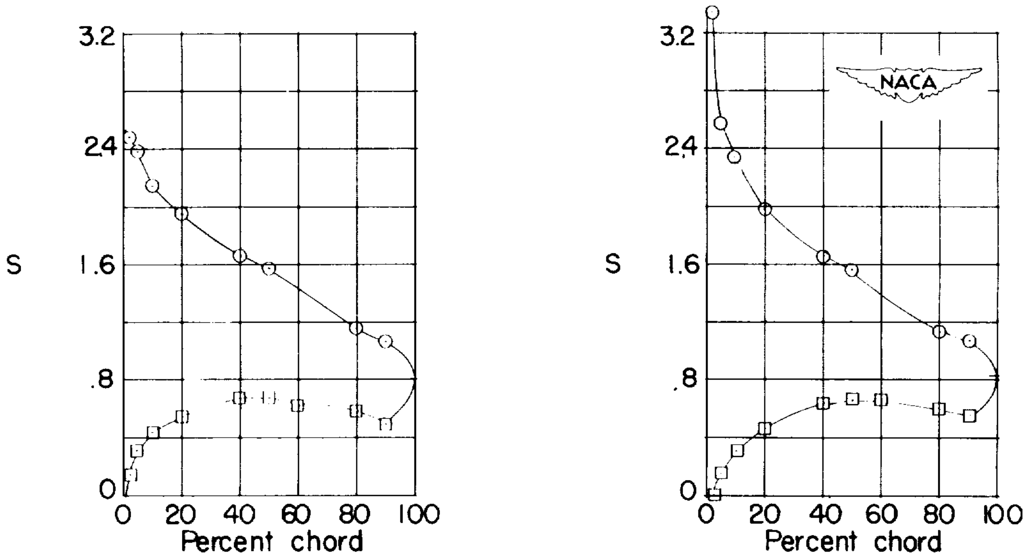

(e) α_1 = 30.0° ; θ = 43.5°.

(f) α_1 = 36.0° ; θ = 47.4°.

Figure 14.- Blade-surface pressure distributions and blade section characteristics for the cascade combination, $\beta_1 = 30^{\circ}$, $\sigma = 1.25$, and blade section, NACA 65-(18)10.

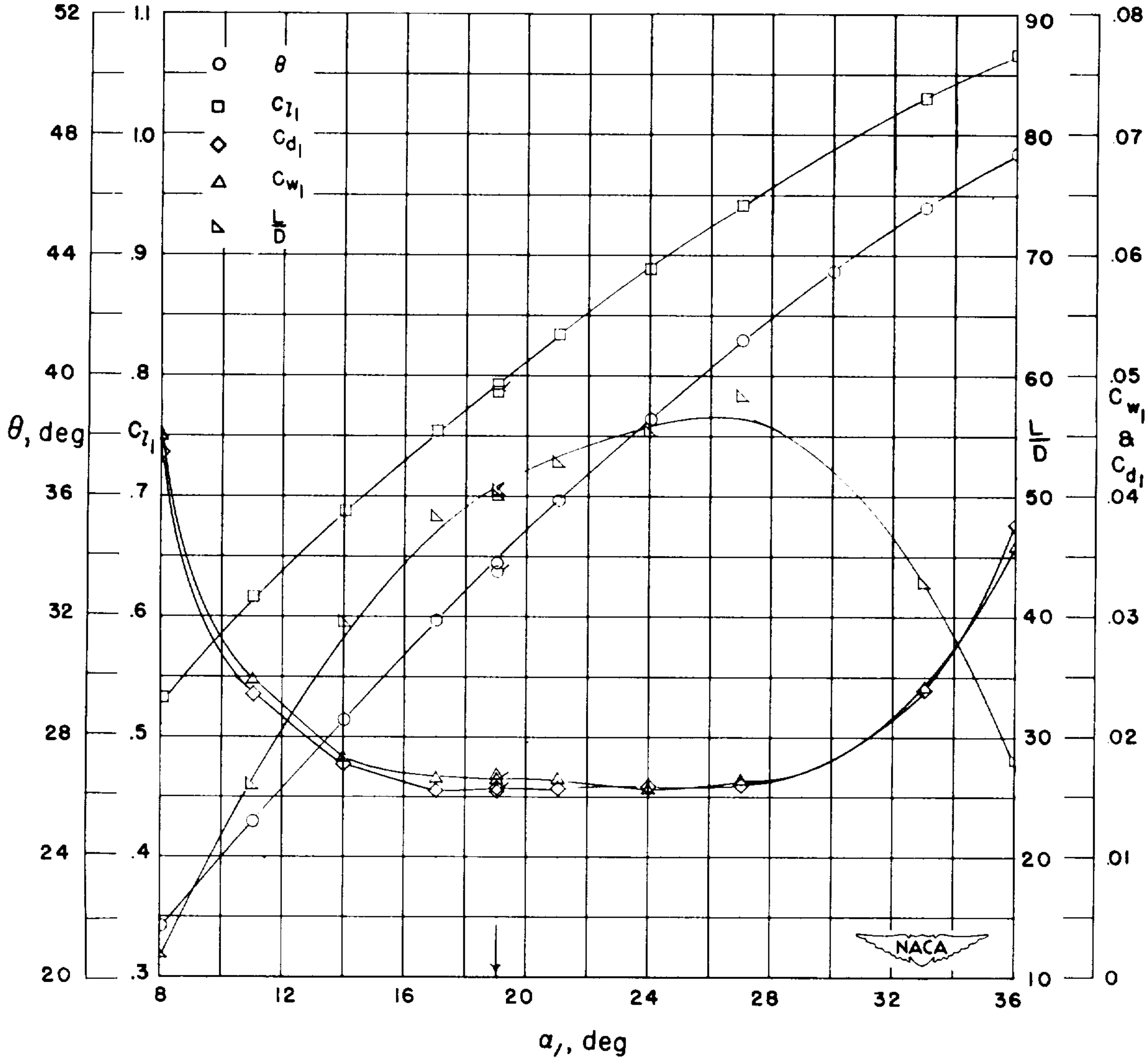

(g) Section characteristics; arrow shows design angle of attack; flagged symbol indicates leading-edge roughness.

Figure 14.- Concluded.

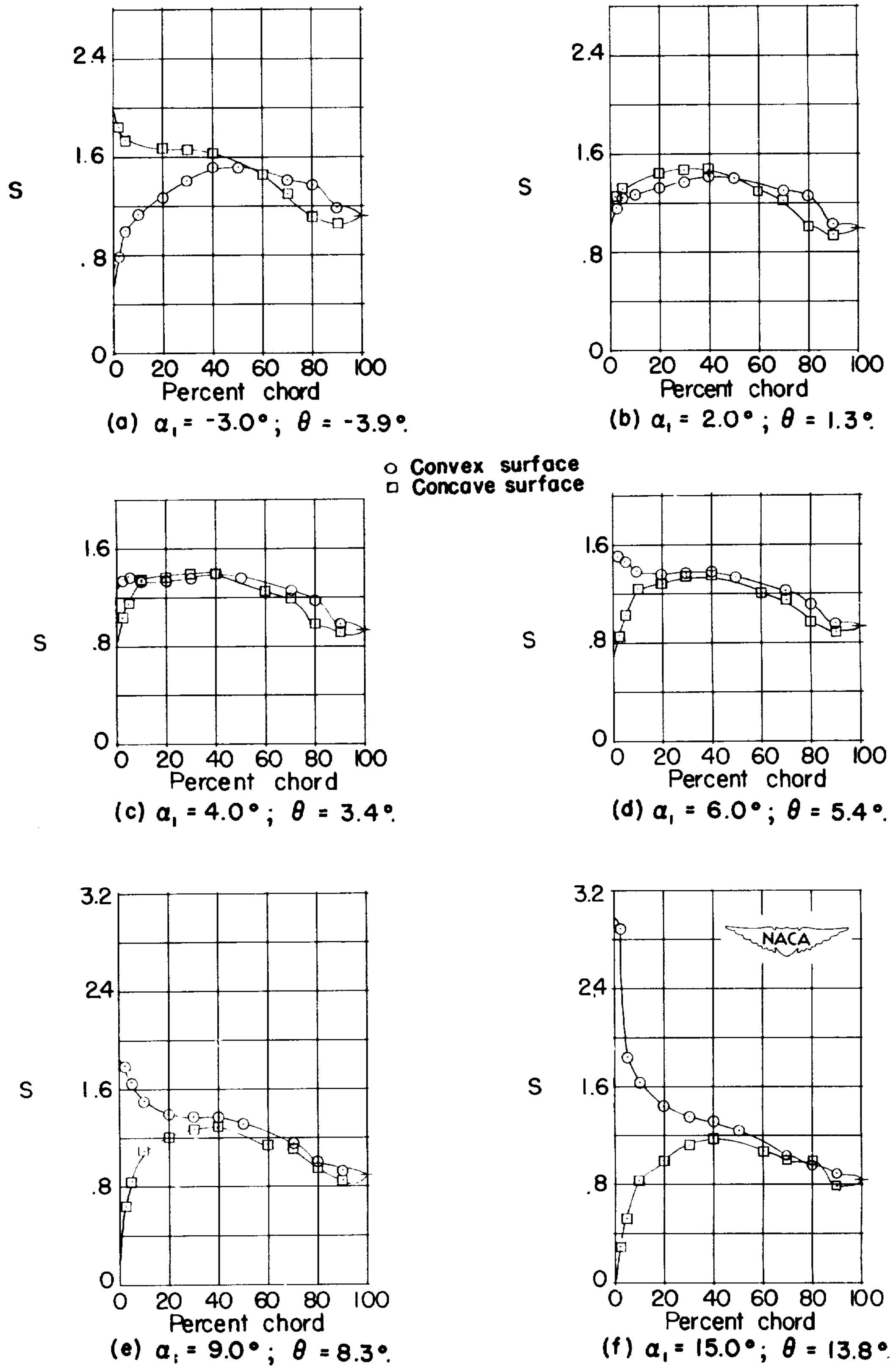

(a) $\alpha_1 = -3.0°$; $\theta = -3.9°$.

(b) $\alpha_1 = 2.0°$; $\theta = 1.3°$.

(c) $\alpha_1 = 4.0°$; $\theta = 3.4°$.

(d) $\alpha_1 = 6.0°$; $\theta = 5.4°$.

(e) $\alpha_1 = 9.0°$; $\theta = 8.3°$.

(f) $\alpha_1 = 15.0°$; $\theta = 13.8°$.

Figure 15.- Blade-surface pressure distributions and blade section characteristics for the cascade combination, $\beta_1 = 30^\circ$, $\sigma = 1.50$, and blade section, NACA 65-010.

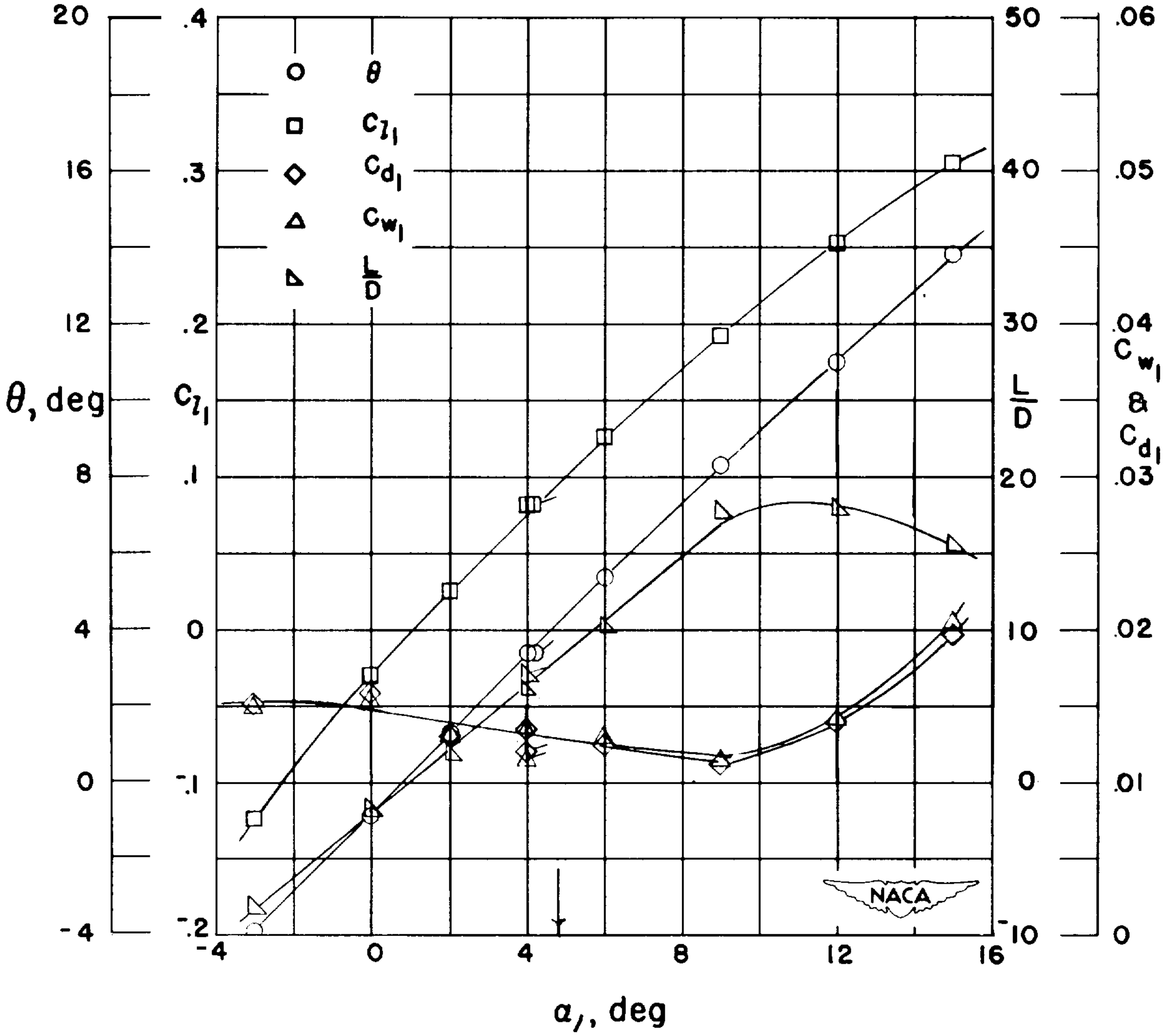

(g) Section characteristics; arrow shows design angle of attack; flagged symbol indicates leading-edge roughness.

Figure 15.- Concluded.

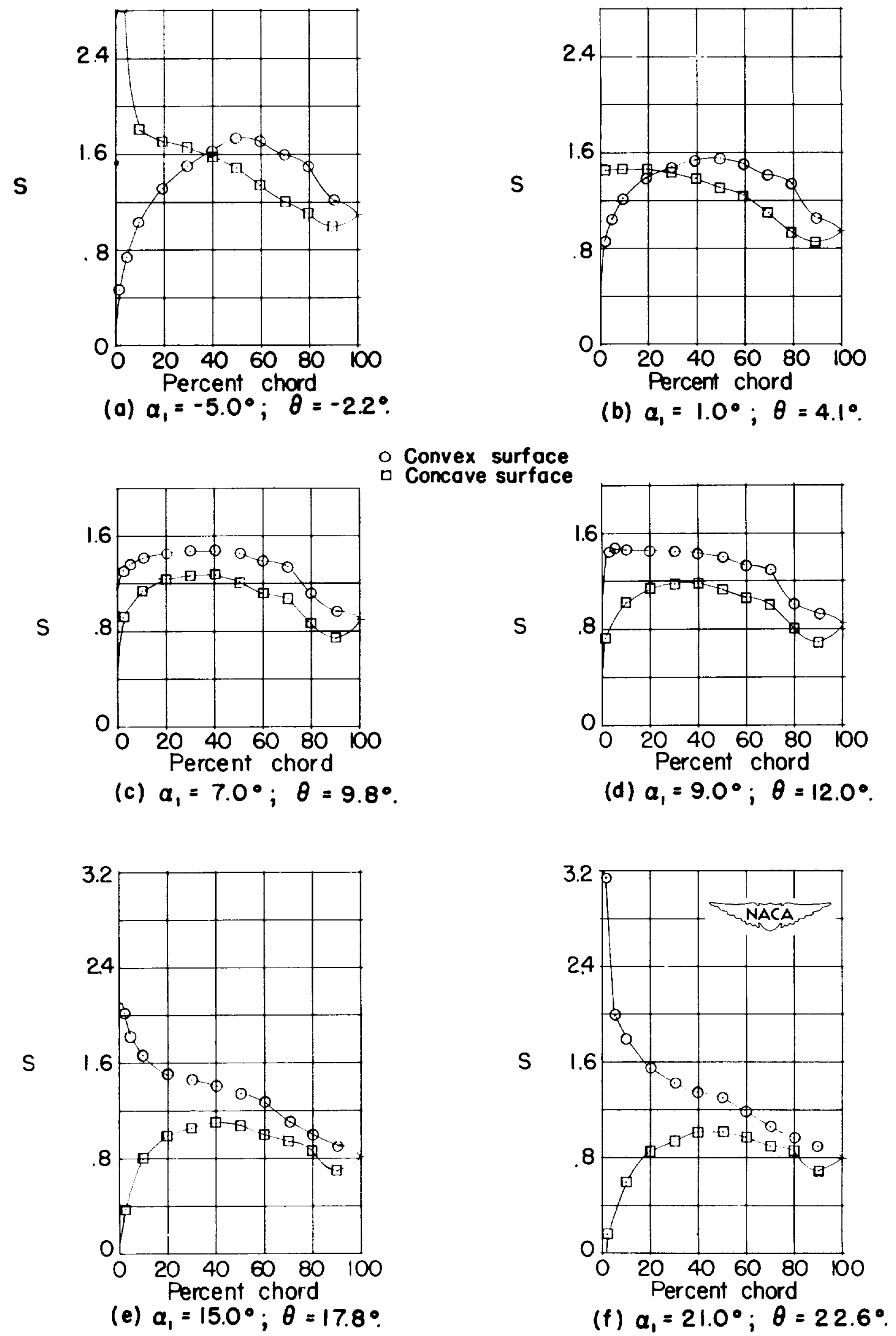

(a) $\alpha_1 = -5.0°$; $\theta = -2.2°$.

(b) $\alpha_1 = 1.0°$; $\theta = 4.1°$.

(c) $\alpha_1 = 7.0°$; $\theta = 9.8°$.

(d) $\alpha_1 = 9.0°$; $\theta = 12.0°$.

(e) $\alpha_1 = 15.0°$; $\theta = 17.8°$.

(f) $\alpha_1 = 21.0°$; $\theta = 22.6°$.

Figure 16.- Blade-surface pressure distributions and blade section characteristics for the cascade combination, $\beta_1 = 30°$, $\sigma = 1.50$, and blade section, NACA 65-410.

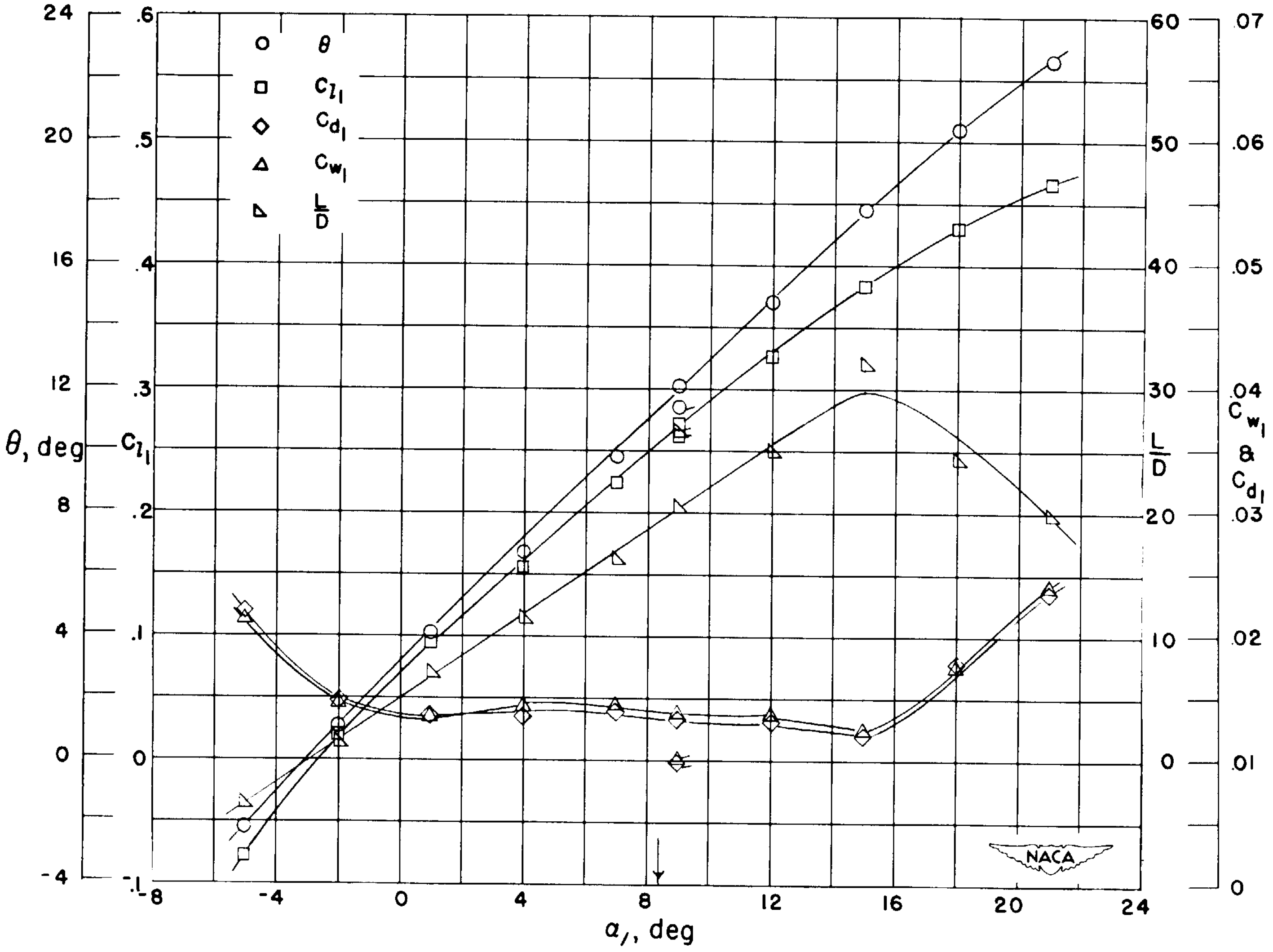

(g) Section characteristics; arrow shows design angle of attack; flagged symbol indicates leading-edge roughness

Figure 16.- Concluded.

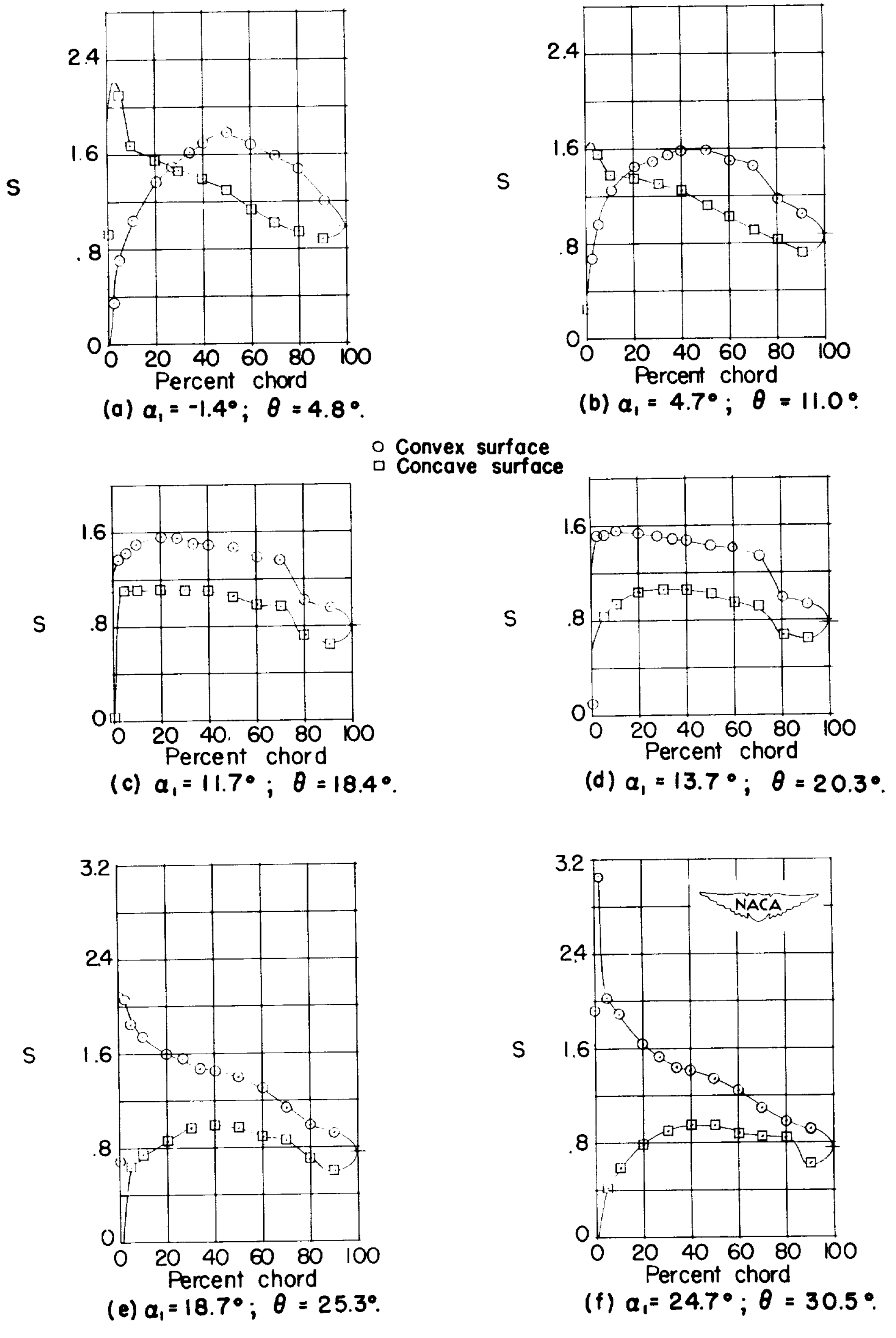

(a) $\alpha_1 = -1.4°$; $\theta = 4.8°$.

(b) $\alpha_1 = 4.7°$; $\theta = 11.0°$.

(c) $\alpha_1 = 11.7°$; $\theta = 18.4°$.

(d) $\alpha_1 = 13.7°$; $\theta = 20.3°$.

(e) $\alpha_1 = 18.7°$; $\theta = 25.3°$.

(f) $\alpha_1 = 24.7°$; $\theta = 30.5°$.

Figure 17.- Blade-surface pressure distributions and blade section characteristics for the cascade combination, $\beta_1 = 30^{\circ}$, $\sigma = 1.50$ and blade section, NACA 65-810.

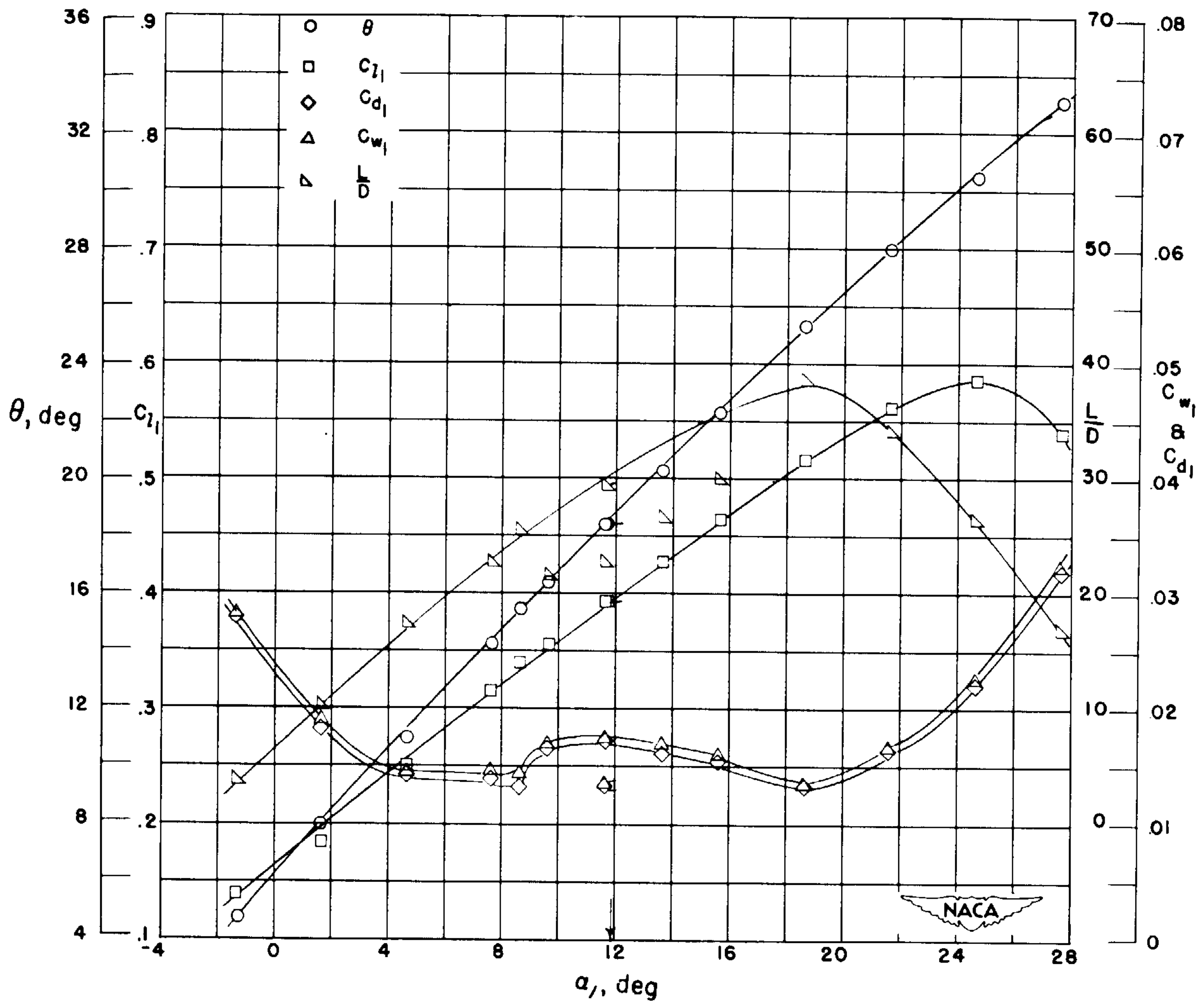

(g) Section characteristics; arrow shows design angle of attack; flagged symbol indicates leading-edge roughness.

Figure 17.- Concluded.

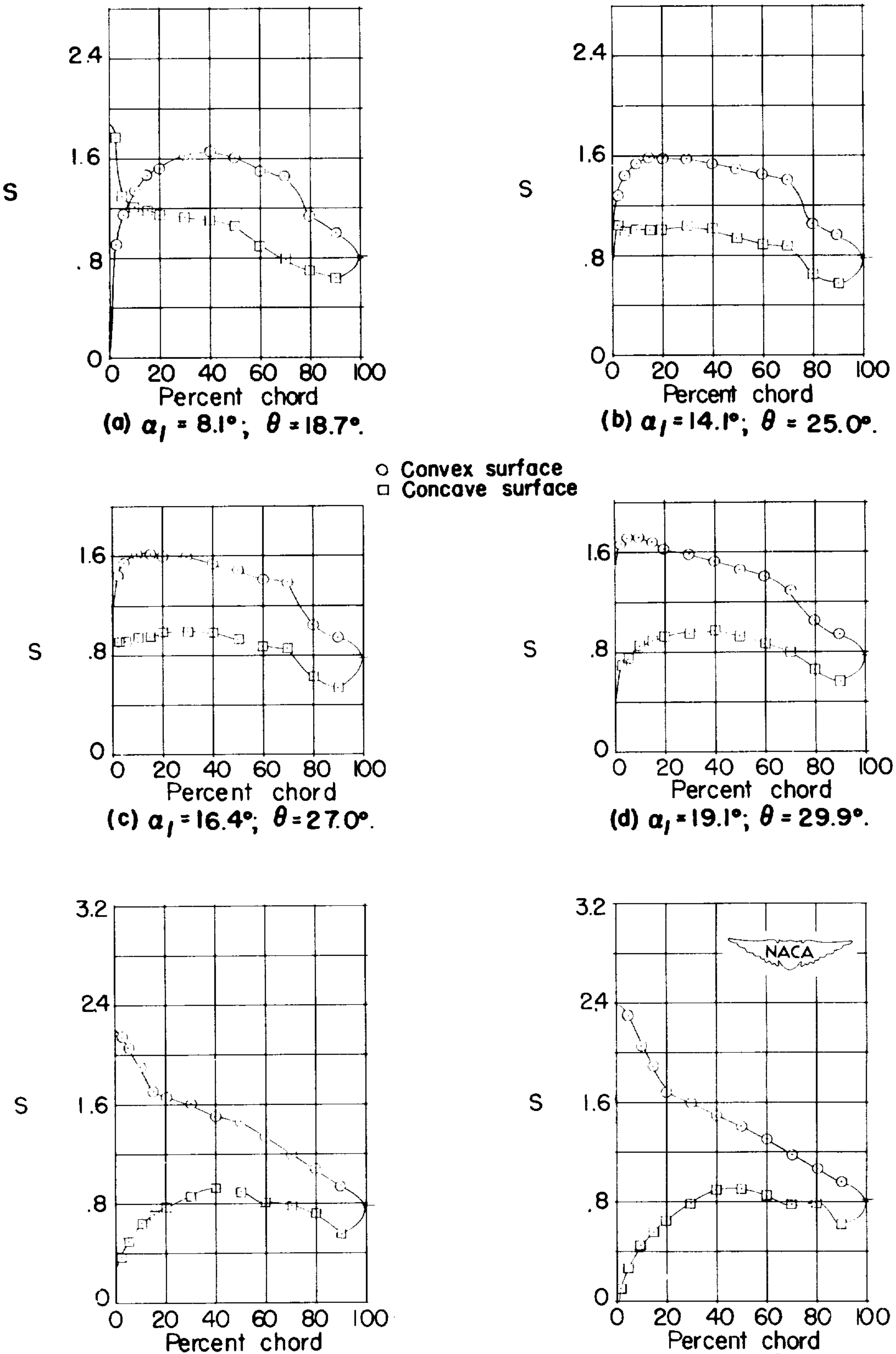

(a) α_l = 8.1°; θ = 18.7°.

(b) α_l = 14.1°; θ = 25.0°.

(c) α_l = 16.4°; θ = 27.0°.

(d) α_l = 19.1°; θ = 29.9°.

(e) α_l = 25.1°; θ = 35.7°.

(f) α_l = 33.1°; θ = 42.8°.

Figure 18.- Blade-surface pressure distributions and blade section characteristics for the cascade combination, $\beta_1 = 30^\circ$, $\sigma = 1.50$, and blade section, NACA 65-(12)10.

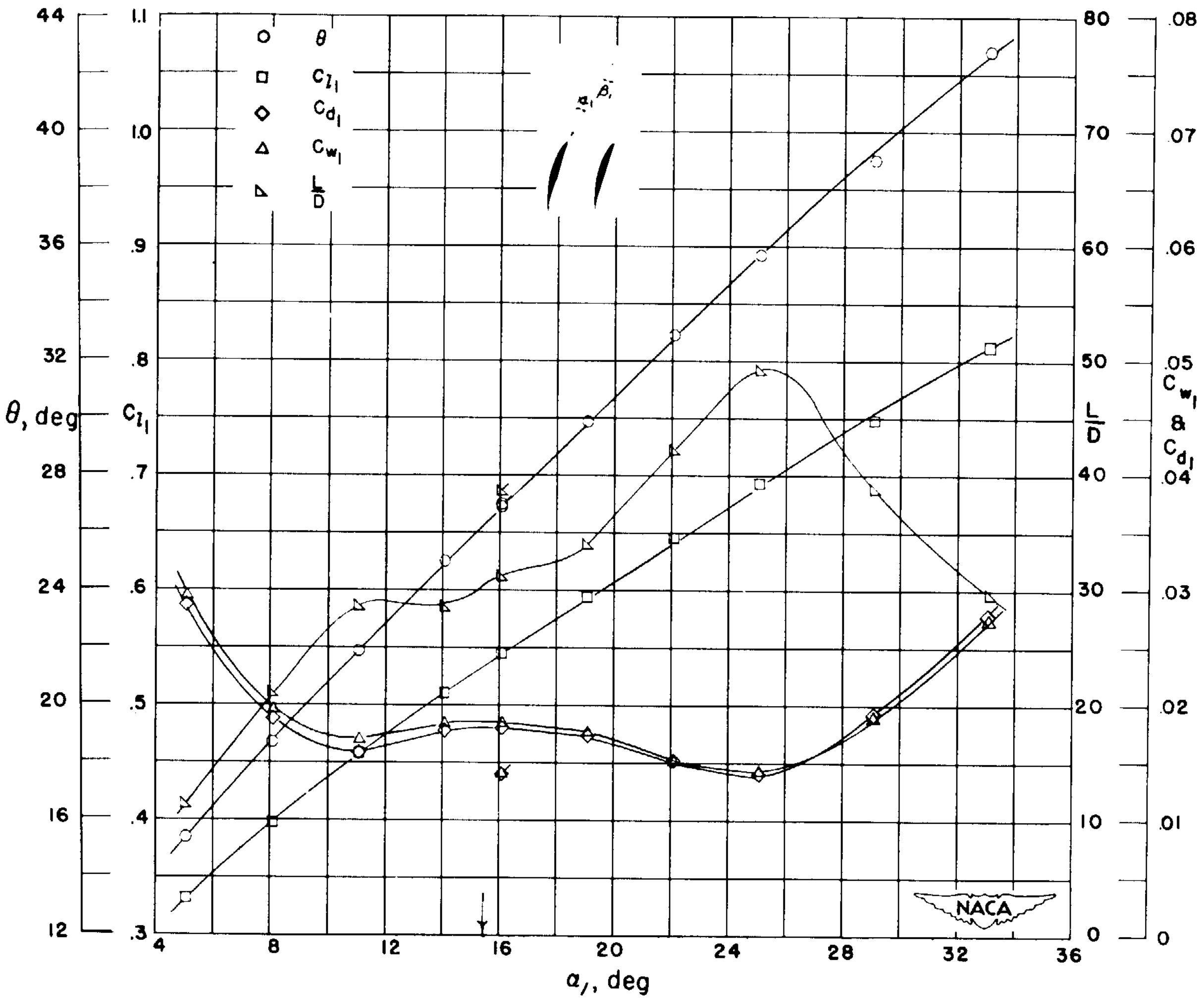

(g) Section characteristics; arrow shows design angle of attack; flagged symbol indicates leading-edge roughness.

Figure 18.- Concluded.

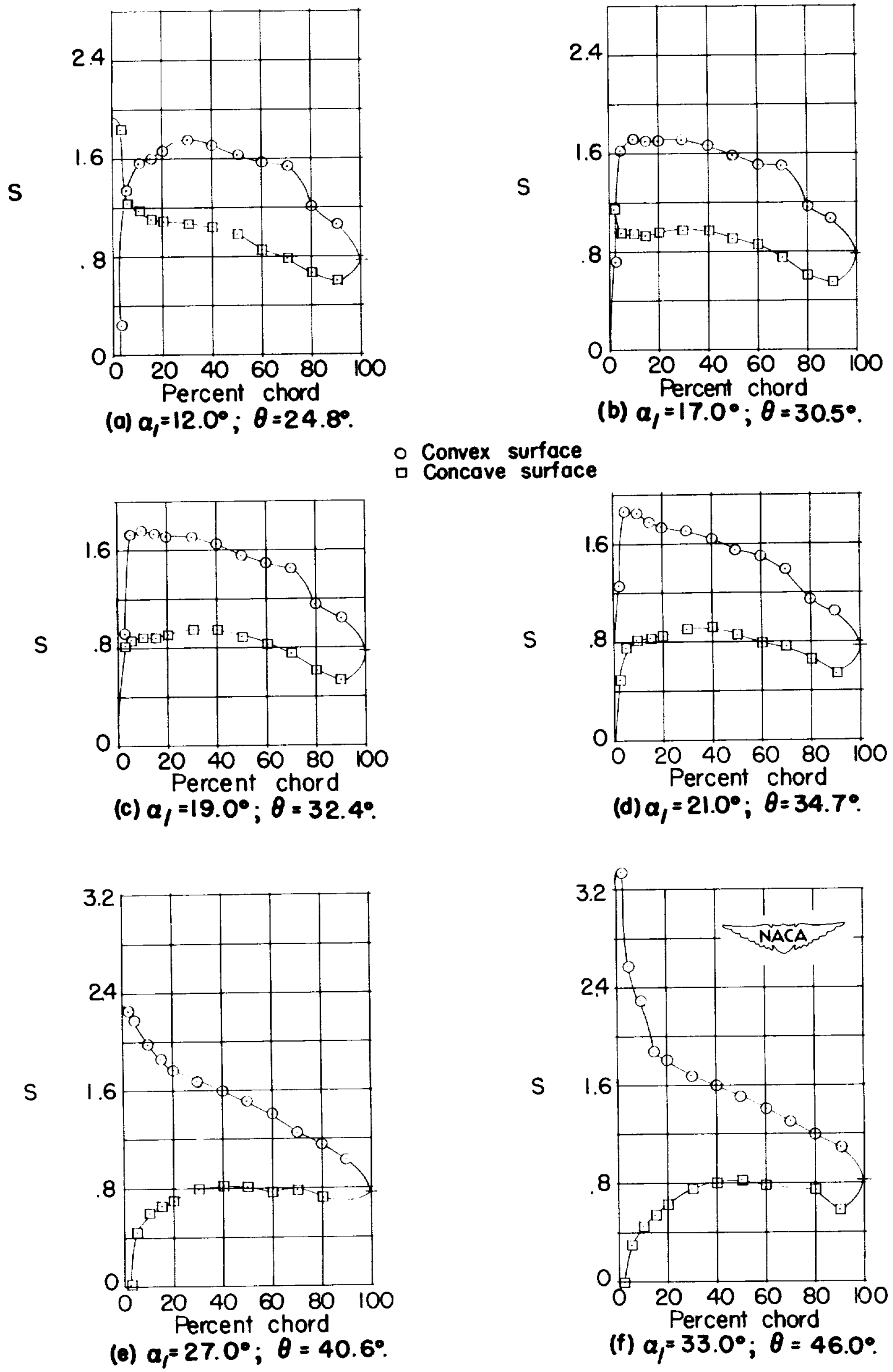

(a) $\alpha_l = 12.0°$; $\theta = 24.8°$.

(b) $\alpha_l = 17.0°$; $\theta = 30.5°$.

(c) $\alpha_l = 19.0°$; $\theta = 32.4°$.

(d) $\alpha_l = 21.0°$; $\theta = 34.7°$.

(e) $\alpha_l = 27.0°$; $\theta = 40.6°$.

(f) $\alpha_l = 33.0°$; $\theta = 46.0°$.

Figure 19.- Blade-surface pressure distributions and blade section characteristics for the cascade combination, $\beta_1 = 30°$, $\sigma = 1.50$, and blade section, NACA 65-(15)10.

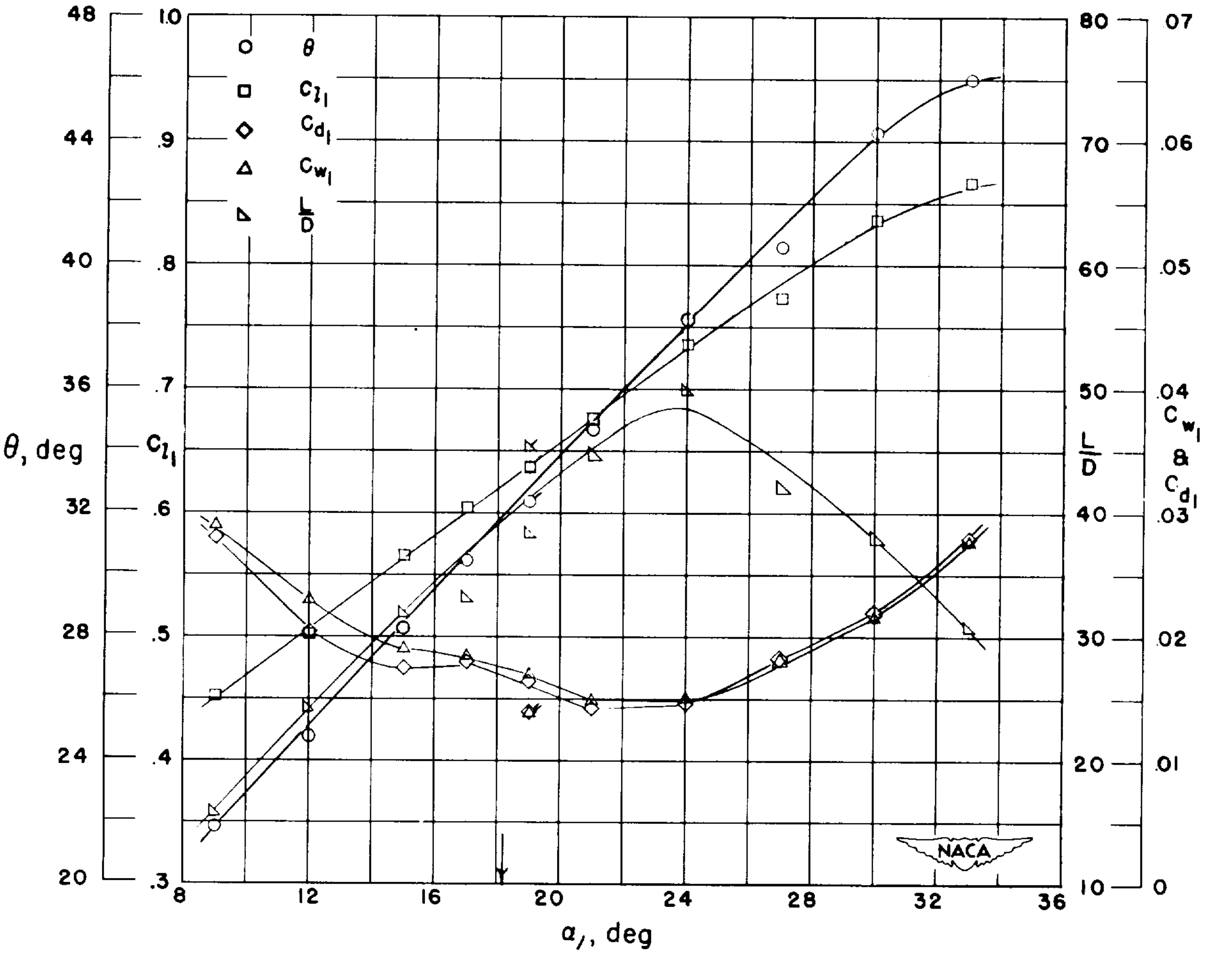

(g) Section characteristics; arrow shows design angle of attack; flagged symbol indicates leading-edge roughness.

Figure 19.- Concluded.

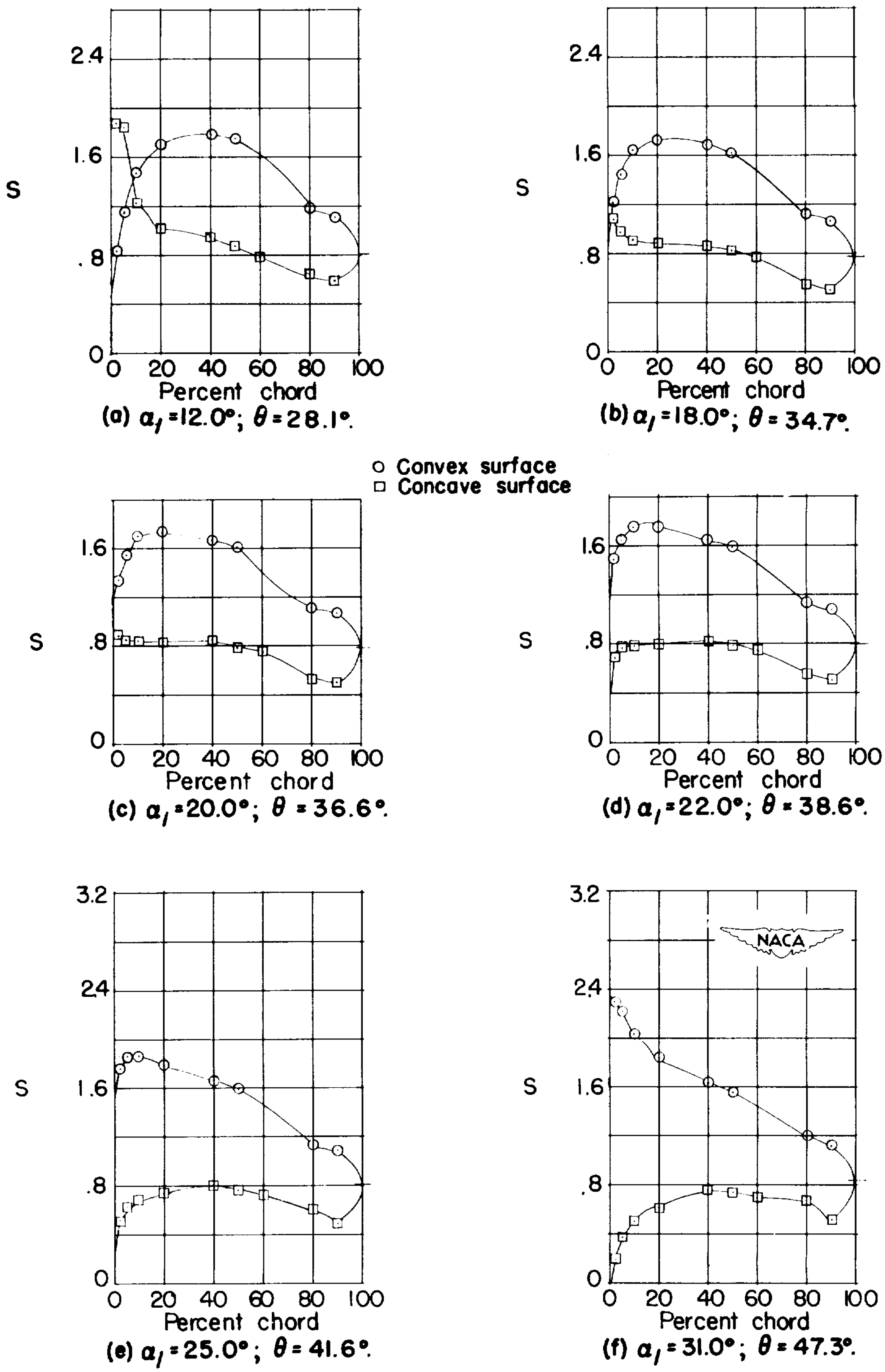

(a) $\alpha_l = 12.0°$; $\theta = 28.1°$.

(b) $\alpha_l = 18.0°$; $\theta = 34.7°$.

(c) $\alpha_l = 20.0°$; $\theta = 36.6°$.

(d) $\alpha_l = 22.0°$; $\theta = 38.6°$.

(e) $\alpha_l = 25.0°$; $\theta = 41.6°$.

(f) $\alpha_l = 31.0°$; $\theta = 47.3°$.

Figure 20.- Blade-surface pressure distributions and blade section characteristics for the cascade combination, $\beta_1 = 30°$, $\sigma = 1.50$, and blade section, NACA 65-(18)10.

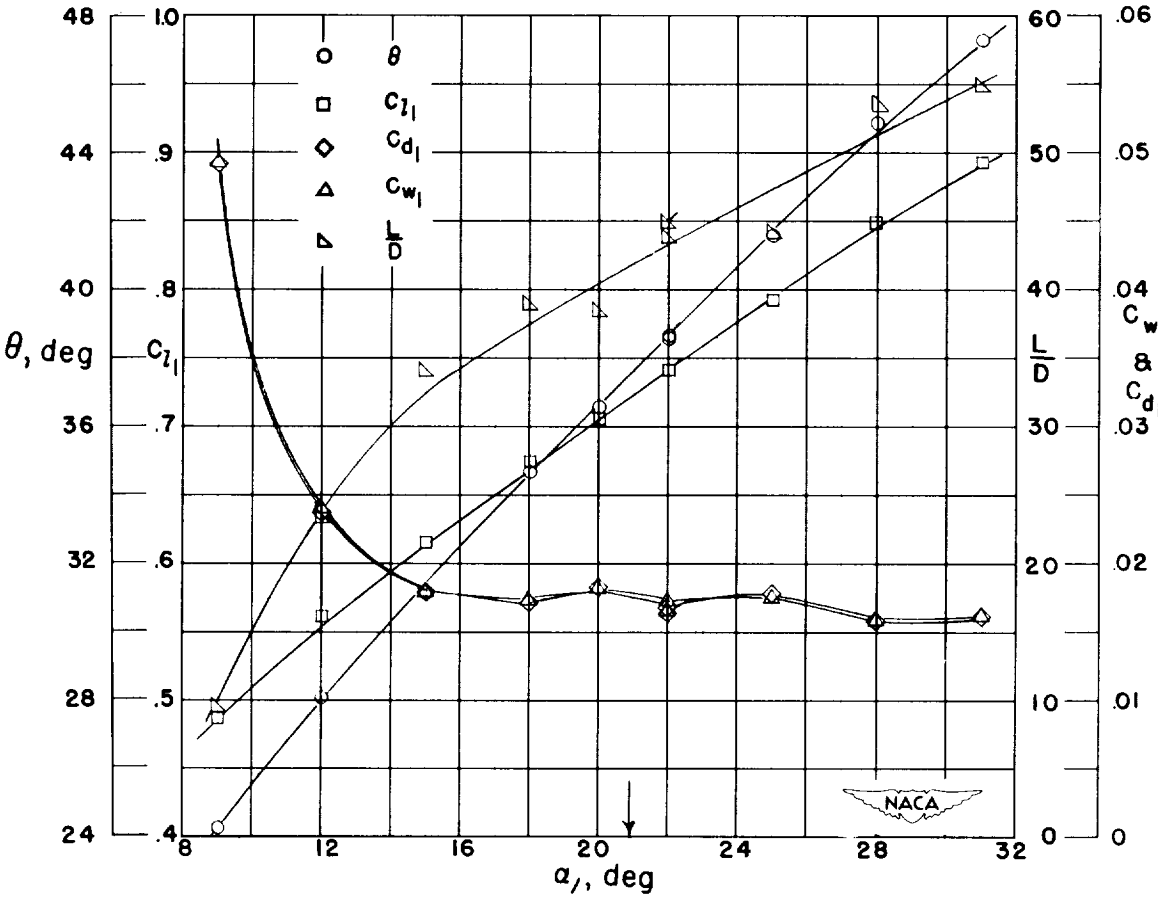

(g) Section characteristics; arrow shows design angle of attack; flagged symbol indicates leading-edge roughness.

Figure 20.- Concluded.

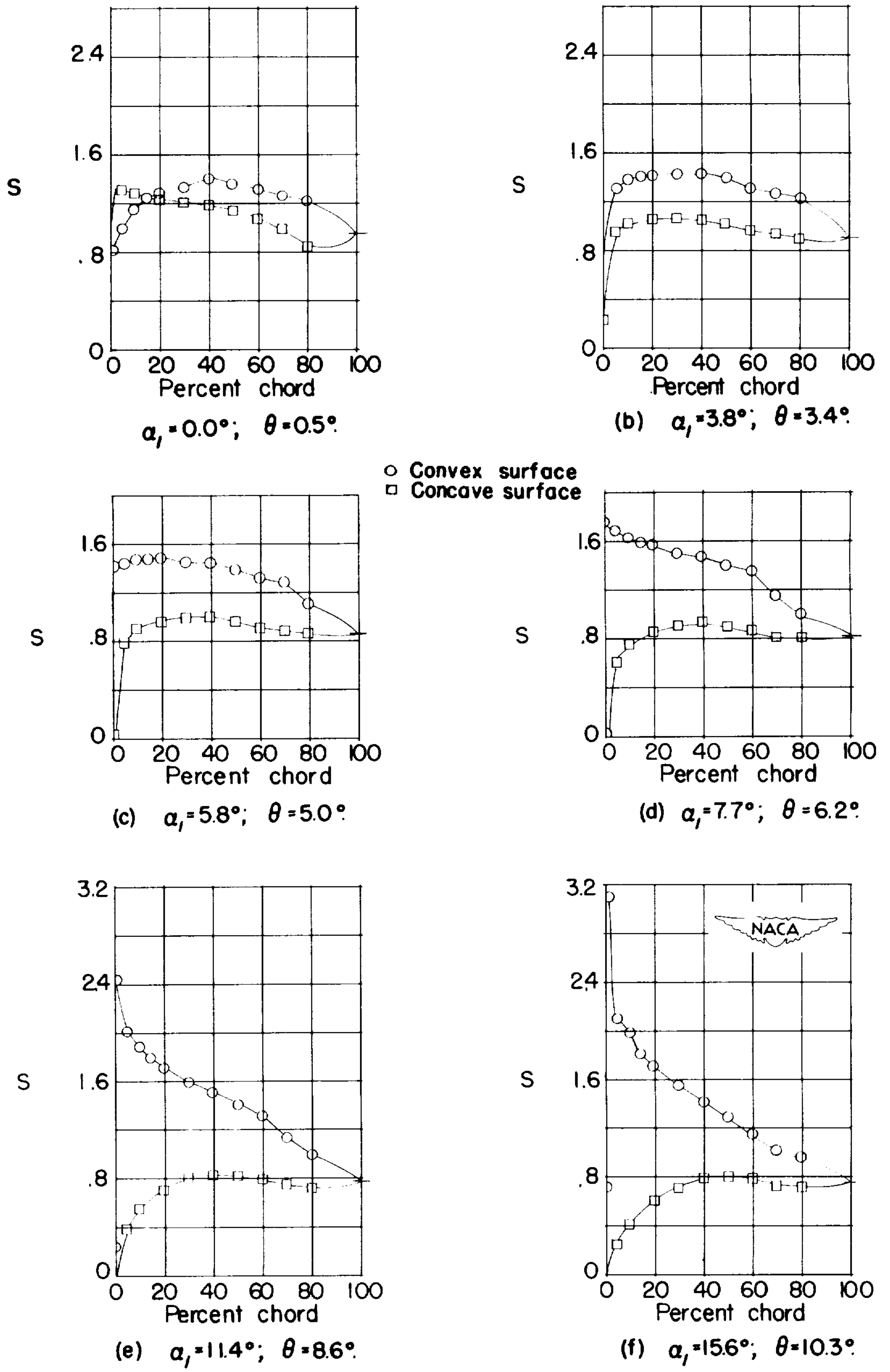

$a_1 = 0.0°$; $\theta = 0.5°$

(b) $a_1 = 3.8°$; $\theta = 3.4°$

(c) $a_1 = 5.8°$; $\theta = 5.0°$

(d) $a_1 = 7.7°$; $\theta = 6.2°$

(e) $a_1 = 11.4°$; $\theta = 8.6°$

(f) $a_1 = 15.6°$; $\theta = 10.3°$

Figure 21.- Blade-surface pressure distributions and blade section characteristics for the cascade combination, $\beta_1 = 45°$, $\sigma = 0.50$, and blade section, NACA 65-410.

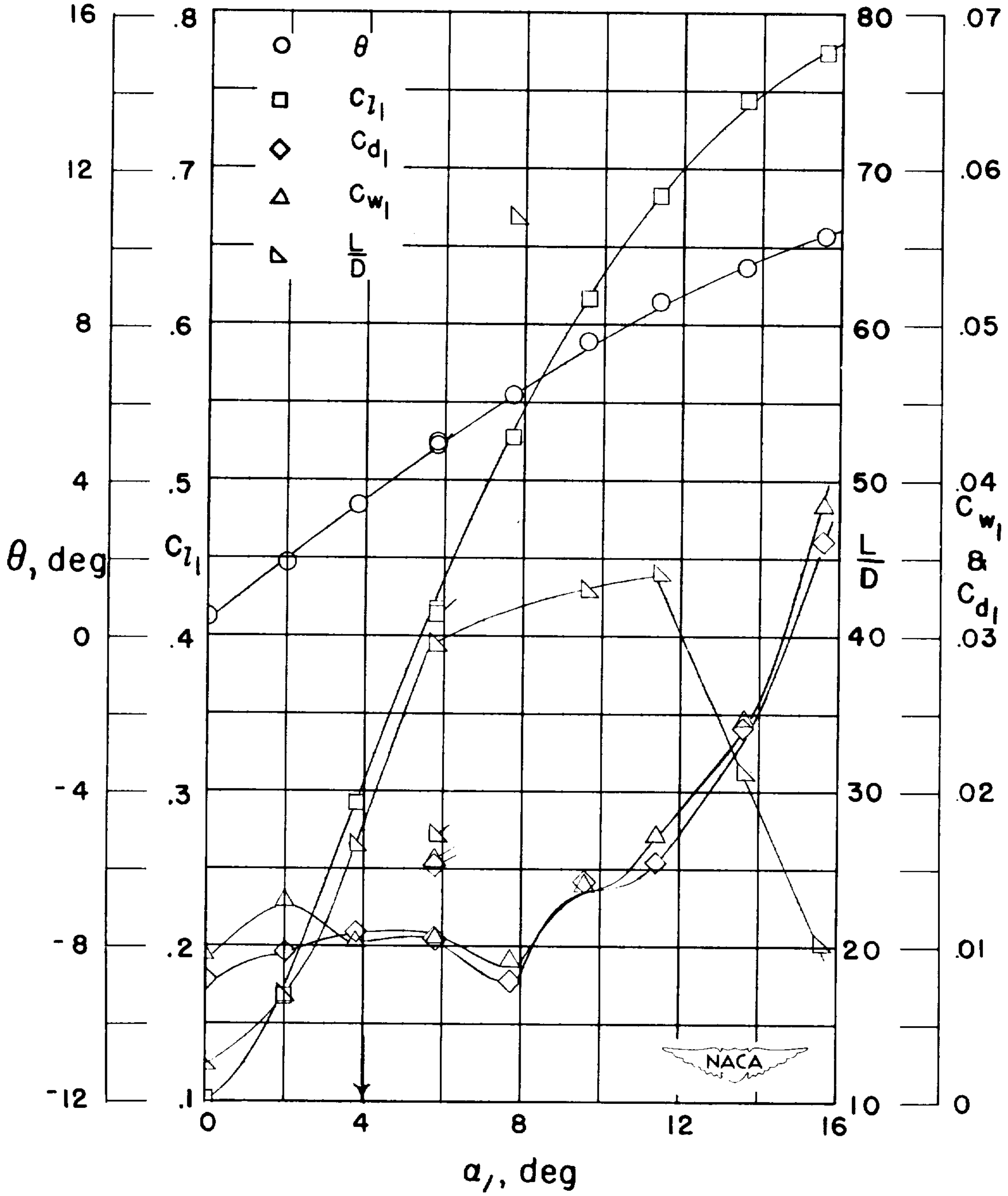

(g) Section characteristics; arrow shows design angle of attack; flagged symbol indicates leading-edge roughness

Figure 21.- Concluded.

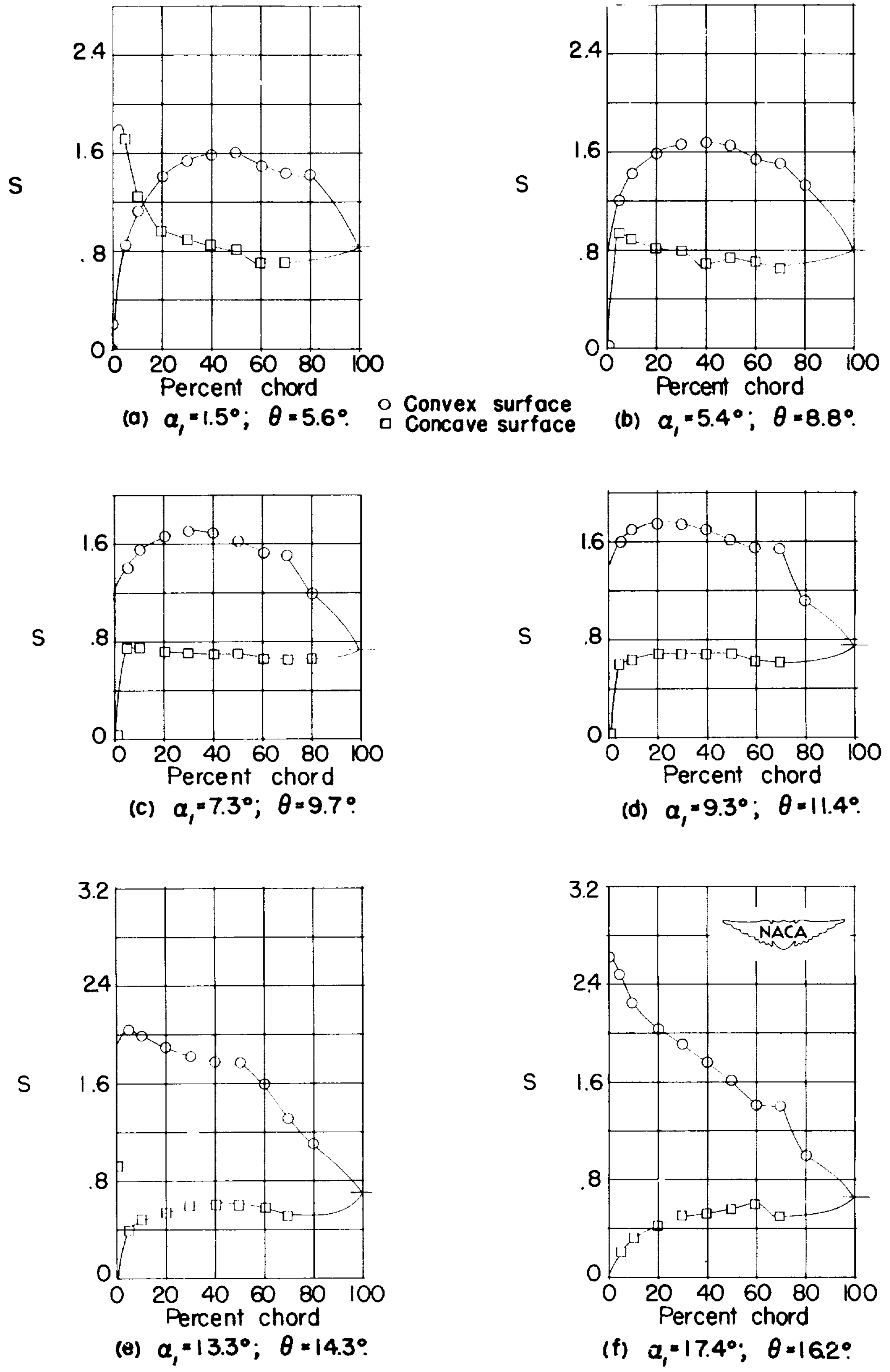

Figure 22.- Blade-surface pressure distributions and blade section characteristics for the cascade combination, $\beta_1 = 45^{\circ}$, $\sigma = 0.50$, and blade section, NACA 65-(12)10.

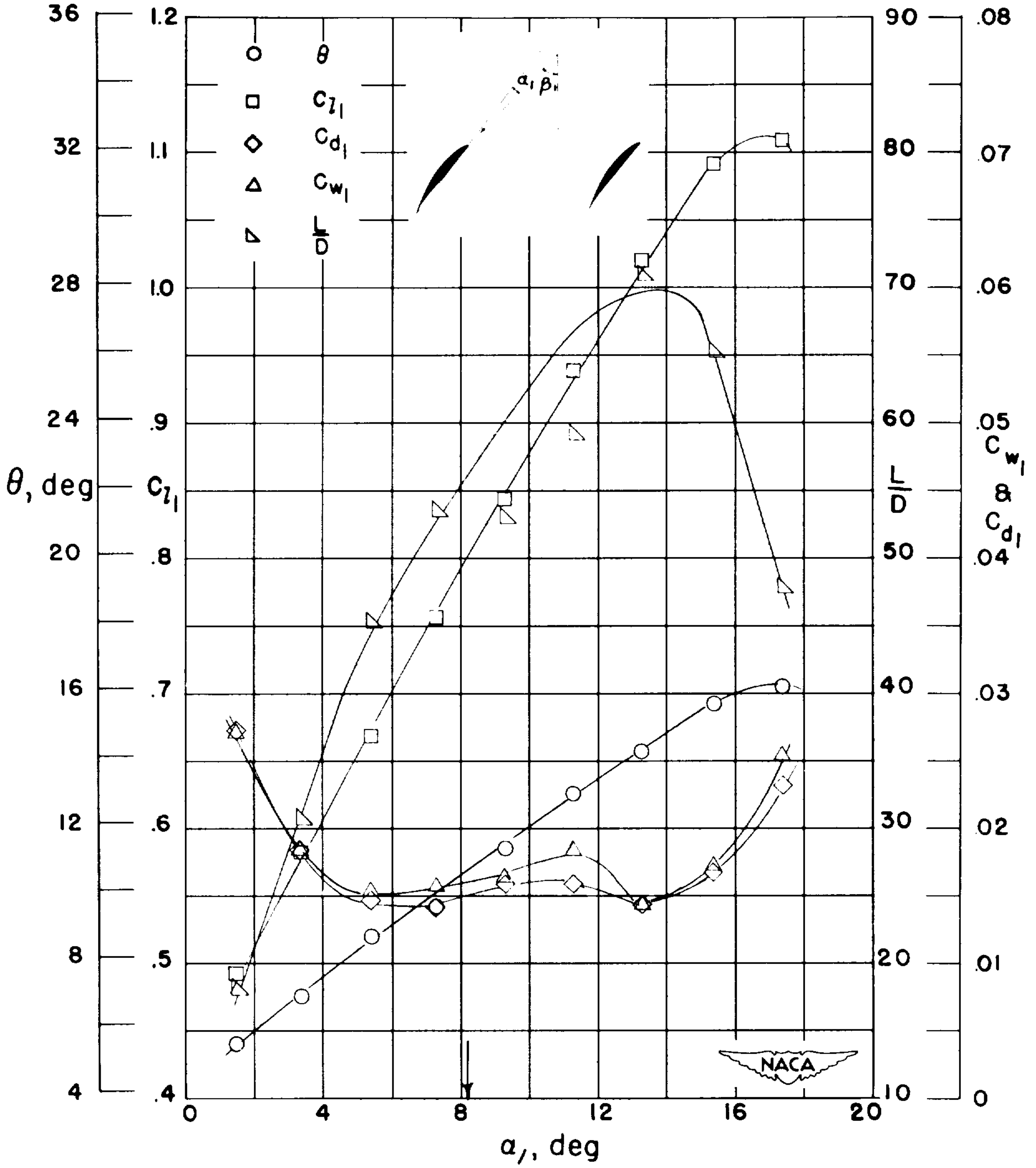

(g) Section characteristics; arrow shows design angle of attack.

Figure 22.- Concluded.

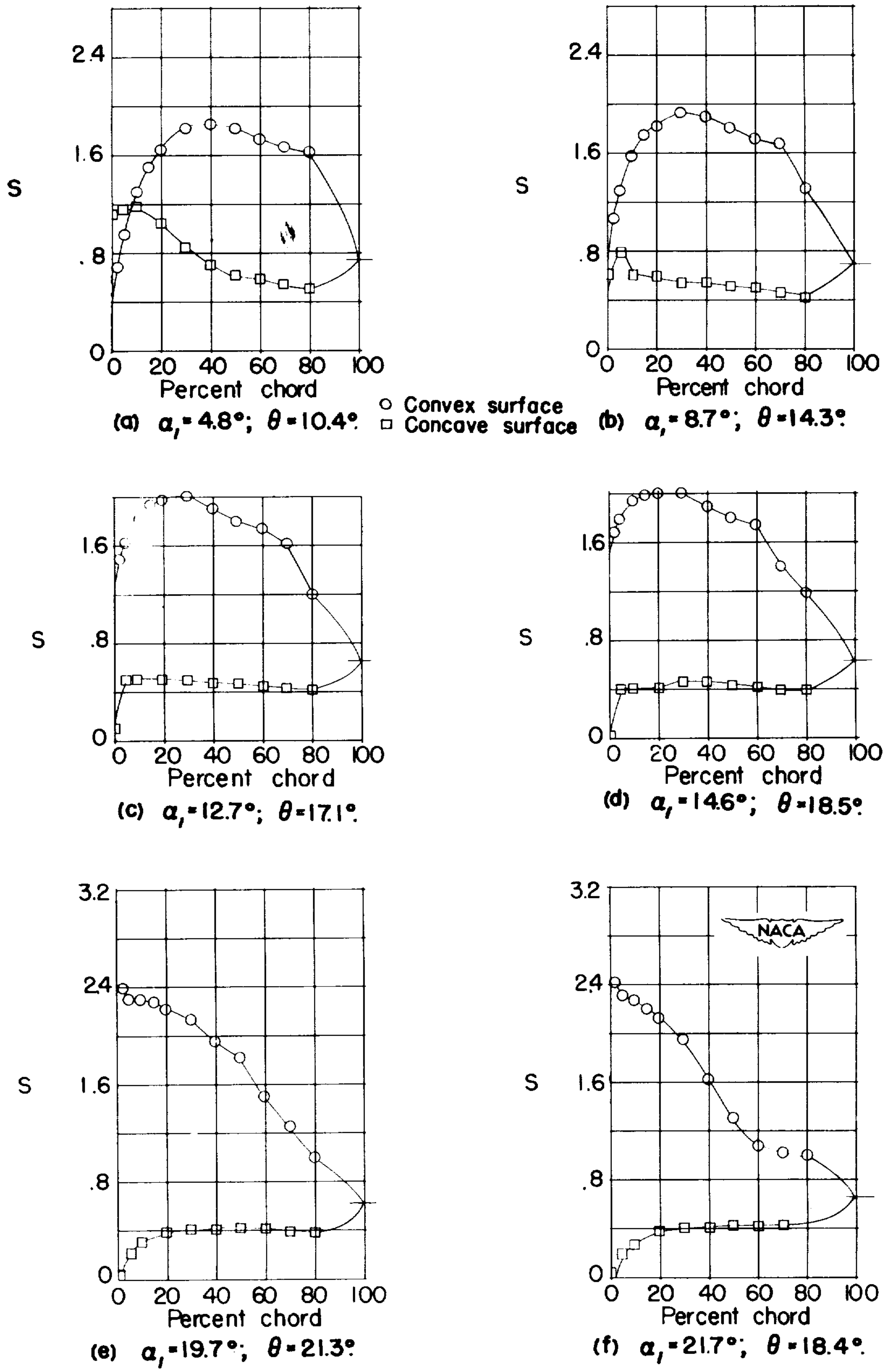

(a) $\alpha_1 = 4.8°$; $\theta = 10.4°$.

(b) $\alpha_1 = 8.7°$; $\theta = 14.3°$.

(c) $\alpha_1 = 12.7°$; $\theta = 17.1°$.

(d) $\alpha_1 = 14.6°$; $\theta = 18.5°$.

(e) $\alpha_1 = 19.7°$; $\theta = 21.3°$.

(f) $\alpha_1 = 21.7°$; $\theta = 18.4°$.

Figure 23.- Blade-surface pressure distributions and blade section characteristics for the cascade combination, $\beta_1 = 45^\circ$, $\sigma = 0.50$, and blade section, NACA 65-(18)10.

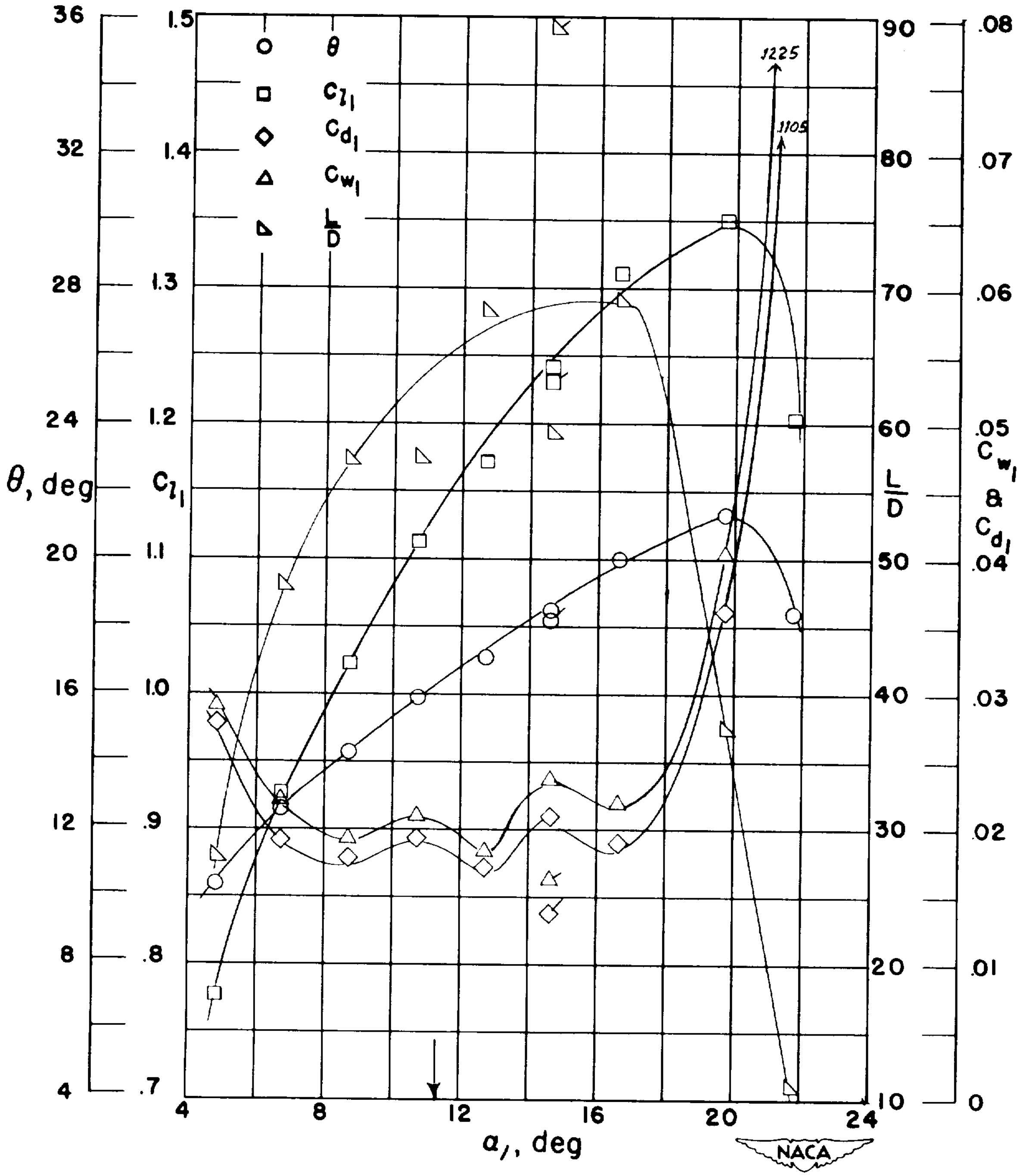

(g) Section characteristics; arrow shows design angle of attack; flagged symbol indicates leading-edge roughness.

Figure 23.- Concluded.

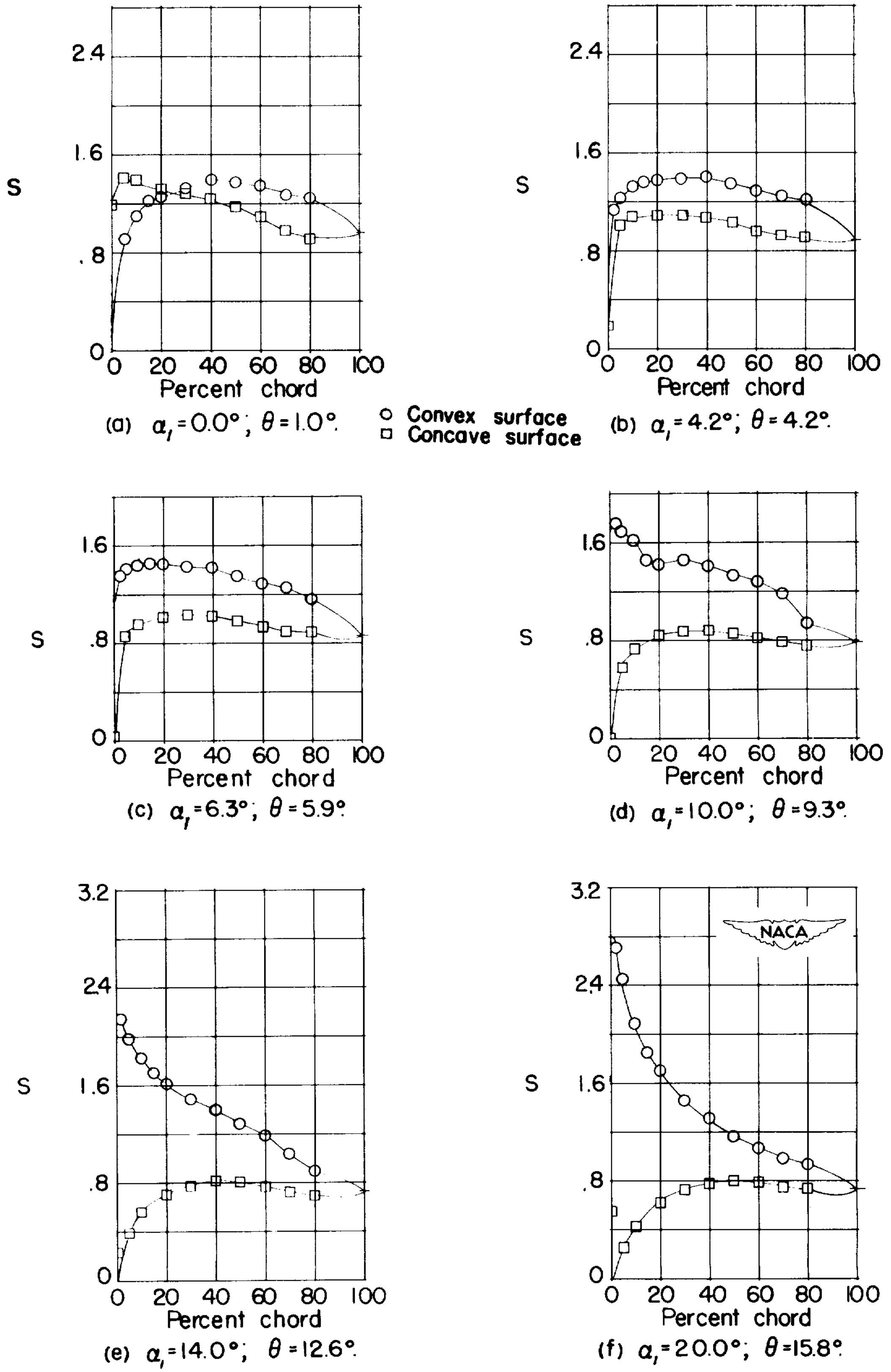

(a) $\alpha_1 = 0.0°$; $\theta = 1.0°$.

(b) $\alpha_1 = 4.2°$; $\theta = 4.2°$.

(c) $\alpha_1 = 6.3°$; $\theta = 5.9°$.

(d) $\alpha_1 = 10.0°$; $\theta = 9.3°$.

(e) $\alpha_1 = 14.0°$; $\theta = 12.6°$.

(f) $\alpha_1 = 20.0°$; $\theta = 15.8°$.

Figure 24.- Blade-surface pressure distributions and blade section characteristics for the cascade combination, $\beta_1 = 45^{\circ}$, $\sigma = 0.75$, and blade section, NACA 65-410.

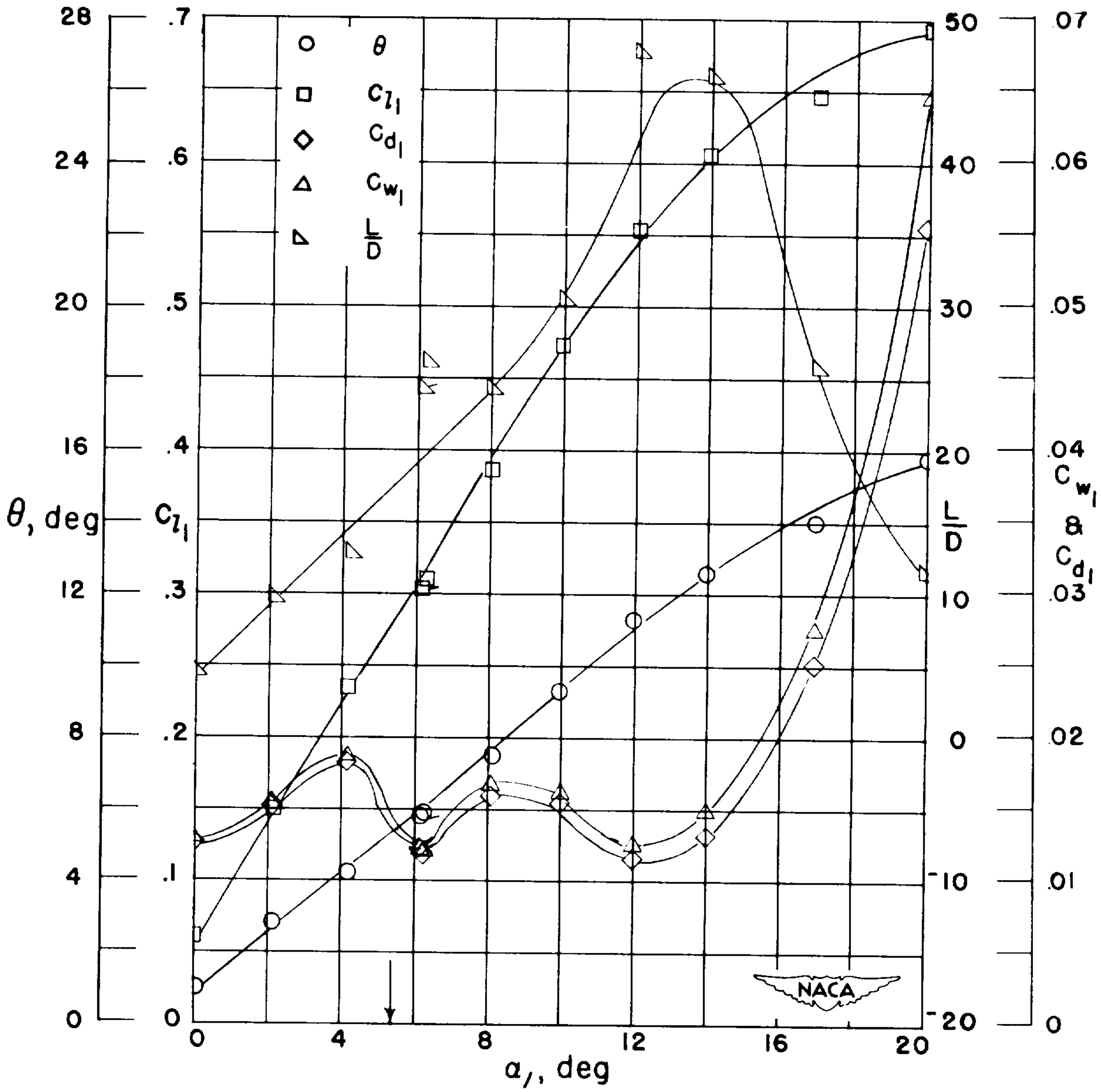

(g) Section characteristics; arrow shows design angle of attack; flagged symbol indicates leading-edge roughness.

Figure 24.- Concluded.

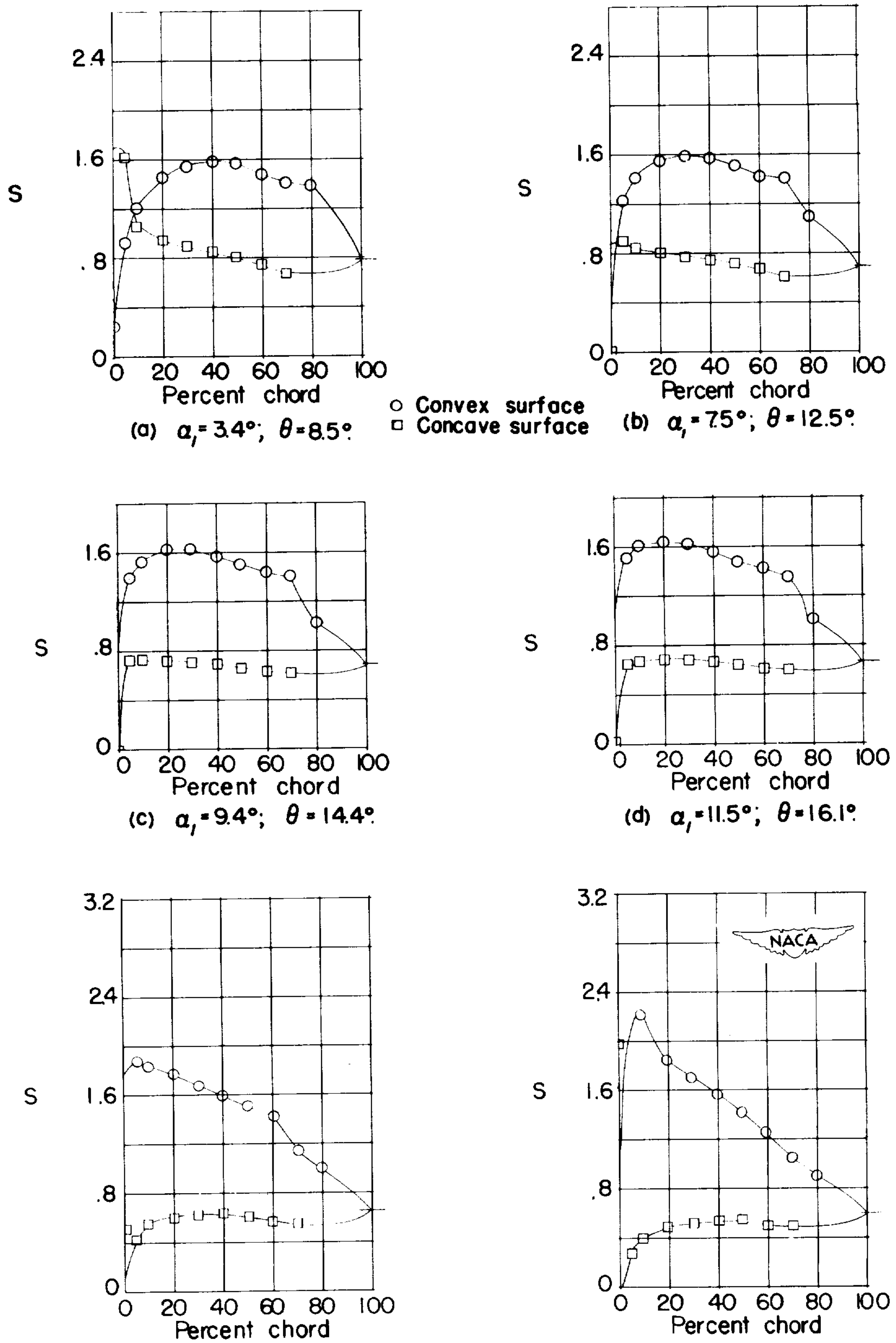

(a) $\alpha_l = 3.4°$; $\theta = 8.5°$

(b) $\alpha_l = 7.5°$; $\theta = 12.5°$

(c) $\alpha_l = 9.4°$; $\theta = 14.4°$

(d) $\alpha_l = 11.5°$; $\theta = 16.1°$

(e) $\alpha_l = 15.4°$; $\theta = 19.6°$

(f) $\alpha_l = 19.5°$; $\theta = 22.7°$

Figure 25.- Blade-surface pressure distributions and blade section characteristics for the cascade combination, $\beta_1 = 45°$, $\sigma = 0.75$, and blade section, NACA 65-(12)10

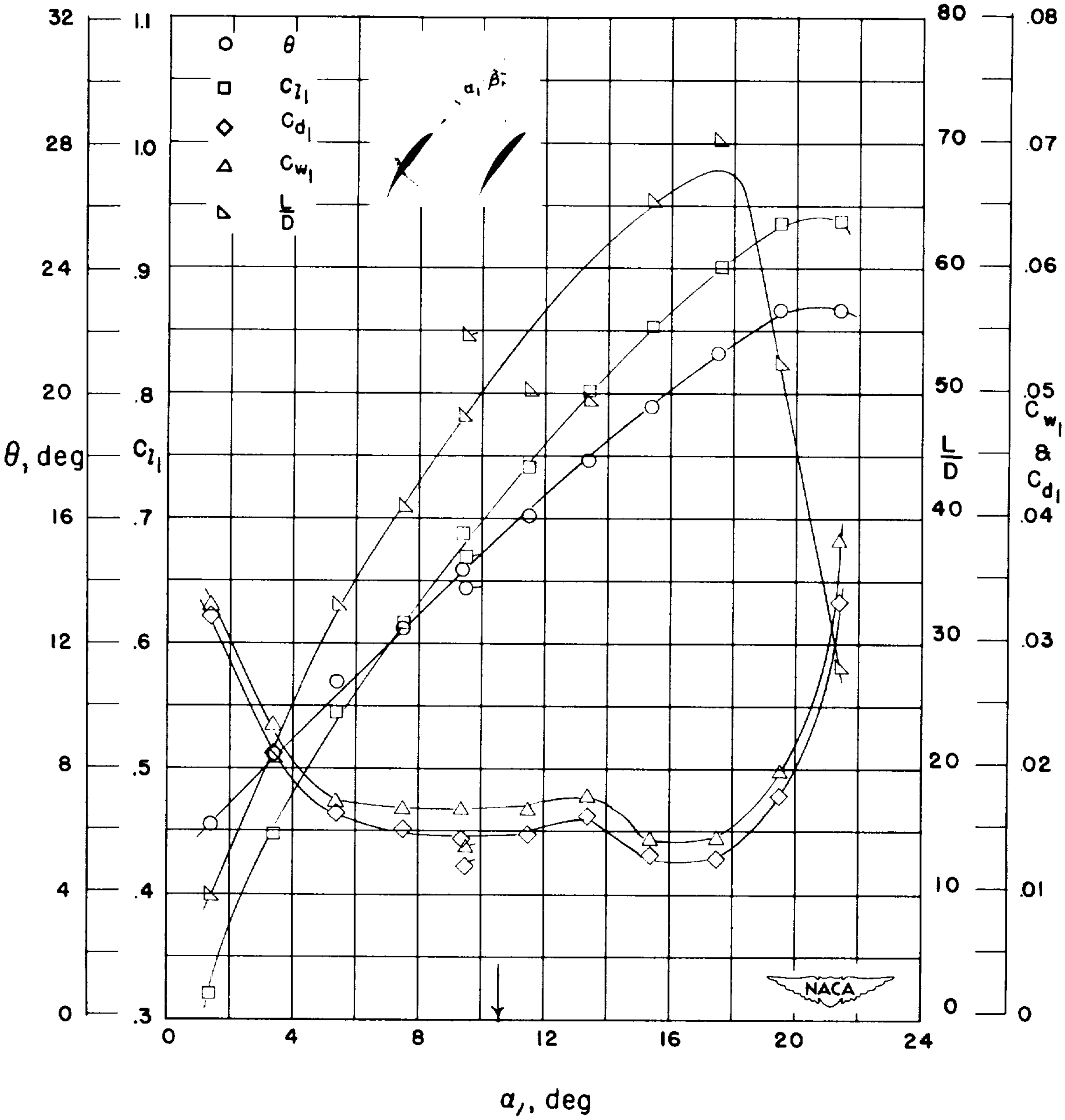

(g) Section characteristics; arrow shows design angle of attack; flagged symbol indicates leading-edge roughness.

Figure 25.- Concluded.

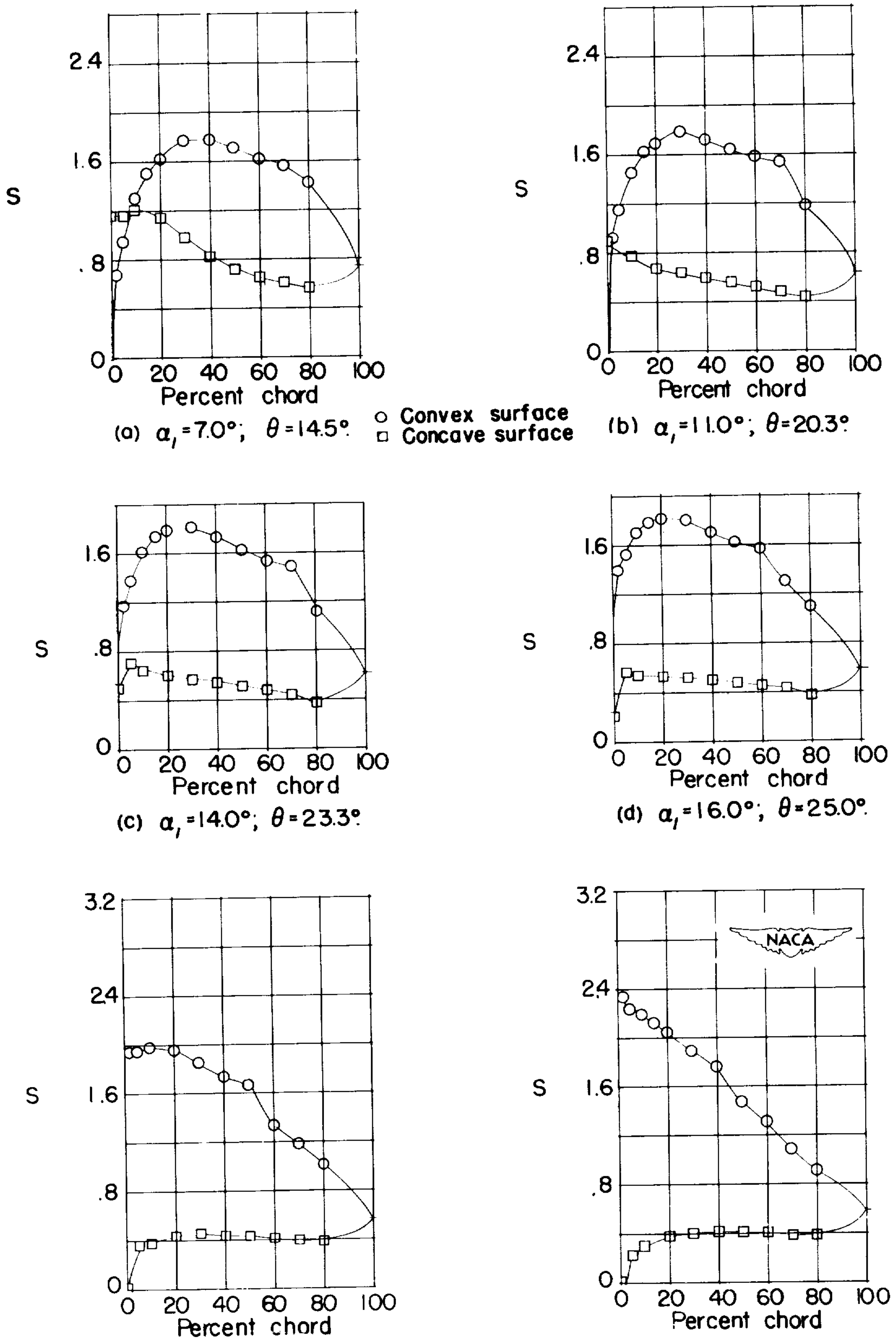

(a) $\alpha_1 = 7.0°$; $\theta = 14.5°$.

(b) $\alpha_1 = 11.0°$; $\theta = 20.3°$.

(c) $\alpha_1 = 14.0°$; $\theta = 23.3°$.

(d) $\alpha_1 = 16.0°$; $\theta = 25.0°$.

(e) $\alpha_1 = 21.0°$; $\theta = 28.6°$.

(f) $\alpha_1 = 24.0°$; $\theta = 29.2°$.

Figure 26.- Blade-surface pressure distributions and blade section characteristics for the cascade combination, $\beta_1 = 45^\circ$, $\sigma = 0.75$, and blade section, NACA 65-(18)10.

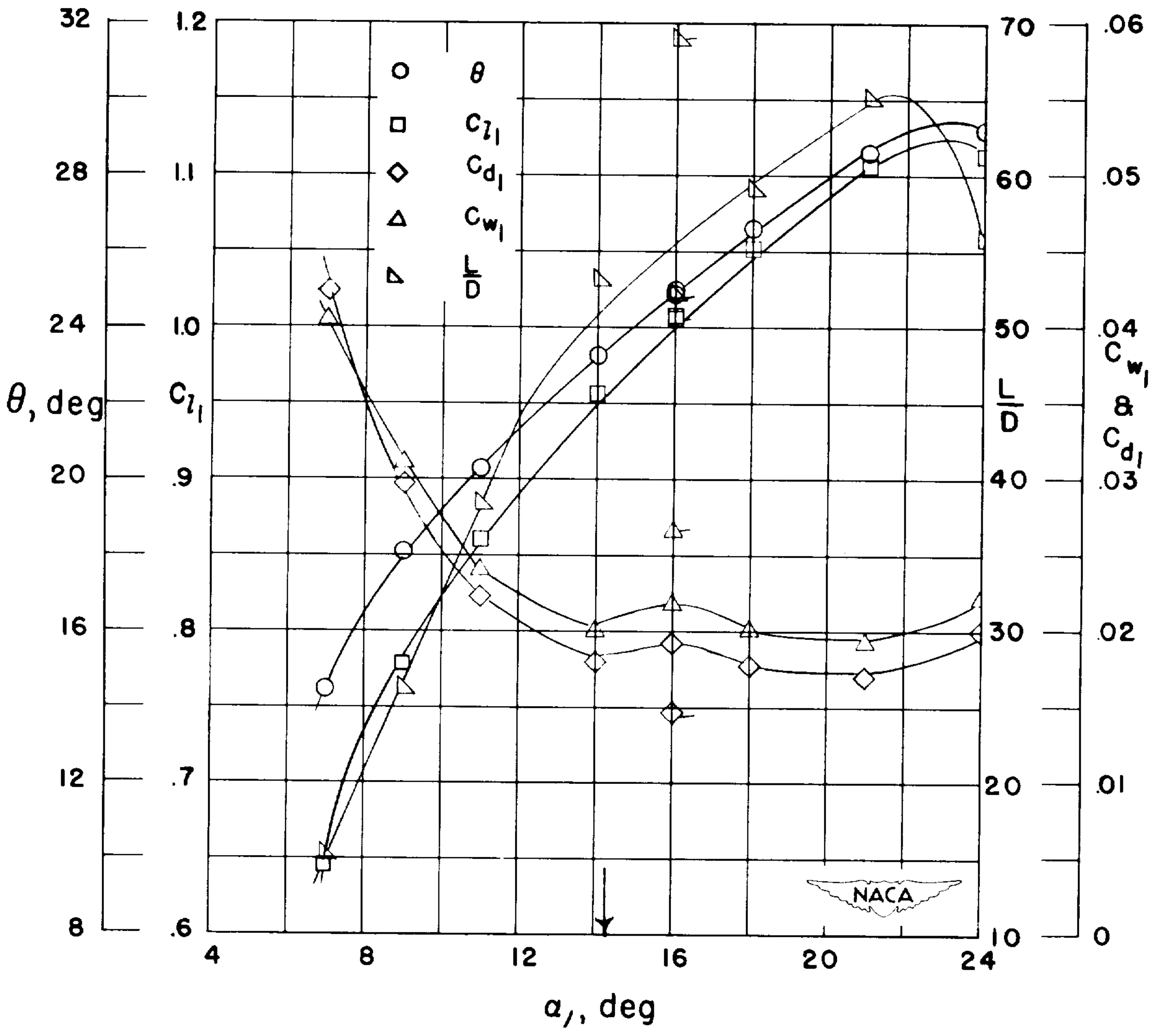

(g) Section characteristics; arrow shows design angle of attack; flagged symbol indicates leading-edge roughness.

Figure 26.- Concluded.

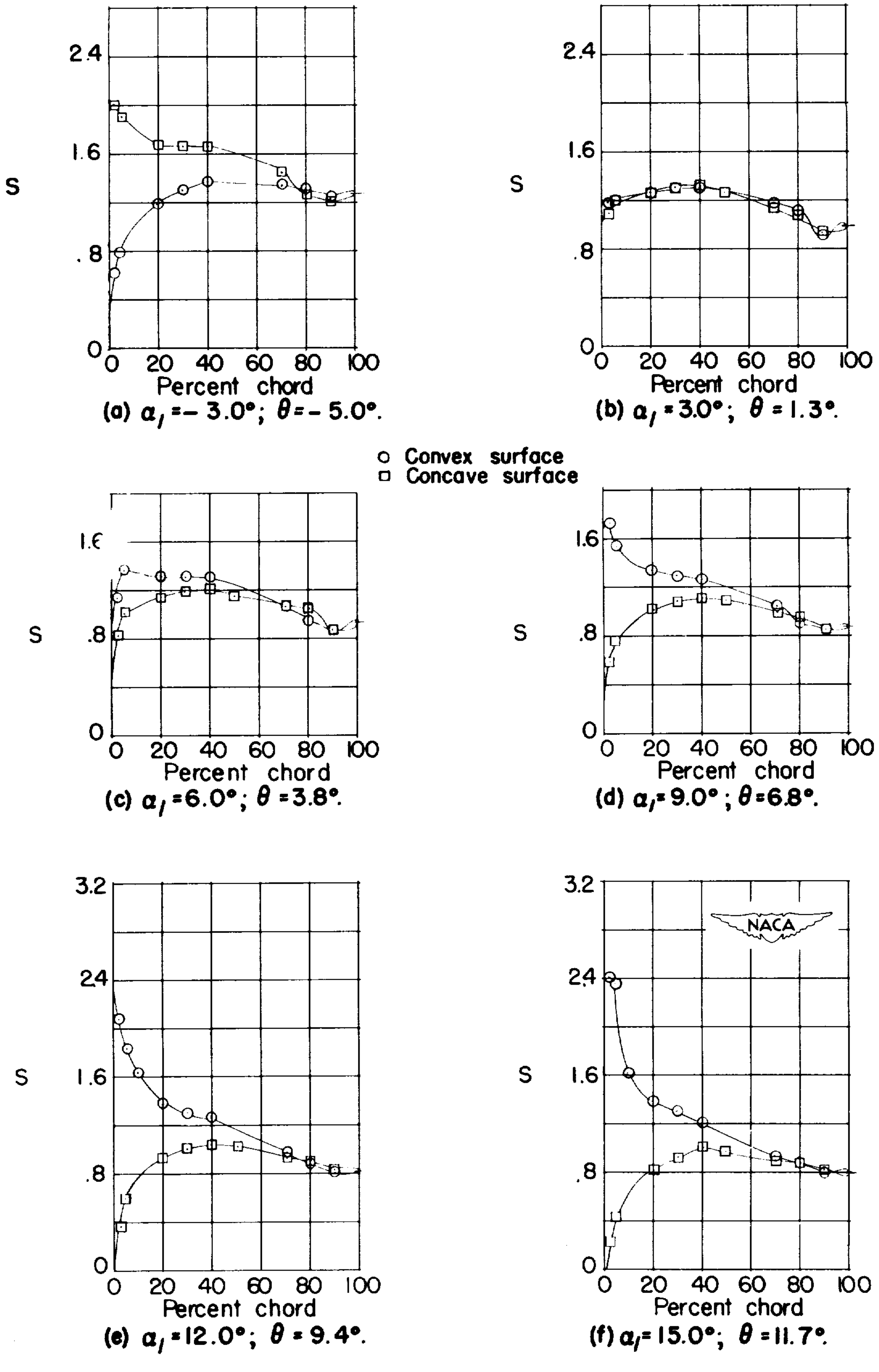

(a) $\alpha_l = -3.0°$; $\theta = -5.0°$.

(b) $\alpha_l = 3.0°$; $\theta = 1.3°$.

(c) $\alpha_l = 6.0°$; $\theta = 3.8°$.

(d) $\alpha_l = 9.0°$; $\theta = 6.8°$.

(e) $\alpha_l = 12.0°$; $\theta = 9.4°$.

(f) $\alpha_l = 15.0°$; $\theta = 11.7°$.

Figure 27.- Blade-surface pressure distributions and blade section characteristics for the cascade combination, $\beta_1 = 45°$, $\sigma = 1.00$, and blade section, NACA 65-010.

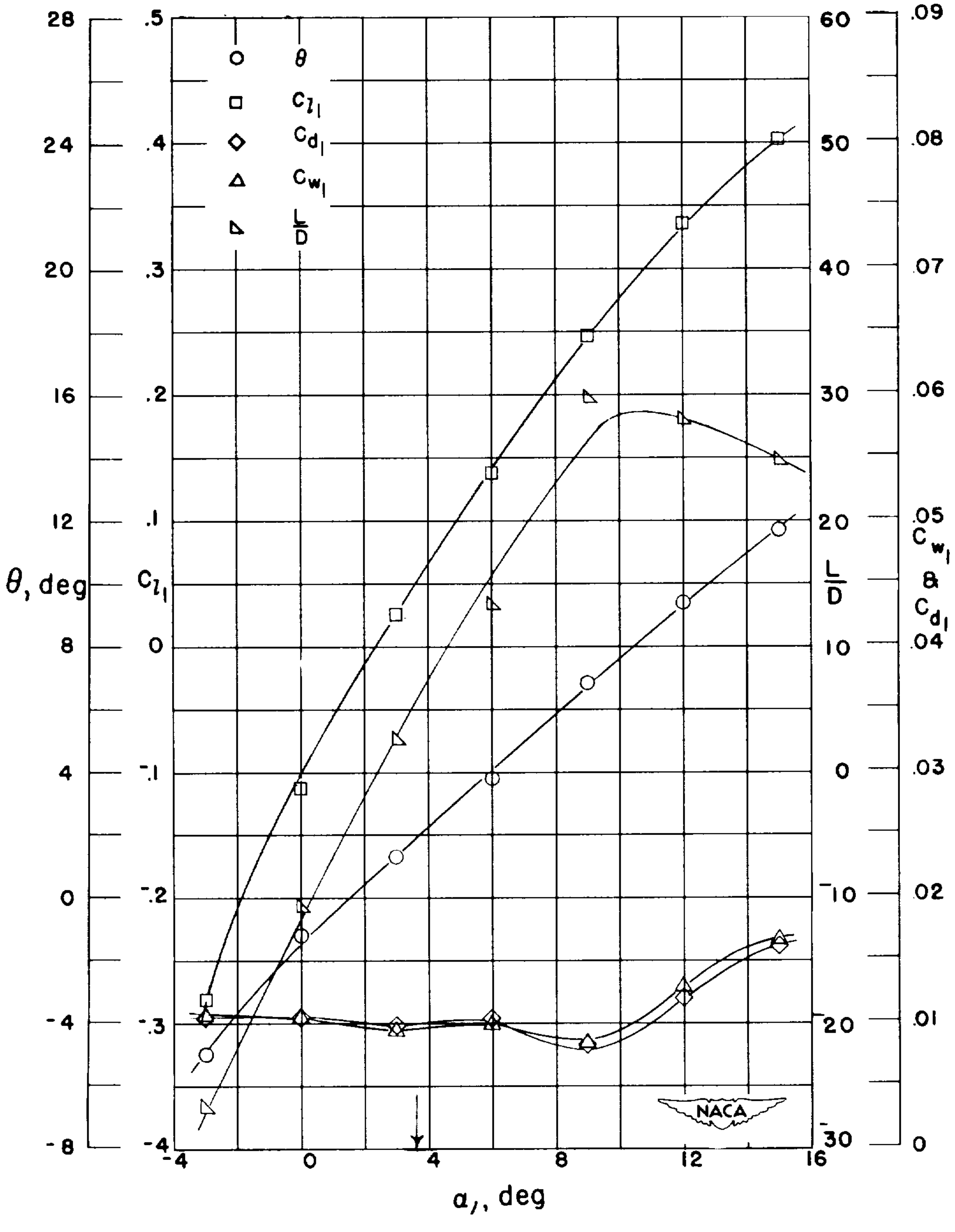

(g) Section characteristics; arrow shows design angle of attack.

Figure 27.- Concluded.

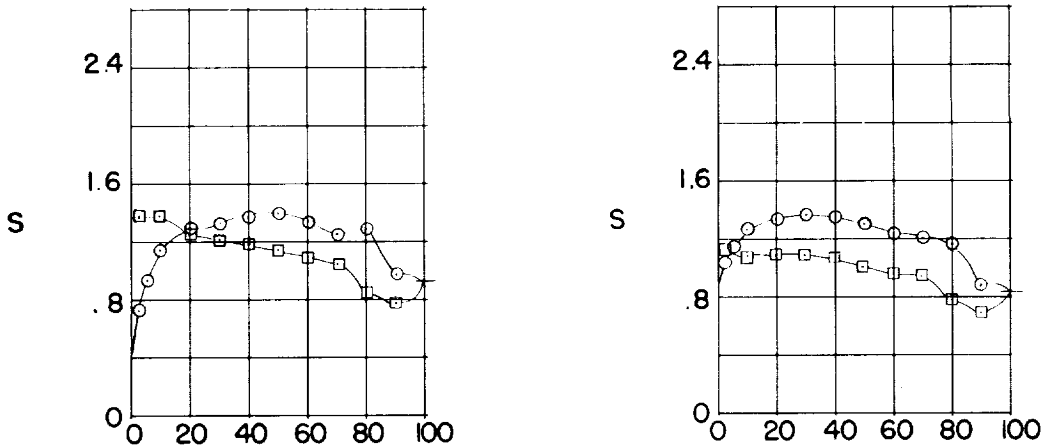

(a) $\alpha_l = 1.0°$; $\theta = 3.3°$.

(b) $\alpha_l = 5.0°$; $\theta = 7.3°$.

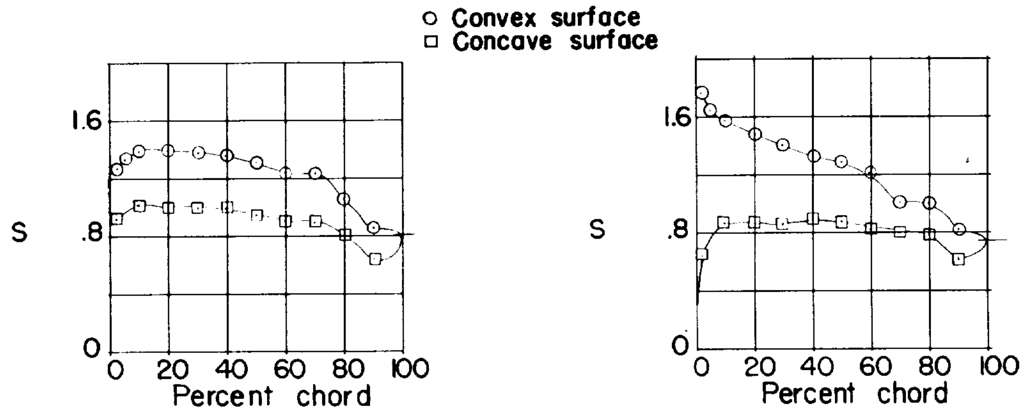

(c) $\alpha_l = 7.0°$; $\theta = 8.6°$.

(d) $\alpha_l = 11.0°$; $\theta = 12.1°$.

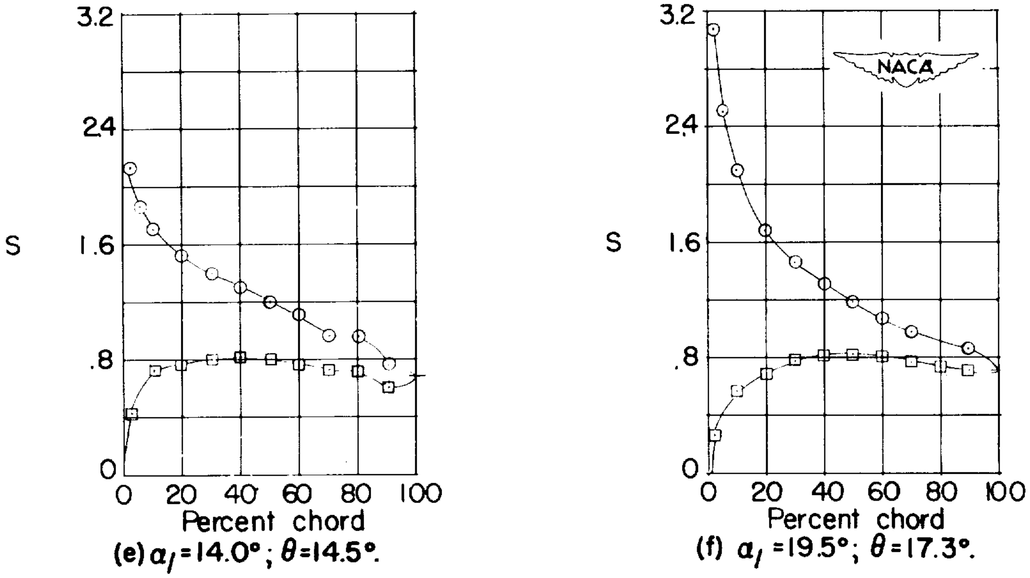

(e) $\alpha_l = 14.0°$; $\theta = 14.5°$.

(f) $\alpha_l = 19.5°$; $\theta = 17.3°$.

Figure 28.- Blade-surface pressure distributions and blade section characteristics for the cascade combination, $\beta_1 = 45^\circ$, $\sigma = 1.00$, and blade section, NACA 65-410.

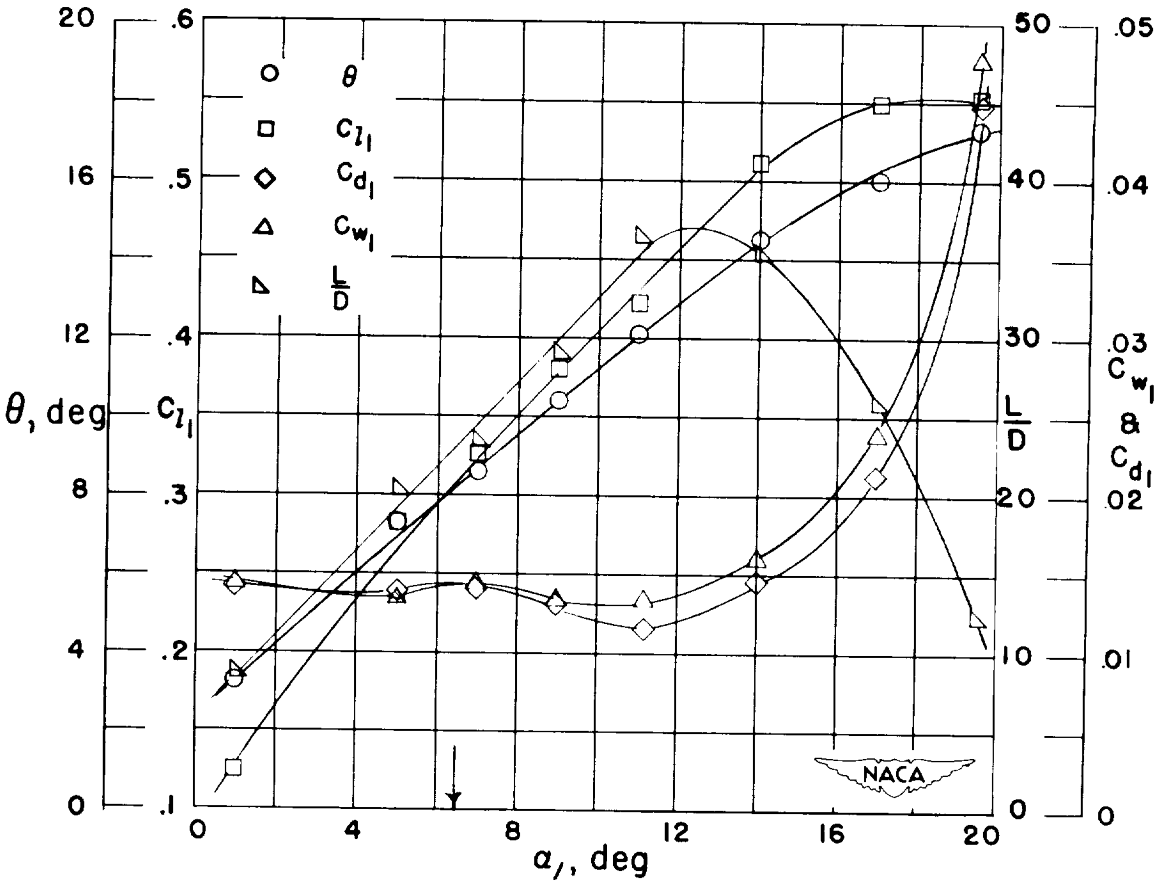

(g) Section characteristics; arrow shows design angle of attack.

Figure 28.- Concluded.

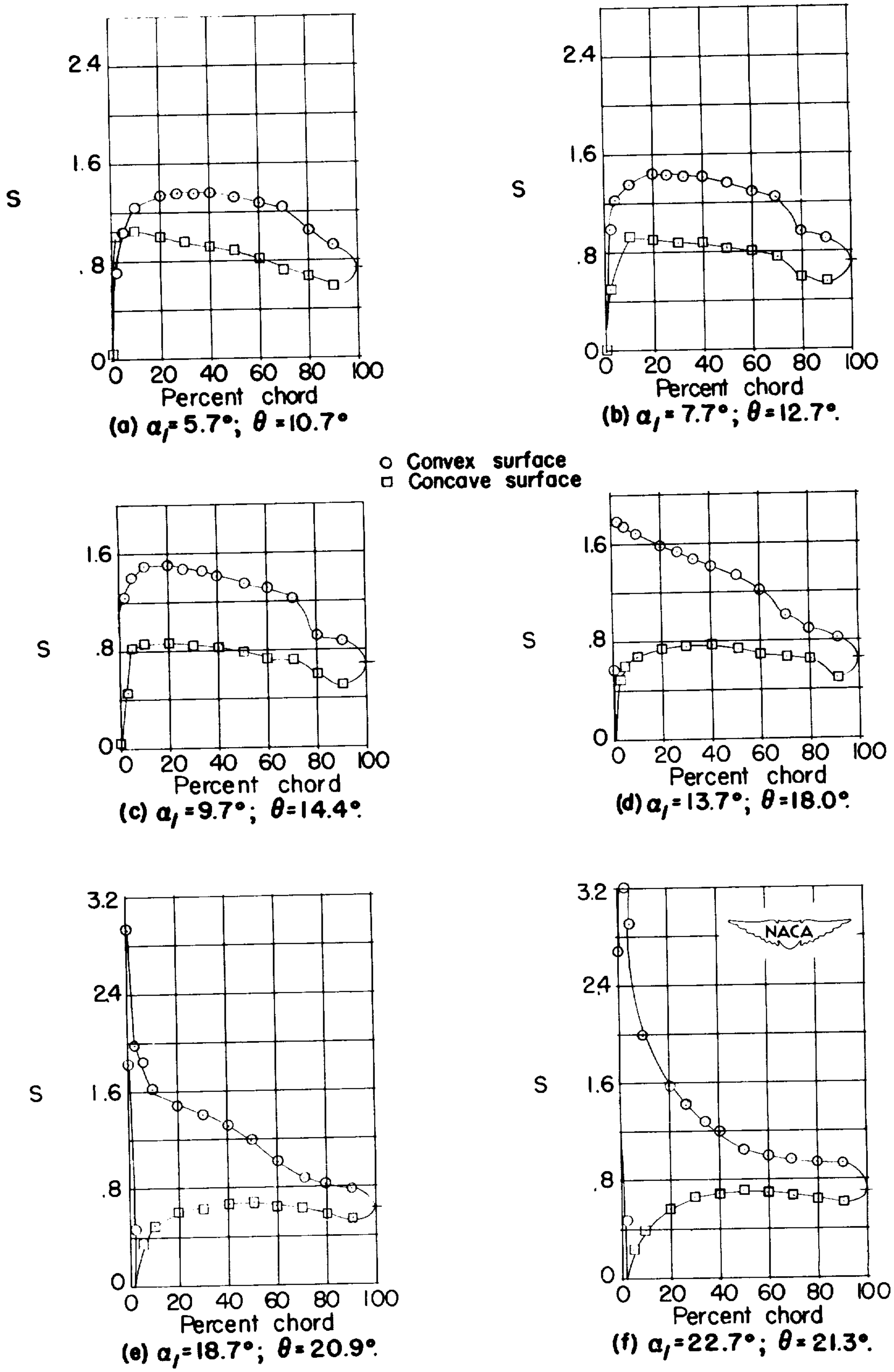

(a) $\alpha_l = 5.7°$; $\theta = 10.7°$

(b) $\alpha_l = 7.7°$; $\theta = 12.7°$.

(c) $\alpha_l = 9.7°$; $\theta = 14.4°$.

(d) $\alpha_l = 13.7°$; $\theta = 18.0°$.

(e) $\alpha_l = 18.7°$; $\theta = 20.9°$.

(f) $\alpha_l = 22.7°$; $\theta = 21.3°$.

Figure 29.- Blade-surface pressure distributions and blade section characteristics for the cascade combination, $\beta_1 = 45^\circ$, $\sigma = 1.00$, and blade section, NACA 65-810.

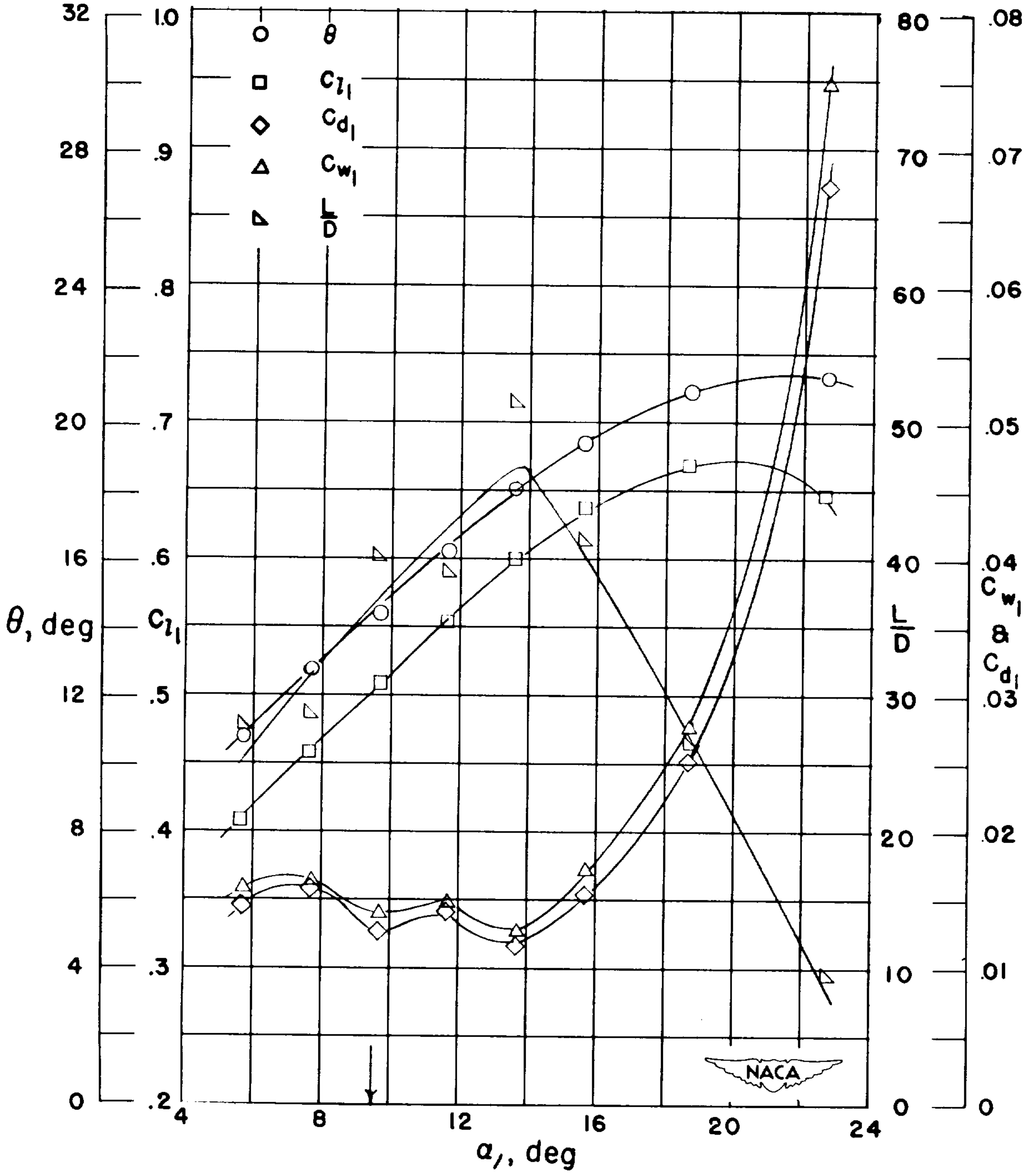

(g) Section characteristics; arrow shows design angle of attack.

Figure 29.- Concluded.

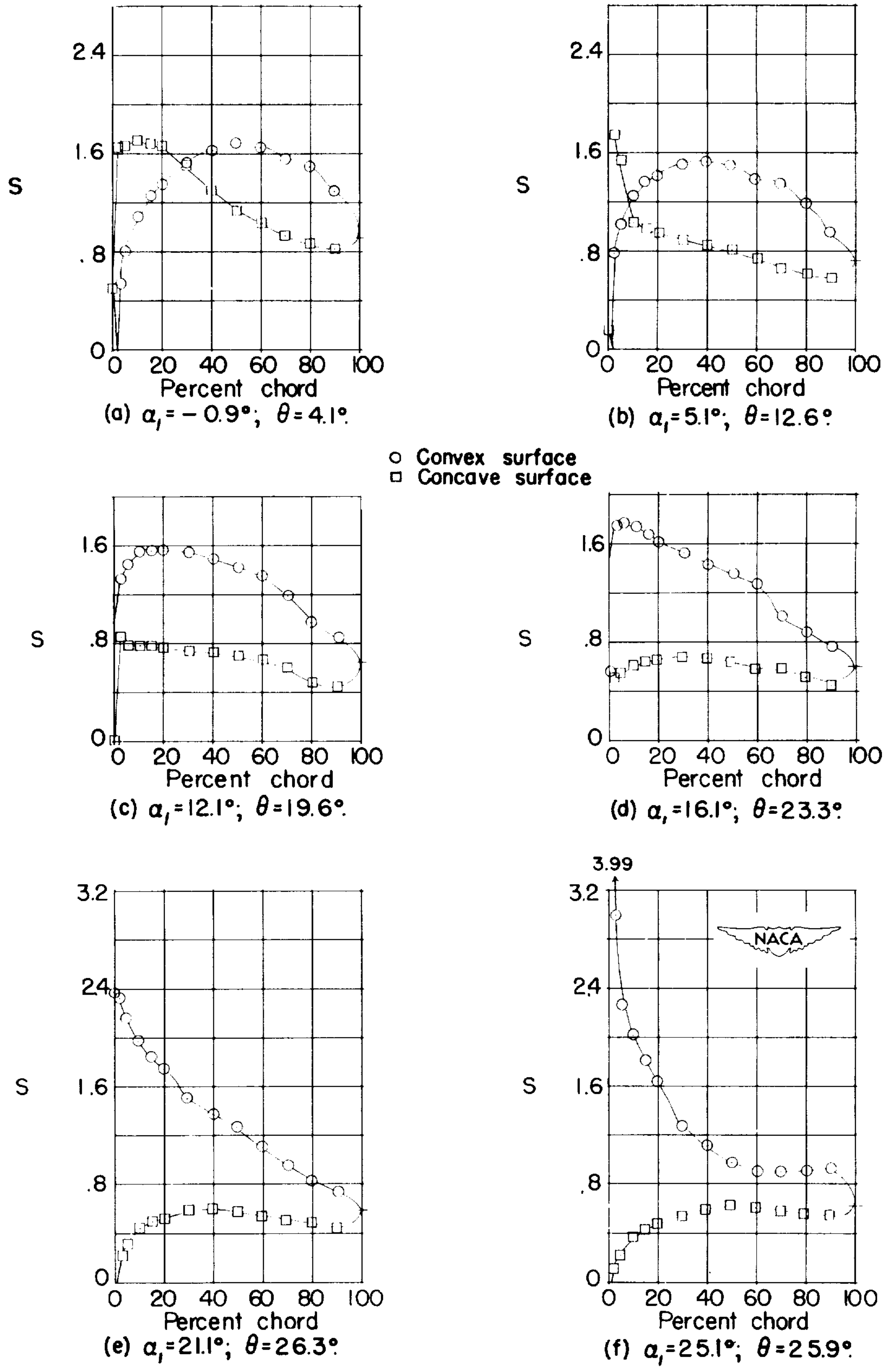

(a) $\alpha_l = -0.9°$; $\theta = 4.1°$

(b) $\alpha_l = 5.1°$; $\theta = 12.6°$

(c) $\alpha_l = 12.1°$; $\theta = 19.6°$

(d) $\alpha_l = 16.1°$; $\theta = 23.3°$

(e) $\alpha_l = 21.1°$; $\theta = 26.3°$

(f) $\alpha_l = 25.1°$; $\theta = 25.9°$

Figure 30.- Blade-surface pressure distributions and blade section characteristics for the cascade combination, $\beta_1 = 45°$, $\sigma = 1.00$, and blade section, NACA 65-(12)10.

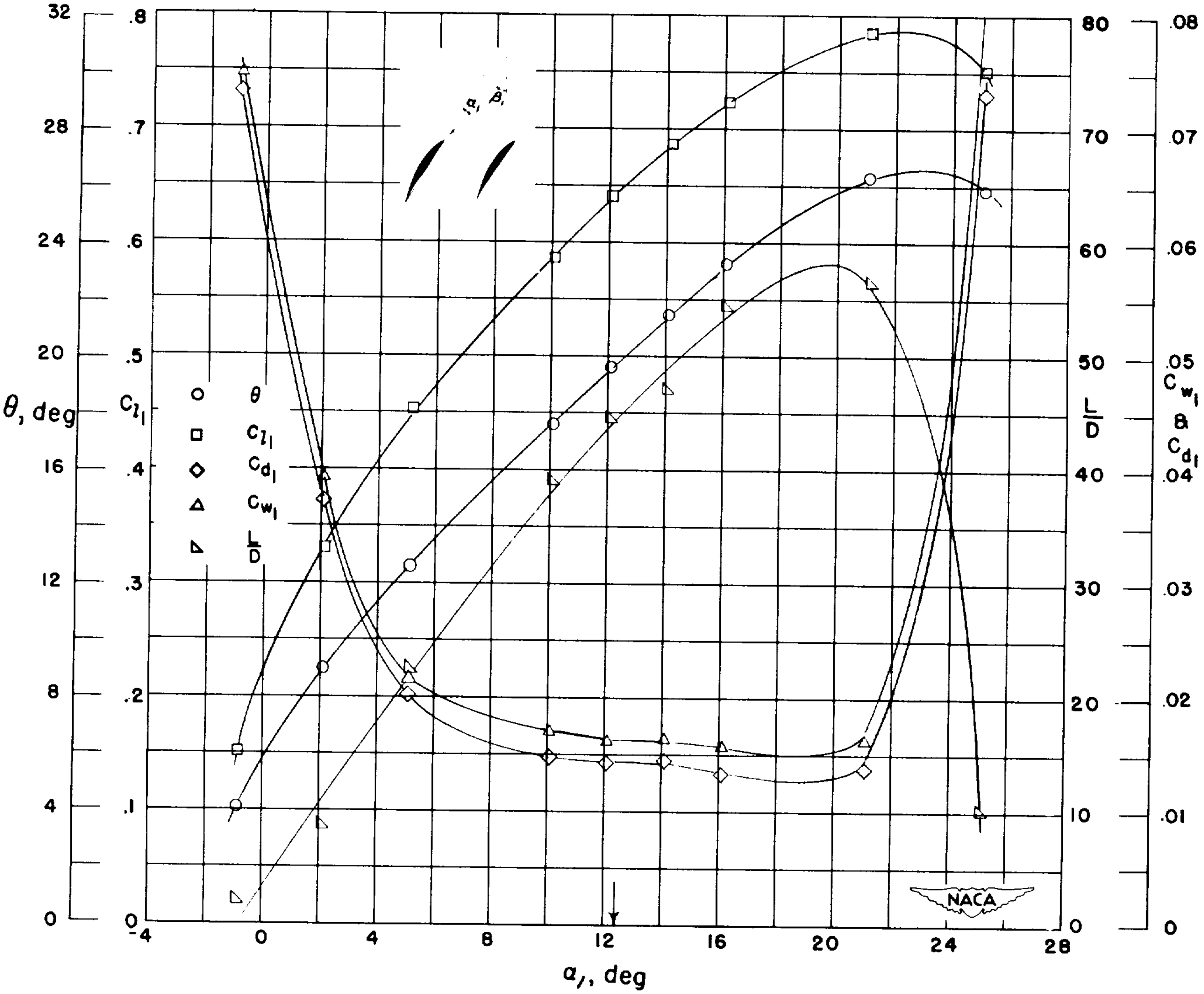

(g) Section characteristics; arrow shows design angle of attack.

Figure 30.- Concluded.

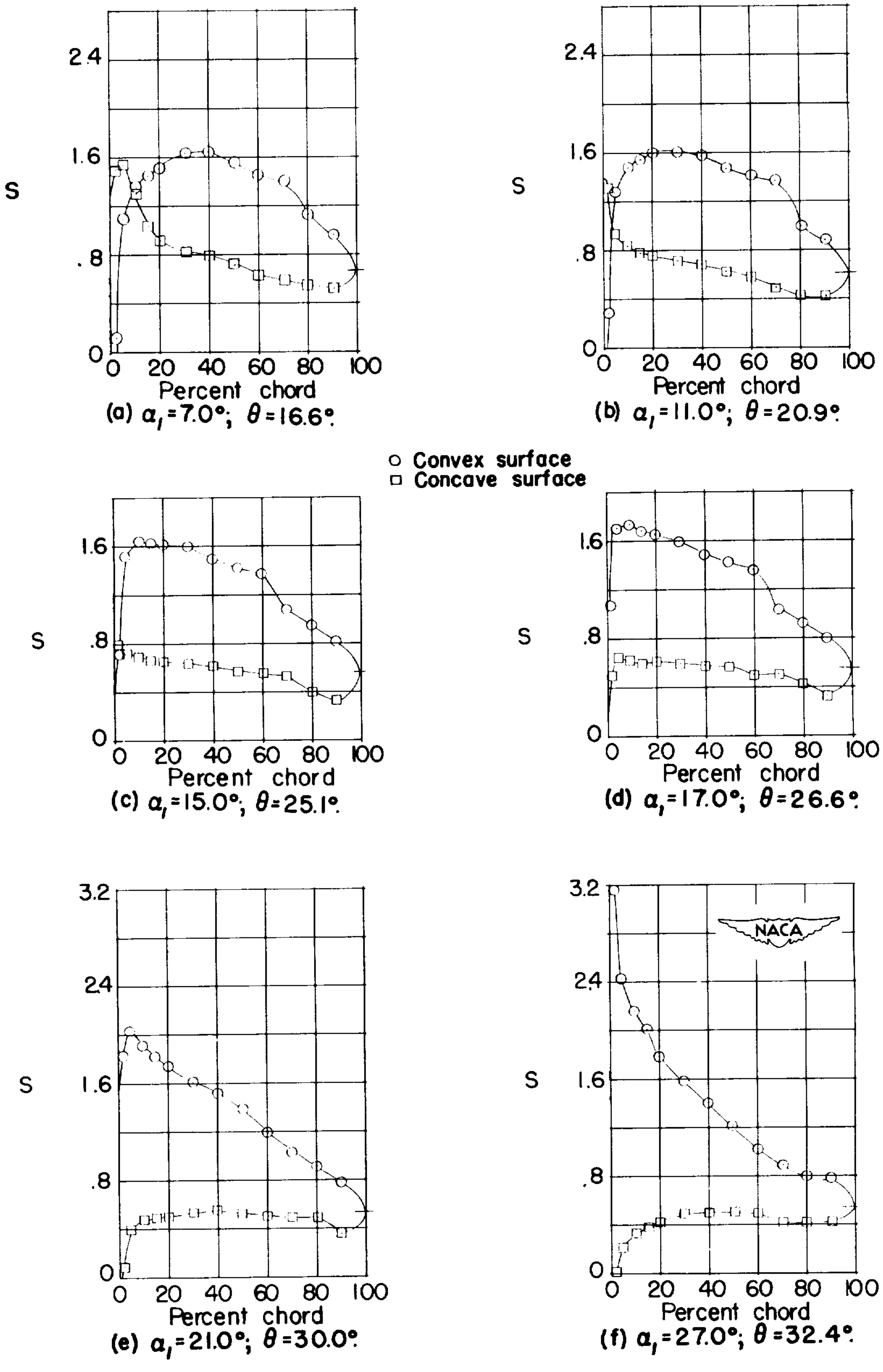

(a) $\alpha_1 = 7.0^\circ$; $\theta = 16.6^\circ$.

(b) $\alpha_1 = 11.0^\circ$; $\theta = 20.9^\circ$.

(c) $\alpha_1 = 15.0^\circ$; $\theta = 25.1^\circ$.

(d) $\alpha_1 = 17.0^\circ$; $\theta = 26.6^\circ$.

(e) $\alpha_1 = 21.0^\circ$; $\theta = 30.0^\circ$.

(f) $\alpha_1 = 27.0^\circ$; $\theta = 32.4^\circ$.

Figure 31.- Blade-surface pressure distributions and blade section characteristics for the cascade combination, $\beta_1 = 45^\circ$, $\sigma = 1.00$, and blade section, NACA 65-(15)10.

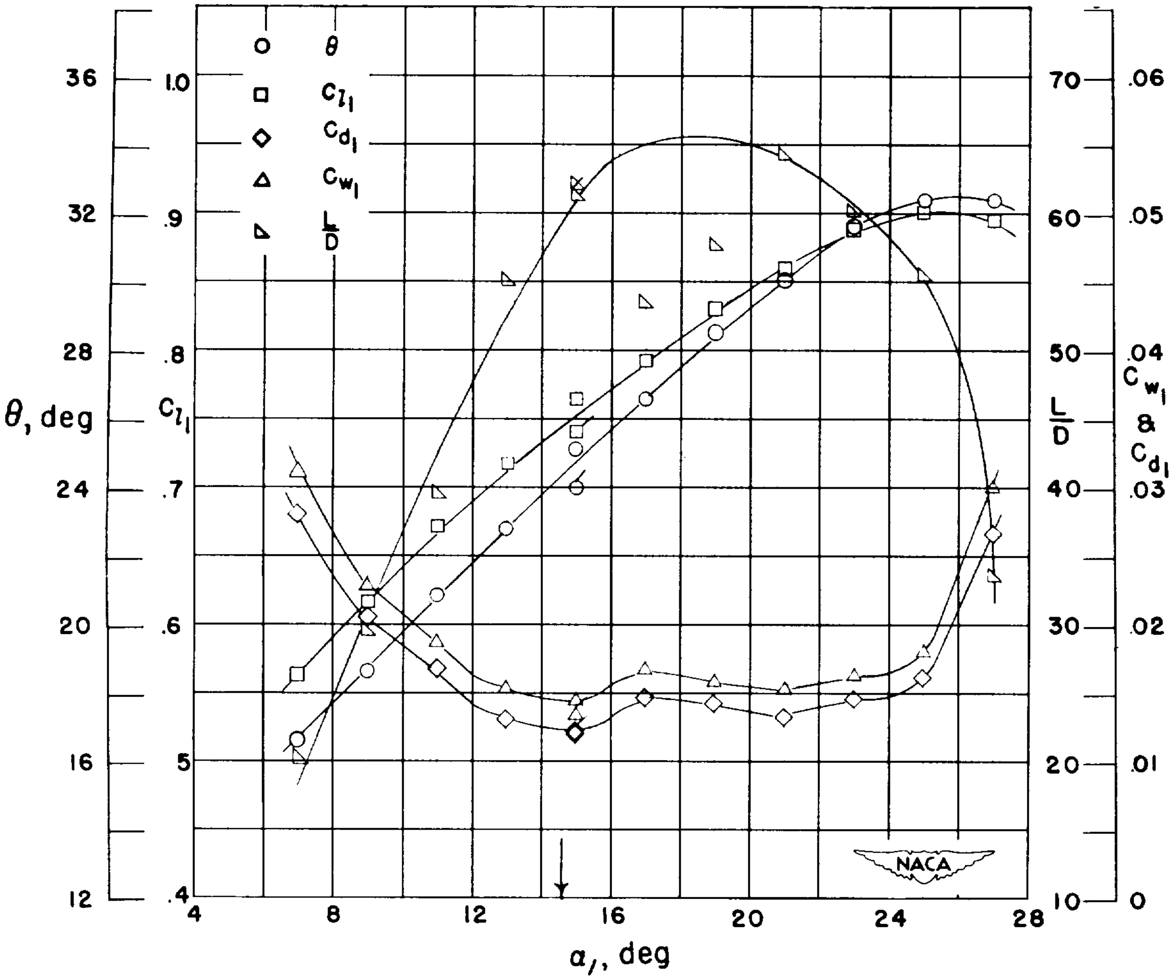

(g) Section characteristics; arrow shows design angle of attack; flagged symbol indicates leading-edge roughness.

Figure 31.- Concluded.

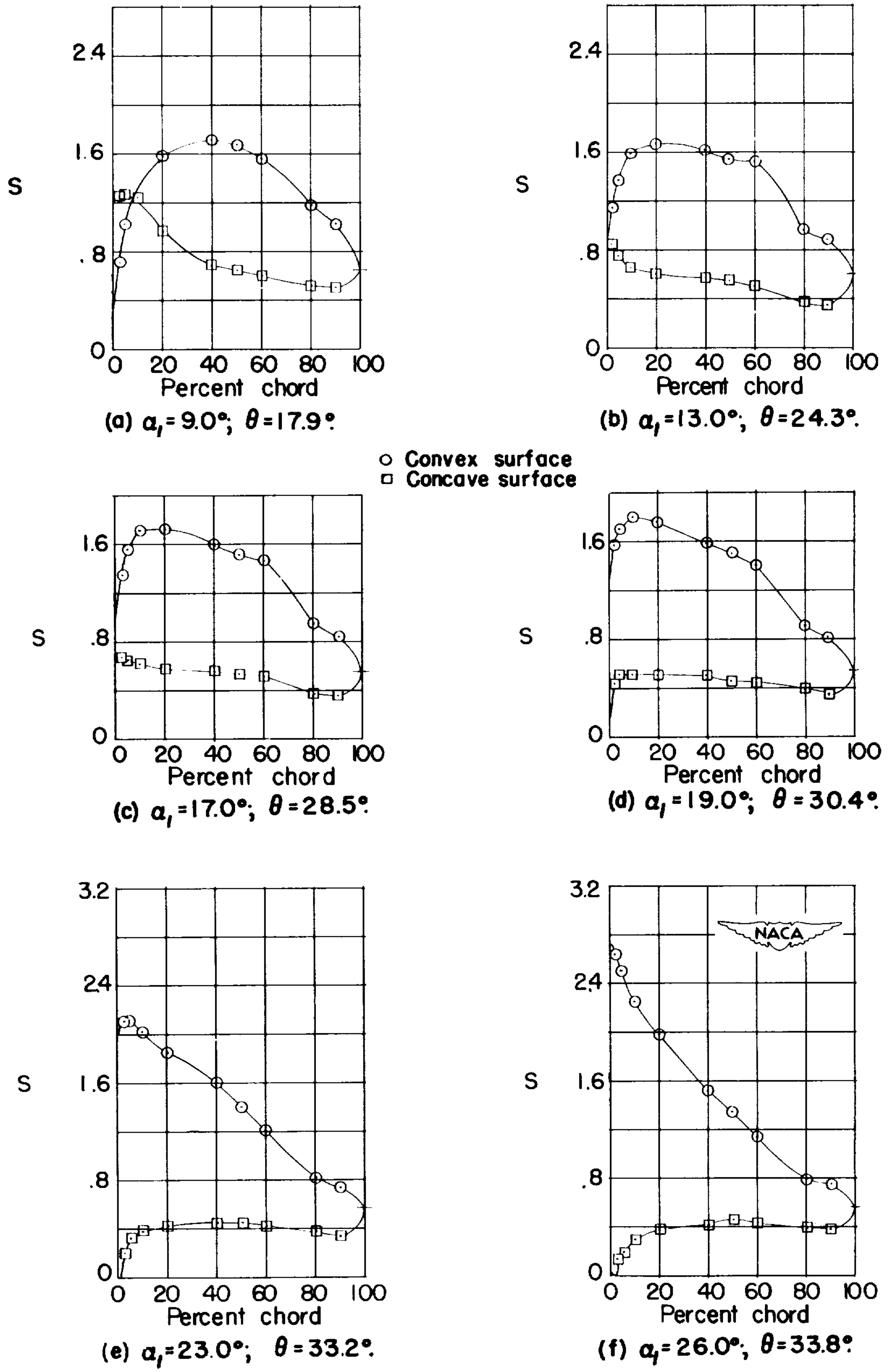

(a) $\alpha_l = 9.0°$; $\theta = 17.9°$.

(b) $\alpha_l = 13.0°$; $\theta = 24.3°$.

(c) $\alpha_l = 17.0°$; $\theta = 28.5°$.

(d) $\alpha_l = 19.0°$; $\theta = 30.4°$.

(e) $\alpha_l = 23.0°$; $\theta = 33.2°$.

(f) $\alpha_l = 26.0°$; $\theta = 33.8°$.

Figure 32.- Blade-surface pressure distributions and blade section characteristics for the cascade combination, $\beta_1 = 45^{\circ}$, $\sigma = 1.00$, and blade section, NACA 65-(18)10.

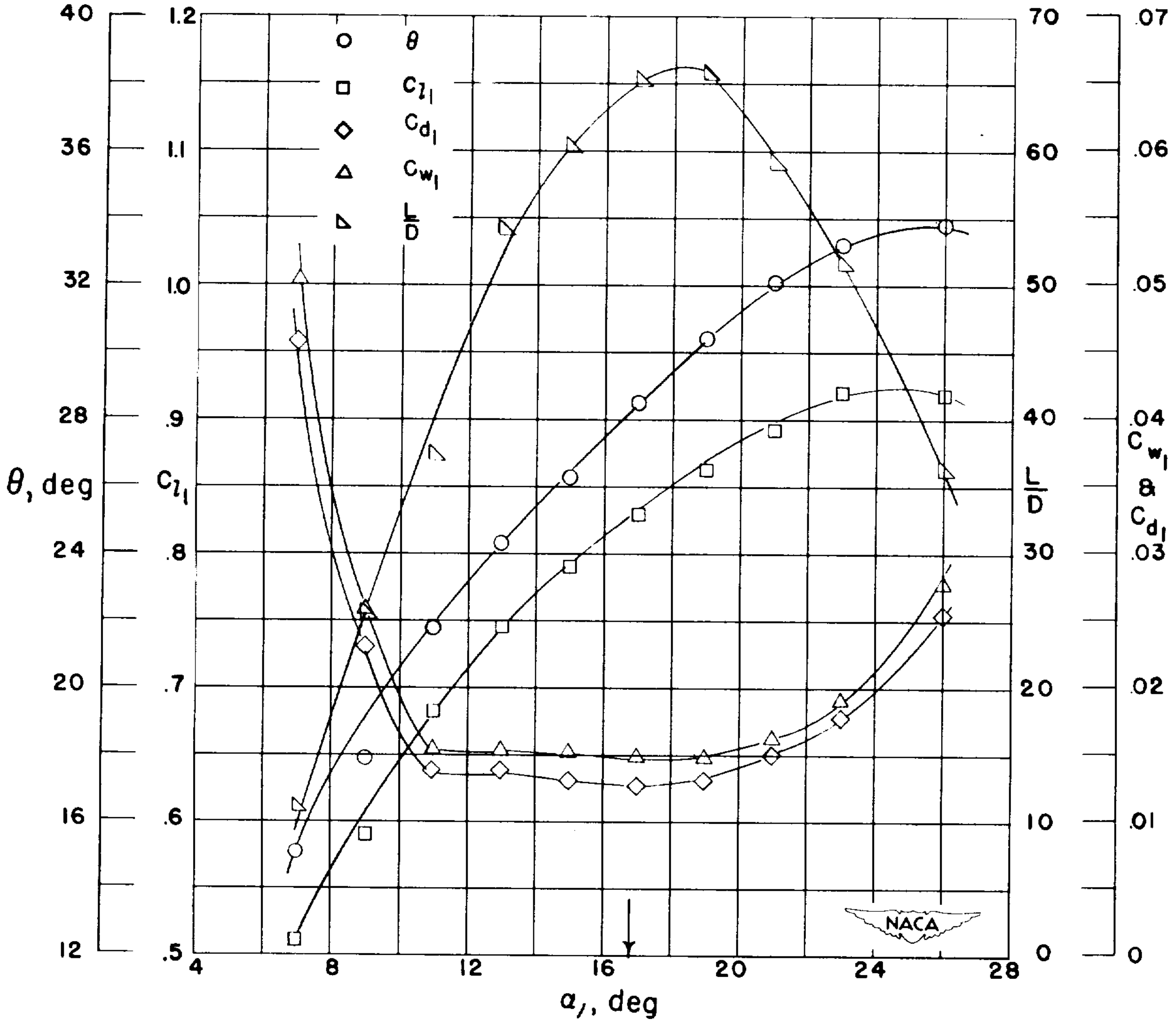

(g) Section characteristics; arrow shows design angle of attack.

Figure 32.- Concluded.

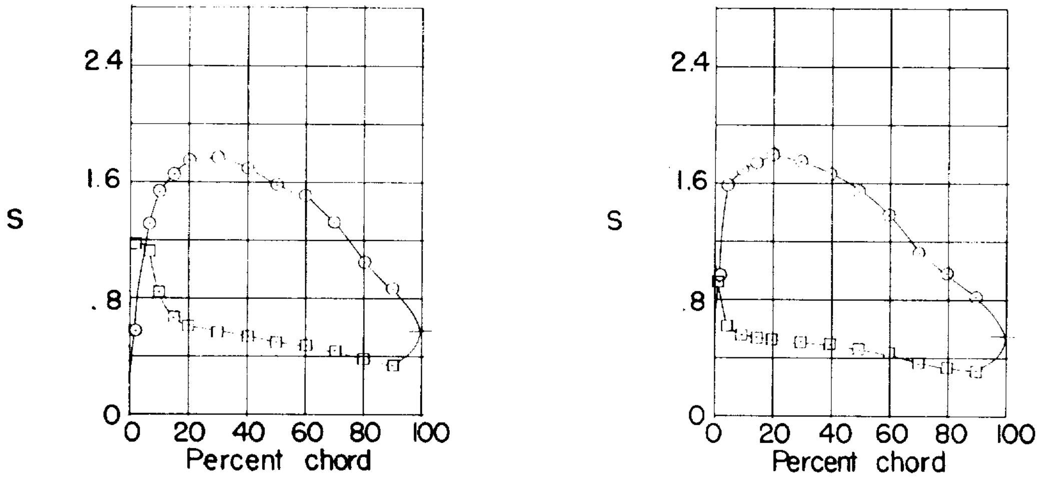

(a) $\alpha_1 = 15.0°$; $\theta = 28.2°$

(b) $\alpha_1 = 18.0°$; $\theta = 31.5°$

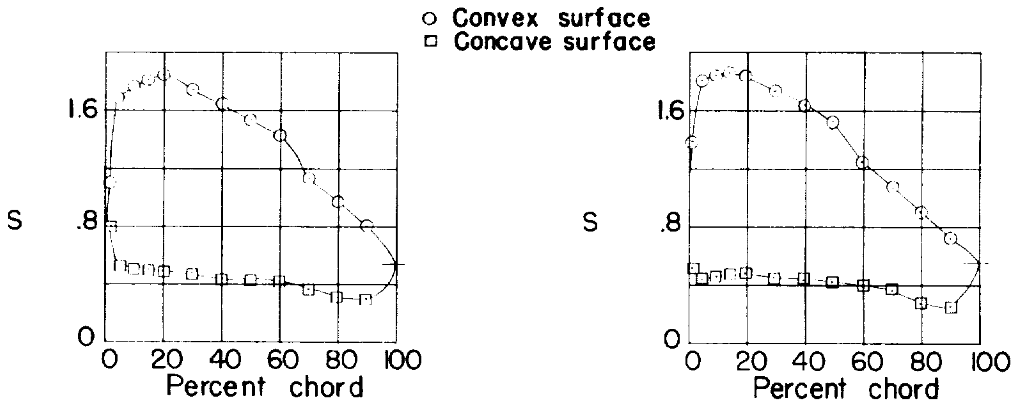

(c) $\alpha_1 = 19.5°$; $\theta = 33.0°$

(d) $\alpha_1 = 21.0°$; $\theta = 34.3°$

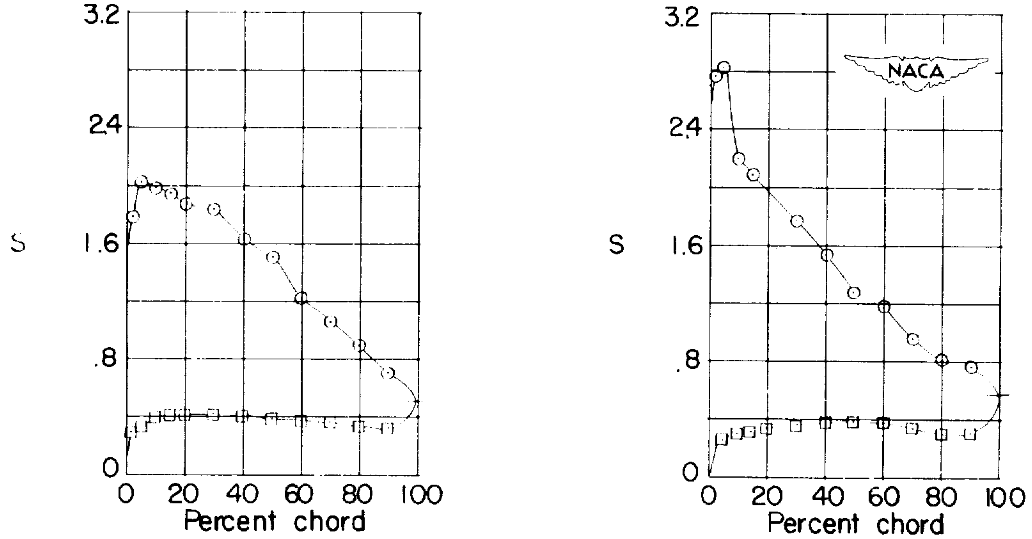

(e) $\alpha_1 = 24.0°$; $\theta = 37.0°$

(f) $\alpha_1 = 30.0°$; $\theta = 40.5°$

Figure 33.- Blade-surface pressure distributions and blade section characteristics for the cascade combination, $\beta_1 = 45°$, $\sigma = 1.00$, and blade section, NACA 65-(21)10.

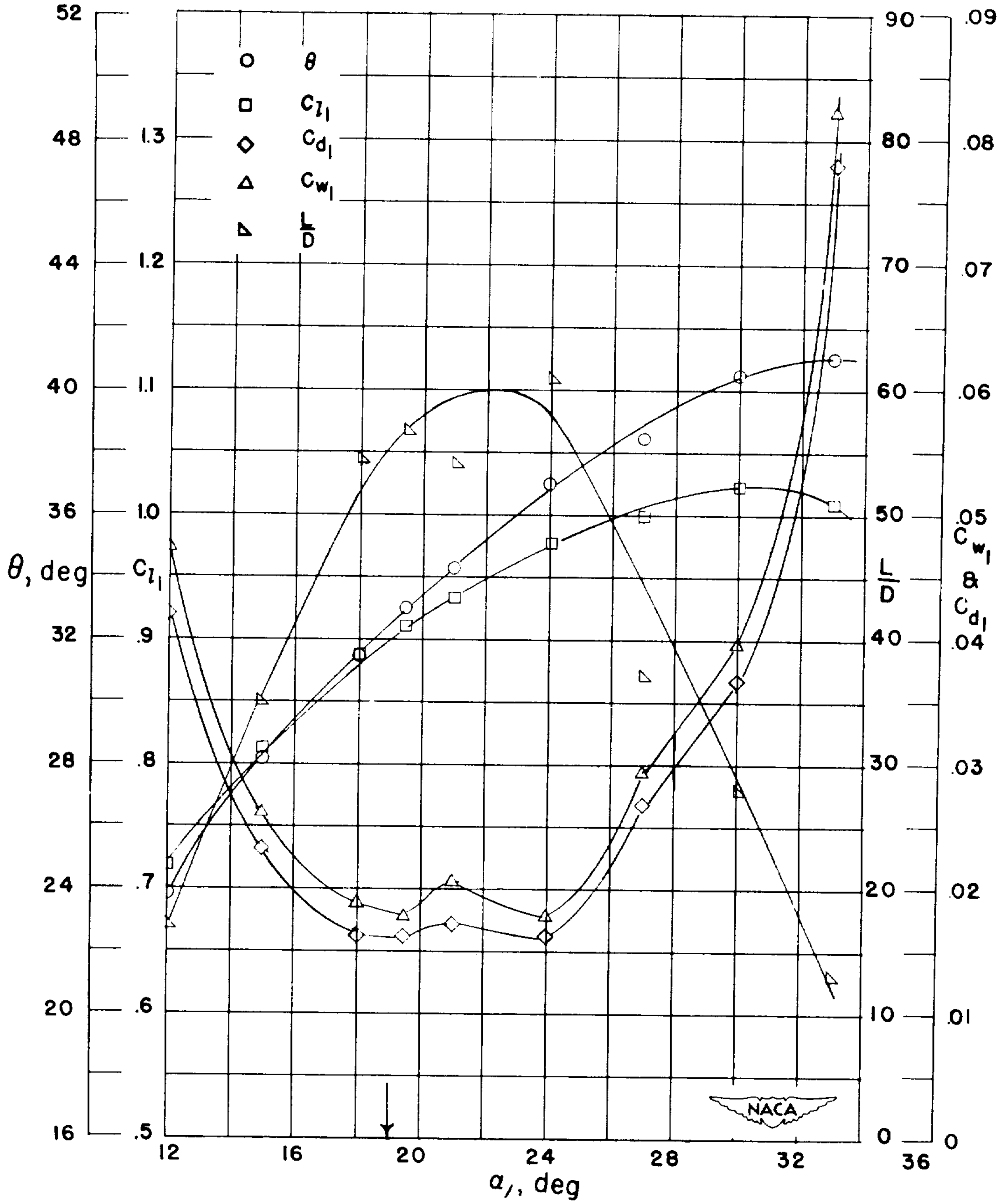

(g) Section characteristics; arrow shows design angle of attack.

Figure 33.- Concluded.

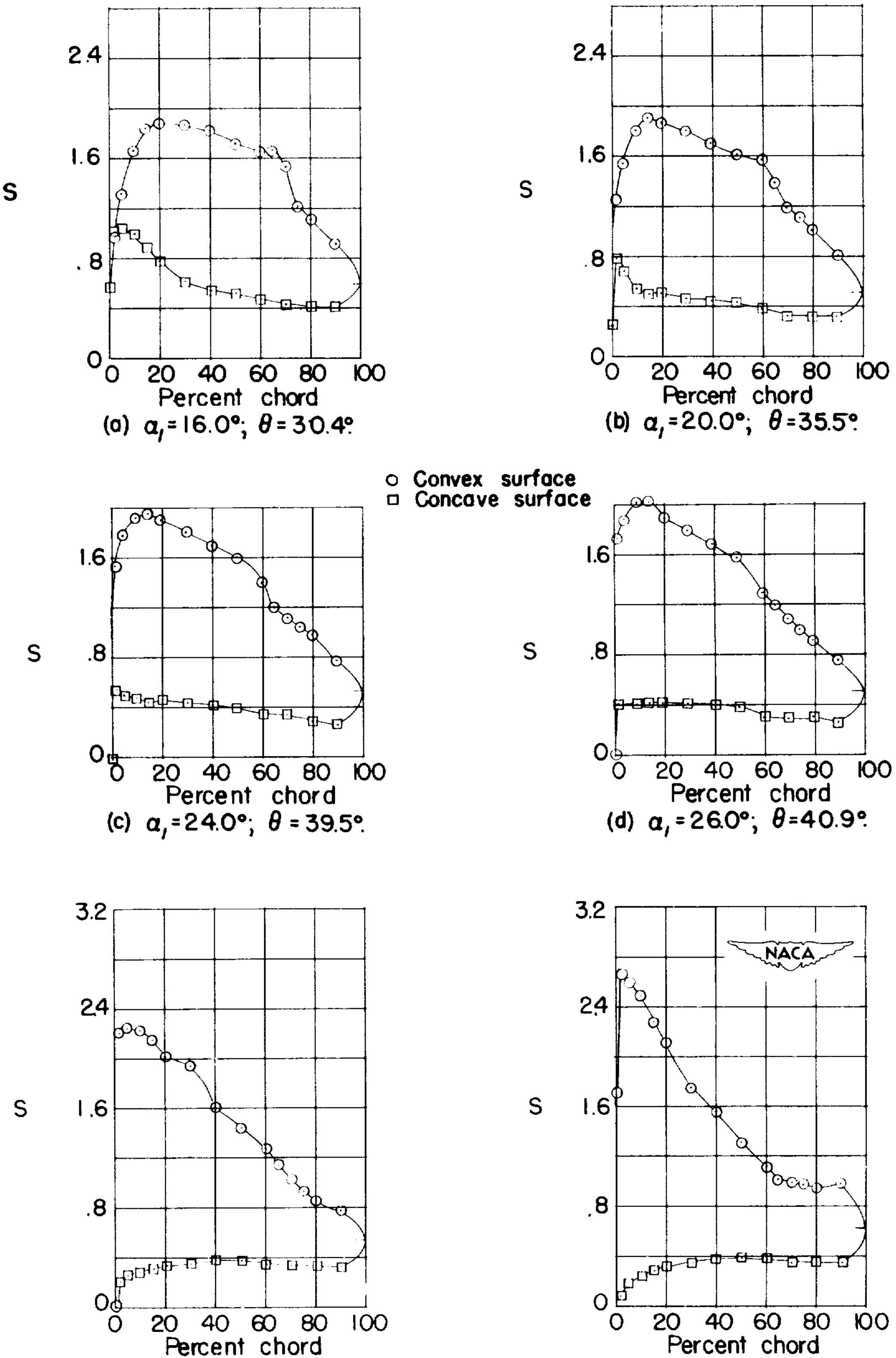

(a) $\alpha_1 = 16.0^\circ$; $\theta = 30.4^\circ$

(b) $\alpha_1 = 20.0^\circ$; $\theta = 35.5^\circ$

(c) $\alpha_1 = 24.0^\circ$; $\theta = 39.5^\circ$

(d) $\alpha_1 = 26.0^\circ$; $\theta = 40.9^\circ$

(e) $\alpha_1 = 30.0^\circ$; $\theta = 42.4^\circ$

(f) $\alpha_1 = 34.0^\circ$; $\theta = 43.2^\circ$.

Figure 34.- Blade-surface pressure distributions and blade section characteristics for the cascade combination, $\beta_1 = 45^\circ$, $\sigma = 1.00$, and blade section, NACA 65-(24)10.

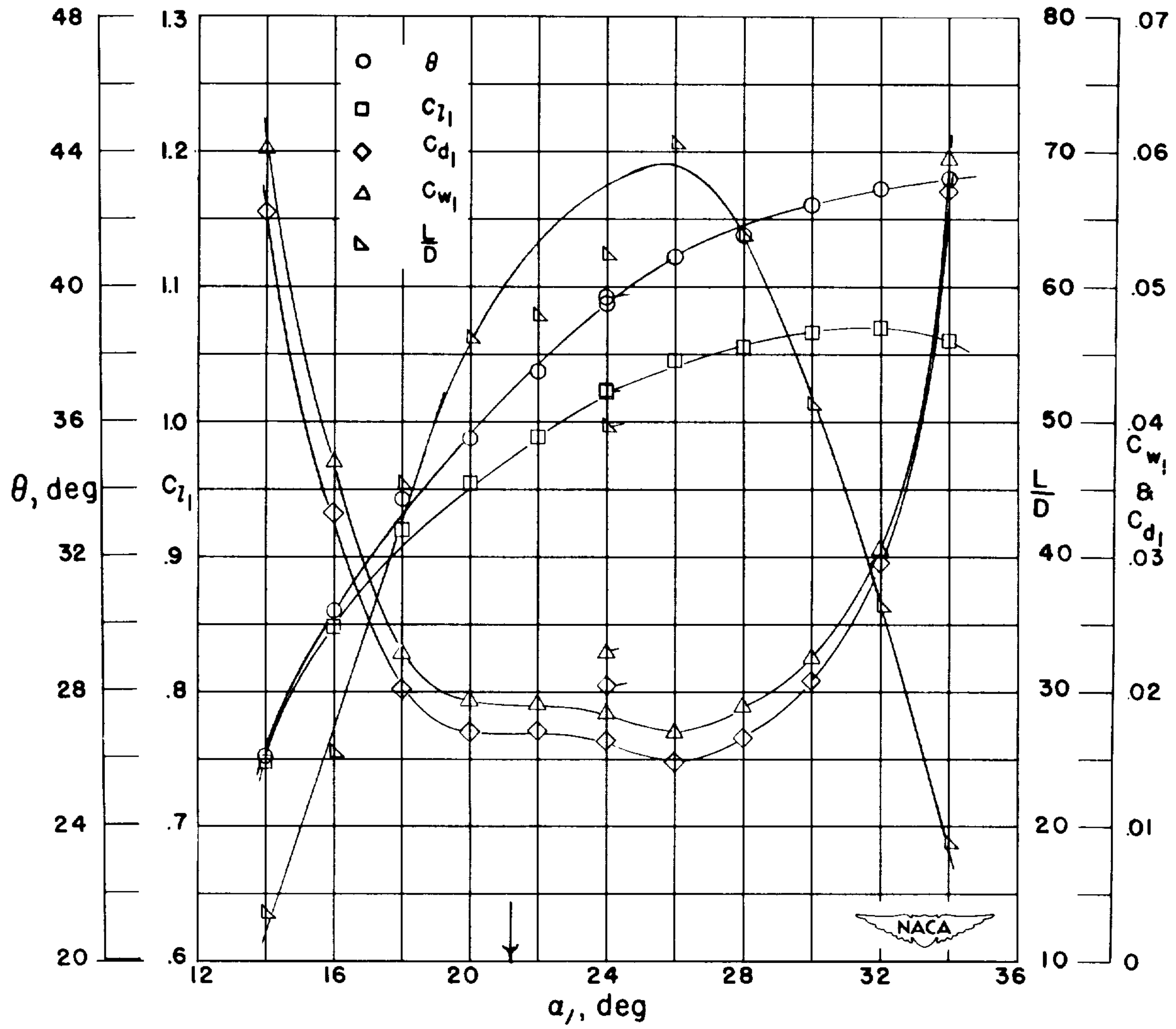

(g) Section characteristics; arrow shows design angle of attack; flagged symbol indicates leading-edge roughness.

Figure 34.- Concluded.

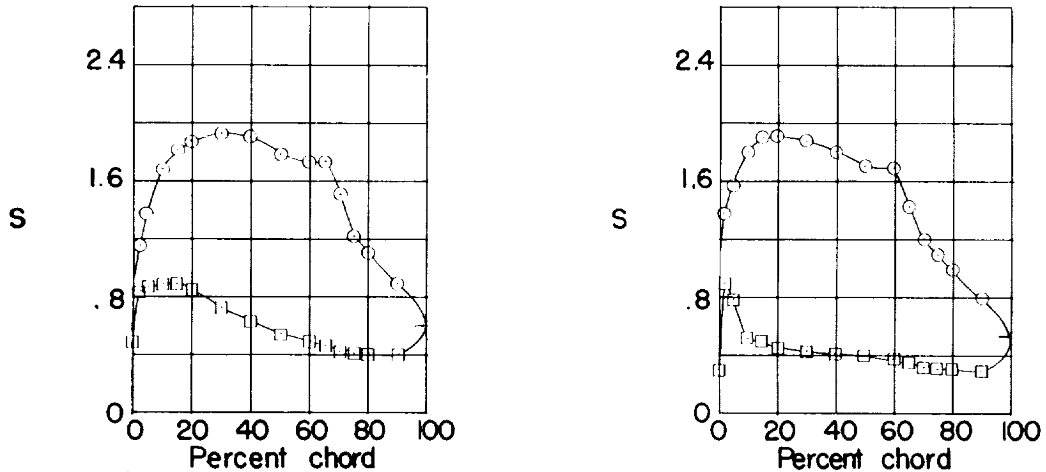

(a) $\alpha_1 = 17.5^\circ$; $\theta = 31.6^\circ$.

(b) $\alpha_1 = 21.0^\circ$; $\theta = 37.1^\circ$.

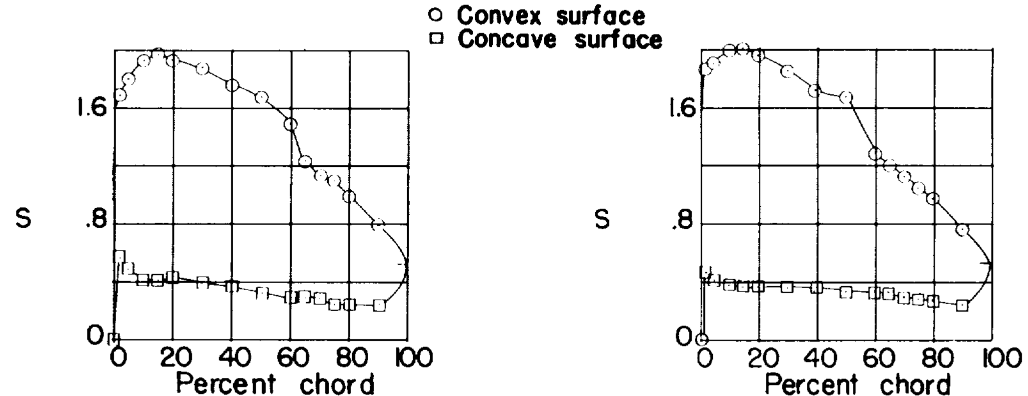

(c) $\alpha_1 = 25.0^\circ$; $\theta = 41.4^\circ$.

(d) $\alpha_1 = 27.0^\circ$; $\theta = 43.4^\circ$.

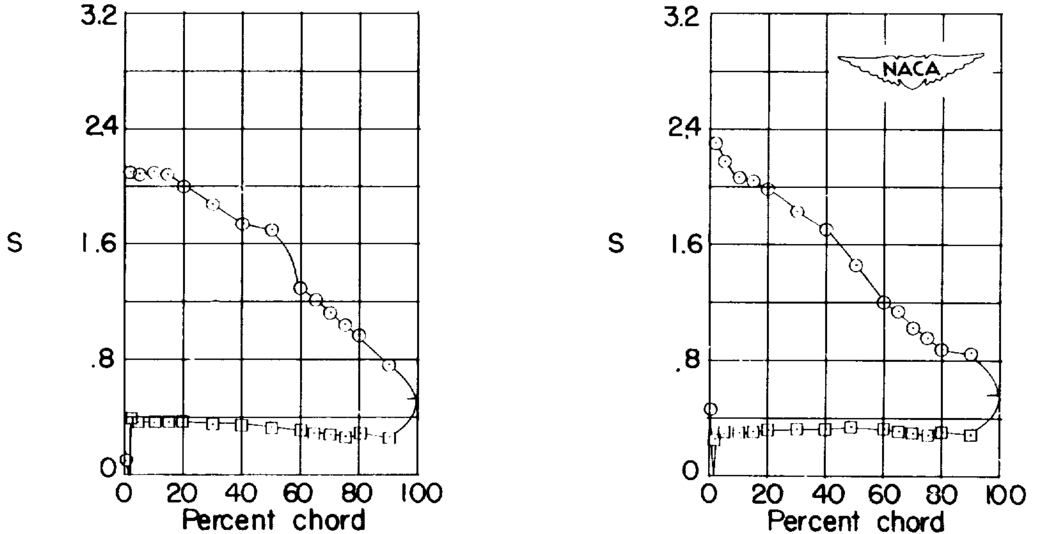

(e) $\alpha_1 = 29.0^\circ$; $\theta = 44.3^\circ$.

(f) $\alpha_1 = 33.0^\circ$; $\theta = 45.5^\circ$.

Figure 35.- Blade-surface pressure distributions and blade section characteristics for the cascade combination, $\beta_1 = 45^\circ$, $\sigma = 1.00$ and blade section, NACA 65-(27)10.

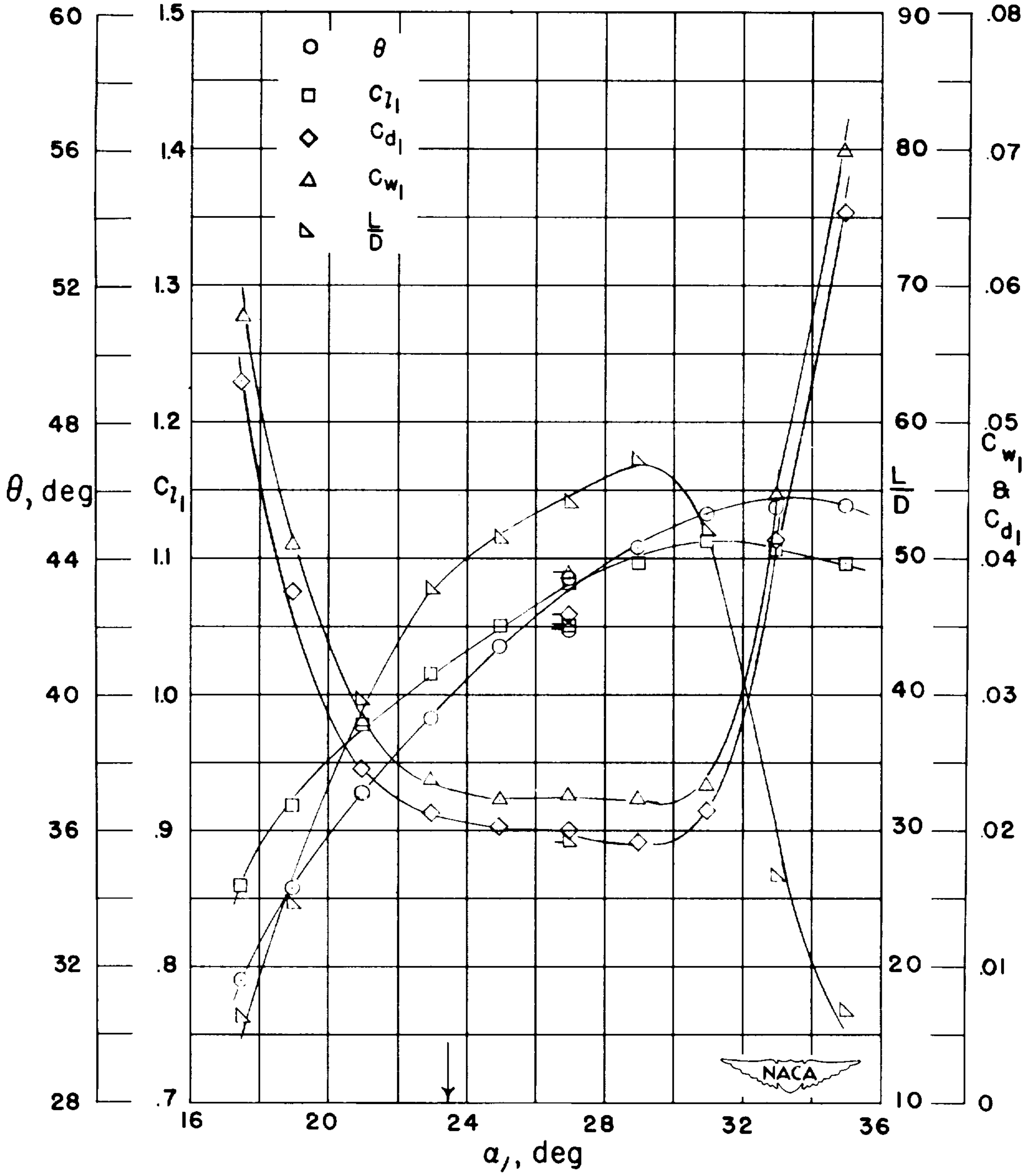

(g) Section characteristics; arrow shows design angle of attack; flagged symbol indicates leading-edge roughness.

Figure 35.- Concluded.

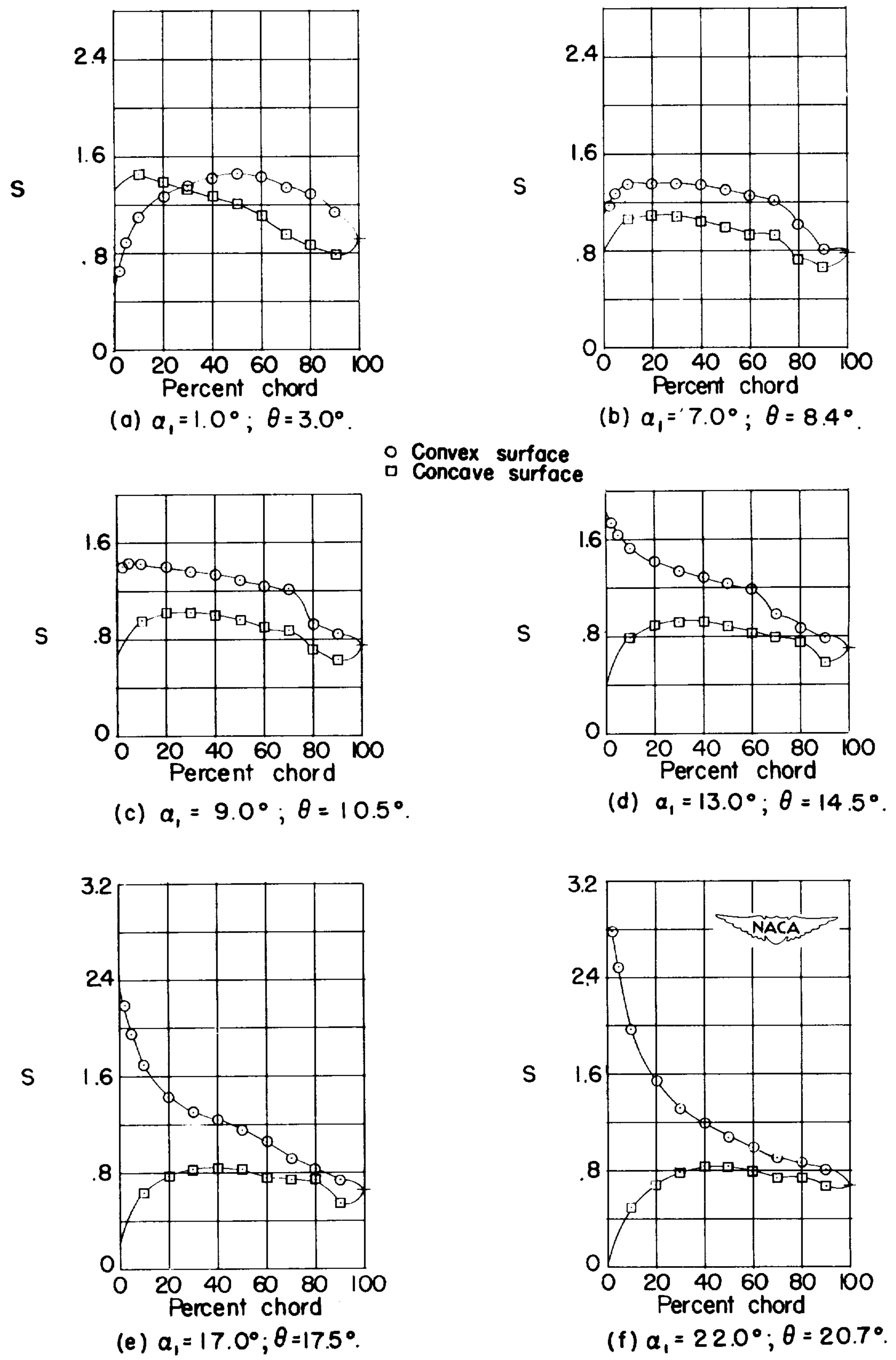

(a) $\alpha_1 = 1.0°$; $\theta = 3.0°$.

(b) $\alpha_1 = 7.0°$; $\theta = 8.4°$.

(c) $\alpha_1 = 9.0°$; $\theta = 10.5°$.

(d) $\alpha_1 = 13.0°$; $\theta = 14.5°$.

(e) $\alpha_1 = 17.0°$; $\theta = 17.5°$.

(f) $\alpha_1 = 22.0°$; $\theta = 20.7°$.

Figure 36.- Blade-surface pressure distributions and blade section characteristics for the cascade combination, $\beta_1 = 45^\circ$, $\sigma = 1.25$, and blade section, NACA 65-410.

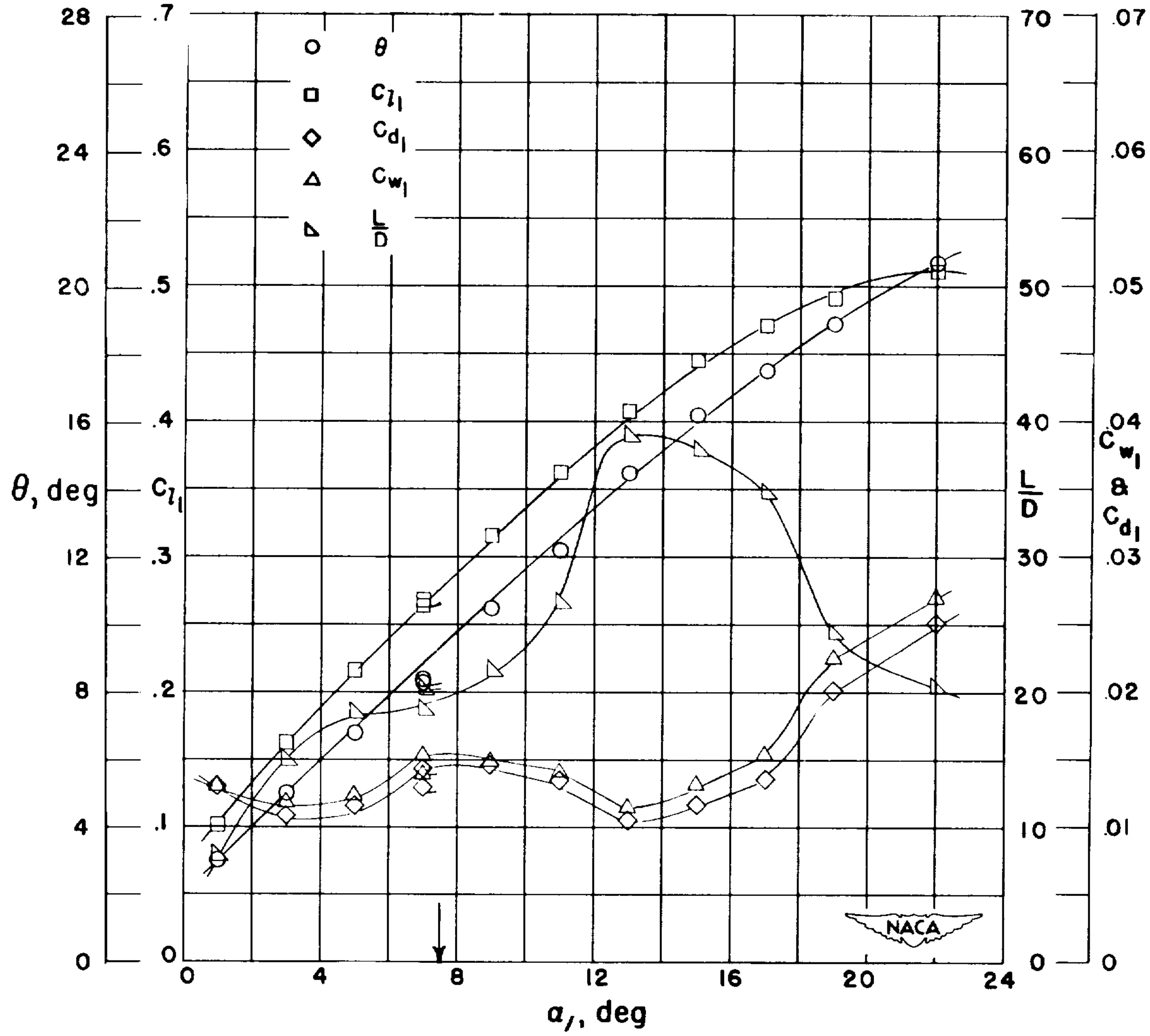

(g) Section characteristics; arrow shows design angle of attack; flagged symbol indicates leading-edge roughness.

Figure 36.- Concluded.

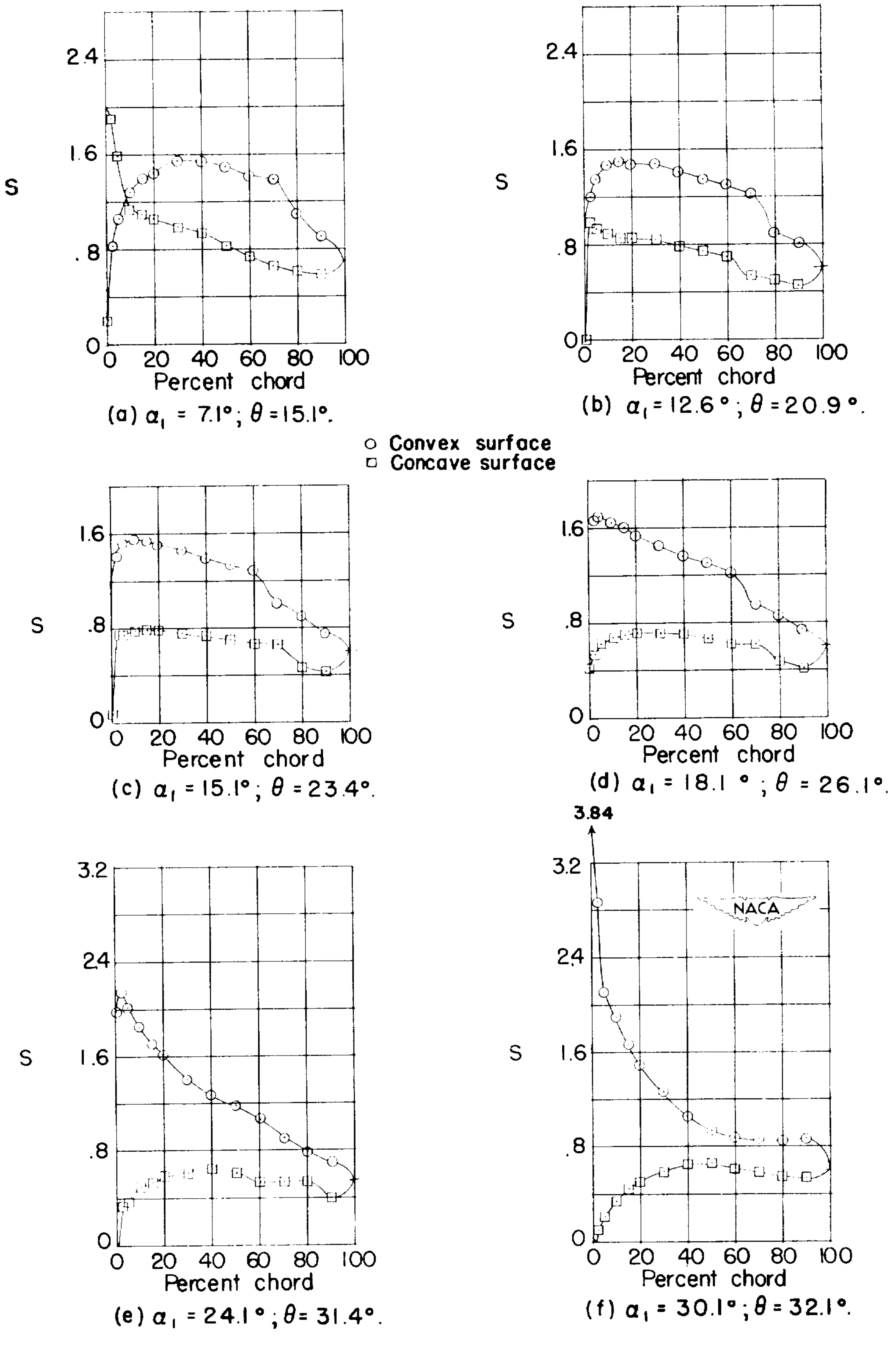
(a) α_1 = 7.1°; θ = 15.1°.

(b) α_1 = 12.6°; θ = 20.9°.

(c) α_1 = 15.1°; θ = 23.4°.

(d) α_1 = 18.1°; θ = 26.1°.

(e) α_1 = 24.1°; θ = 31.4°.

(f) α_1 = 30.1°; θ = 32.1°.

Figure 37.- Blade-surface pressure distributions and blade section characteristics for the cascade combination, $\beta_1 = 45^\circ$, $\sigma = 1.25$, and blade section, NACA 65-(12)10.

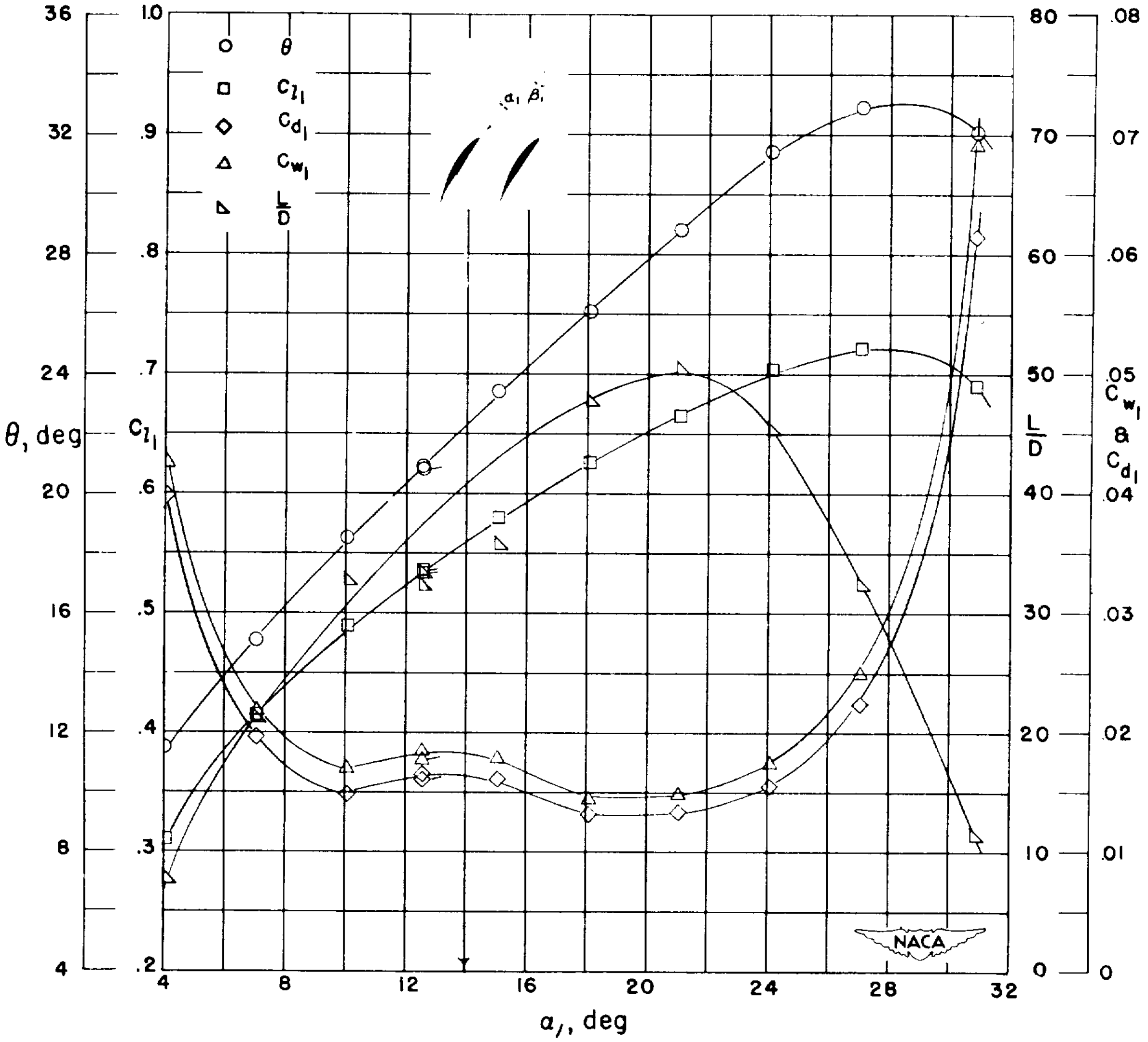

(g) Section characteristics, arrow shows design angle of attack; flagged symbol indicates leading-edge roughness.

Figure 37.- Concluded.

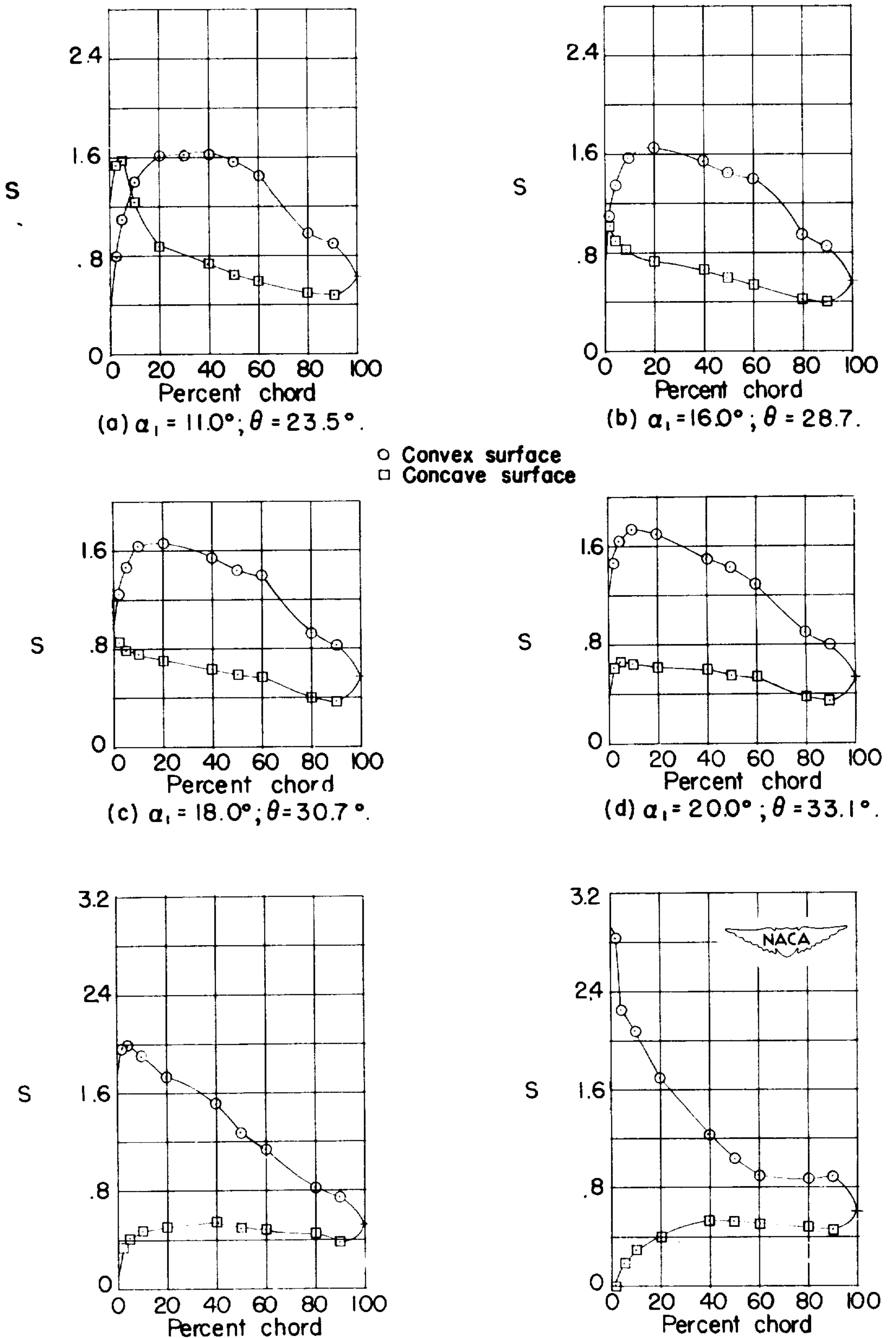

(a) α_1 = 11.0°; θ = 23.5°.

(b) α_1 = 16.0°; θ = 28.7.

(c) α_1 = 18.0°; θ = 30.7°.

(d) α_1 = 20.0°; θ = 33.1°.

(f) α_1 = 35.0°; θ = 42.5°.

(e) α_1 = 26.0°; θ = 38.0°.

Figure 38.- Blade-surface pressure distributions and blade section characteristics for the cascade combination, $\beta_1 = 45^\circ$, $\sigma = 1.25$, and blade section, NACA 65-(18)10.

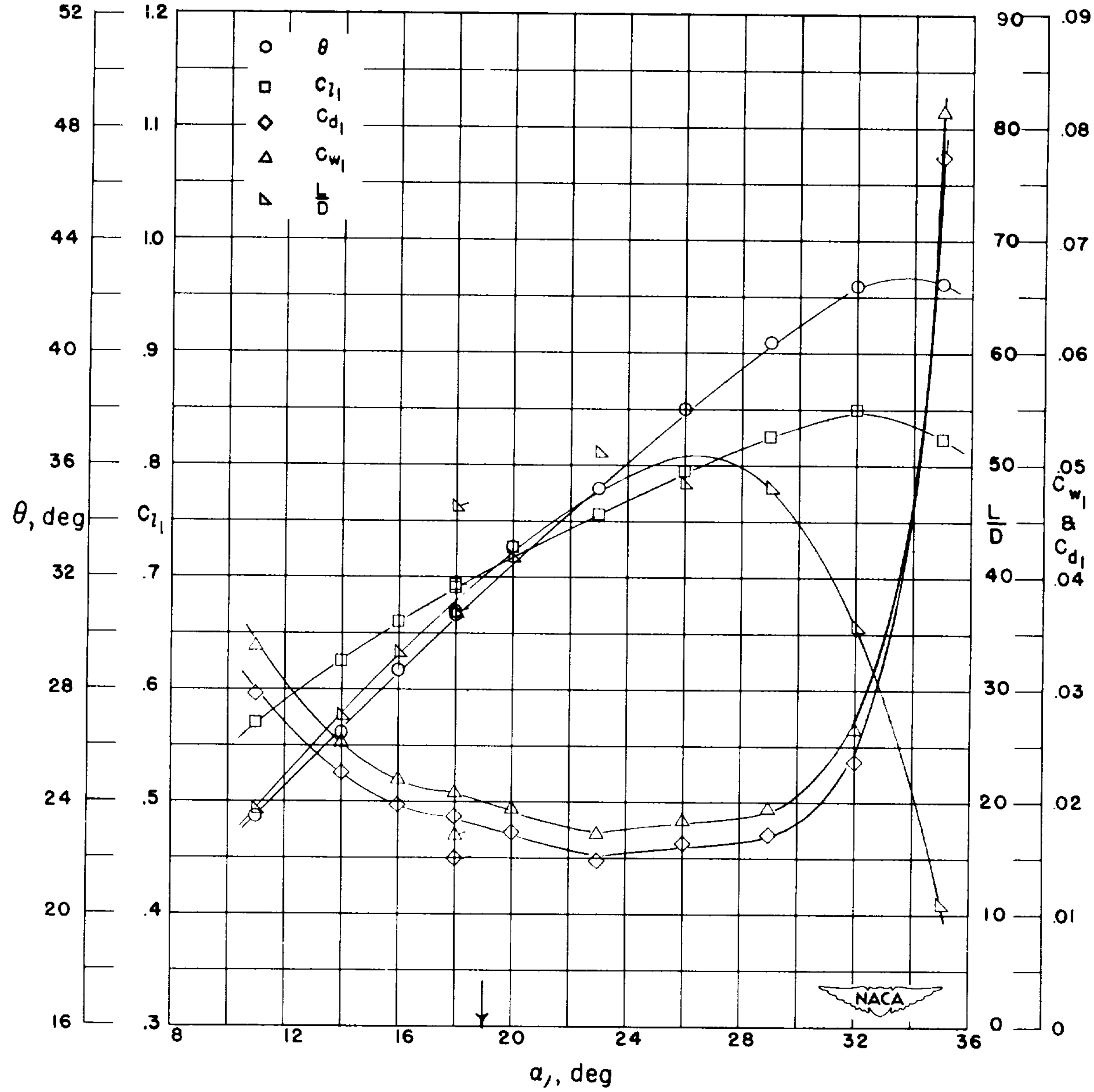

(g) Section characteristics; arrow shows design angle of attack, flagged symbol indicates leading-edge roughness.

Figure 38.- Concluded.

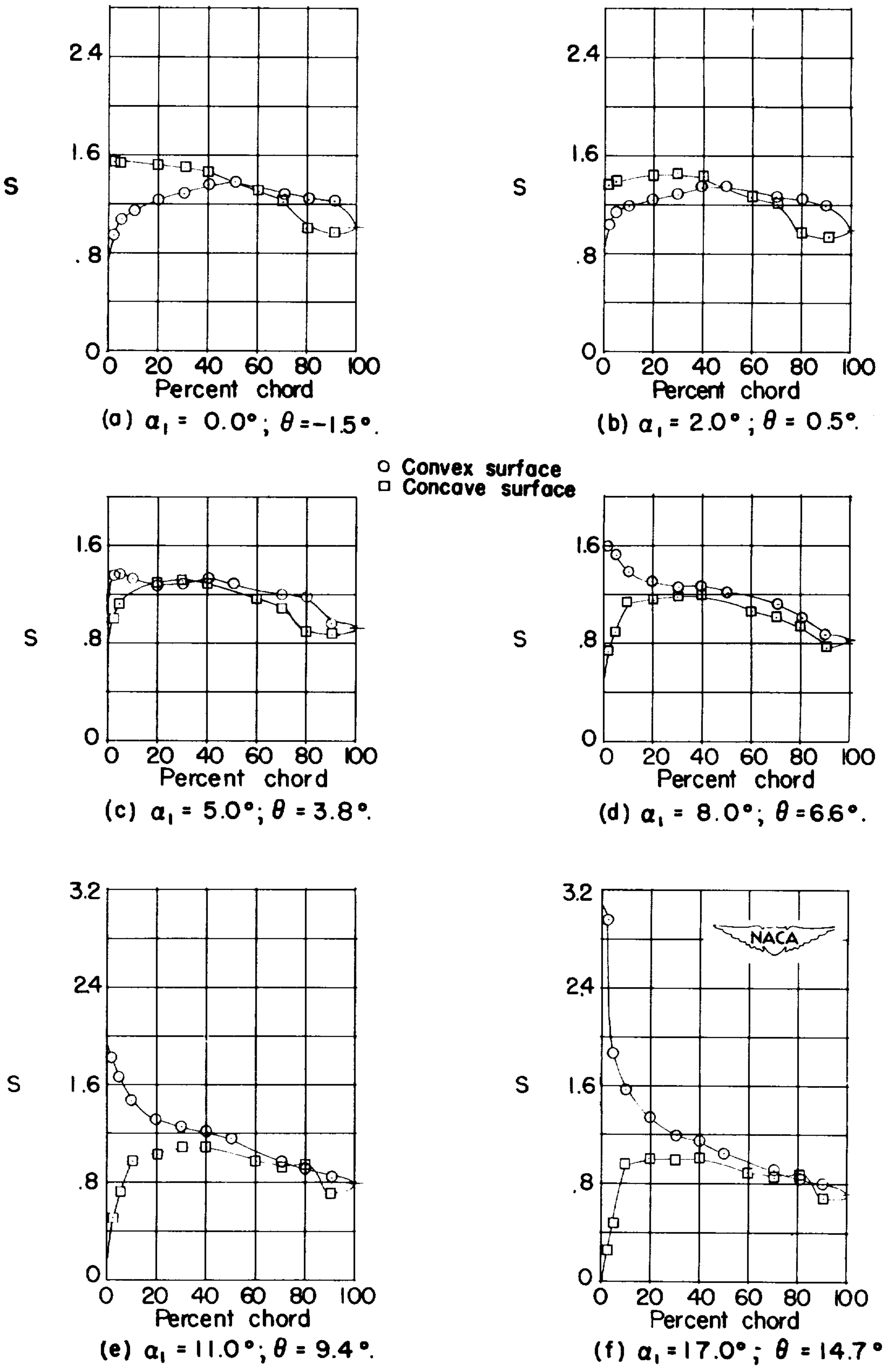

(a) α_1 = 0.0°; θ = −1.5°.

(b) α_1 = 2.0°; θ = 0.5°.

(c) α_1 = 5.0°; θ = 3.8°.

(d) α_1 = 8.0°; θ = 6.6°.

(e) α_1 = 11.0°; θ = 9.4°.

(f) α_1 = 17.0°; θ = 14.7°.

Figure 39.- Blade-surface pressure distributions and blade section characteristics for the cascade combination, $\beta_1 = 45^\circ$, $\sigma = 1.50$, and blade section, NACA 65-010.

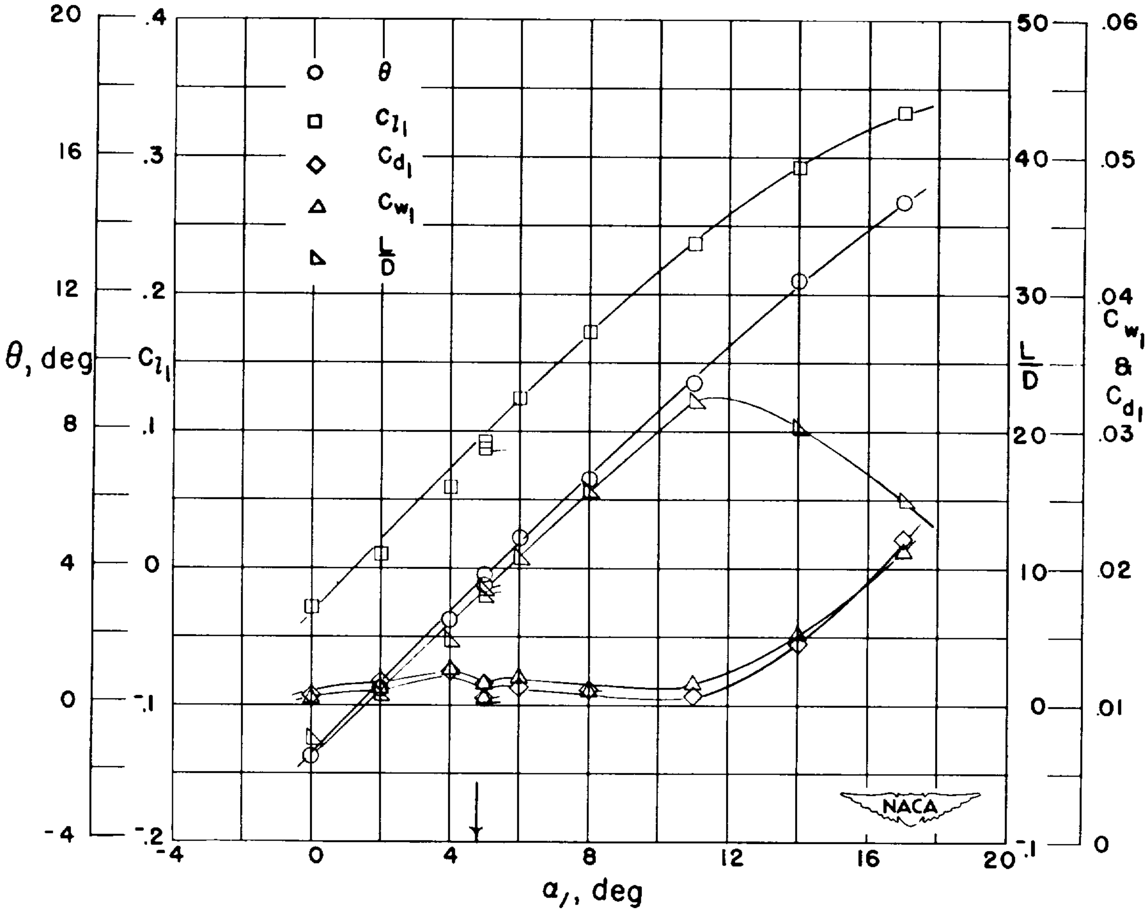

(g) Section characteristics; arrow shows design angle of attack; flagged symbol indicates leading-edge roughness.

Figure 39.- Concluded.

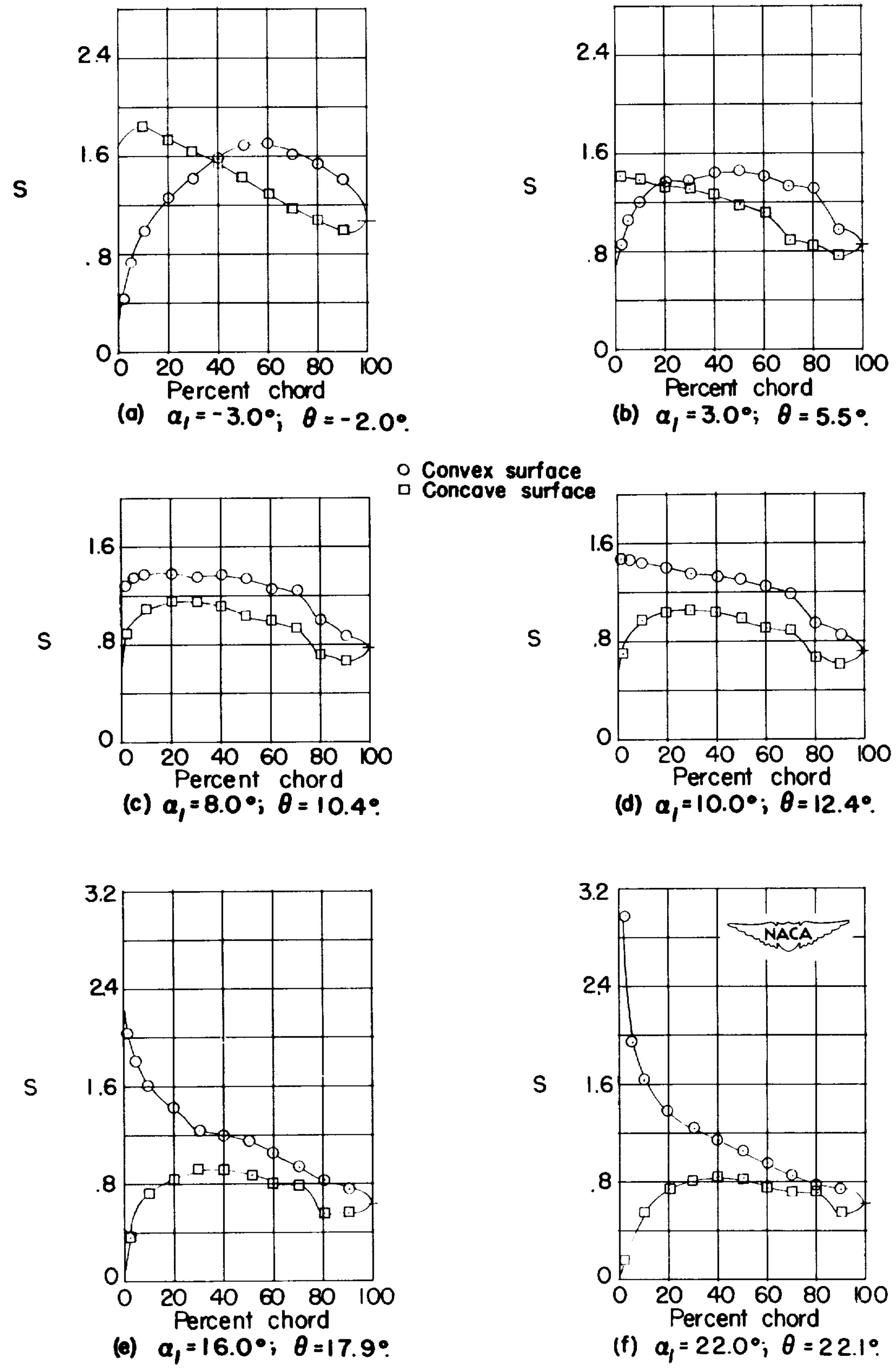

(a) $a_l = -3.0°$; $\theta = -2.0°$.

(b) $a_l = 3.0°$; $\theta = 5.5°$.

(c) $a_l = 8.0°$; $\theta = 10.4°$.

(d) $a_l = 10.0°$; $\theta = 12.4°$.

(e) $a_l = 16.0°$; $\theta = 17.9°$.

(f) $a_l = 22.0°$; $\theta = 22.1°$.

Figure 40.- Blade-surface pressure distributions and blade section characteristics for the cascade combination, $\beta_1 = 45°$, $\sigma = 1.50$, and blade section, NACA 65-410.

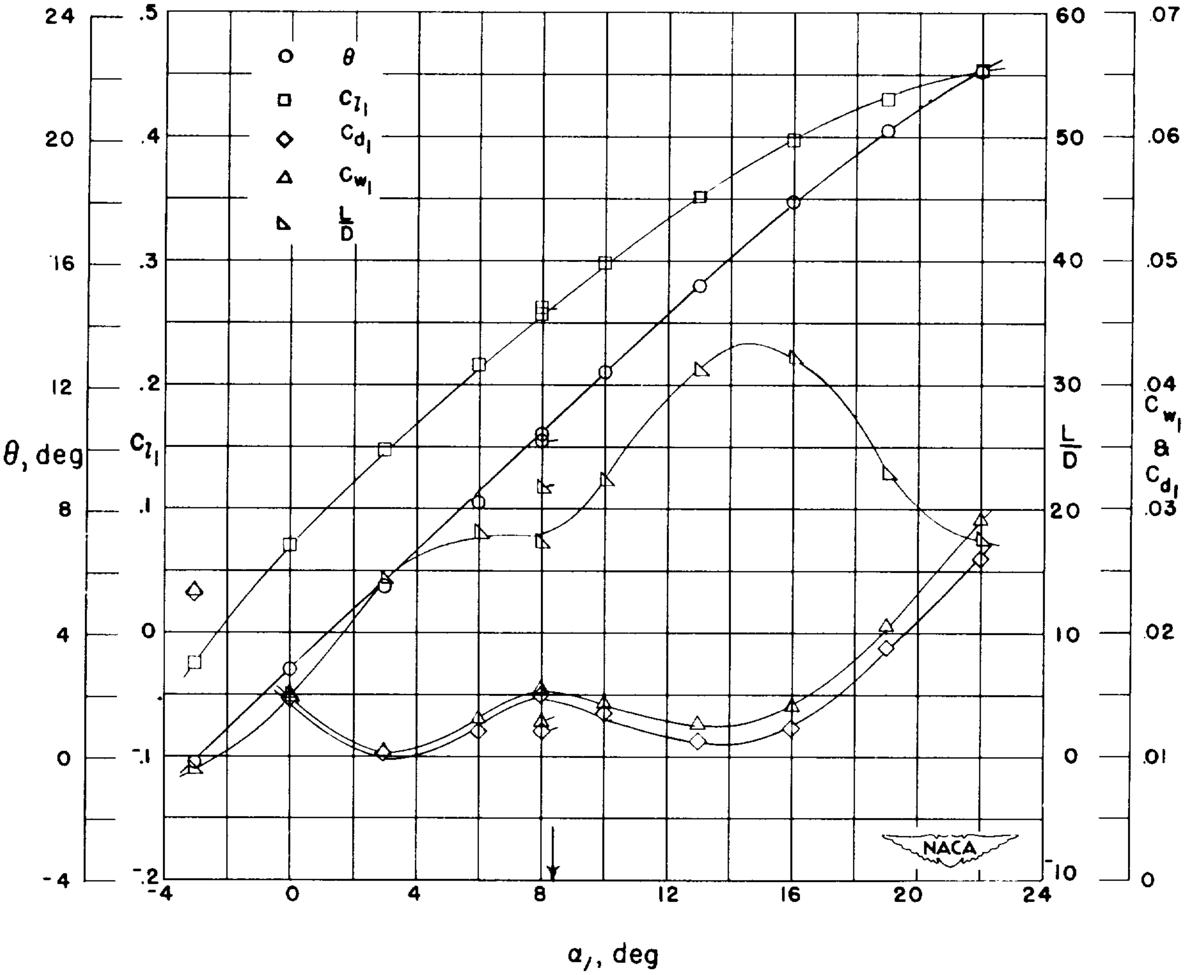

(g) Section characteristics; arrow shows design angle of attack; flagged symbol indicates leading-edge roughness.

Figure 40.- Concluded.

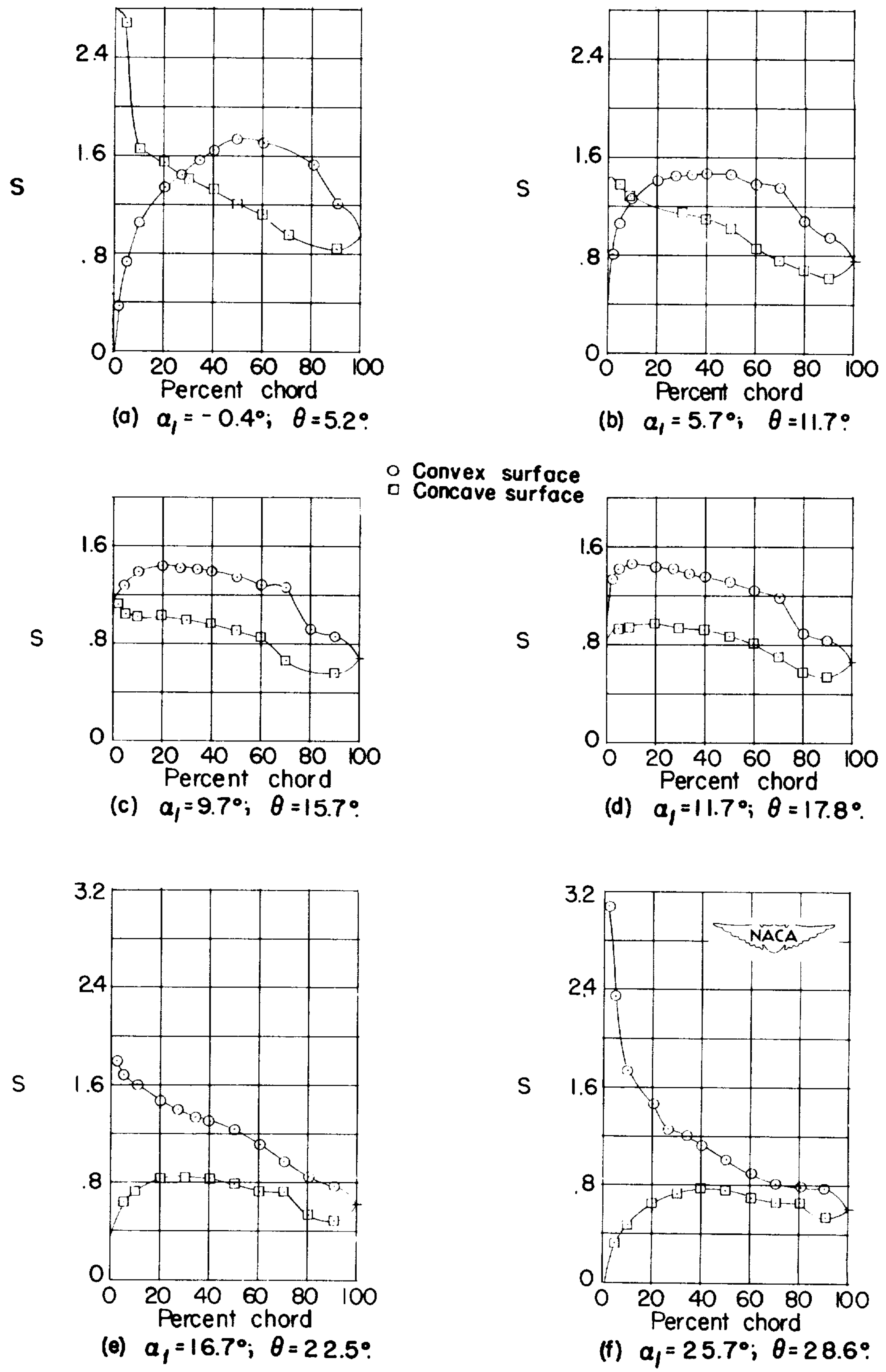

Figure 41.- Blade-surface pressure distributions and blade section characteristics for the cascade combination, $\beta_1 = 45^\circ$, $\sigma = 1.50$, and blade section, NACA 65-810.

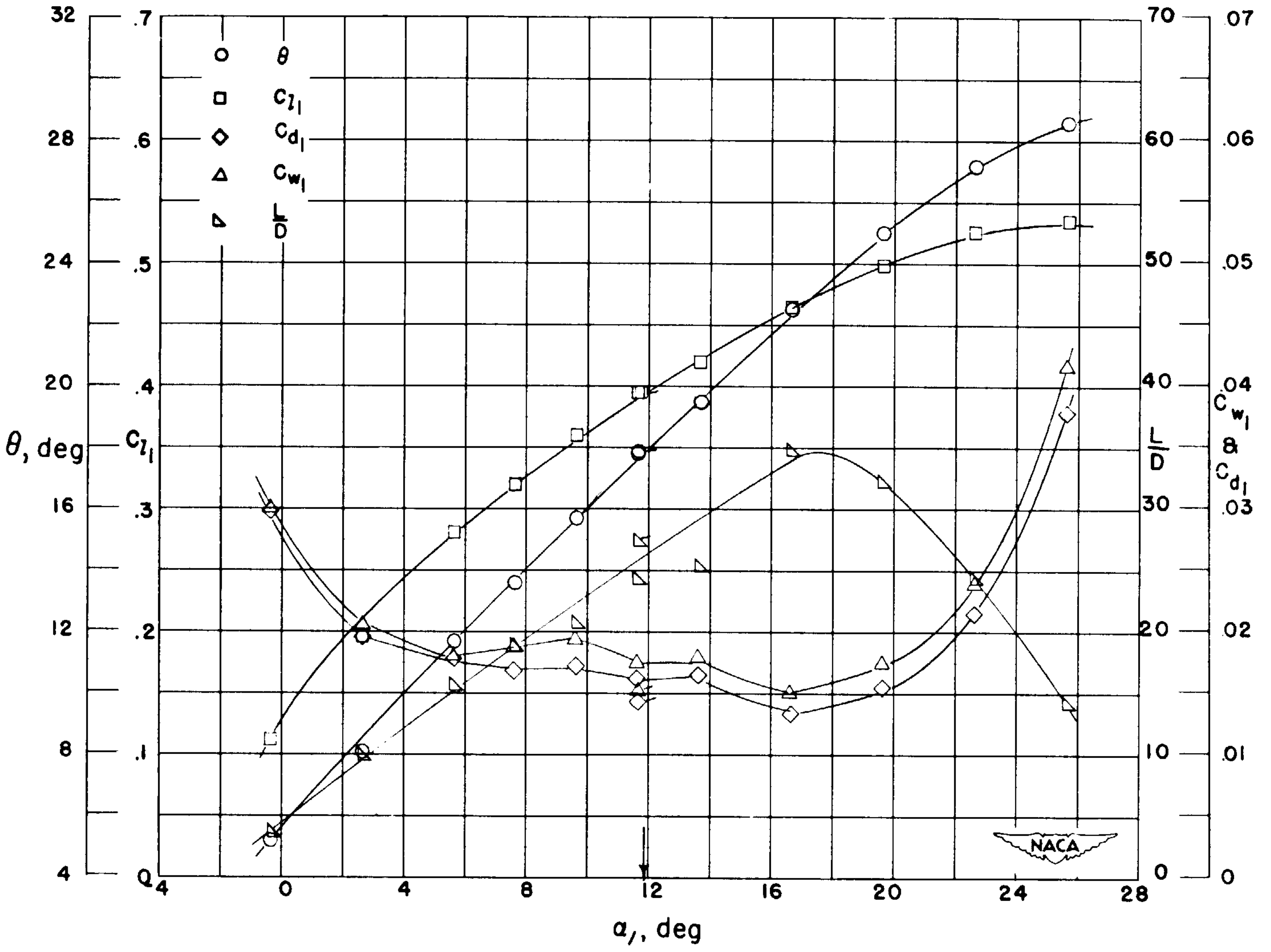

(g) Section characteristics; arrow shows design angle of attack; flagged symbol indicates leading-edge roughness.

Figure 41.- Concluded.

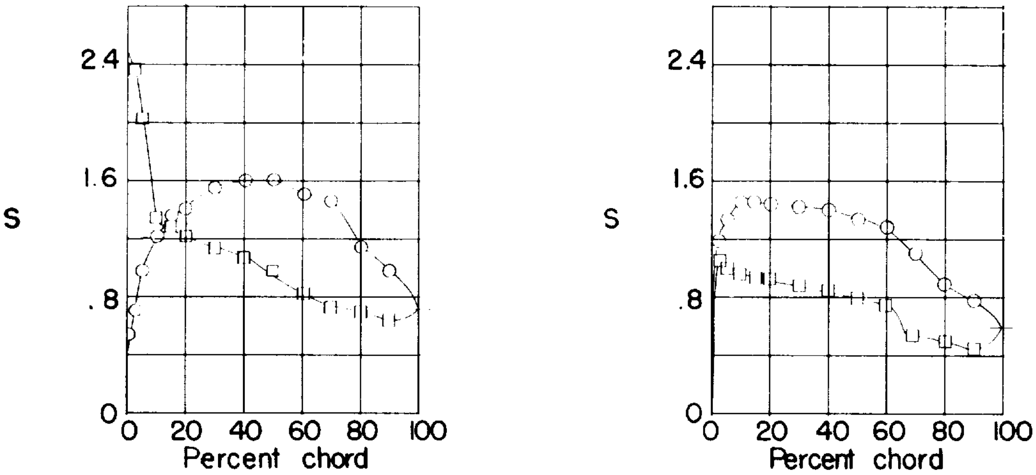

(a) $\alpha_1 = 5.1°$; $\theta = 13.9°$

(b) $\alpha_1 = 12.1°$; $\theta = 21.4°$

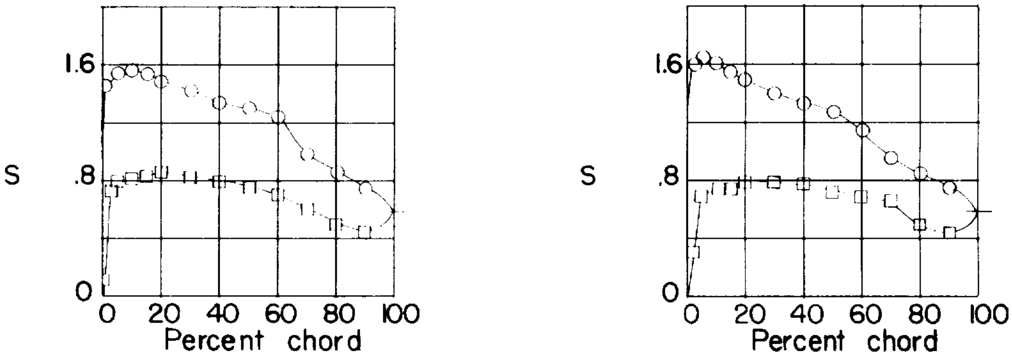

(c) $\alpha_1 = 16.1°$; $\theta = 25.5°$

(d) $\alpha_1 = 18.1°$; $\theta = 27.3°$

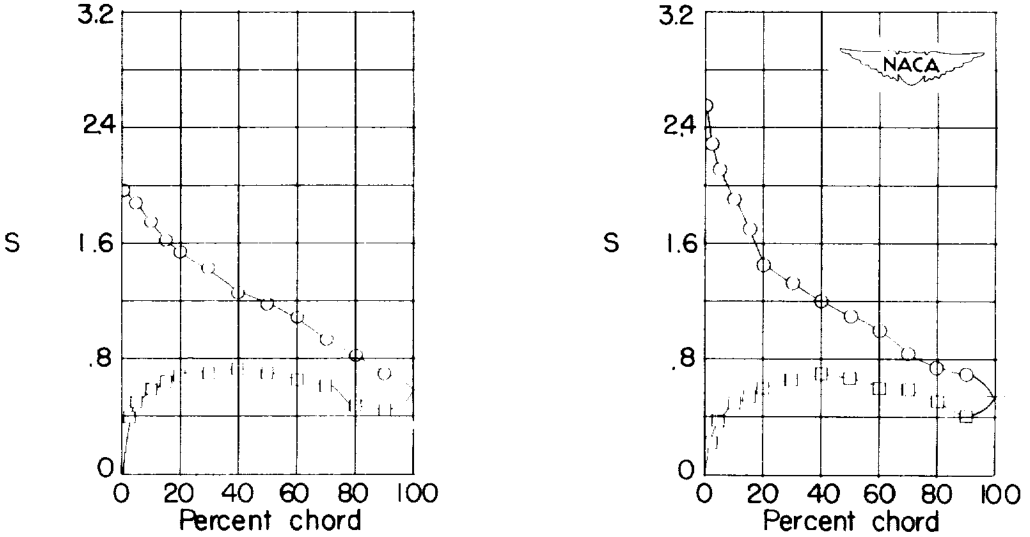

(e) $\alpha_1 = 22.1°$; $\theta = 30.6°$

(f) $\alpha_1 = 27.6°$; $\theta = 35.0°$

Figure 42.- Blade-surface pressure distributions and blade section characteristics for the cascade combination, $\beta_1 = 45°$, $\sigma = 1.50$, and blade section, NACA 65-(12)10.

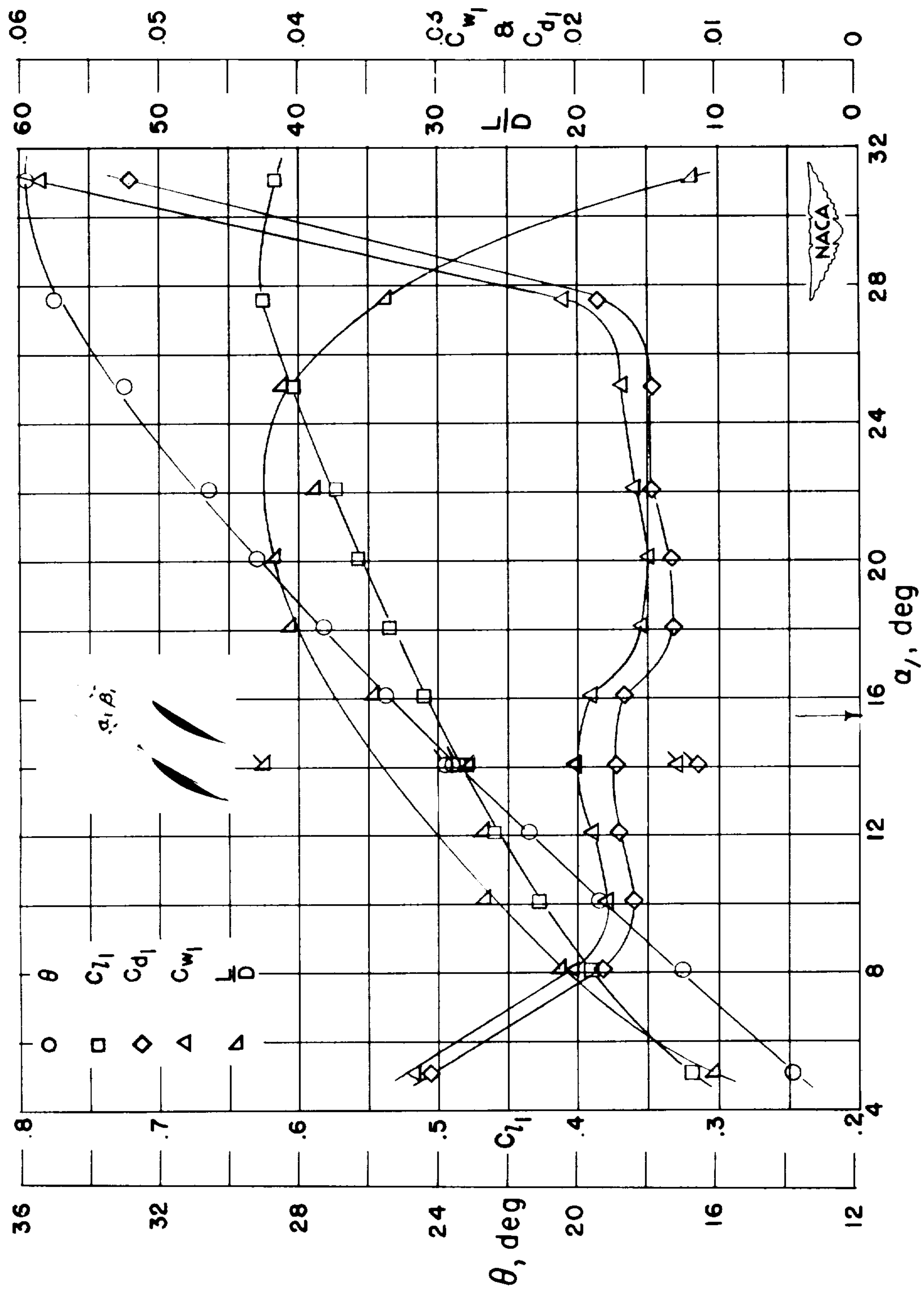

(g) Section characteristics; arrow shows design angle of attack; flagged symbol indicates leading-edge roughness.

Figure 42.- Concluded.

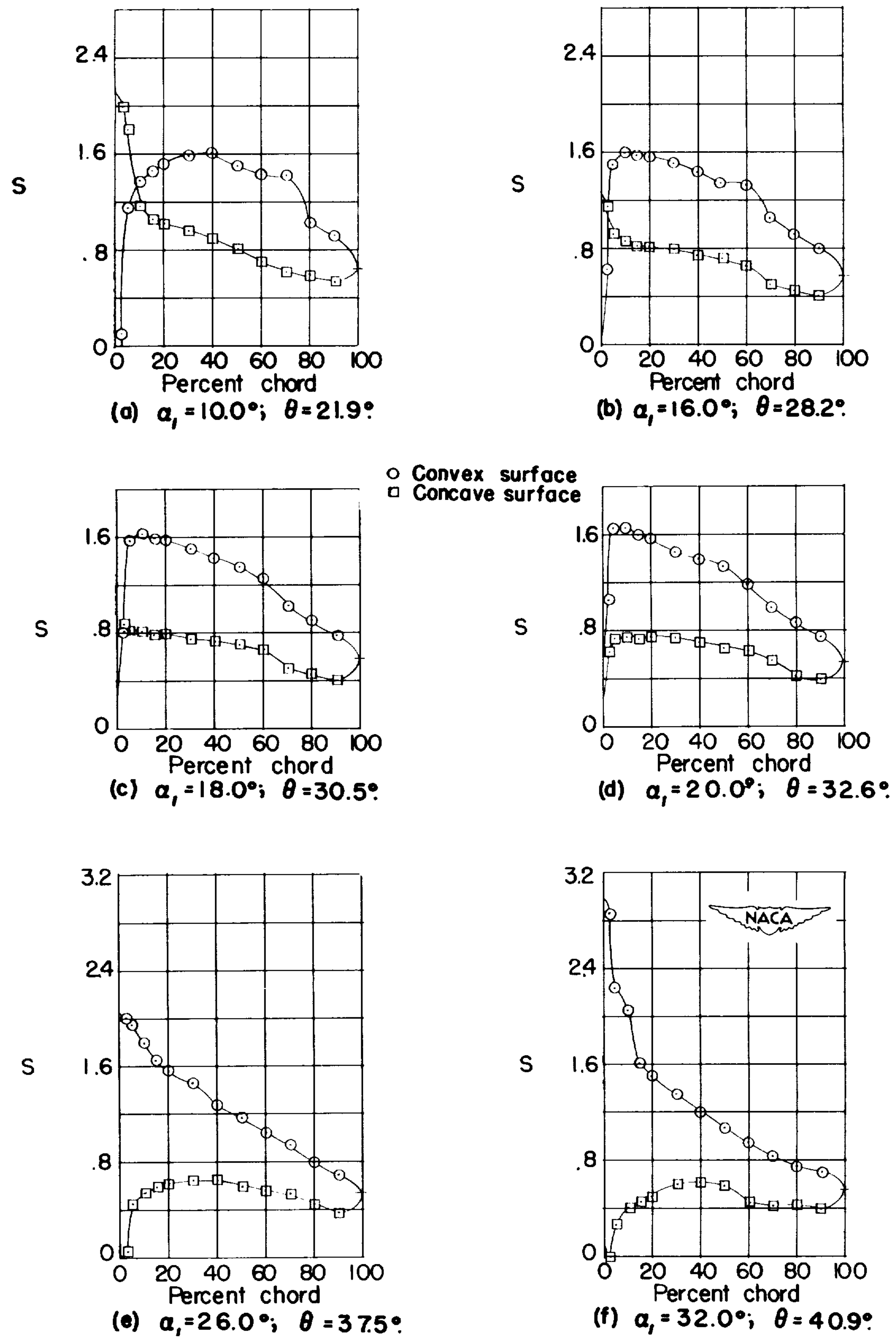

(a) $\alpha_1 = 10.0^\circ$; $\theta = 21.9^\circ$

(b) $\alpha_1 = 16.0^\circ$; $\theta = 28.2^\circ$

(c) $\alpha_1 = 18.0^\circ$; $\theta = 30.5^\circ$

(d) $\alpha_1 = 20.0^\circ$; $\theta = 32.6^\circ$

(e) $\alpha_1 = 26.0^\circ$; $\theta = 37.5^\circ$

(f) $\alpha_1 = 32.0^\circ$; $\theta = 40.9^\circ$

Figure 43.- Blade-surface pressure distributions and blade section characteristics for the cascade combination, $\beta_1 = 45^\circ$, $\sigma = 1.50$, and blade section, NACA 65-(15)10.

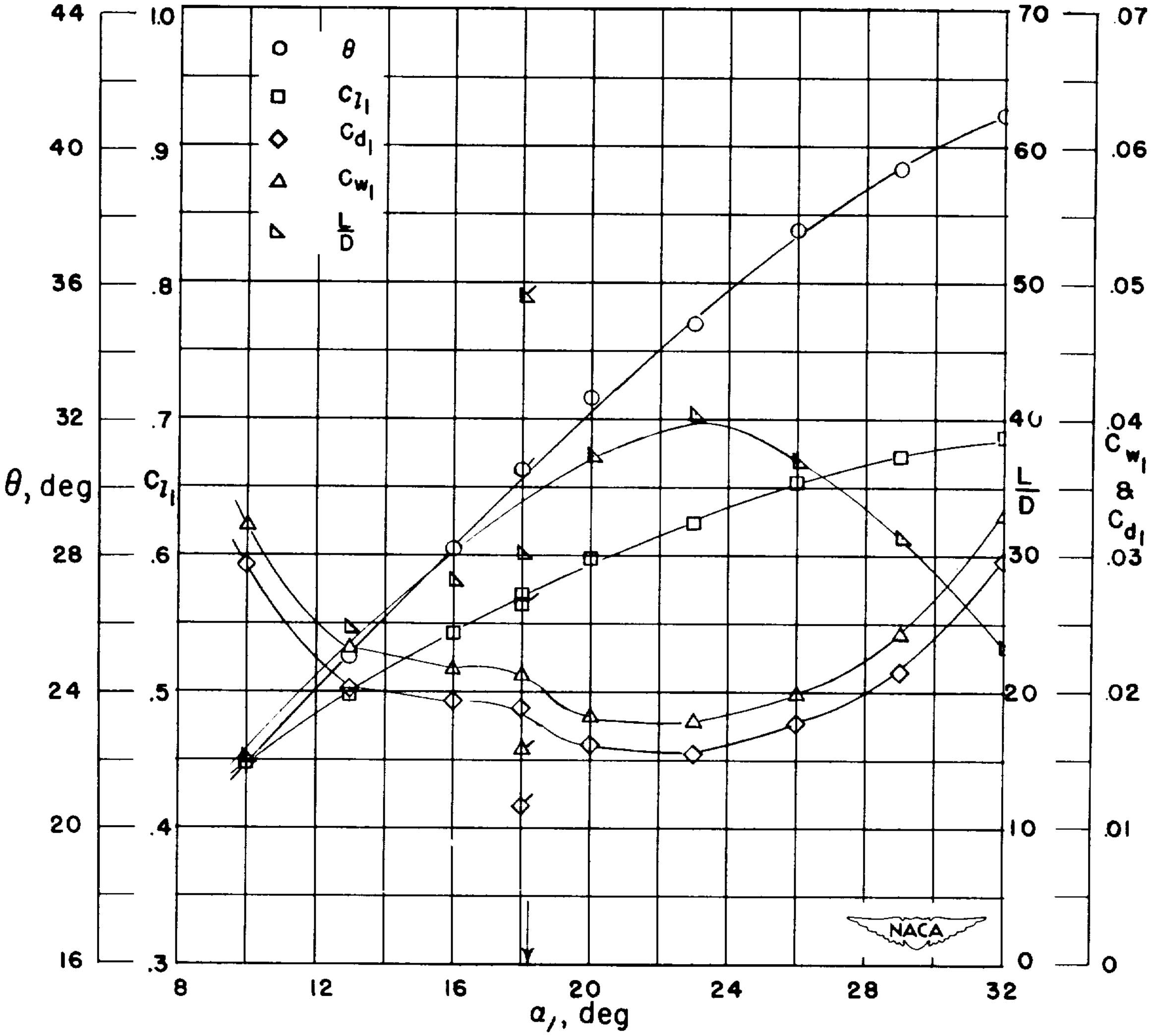

(g) Section characteristics; arrow shows design angle of attack; flagged symbol indicates leading-edge roughness.

Figure 43.- Concluded.

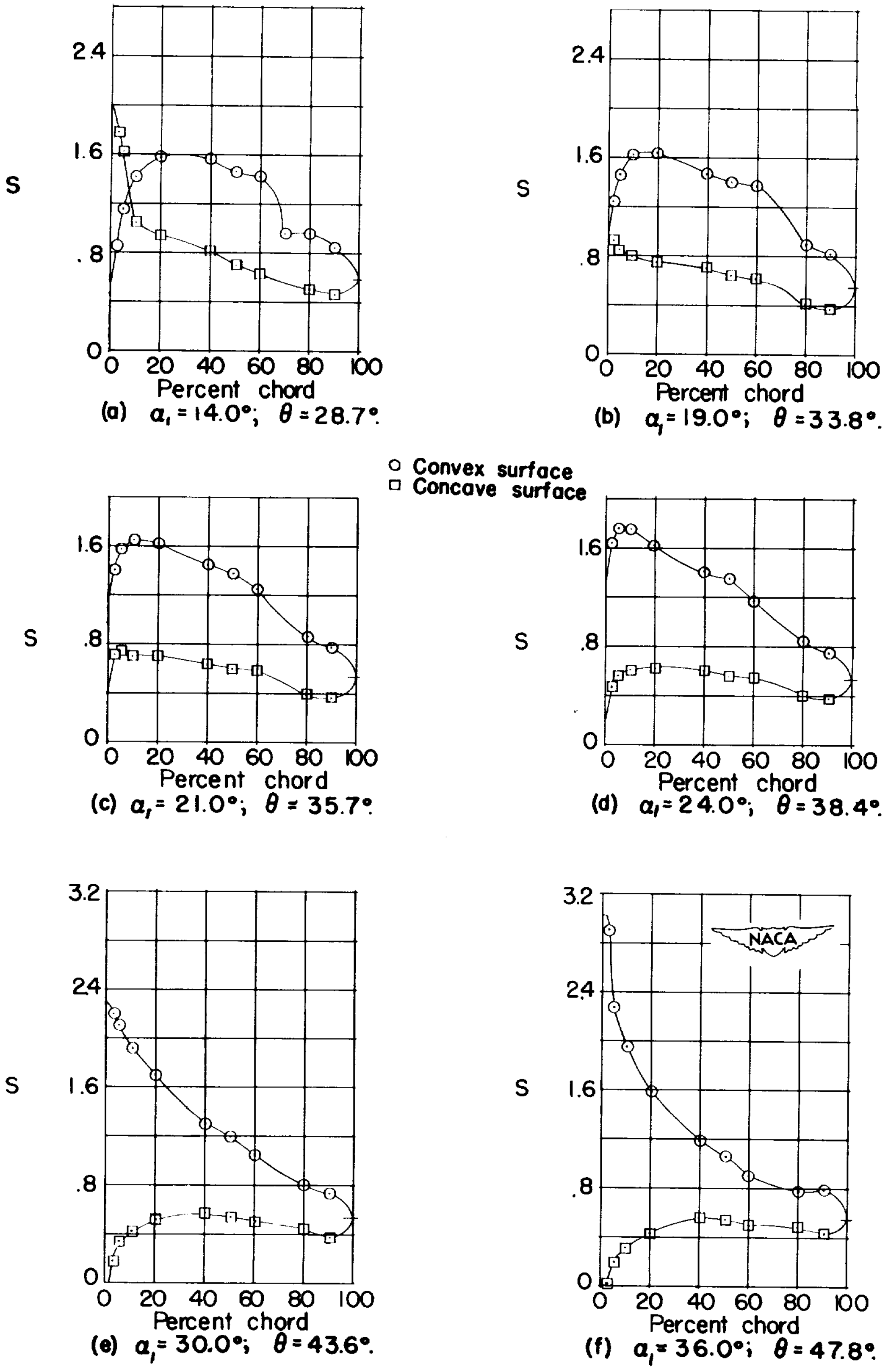

(a) $\alpha_1 = 14.0°$; $\theta = 28.7°$.

(b) $\alpha_1 = 19.0°$; $\theta = 33.8°$.

(c) $\alpha_1 = 21.0°$; $\theta = 35.7°$.

(d) $\alpha_1 = 24.0°$; $\theta = 38.4°$.

(e) $\alpha_1 = 30.0°$; $\theta = 43.6°$.

(f) $\alpha_1 = 36.0°$; $\theta = 47.8°$.

Figure 44.- Blade-surface pressure distributions and blade section characteristics for the cascade combination, $\beta_1 = 45°$, $\sigma = 1.50$, and blade section, NACA 65-(18)10.

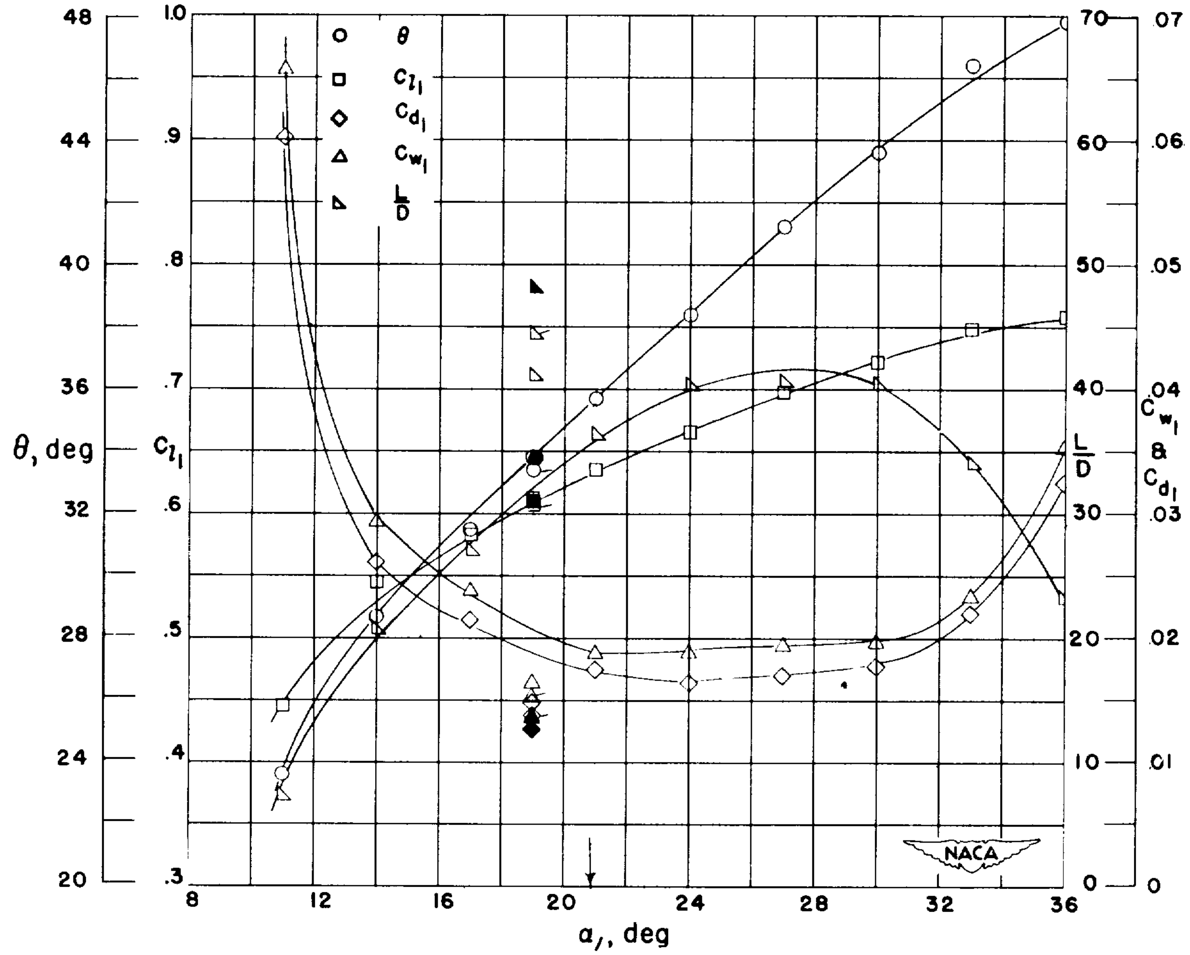

(g) Section characteristics; arrow shows design angle of attack, flagged symbol indicates leading-edge roughness; solid symbol indicates high Reynolds number.

Figure 44.- Concluded.

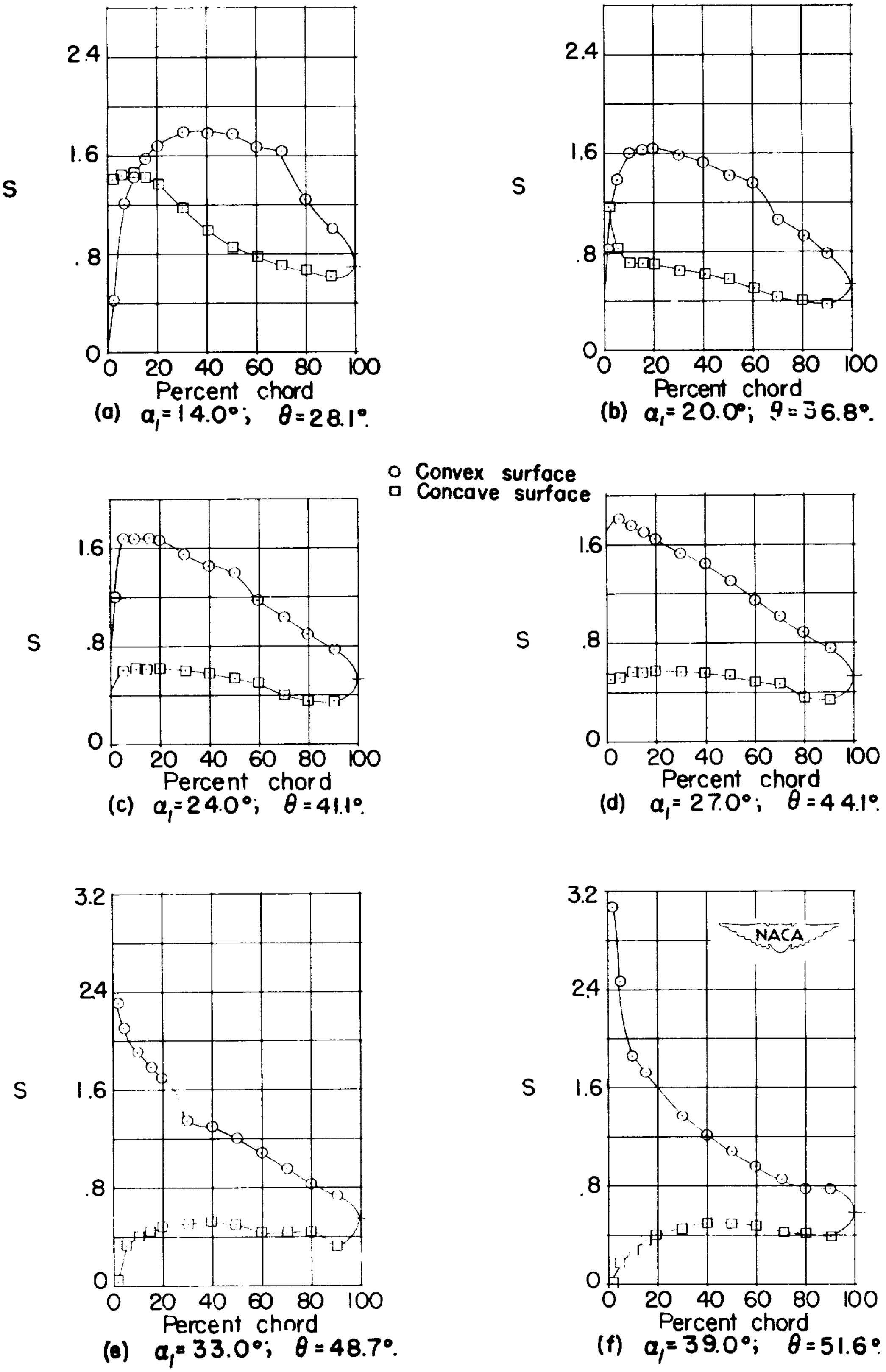

(a) $\alpha_1 = 14.0°$; $\theta = 28.1°$.

(b) $\alpha_1 = 20.0°$; $\theta = 36.8°$.

(c) $\alpha_1 = 24.0°$; $\theta = 41.1°$.

(d) $\alpha_1 = 27.0°$; $\theta = 44.1°$.

(e) $\alpha_1 = 33.0°$; $\theta = 48.7°$.

(f) $\alpha_1 = 39.0°$; $\theta = 51.6°$.

Figure 45.- Blade-surface pressure distributions and blade section characteristics for the cascade combination, $\beta_1 = 45°$, $\sigma = 1.50$, and blade section, NACA 65-(21)10.

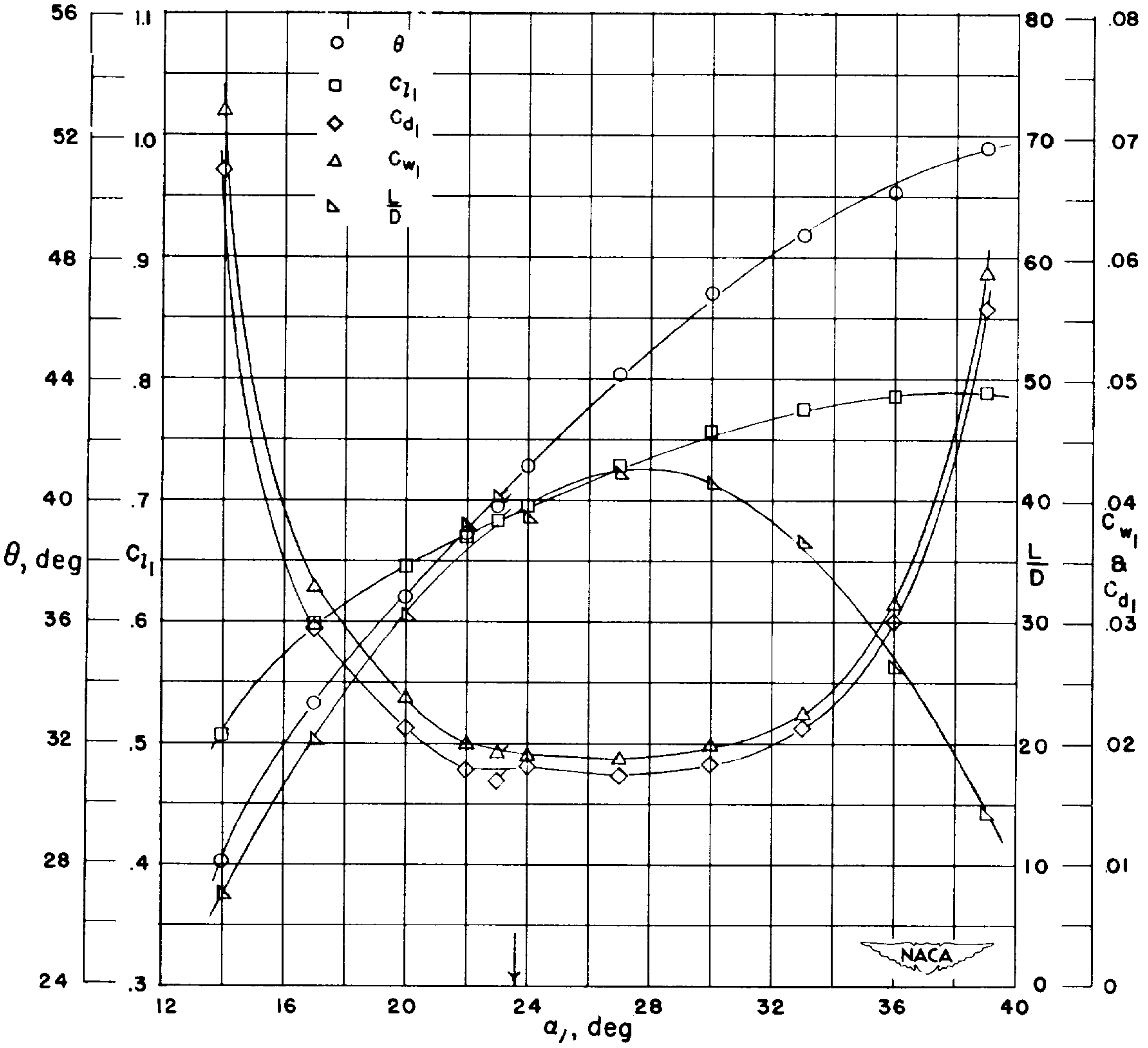

(g) Section characteristics; arrow shows design angle of attack; flagged symbol indicates leading-edge roughness.

Figure 45.- Concluded.

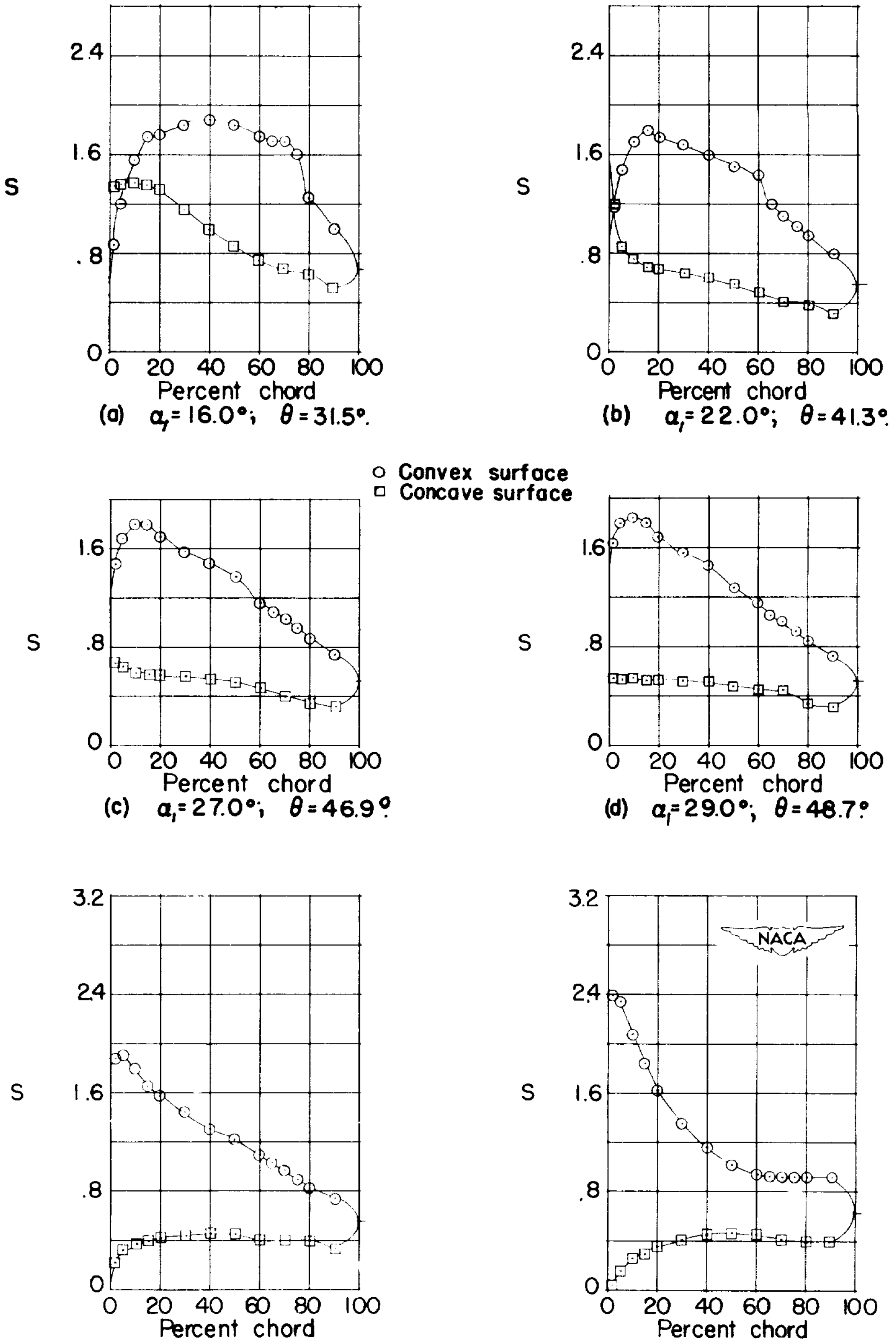

(a) $a_1 = 16.0°$; $\theta = 31.5°$.

(b) $a_1 = 22.0°$; $\theta = 41.3°$.

(c) $a_1 = 27.0°$; $\theta = 46.9°$.

(d) $a_1 = 29.0°$; $\theta = 48.7°$.

(e) $a_1 = 35.0°$; $\theta = 52.9°$.

(f) $a_1 = 41.0°$; $\theta = 57.9°$.

Figure 46.- Blade-surface pressure distributions and blade section characteristics for the cascade combination, $\beta_1 = 45°$, $\sigma = 1.50$, and blade section, NACA 65-(24)10.

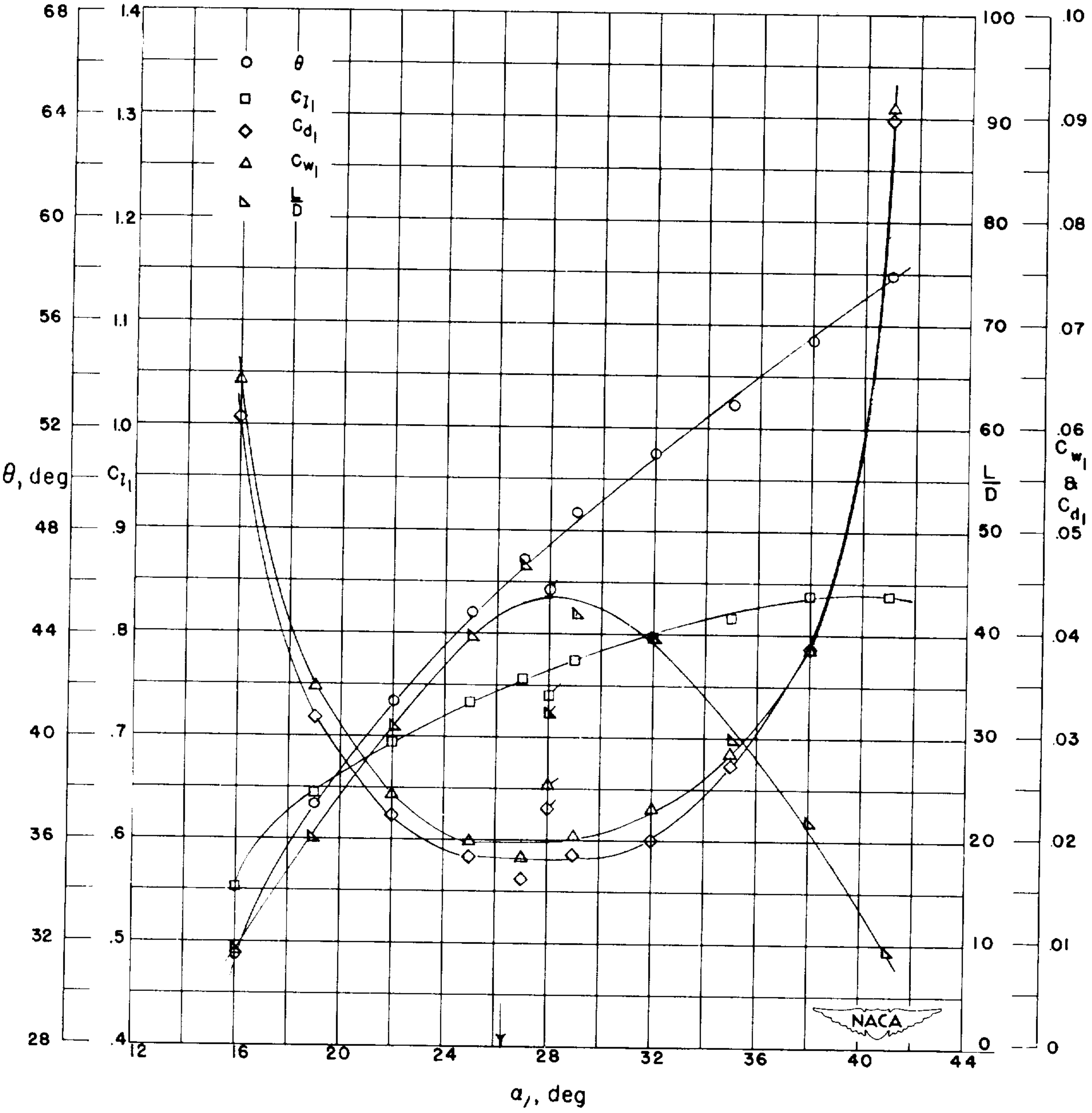

(g) Section characteristics; arrow shows design angle of attack; flagged symbol indicates leading-edge roughness.

Figure 46.- Concluded.

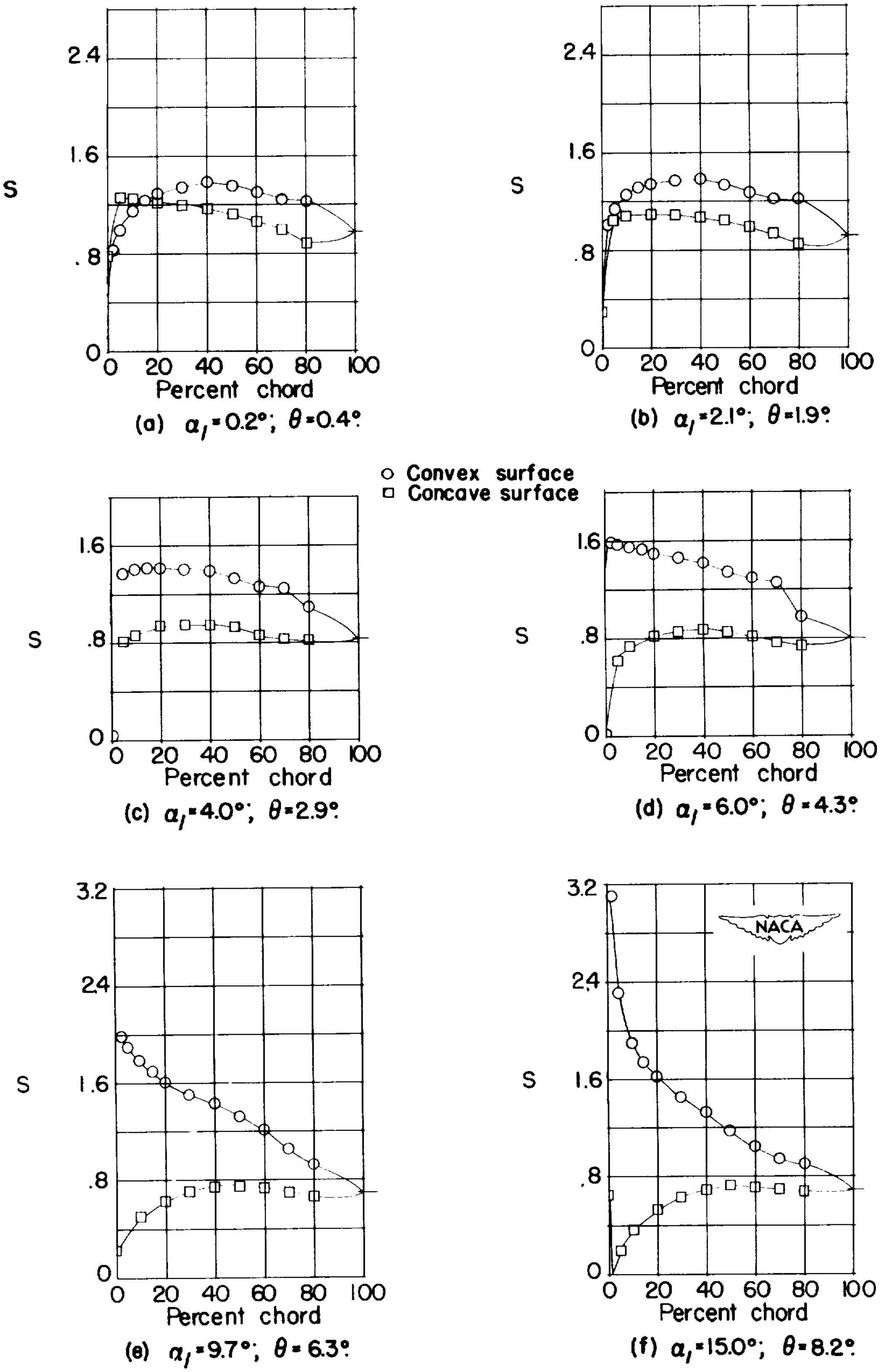

(a) $\alpha_l = 0.2°$; $\theta = 0.4°$

(b) $\alpha_l = 2.1°$; $\theta = 1.9°$

(c) $\alpha_l = 4.0°$; $\theta = 2.9°$

(d) $\alpha_l = 6.0°$; $\theta = 4.3°$

(e) $\alpha_l = 9.7°$; $\theta = 6.3°$

(f) $\alpha_l = 15.0°$; $\theta = 8.2°$

Figure 47.- Blade-surface pressure distributions and blade section characteristics for the cascade combination, $\beta_1 = 60°$, $\sigma = 0.50$, and blade section, NACA 65-410.

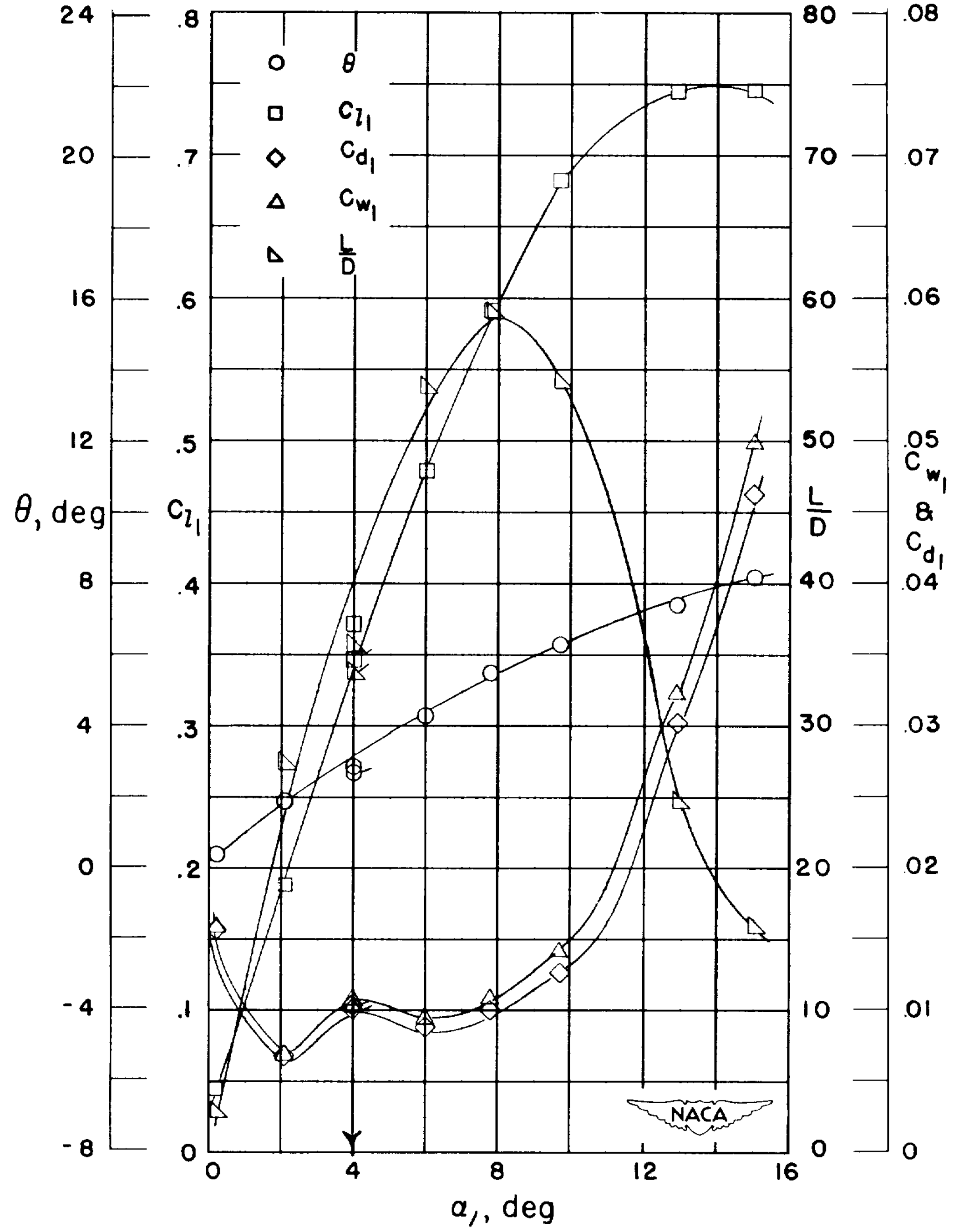

(g) Section characteristics; arrow shows design angle of attack; flagged symbol indicates leading-edge roughness

Figure 47.- Concluded.

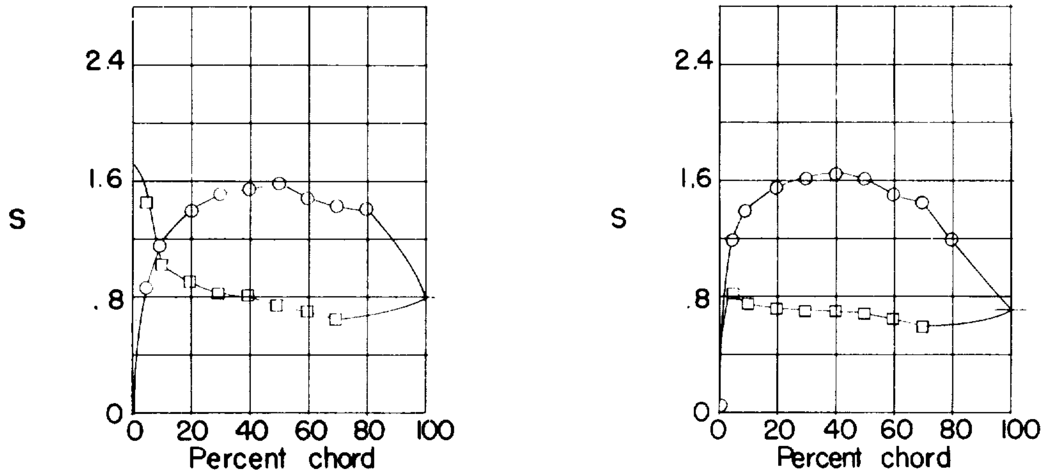

(a) $\alpha_1 = 1.4°$; $\theta = 4.6°$

(b) $\alpha_1 = 5.3°$; $\theta = 7.3°$

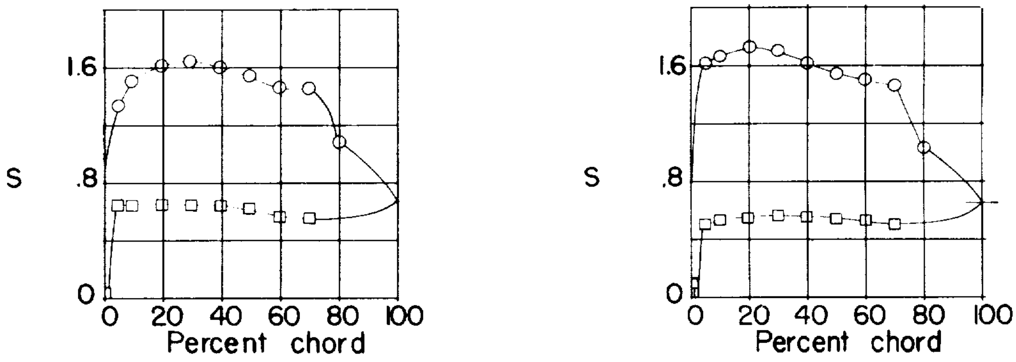

(c) $\alpha_1 = 7.3°$; $\theta = 8.3°$

(d) $\alpha_1 = 9.2°$; $\theta = 9.5°$

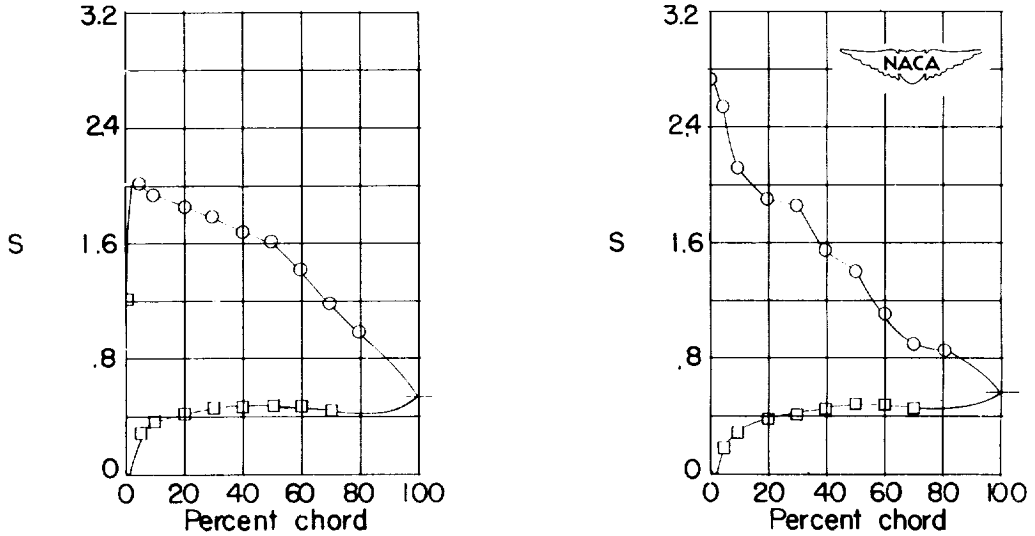

(e) $\alpha_1 = 13.2°$; $\theta = 12.0°$

(f) $\alpha_1 = 17.1°$; $\theta = 12.4°$

Figure 48.- Blade-surface pressure distributions and blade section characteristics for the cascade combination, $\beta_1 = 60°$, $\sigma = 0.50$, and blade section, NACA 65-(12)10.

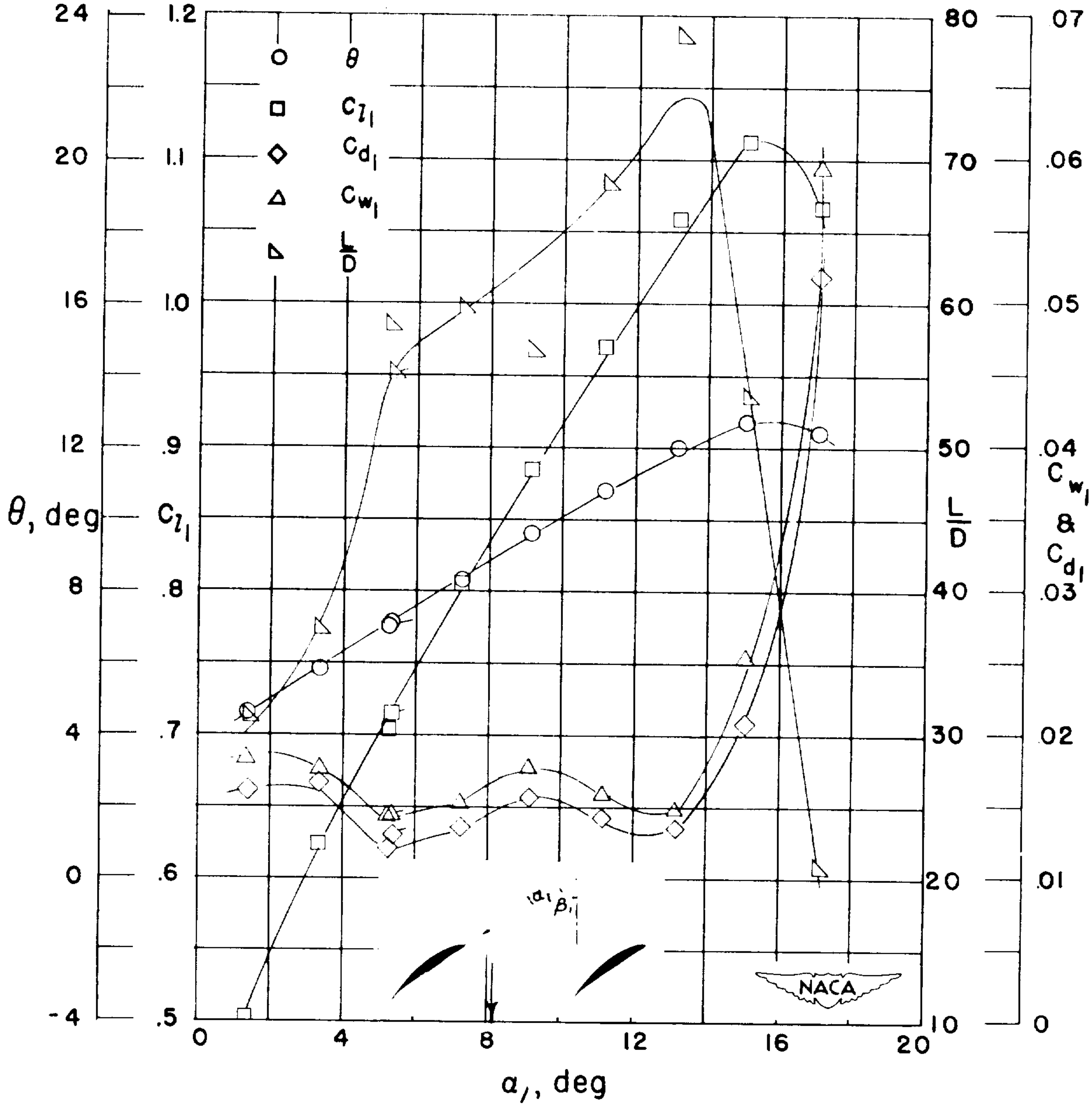

(g) Section characteristics; arrow shows design angle of attack, flagged symbol indicates leading-edge roughness.

Figure 48.- Concluded.

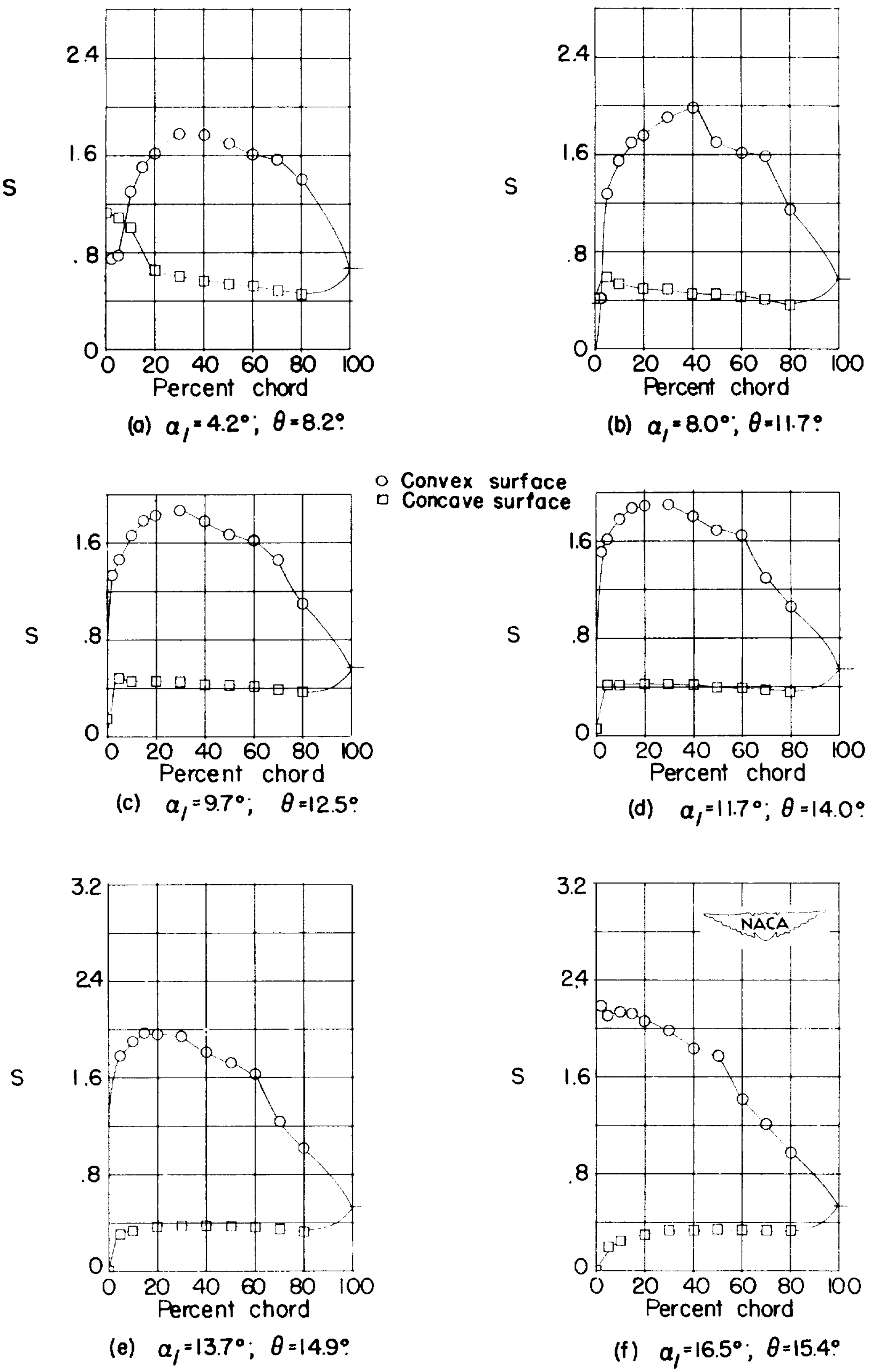

(a) $a_l = 4.2°$; $\theta = 8.2°$

(b) $a_l = 8.0°$; $\theta = 11.7°$

(c) $a_l = 9.7°$; $\theta = 12.5°$

(d) $a_l = 11.7°$; $\theta = 14.0°$

(e) $a_l = 13.7°$; $\theta = 14.9°$

(f) $a_l = 16.5°$; $\theta = 15.4°$

Figure 49.- Blade-surface pressure distributions and blade section characteristics for the cascade combination, $\beta_1 = 60°$, $\sigma = 0.50$, and blade section, NACA 65-(18)10.

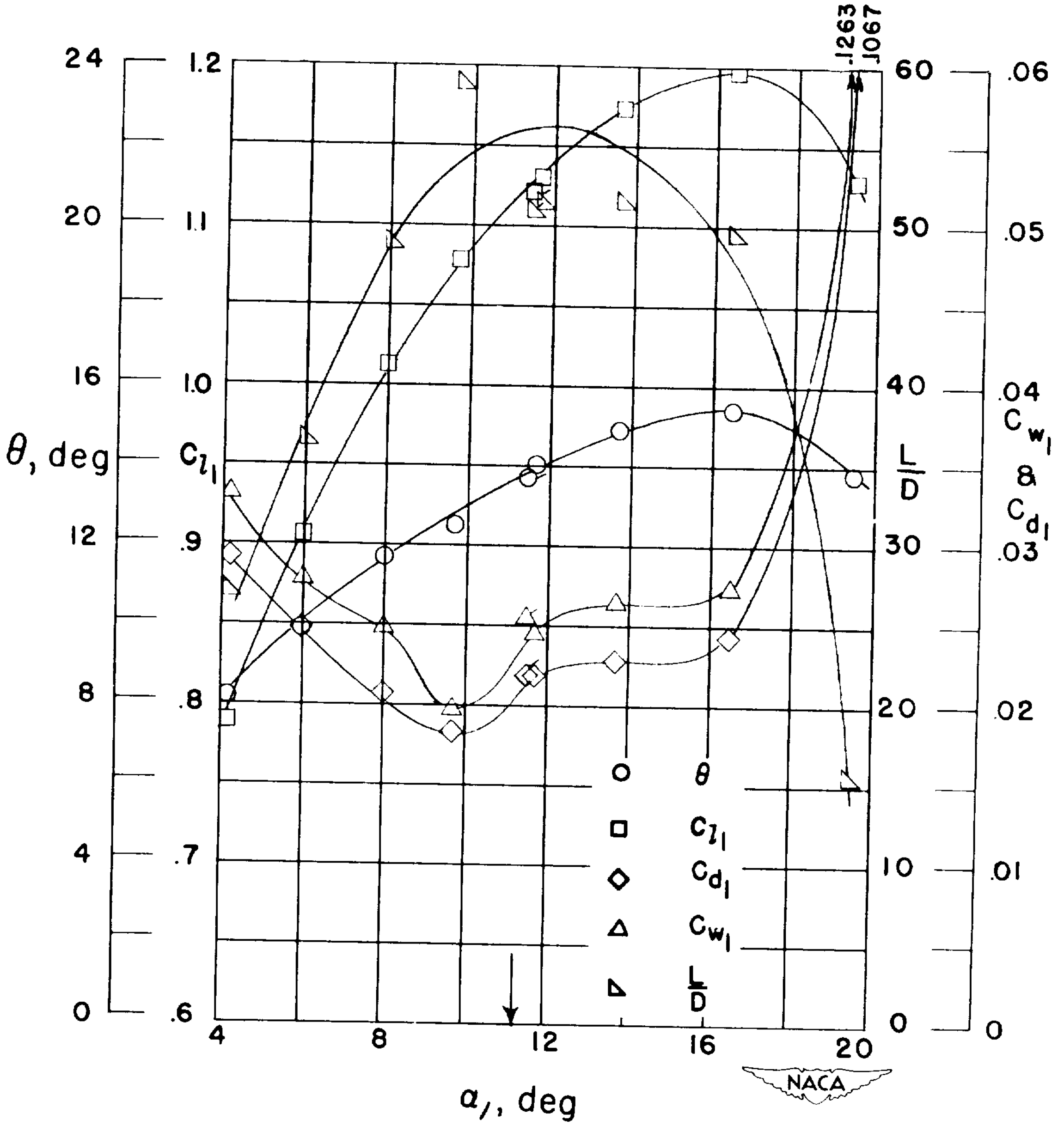

(g) Section characteristics; arrow shows design angle of attack; flagged symbol indicates leading-edge roughness.

Figure 49.- Concluded.

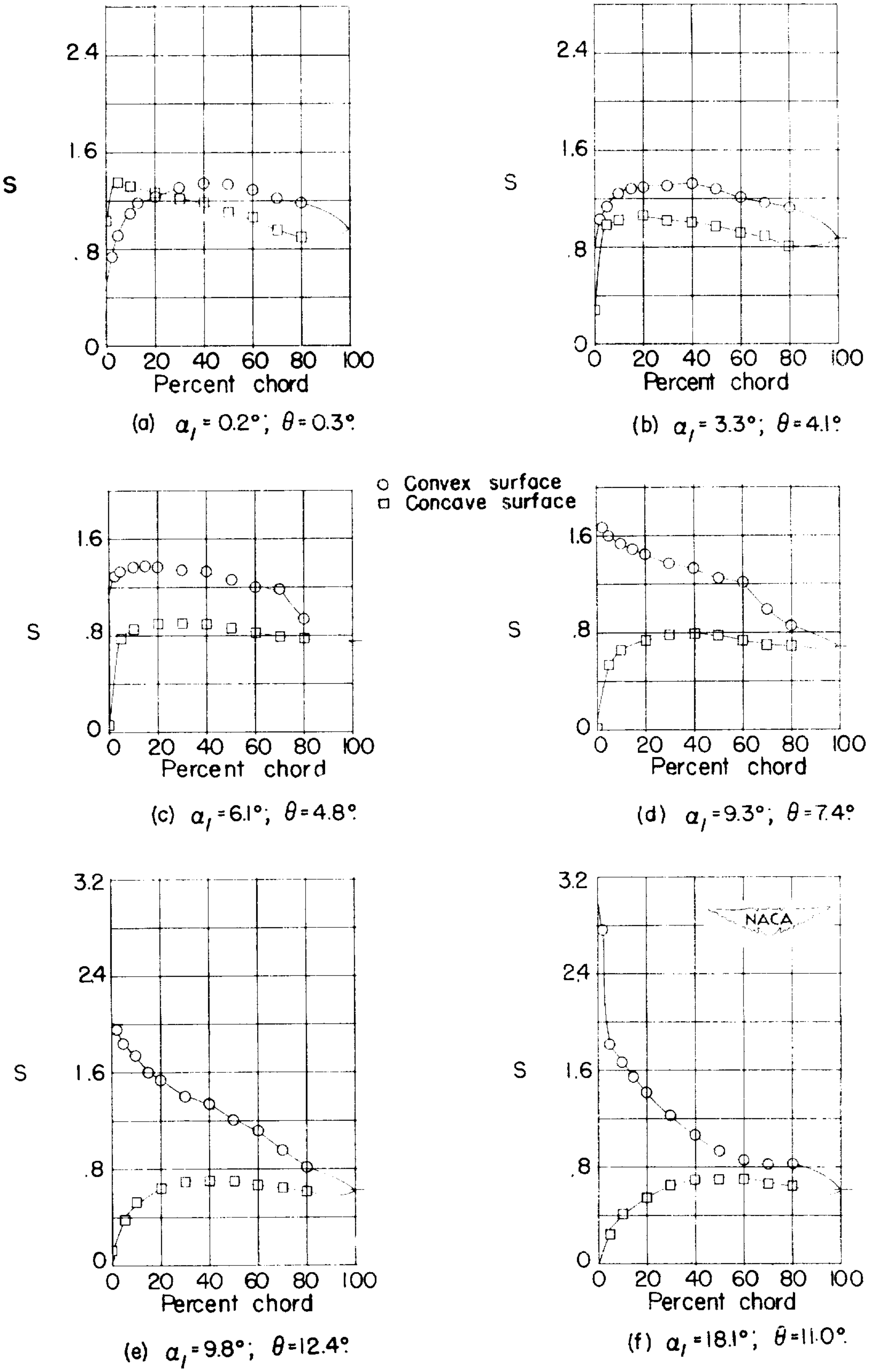

Figure 50.- Blade-surface pressure distributions and blade section characteristics for the cascade combination, $\beta_1 = 60^\circ$, $\sigma = 0.75$, and blade section, NACA 65-410.

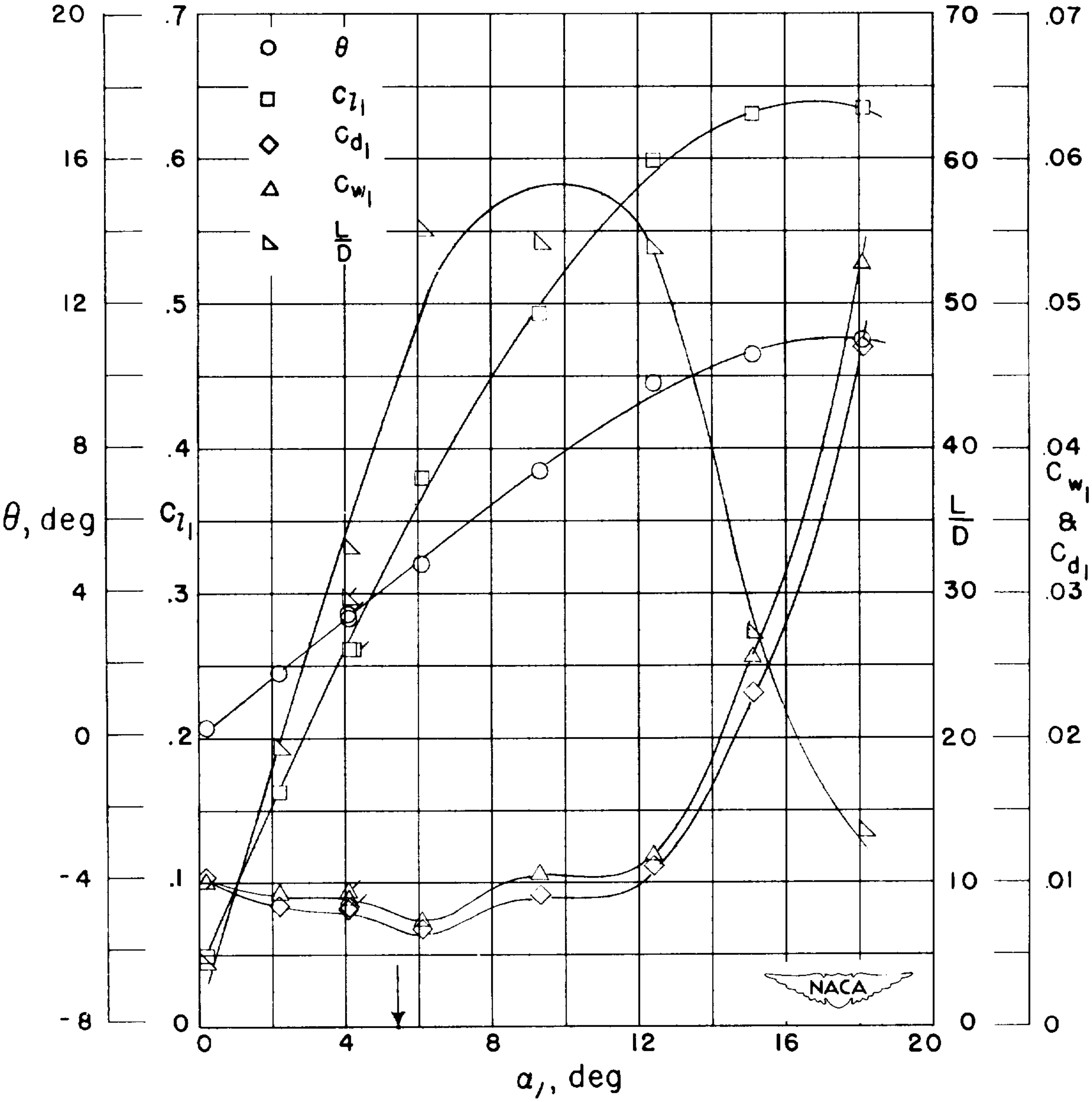

(g) Section characteristics; arrow shows design angle of attack; flagged symbol indicates leading-edge roughness.

Figure 50.- Concluded.

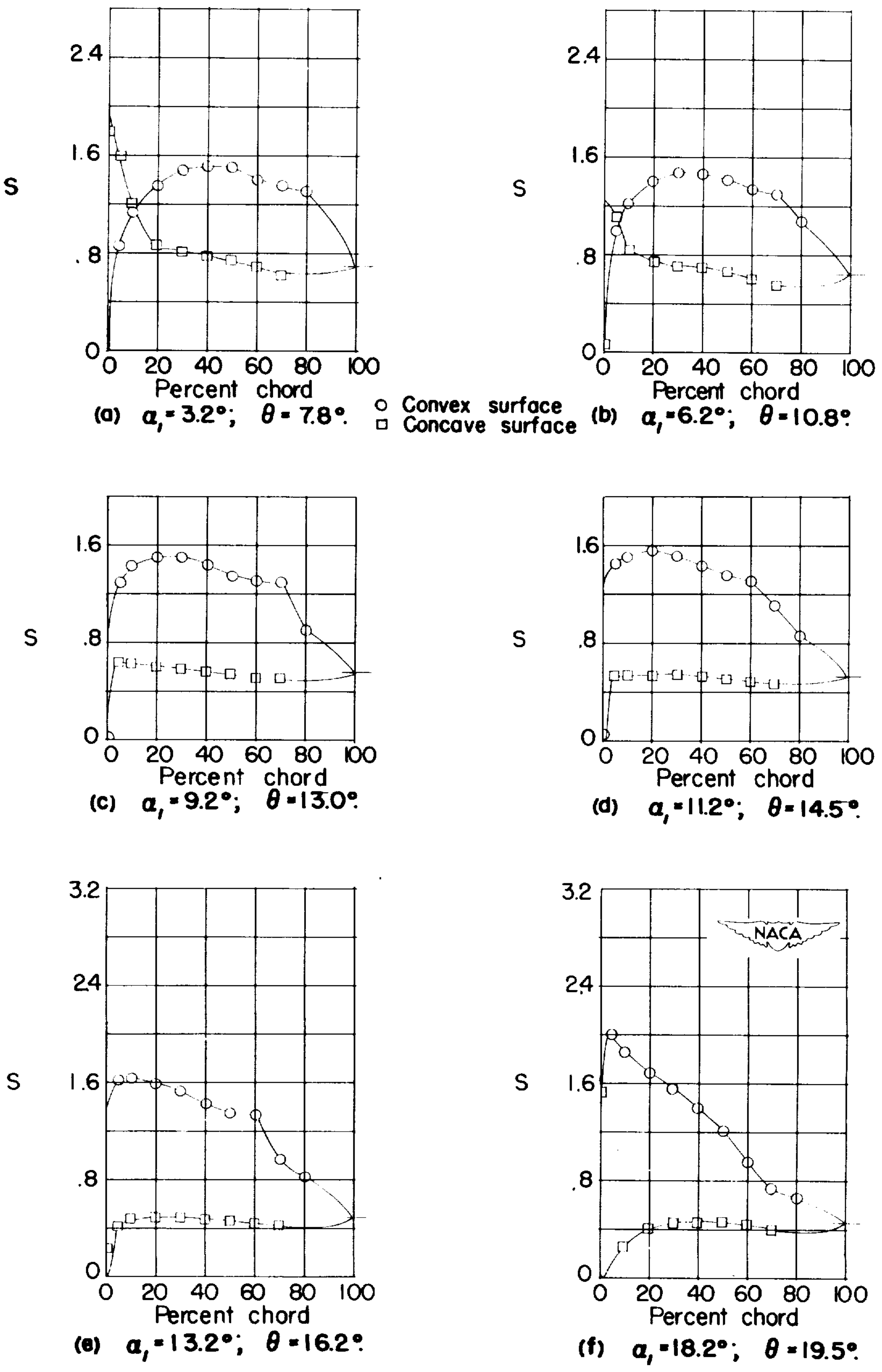

(a) $\alpha_1 = 3.2°$; $\theta = 7.8°$.

(b) $\alpha_1 = 6.2°$; $\theta = 10.8°$.

(c) $\alpha_1 = 9.2°$; $\theta = 13.0°$.

(d) $\alpha_1 = 11.2°$; $\theta = 14.5°$.

(e) $\alpha_1 = 13.2°$; $\theta = 16.2°$.

(f) $\alpha_1 = 18.2°$; $\theta = 19.5°$.

Figure 51.- Blade-surface pressure distributions and blade section characteristics for the cascade combination, $\beta_1 = 60^\circ$, $\sigma = 0.75$, and blade section, NACA 65-(12)10.

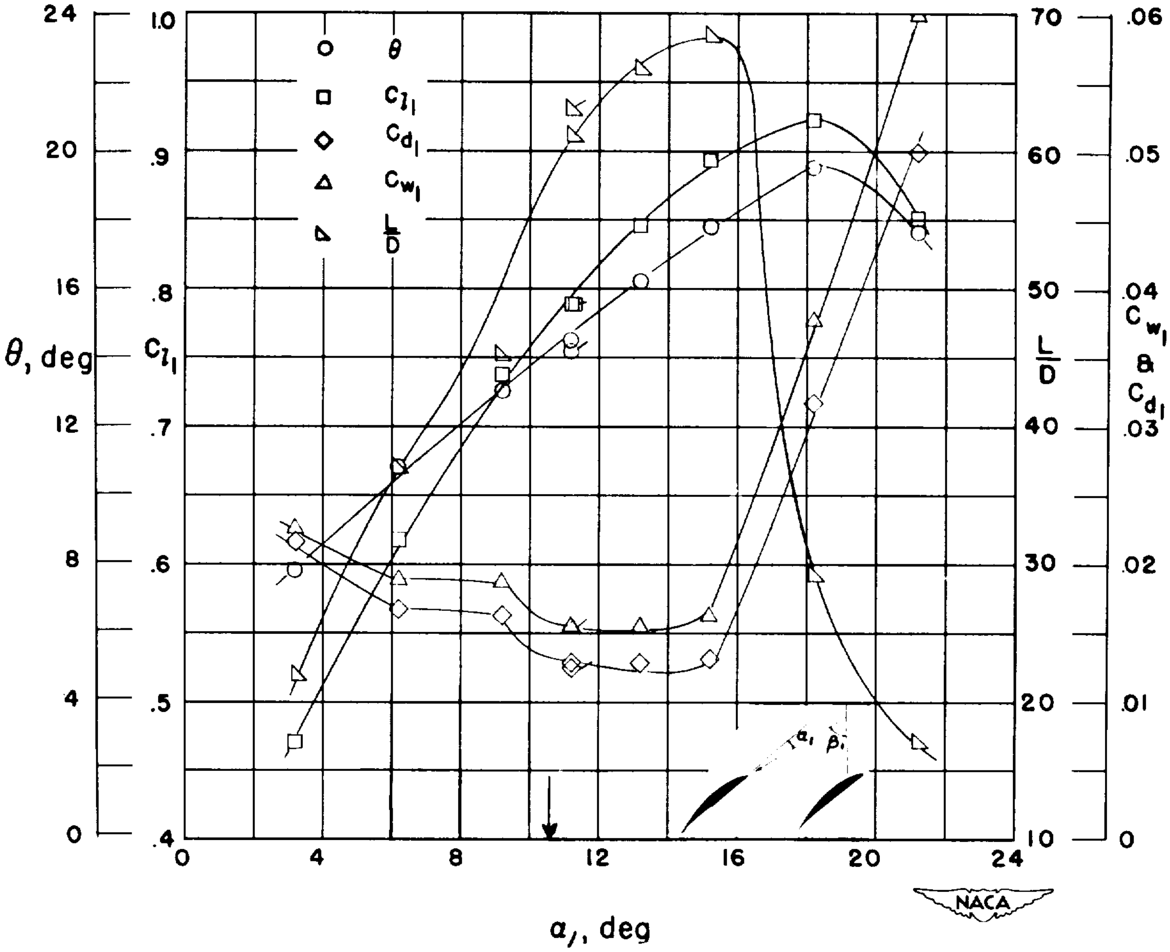

(g) Section characteristics; arrow shows design angle of attack; flagged symbol indicates leading-edge roughness.

Figure 51.- Concluded.

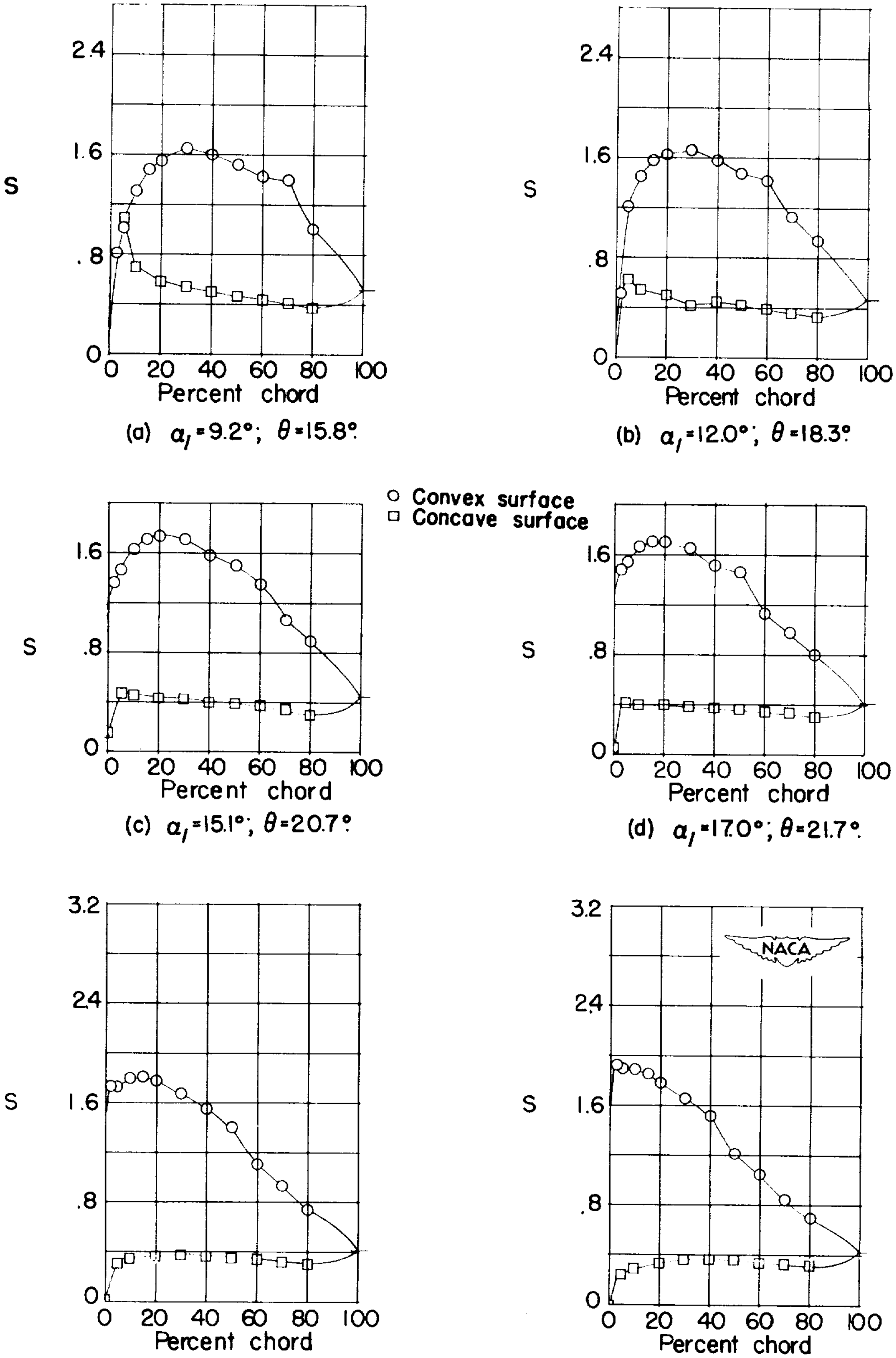

(a) $\alpha_l = 9.2^\circ$; $\theta = 15.8^\circ$.

(b) $\alpha_l = 12.0^\circ$; $\theta = 18.3^\circ$.

(c) $\alpha_l = 15.1^\circ$; $\theta = 20.7^\circ$.

(d) $\alpha_l = 17.0^\circ$; $\theta = 21.7^\circ$.

(e) $\alpha_l = 19.0^\circ$; $\theta = 22.7^\circ$.

(f) $\alpha_l = 22.0^\circ$; $\theta = 22.7^\circ$.

Figure 52.- Blade-surface pressure distributions and blade section characteristics for the cascade combination, $\beta_1 = 60^\circ$, $\sigma = 0.75$, and blade section, NACA 65-(18)10.

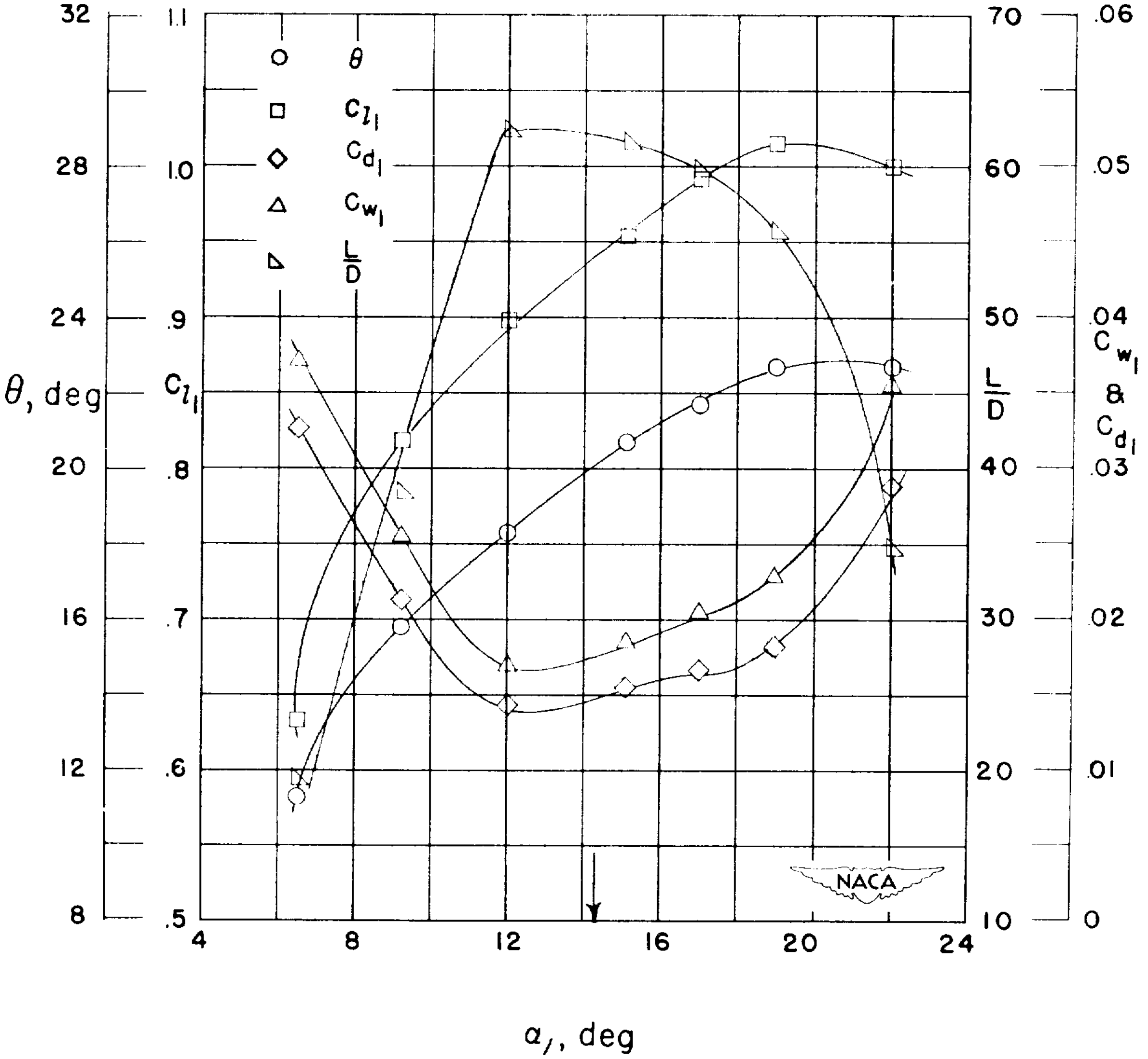

(g) Section characteristics; arrow shows design angle of attack.

Figure 52.- Concluded.

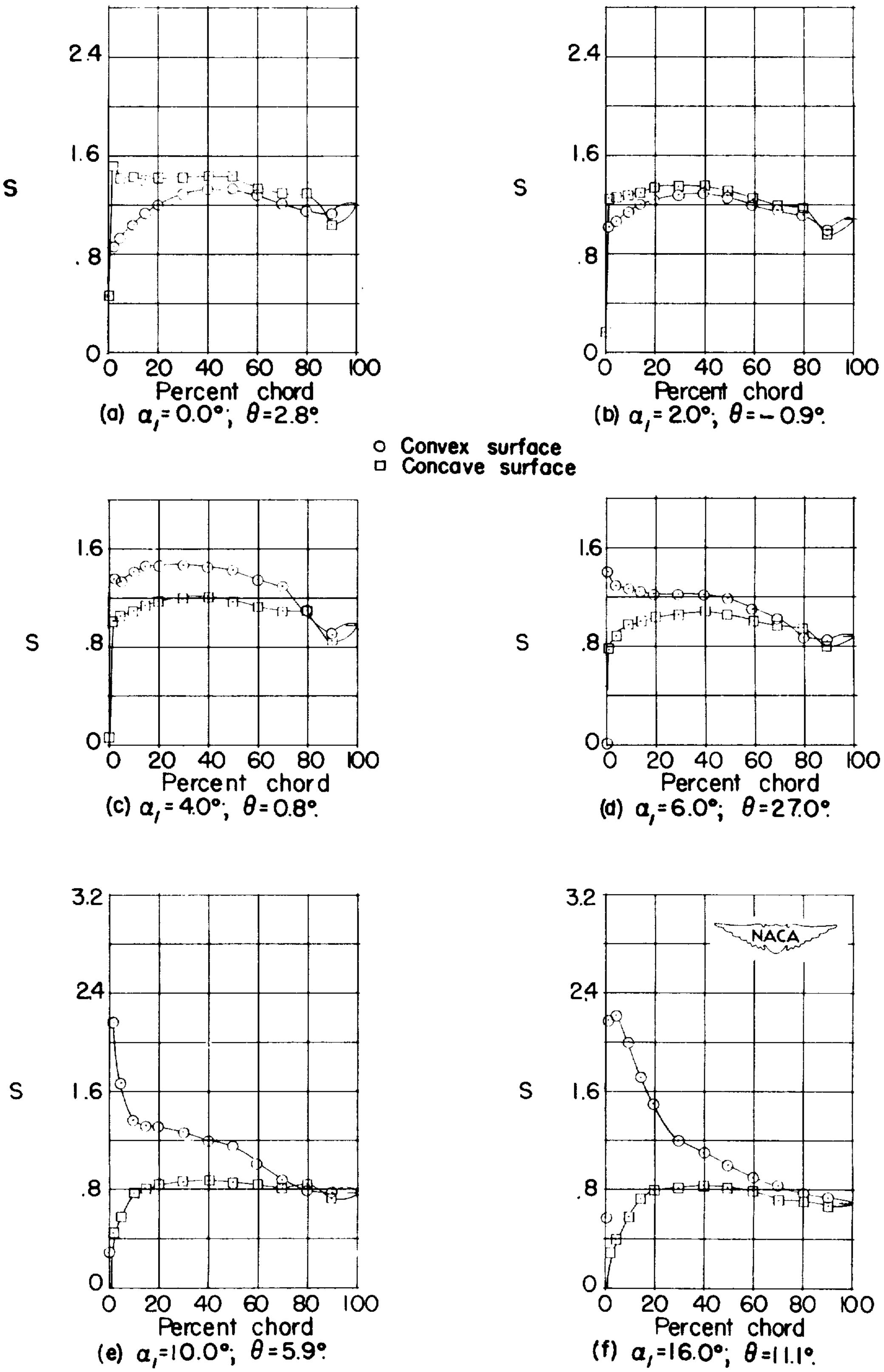

(a) $\alpha_l = 0.0°$; $\theta = 2.8°$.

(b) $\alpha_l = 2.0°$; $\theta = -0.9°$.

(c) $\alpha_l = 4.0°$; $\theta = 0.8°$.

(d) $\alpha_l = 6.0°$; $\theta = 27.0°$.

(e) $\alpha_l = 10.0°$; $\theta = 5.9°$.

(f) $\alpha_l = 16.0°$; $\theta = 11.1°$.

Figure 53.- Blade-surface pressure distributions and blade section characteristics for the cascade combination, $\beta_1 = 60°$, $\sigma = 1.00$, and blade section, NACA 65-010.

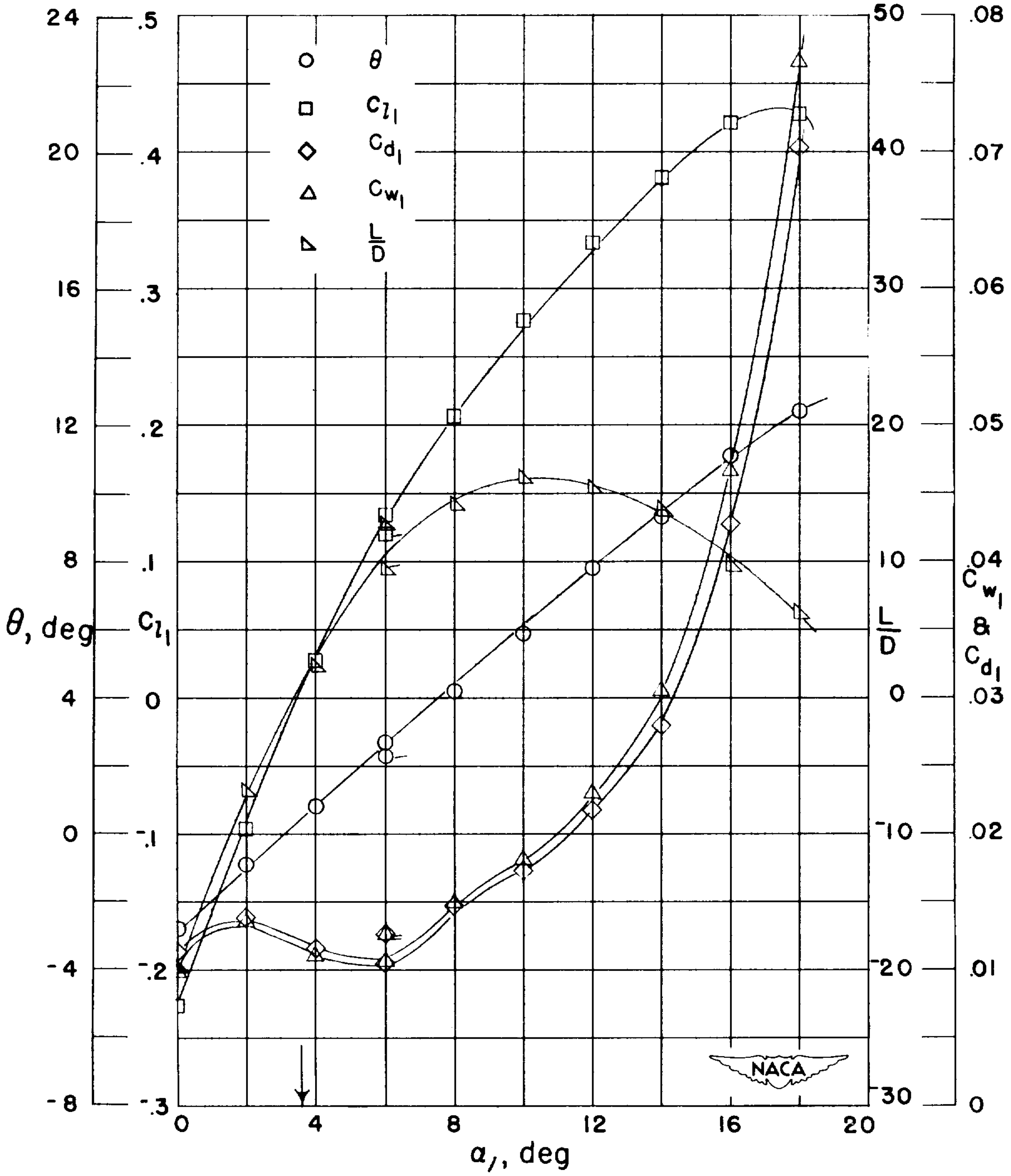

(g) Section characteristics; arrow shows design angle of attack; flagged symbol indicates leading-edge roughness.

Figure 53.- Concluded.

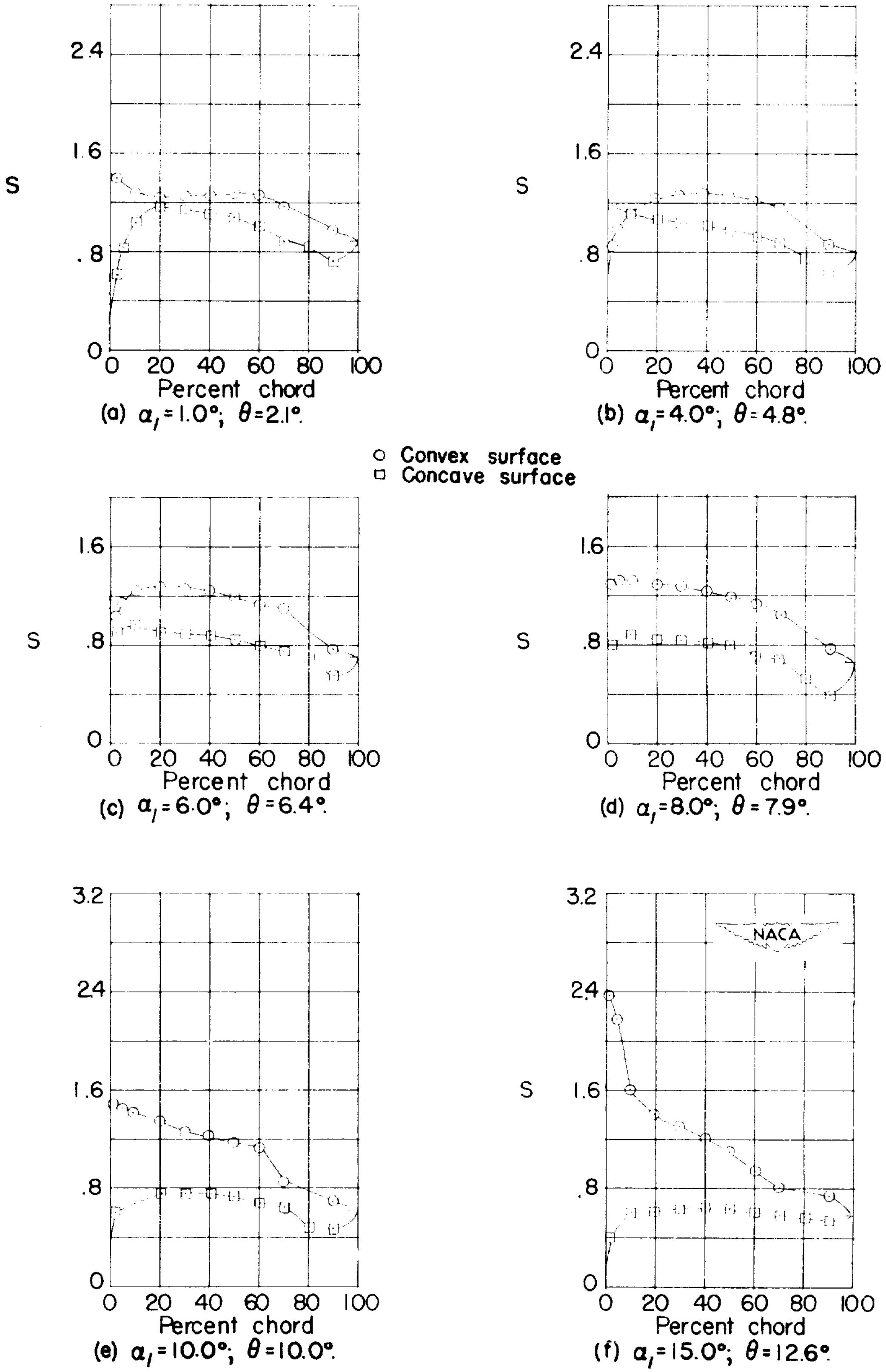

(a) α_l = 1.0°; θ=2.1°.

(b) α_l = 4.0°; θ = 4.8°.

(c) α_l = 6.0°; θ = 6.4°.

(d) α_l = 8.0°; θ = 7.9°.

(e) α_l = 10.0°; θ = 10.0°.

(f) α_l = 15.0°; θ = 12.6°.

Figure 54.- Blade-surface pressure distributions and blade section characteristics for the cascade combination, $\beta_1 = 60^\circ$, $\sigma = 1.00$, and blade section, NACA 65-410.

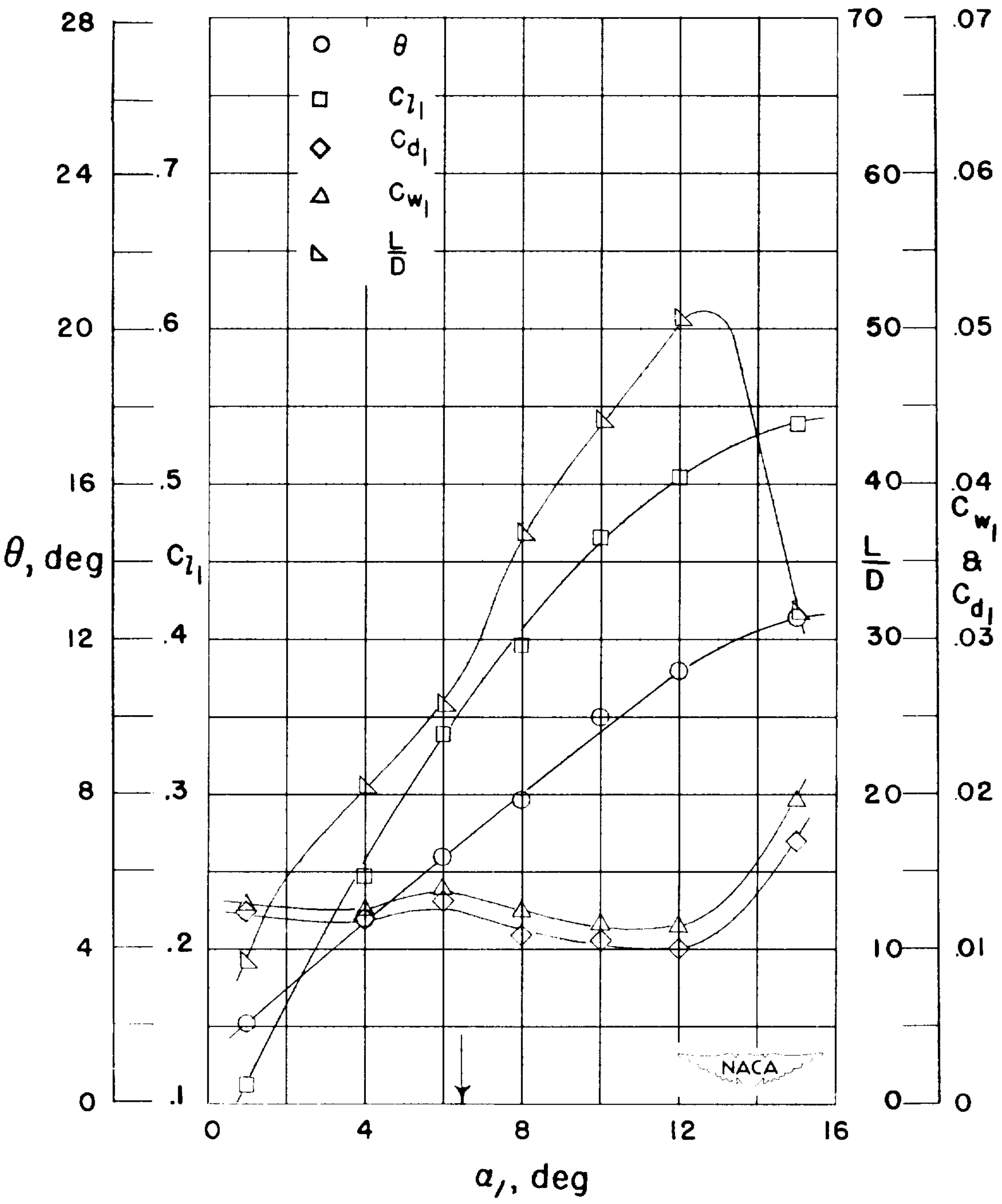

(g) Section characteristics; arrow shows design angle of attack.

Figure 54.- Concluded.

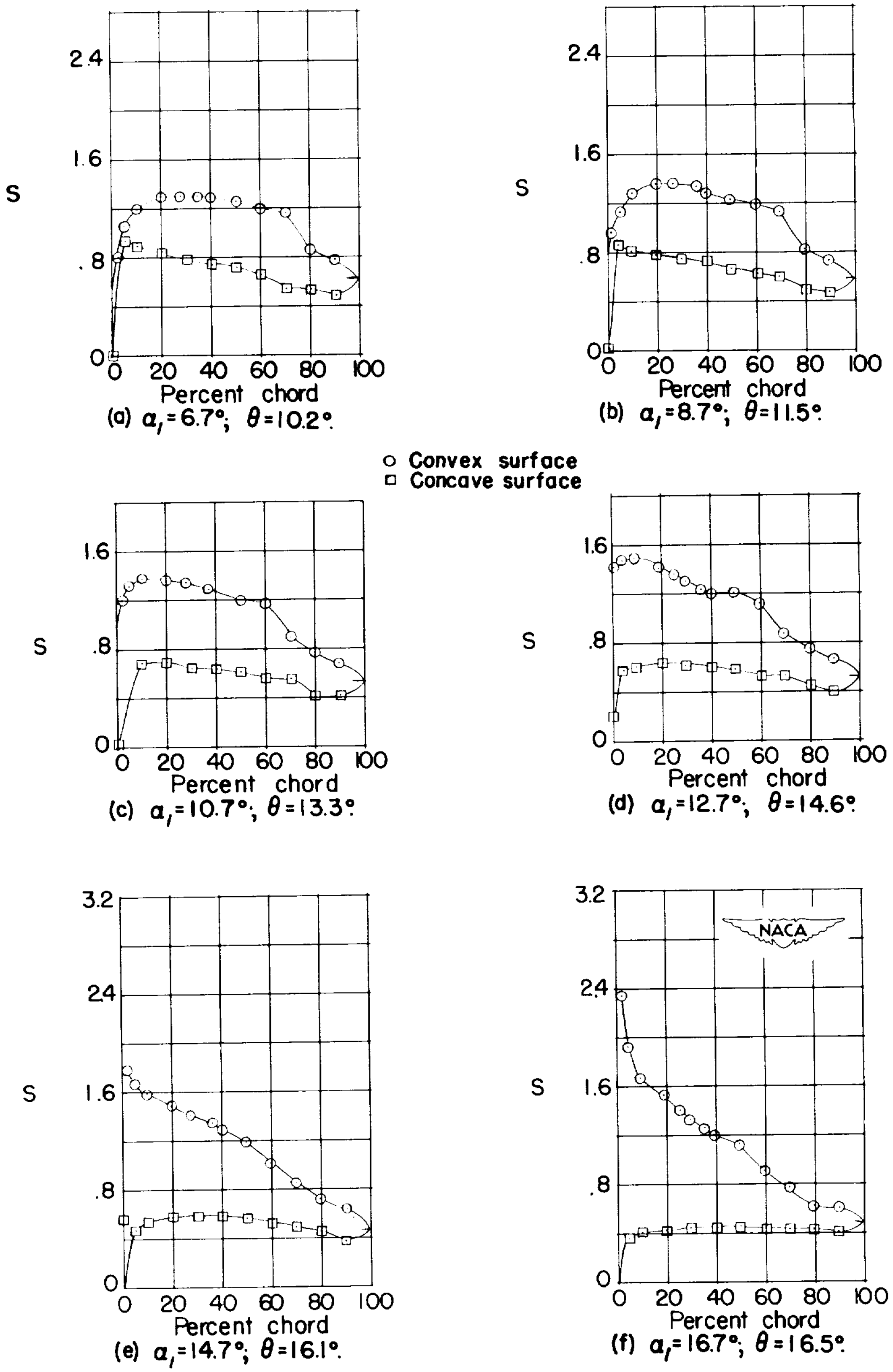

(a) $a_l = 6.7°$; $\theta = 10.2°$.

(b) $a_l = 8.7°$; $\theta = 11.5°$.

(c) $a_l = 10.7°$; $\theta = 13.3°$.

(d) $a_l = 12.7°$; $\theta = 14.6°$.

(e) $a_l = 14.7°$; $\theta = 16.1°$.

(f) $a_l = 16.7°$; $\theta = 16.5°$.

Figure 55.- Blade-surface pressure distributions and blade section characteristics for the cascade combination, $\beta_1 = 60°$, $\sigma = 1.00$, and blade section, NACA 65-810.

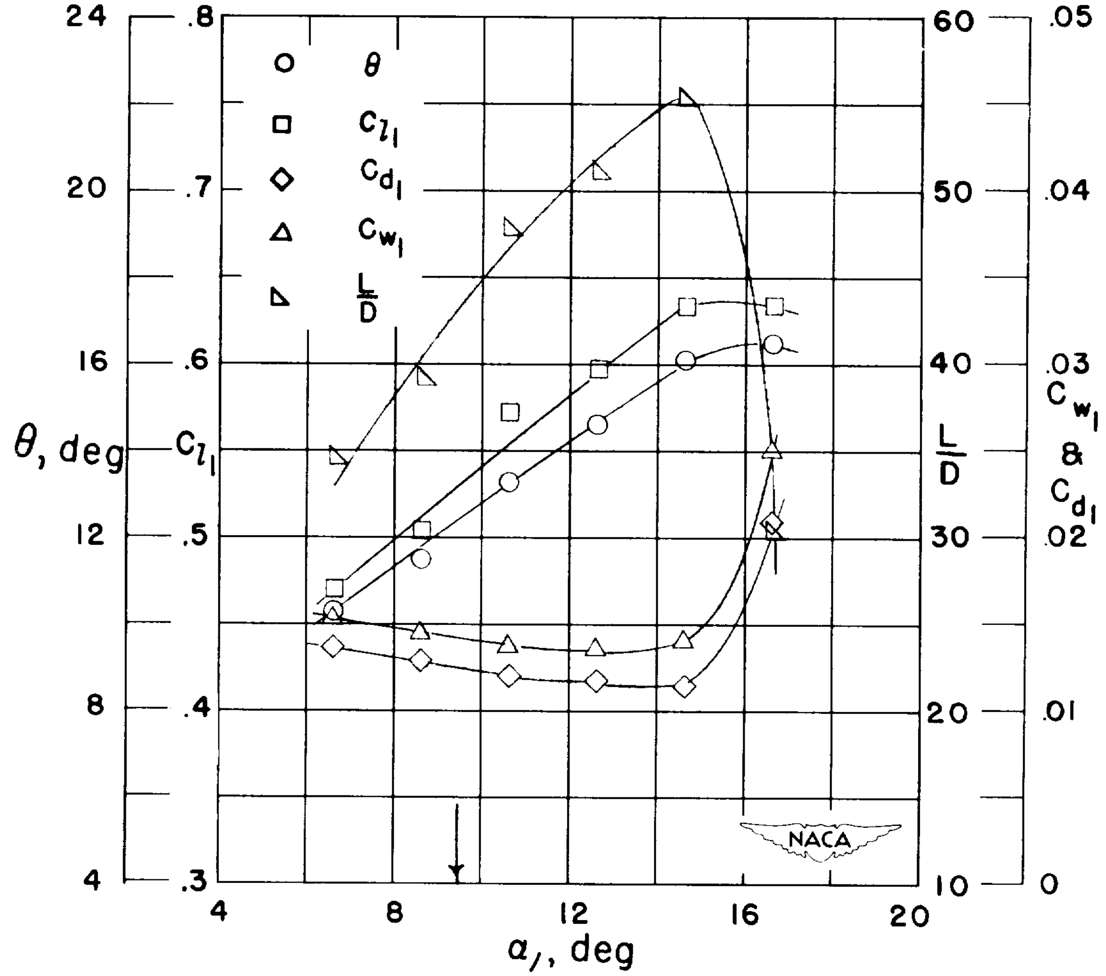

(g) Section characteristics; arrow shows design angle of attack.

Figure 55.- Concluded.

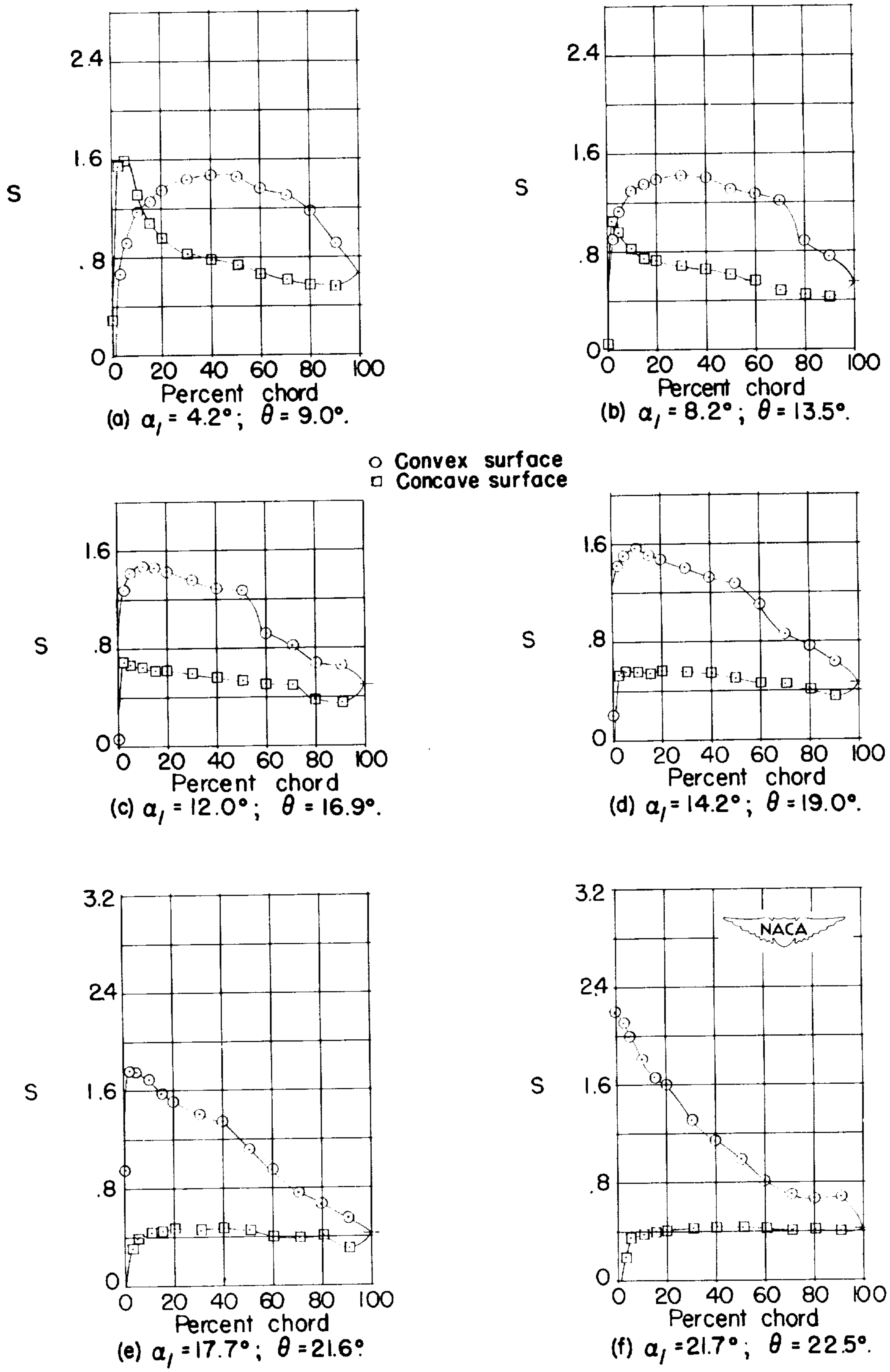

(a) α_l = 4.2°; θ = 9.0°.

(b) α_l = 8.2°; θ = 13.5°.

(c) α_l = 12.0°; θ = 16.9°.

(d) α_l = 14.2°; θ = 19.0°.

(e) α_l = 17.7°; θ = 21.6°.

(f) α_l = 21.7°; θ = 22.5°.

Figure 56.- Blade-surface pressure distributions and blade section characteristics for the cascade combination, $\beta_1 = 60^\circ$, $\sigma = 1.00$, and blade section, NACA 65-(12)10.

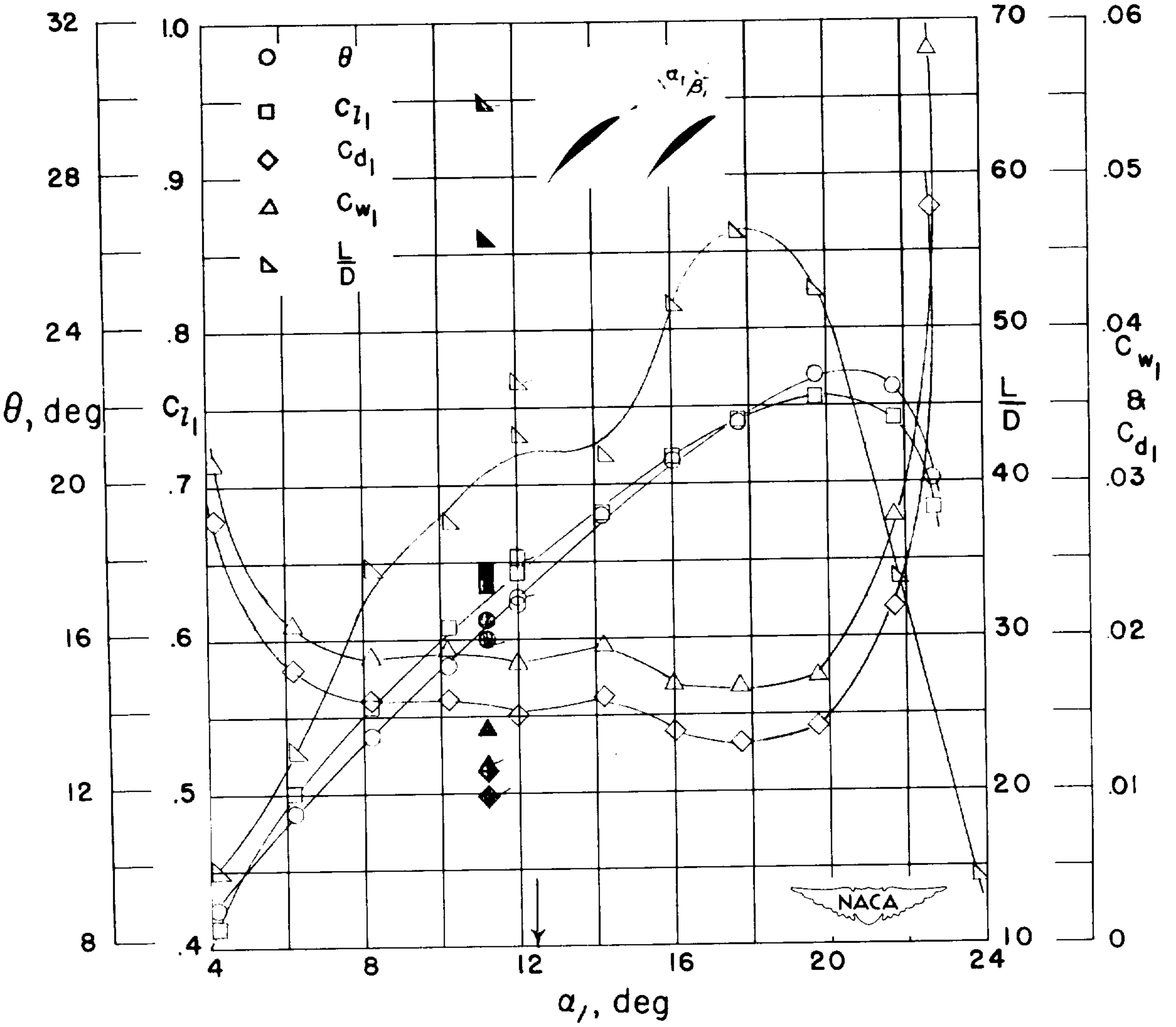

(g) Section characteristics; arrow shows design angle of attack; flagged symbol indicates leading-edge roughness; solid symbol indicates high Reynolds number.

Figure 56.- Concluded.

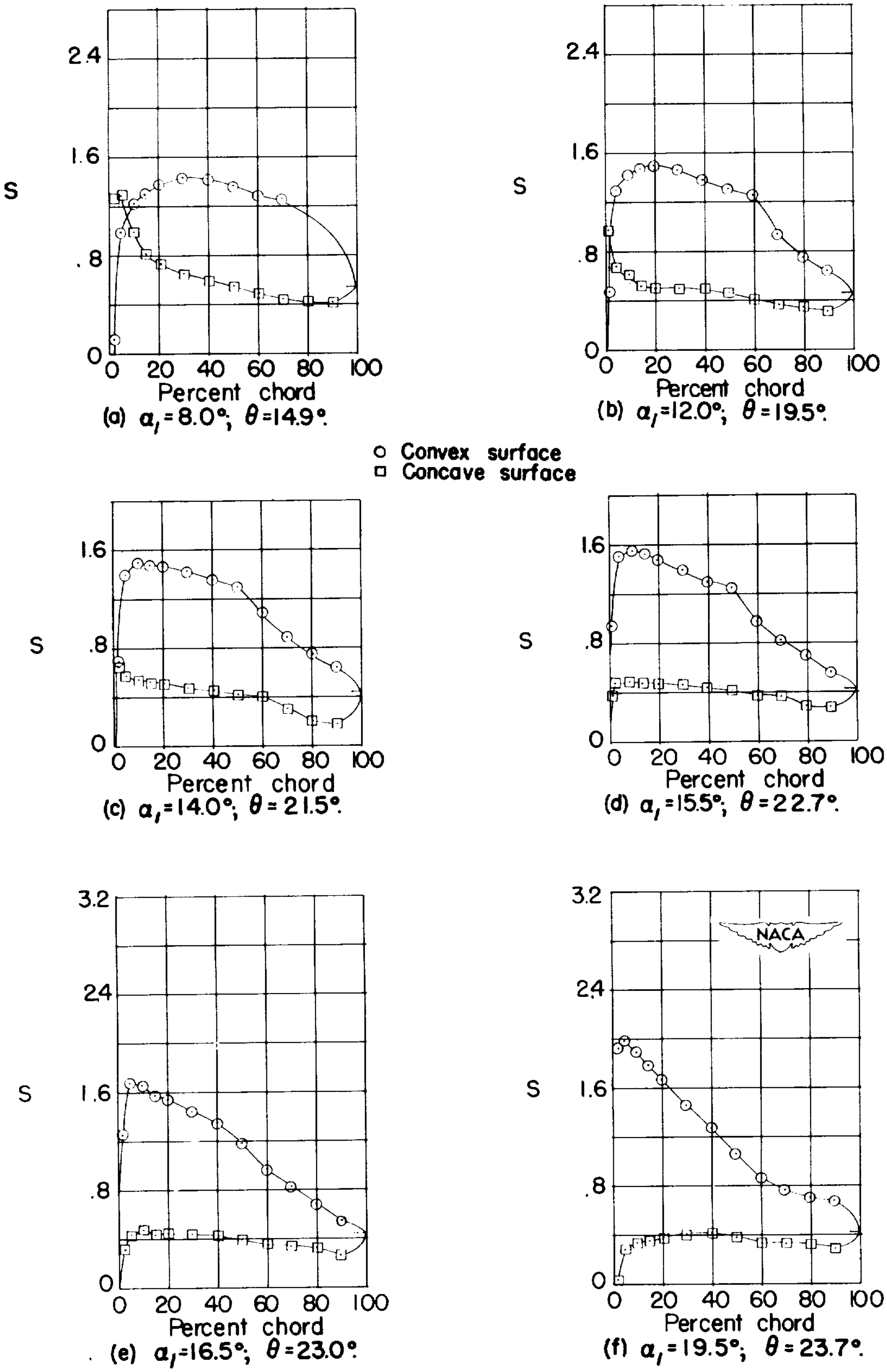

Figure 57.- Blade-surface pressure distributions and blade section characteristics for the cascade combination, $\beta_1 = 60°$, $\sigma = 1.00$, and blade section, NACA 65-(15)10.

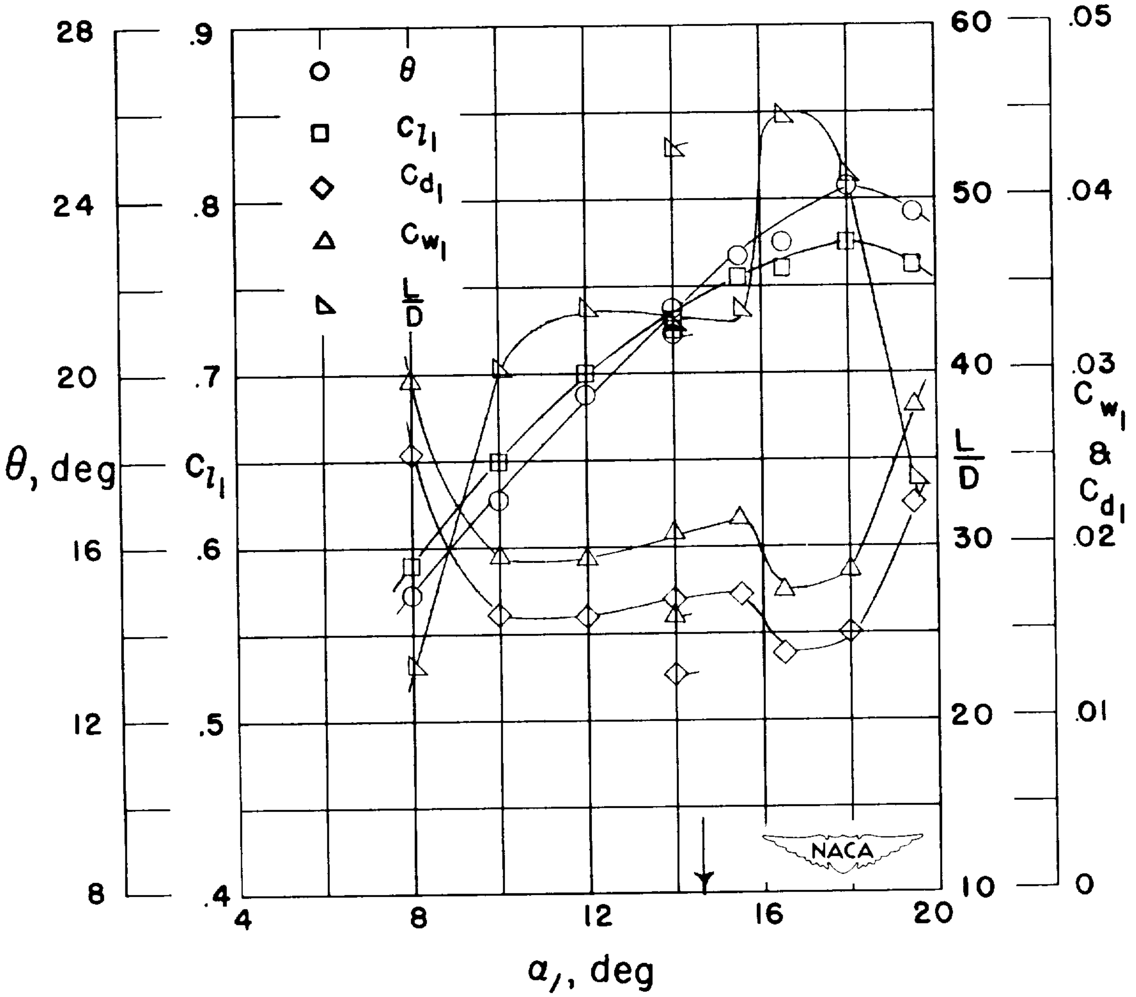

(g) Section characteristics; arrow shows design angle of attack; flagged symbol indicates leading-edge roughness.

Figure 57.- Concluded.

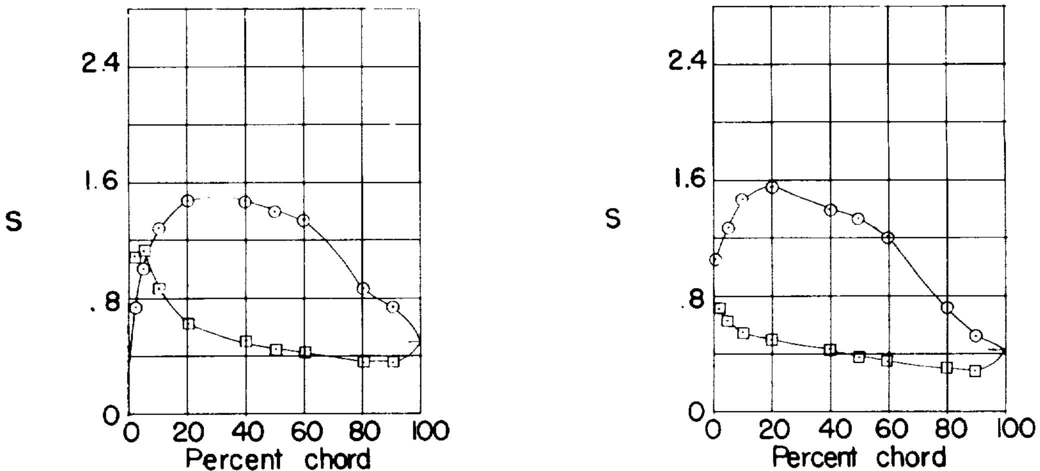

(a) $\alpha_1 = 10.0°$; $\theta = 17.4°$. (b) $\alpha_1 = 14.0°$; $\theta = 21.9°$.

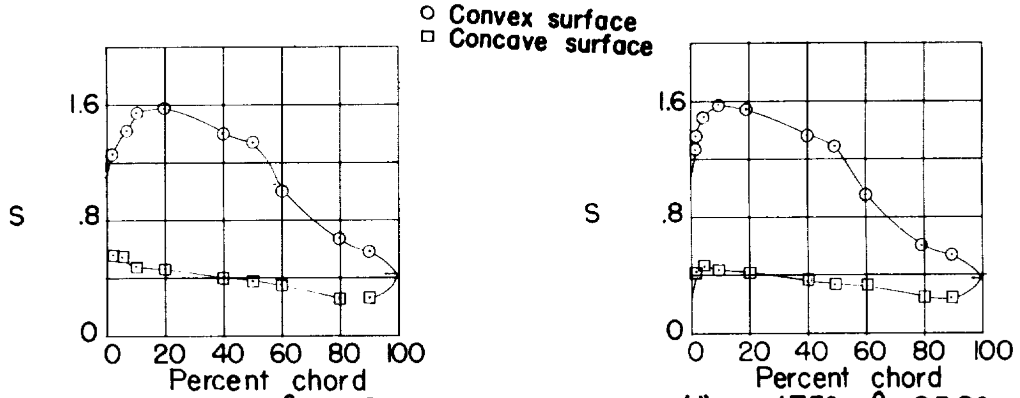

(c) $\alpha_1 = 16.0°$; $\theta = 24.2°$. (d) $\alpha_1 = 17.5°$; $\theta = 25.2°$.

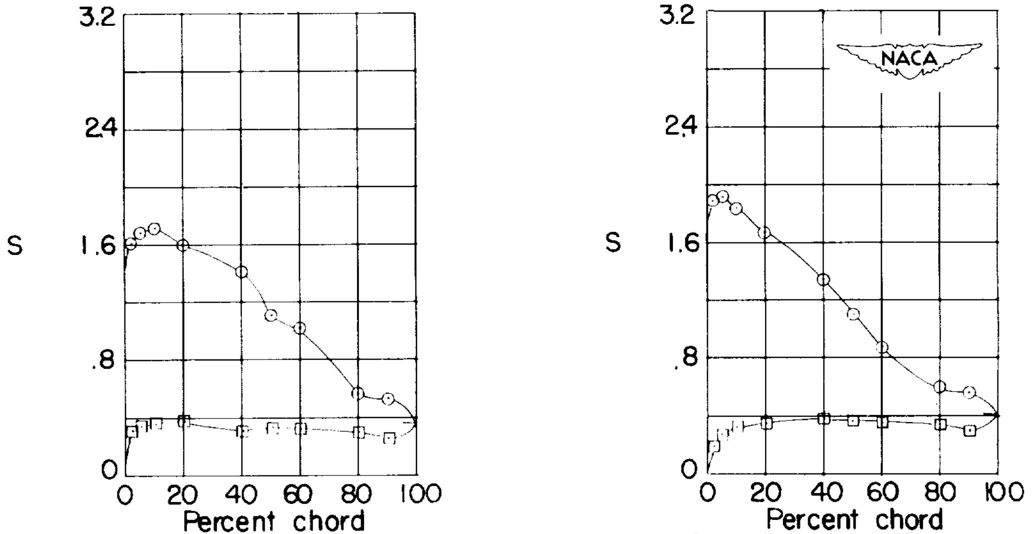

(e) $\alpha_1 = 20.0°$; $\theta = 26.4°$. (f) $\alpha_1 = 22.0°$; $\theta = 26.3°$.

Figure 58.- Blade-surface pressure distributions and blade section characteristics for the cascade combination, $\beta_1 = 60°$, $\sigma = 1.00$, and blade section, NACA 65-(18)10.

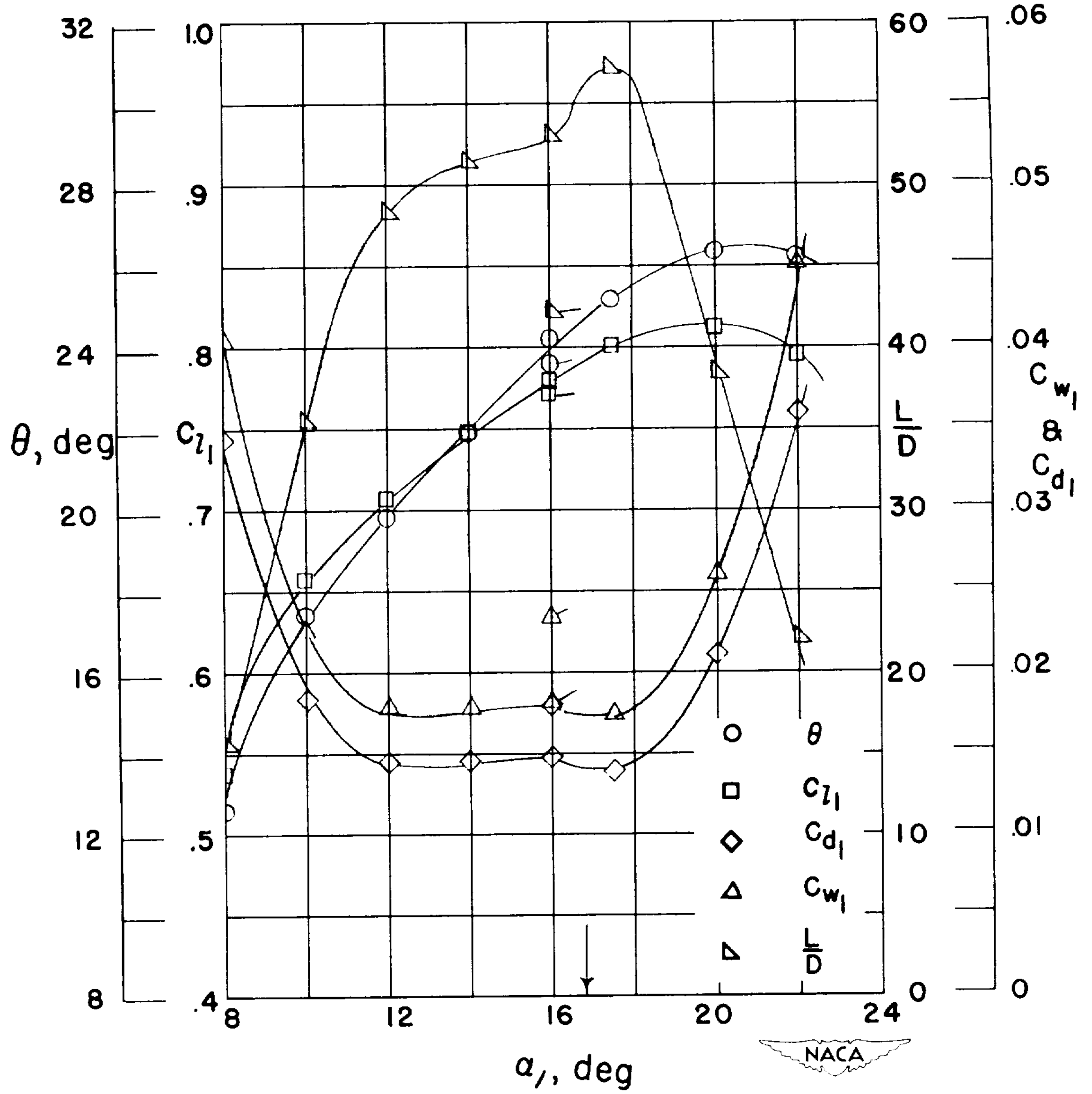

(g) Section characteristics; arrow shows design angle of attack; flagged symbol indicates leading-edge roughness.

Figure 58.- Concluded.

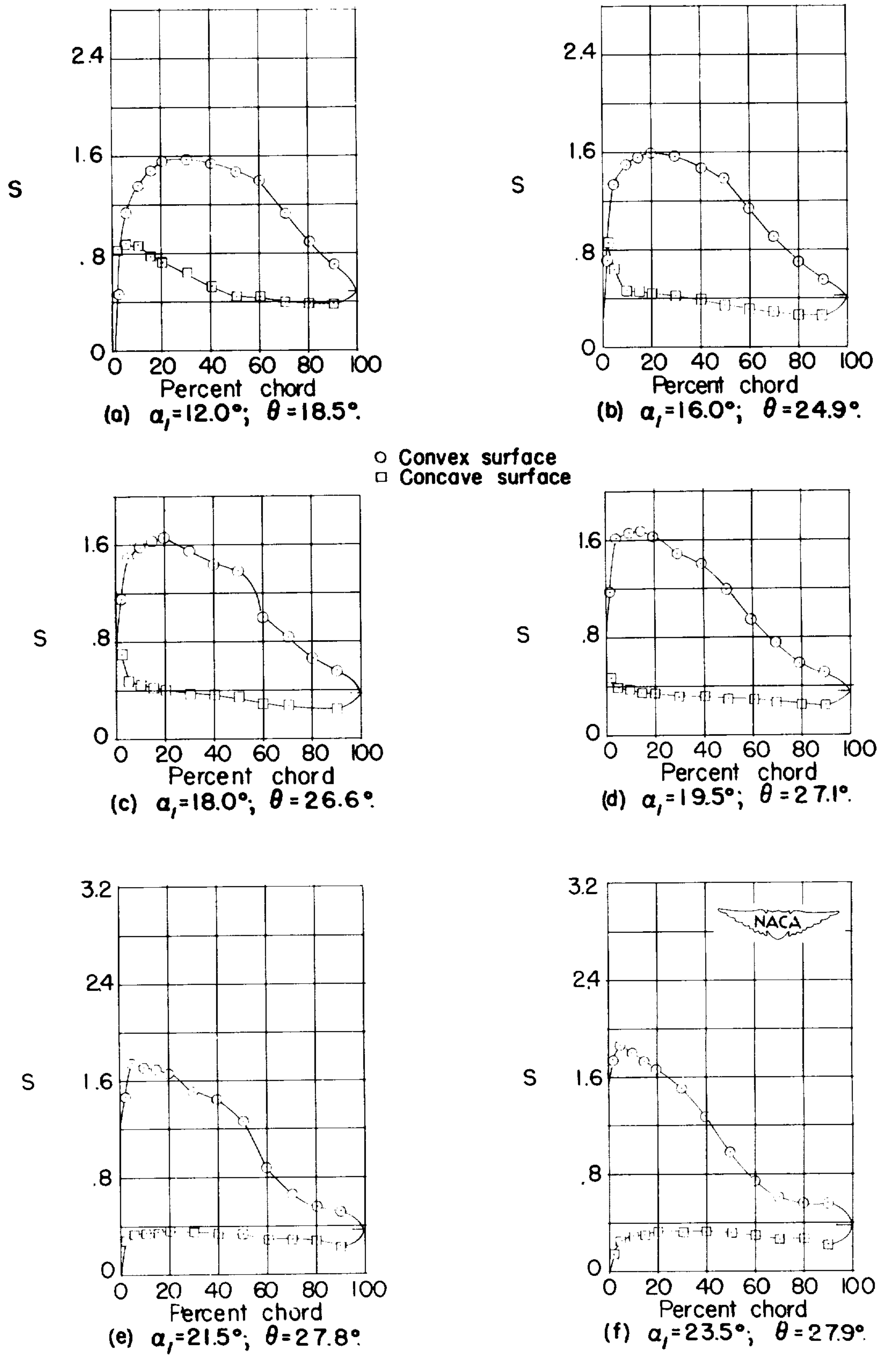

(a) α_1=12.0°; θ=18.5°.

(b) α_1=16.0°; θ=24.9°.

(c) α_1=18.0°; θ=26.6°.

(d) α_1=19.5°; θ=27.1°.

(e) α_1=21.5°; θ=27.8°.

(f) α_1=23.5°; θ=27.9°.

Figure 59.- Blade-surface pressure distributions and blade section characteristics for the cascade combination, $\beta_1 = 60^\circ$, $\sigma = 1.00$, and blade section, NACA 65-(21)10.

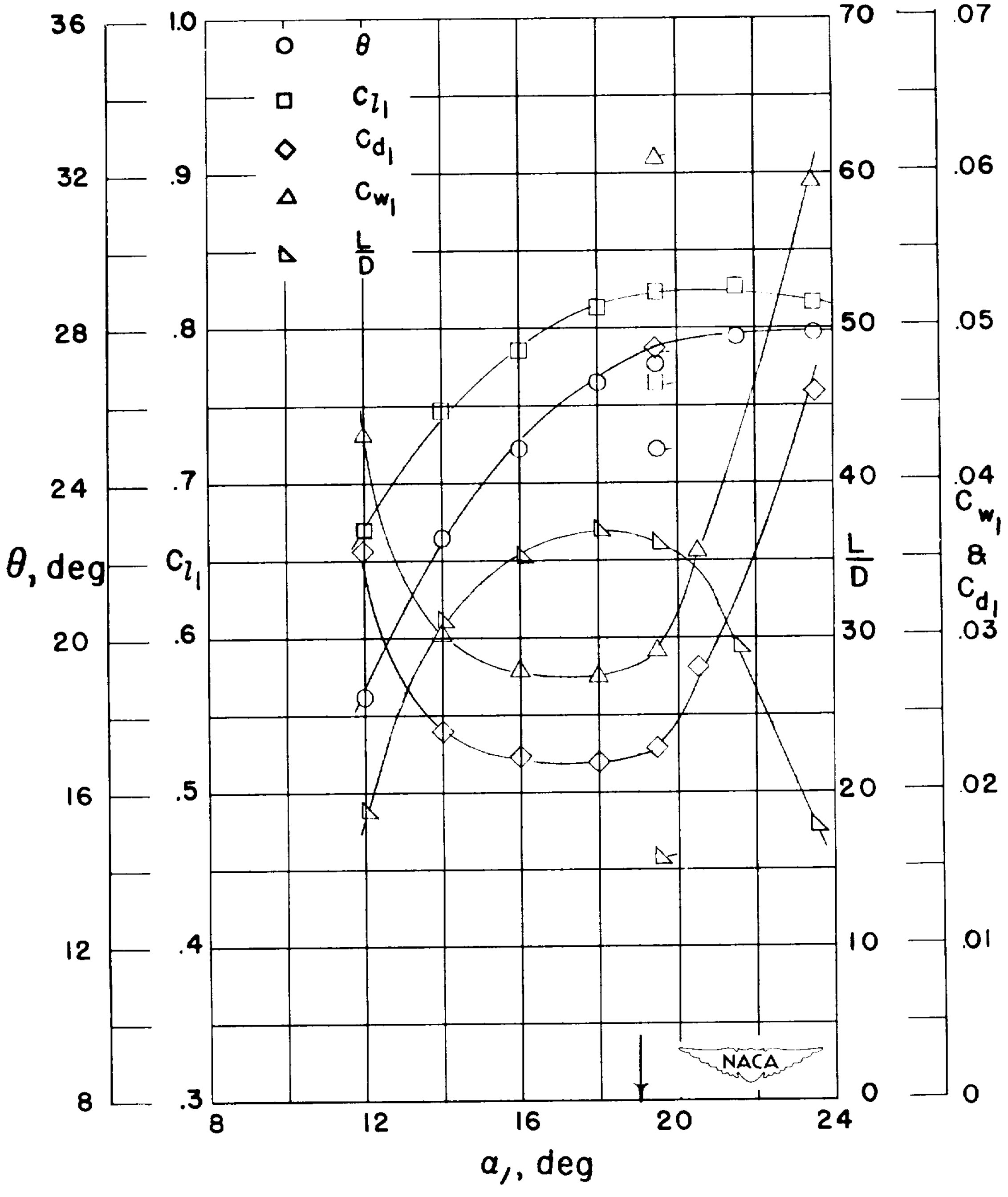

(g) Section characteristics; arrow shows design angle of attack; flagged symbol indicates leading-edge roughness.

Figure 59.- Concluded.

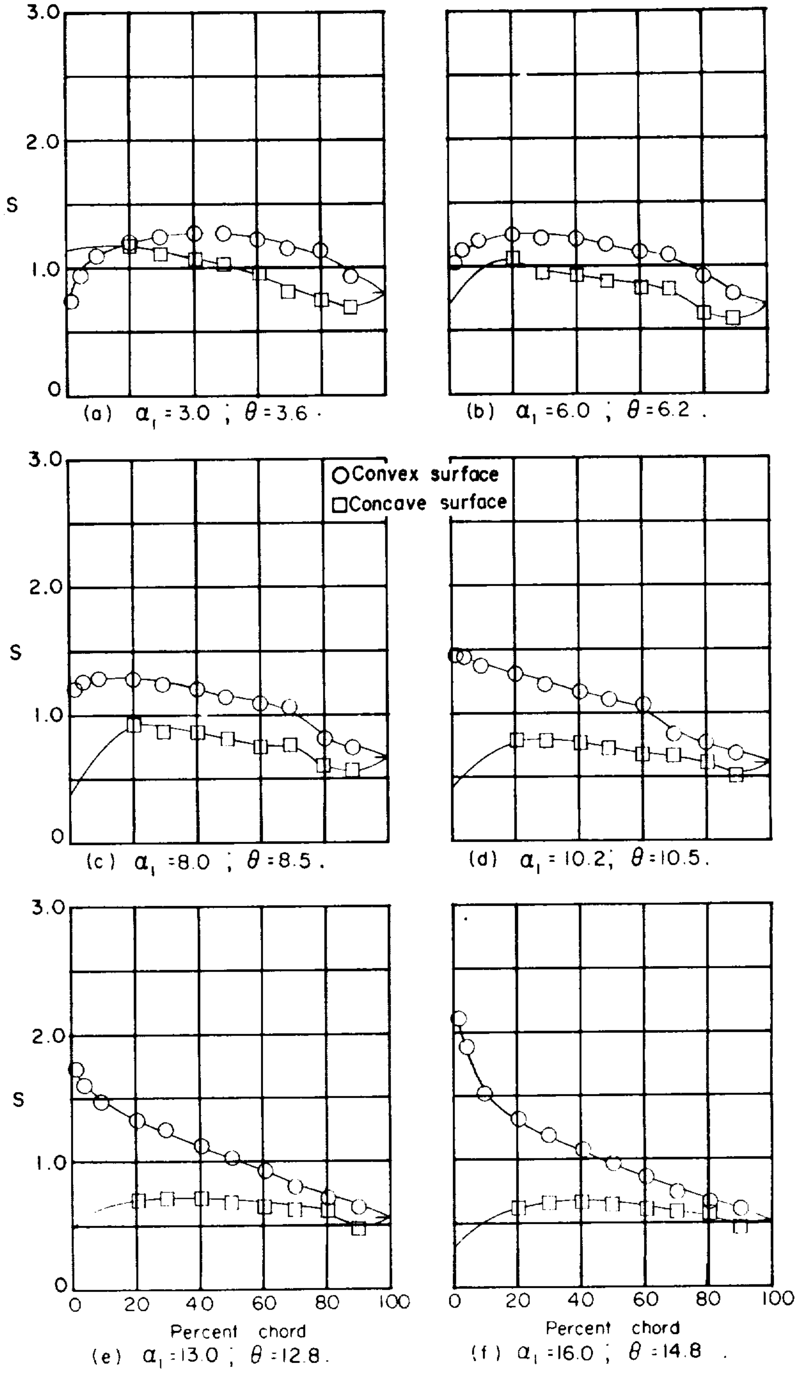

(a) $\alpha_1 = 3.0$; $\theta = 3.6$.

(b) $\alpha_1 = 6.0$; $\theta = 6.2$.

(c) $\alpha_1 = 8.0$; $\theta = 8.5$.

(d) $\alpha_1 = 10.2$; $\theta = 10.5$.

(e) $\alpha_1 = 13.0$; $\theta = 12.8$.

(f) $\alpha_1 = 16.0$; $\theta = 14.8$.

Figure 60.- Blade-surface pressure distributions and blade section characteristics for the cascade combination, $\beta_1 = 60^\circ$, $\sigma = 1.25$, and blade section, NACA 65-410.

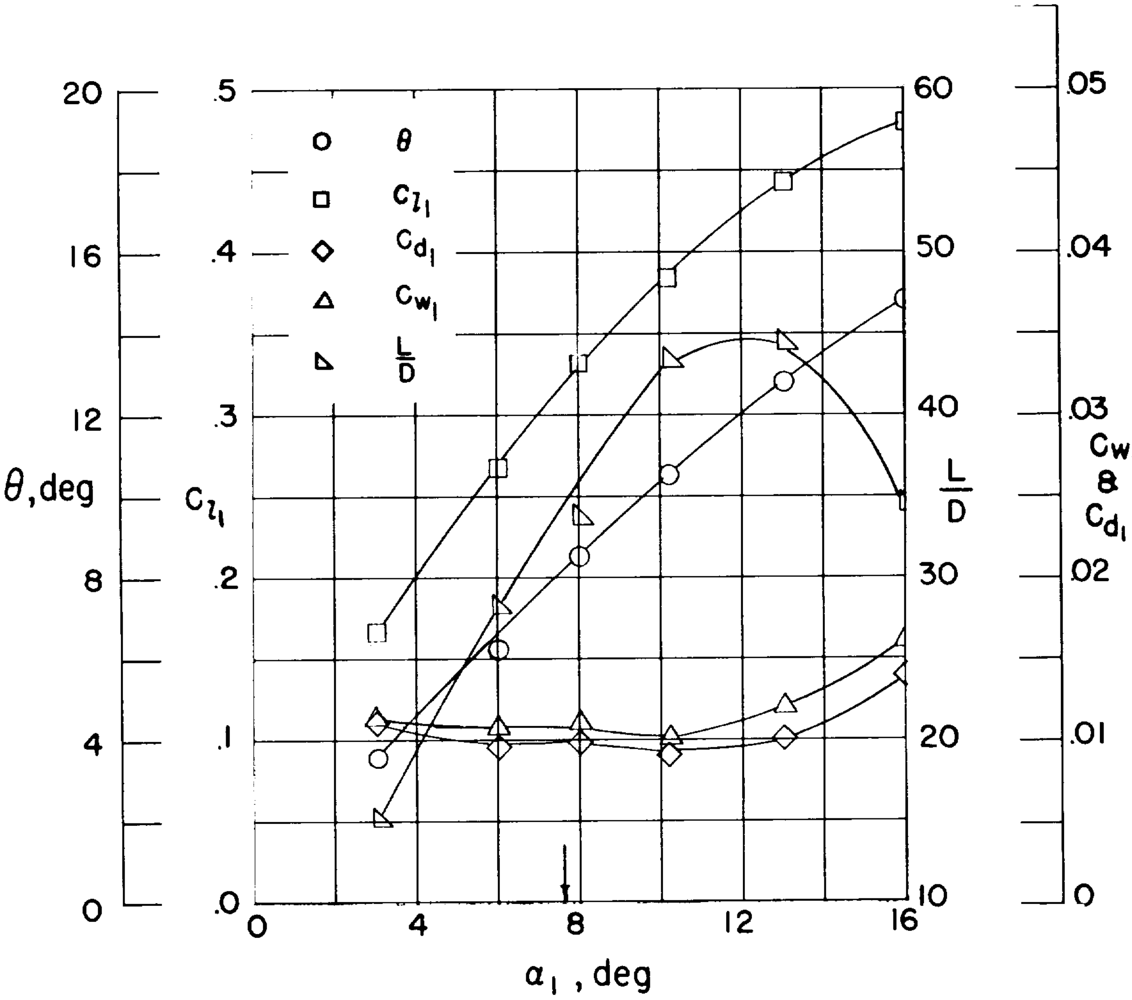

(g) Section characteristics; arrow shows design angle of attack; flagged symbol indicates roughness.

Figure 60.- Concluded.

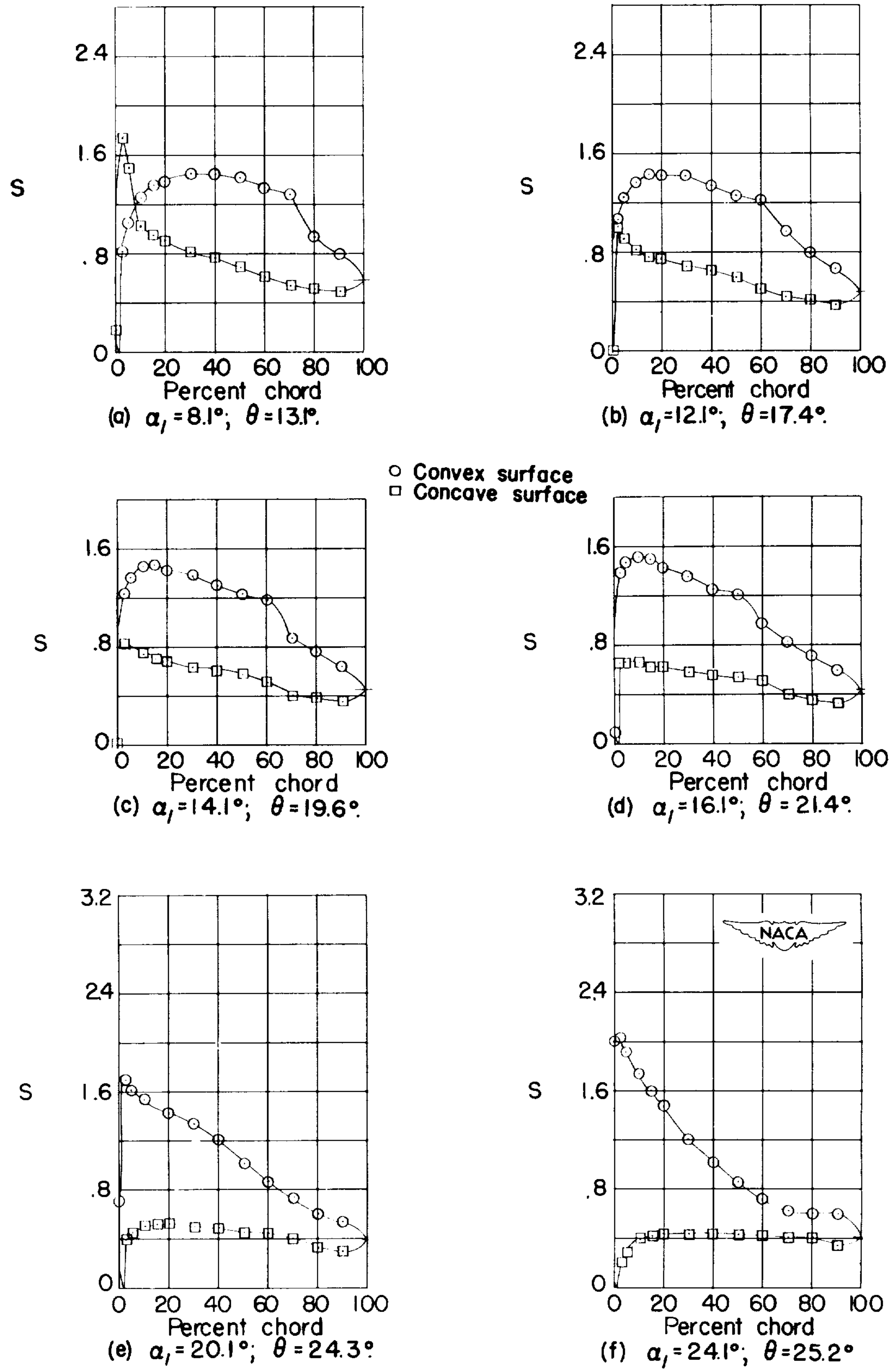

(a) $\alpha_1 = 8.1°$; $\theta = 13.1°$.
(b) $\alpha_1 = 12.1°$; $\theta = 17.4°$.
(c) $\alpha_1 = 14.1°$; $\theta = 19.6°$.
(d) $\alpha_1 = 16.1°$; $\theta = 21.4°$.
(e) $\alpha_1 = 20.1°$; $\theta = 24.3°$
(f) $\alpha_1 = 24.1°$; $\theta = 25.2°$

Figure 61.- Blade-surface pressure distributions and blade section characteristics for the cascade combination, $\beta_1 = 60°$, $\sigma = 1.25$, and blade section, NACA 65-(12)10.

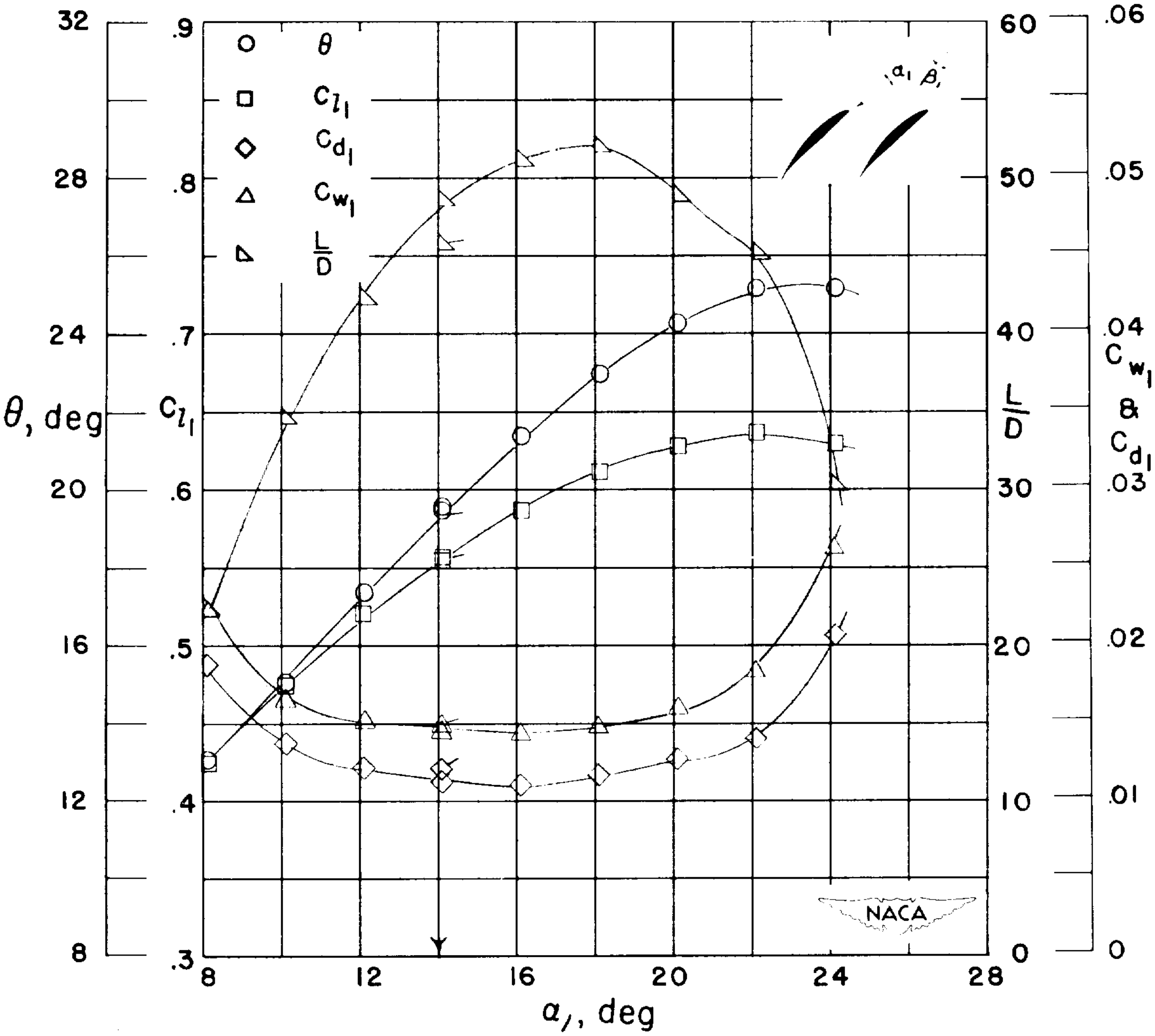

(g) Section characteristics; arrow shows design angle of attack; flagged symbol indicates leading-edge roughness.

Figure 61.- Concluded.

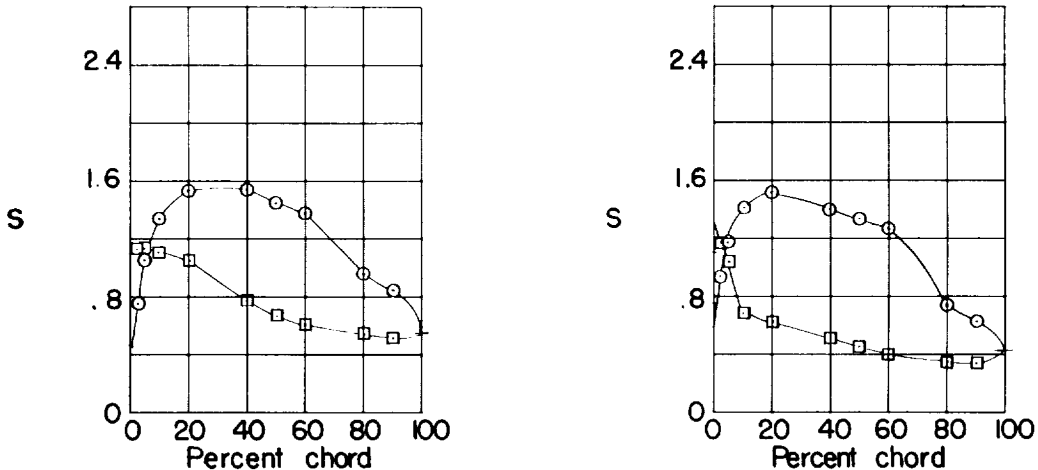

(a) $\alpha_1 = 12.0°$; $\theta = 17.2°$. (b) $\alpha_1 = 16.0°$; $\theta = 24.4°$.

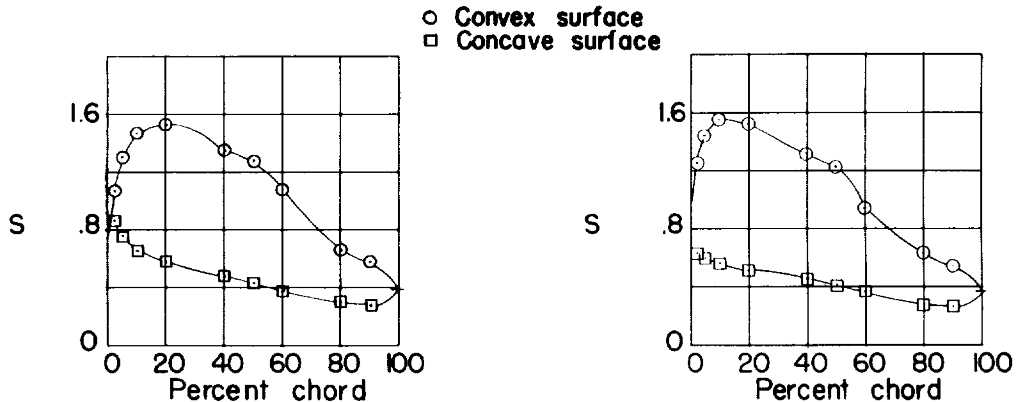

(c) $\alpha_1 = 18.0°$; $\theta = 27.2°$. (d) $\alpha_1 = 20.0°$; $\theta = 28.8°$.

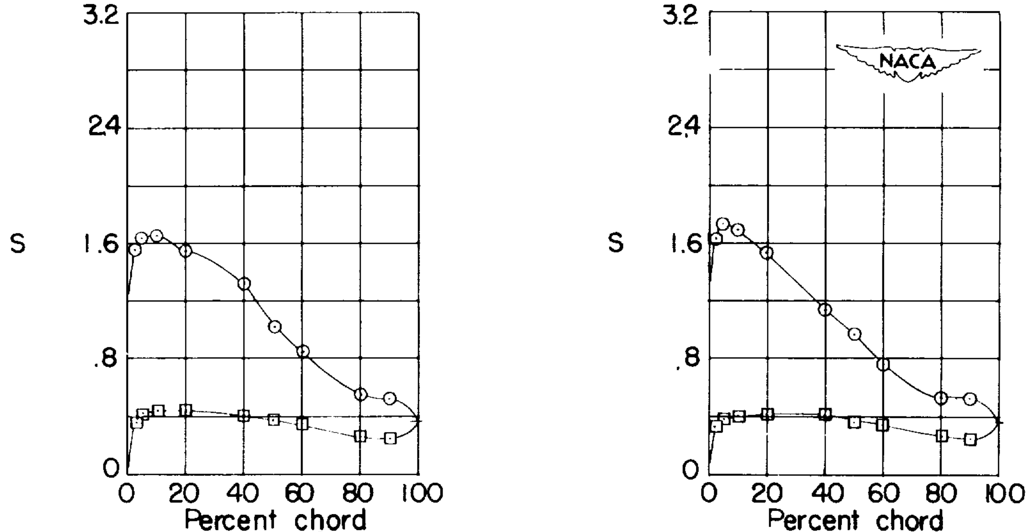

(e) $\alpha_1 = 22.0°$; $\theta = 29.9°$. (f) $\alpha_1 = 24.0°$; $\theta = 30.0°$.

Figure 62.- Blade-surface pressure distributions and blade section characteristics for the cascade combination, $\beta_1 = 60°$, $\sigma = 1.25$, and blade section, NACA 65-(18)10.

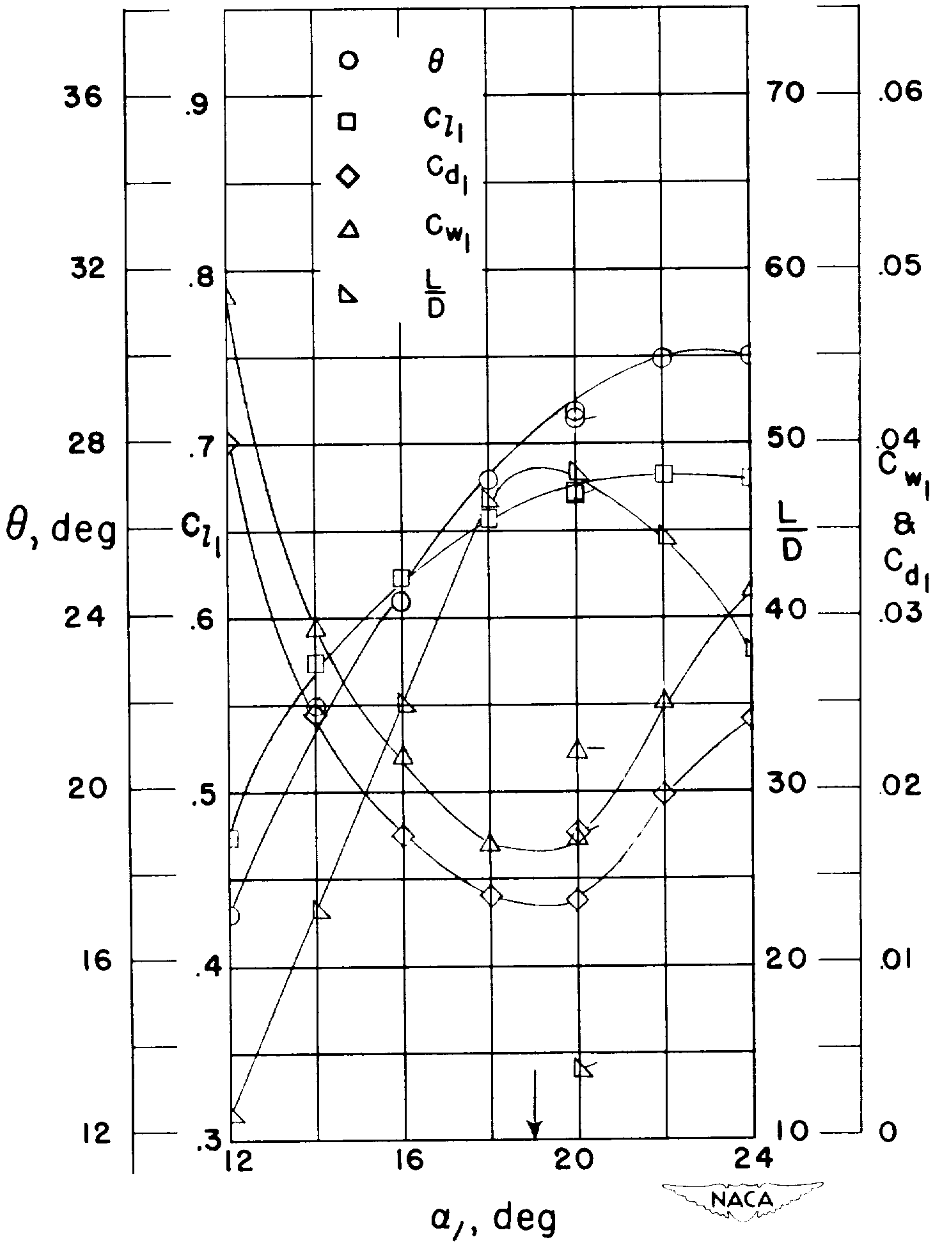

(g) Section characteristics; arrow shows design angle of attack; flagged symbol indicates leading-edge roughness.

Figure 62.- Concluded.

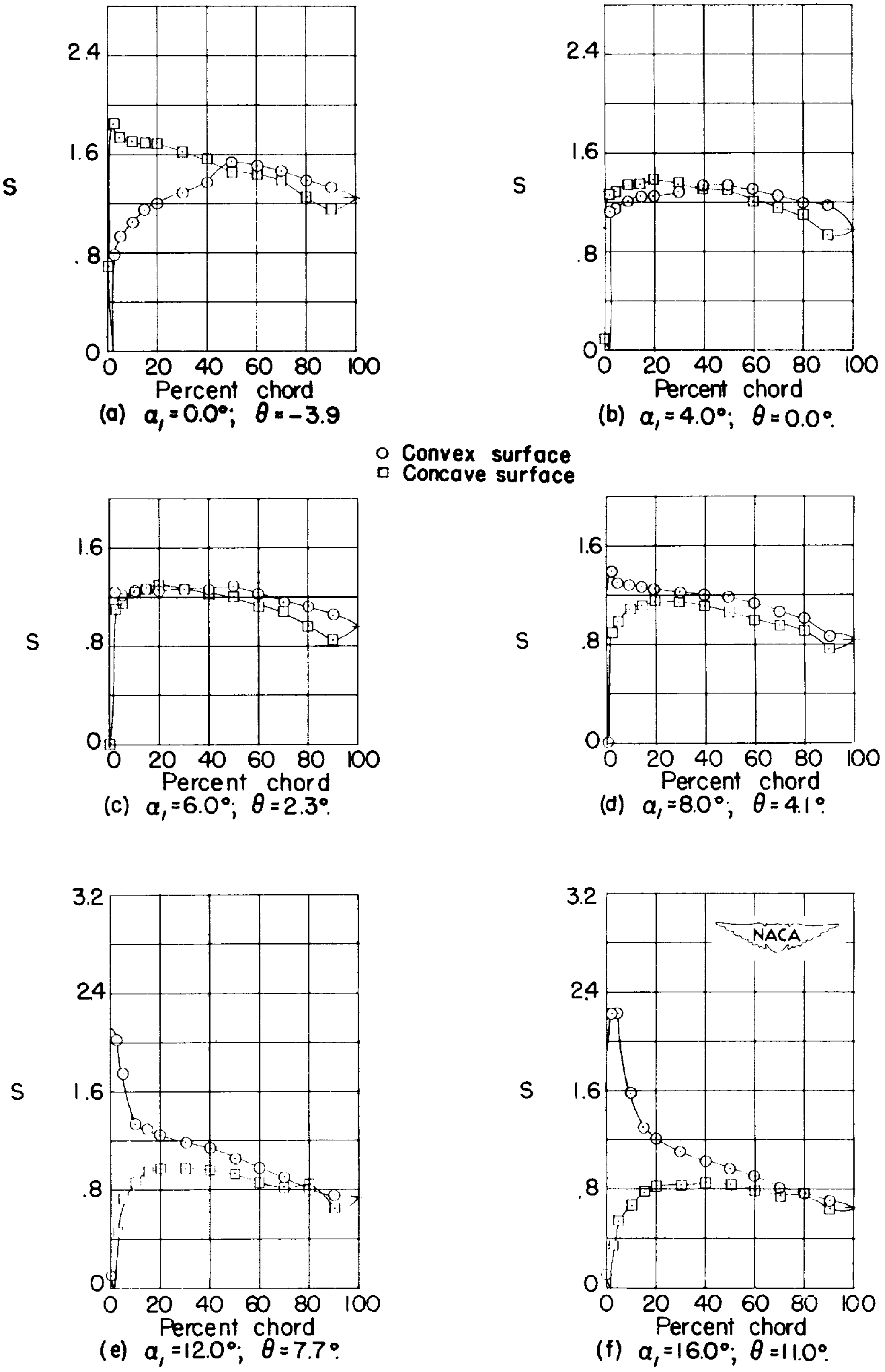

Figure 63.- Blade-surface pressure distributions and blade section characteristics for the cascade combination, $\beta_1 = 60°$, $\sigma = 1.50$, and blade section, NACA 65-010.

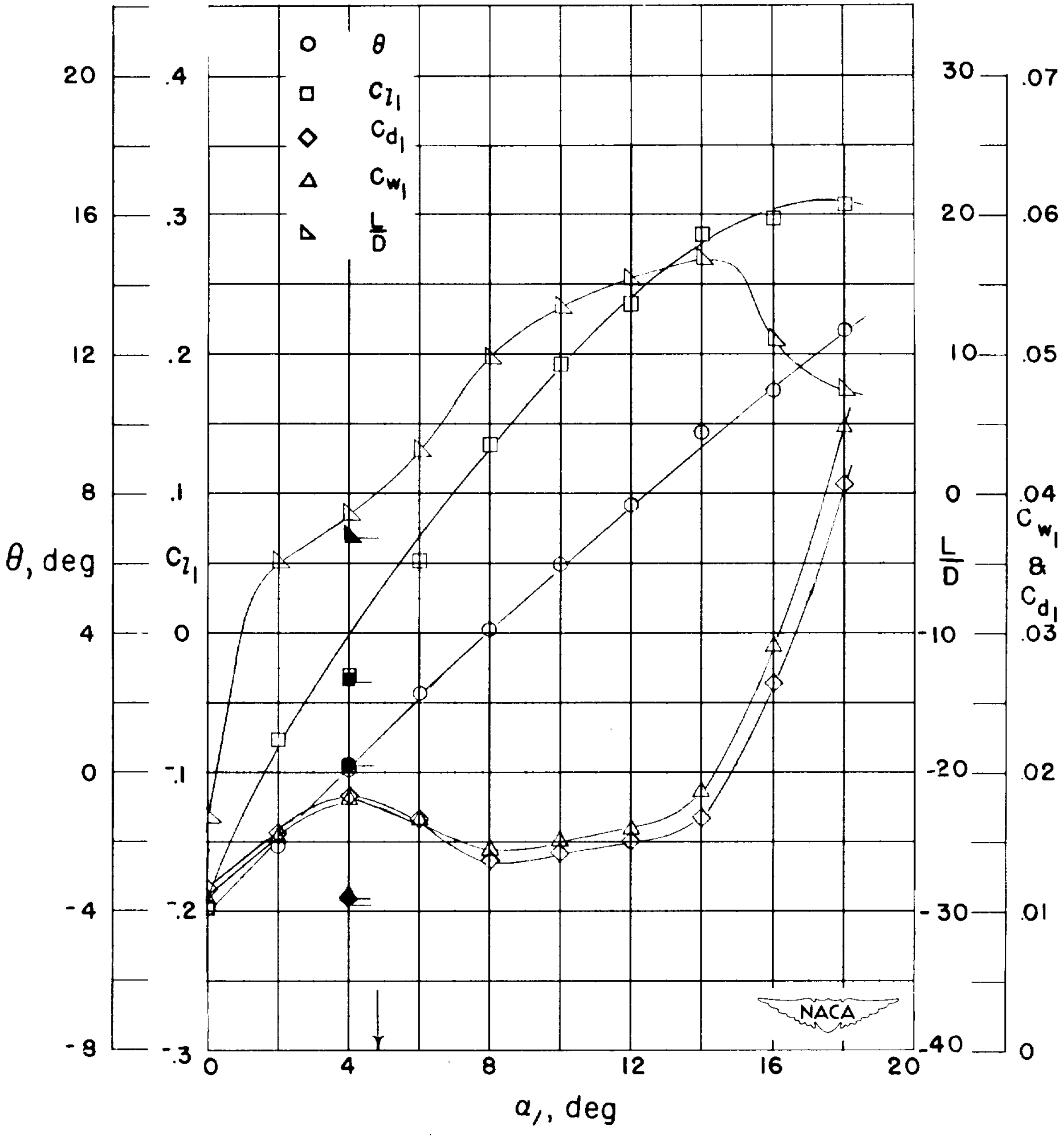

(g) Section characteristics; arrow shows design angle of attack; flagged symbol indicates leading-edge roughness; solid symbol indicates high Reynolds number.

Figure 63.- Concluded.

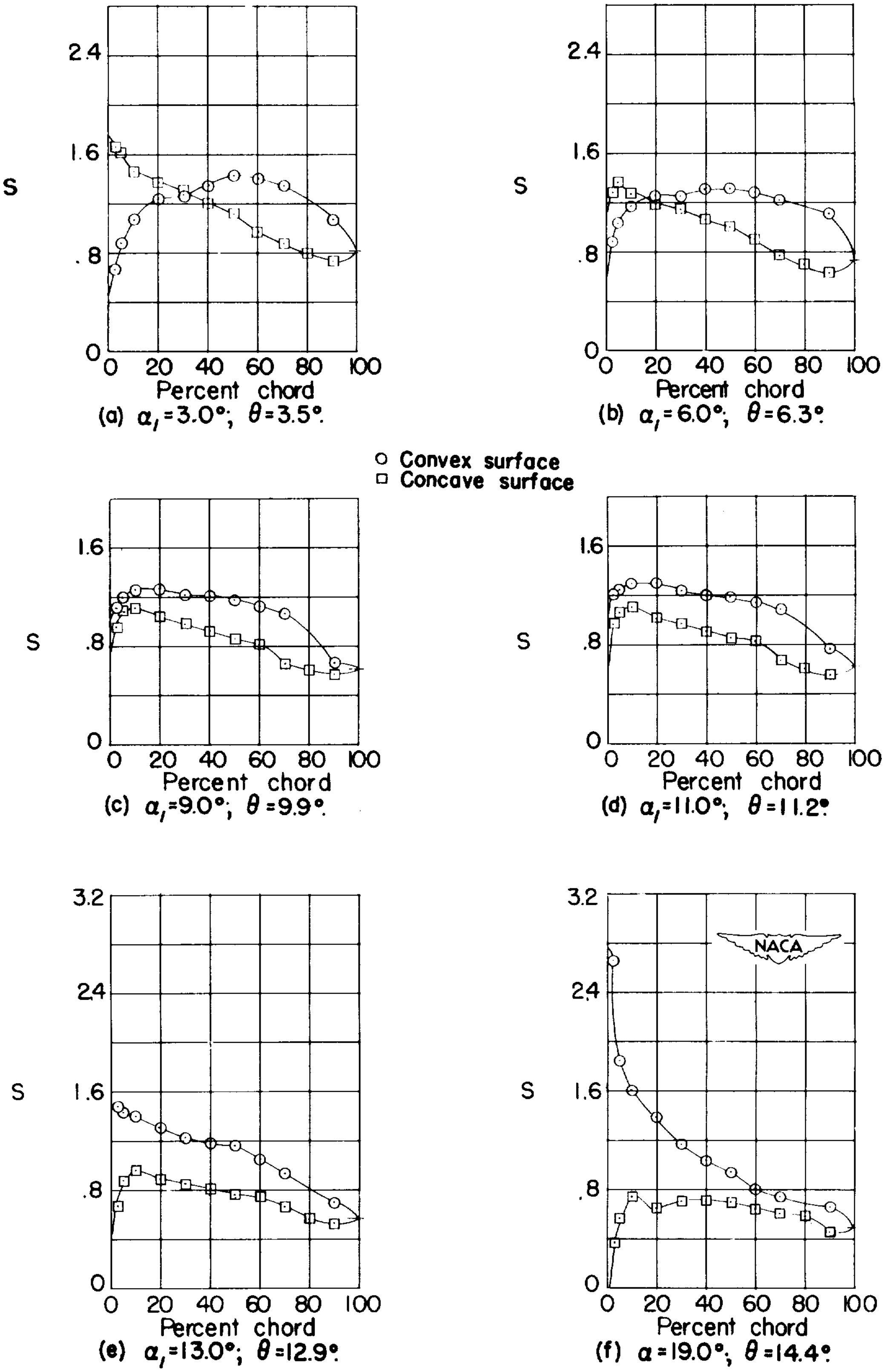

(a) $\alpha_l = 3.0^\circ$; $\theta = 3.5^\circ$.

(b) $\alpha_l = 6.0^\circ$; $\theta = 6.3^\circ$.

(c) $\alpha_l = 9.0^\circ$; $\theta = 9.9^\circ$.

(d) $\alpha_l = 11.0^\circ$; $\theta = 11.2^\circ$.

(e) $\alpha_l = 13.0^\circ$; $\theta = 12.9^\circ$.

(f) $\alpha = 19.0^\circ$; $\theta = 14.4^\circ$.

Figure 64.- Blade-surface pressure distributions and blade section characteristics for the cascade combination, $\beta_1 = 60^\circ$, $\sigma = 1.50$, and blade section, NACA 65-410.

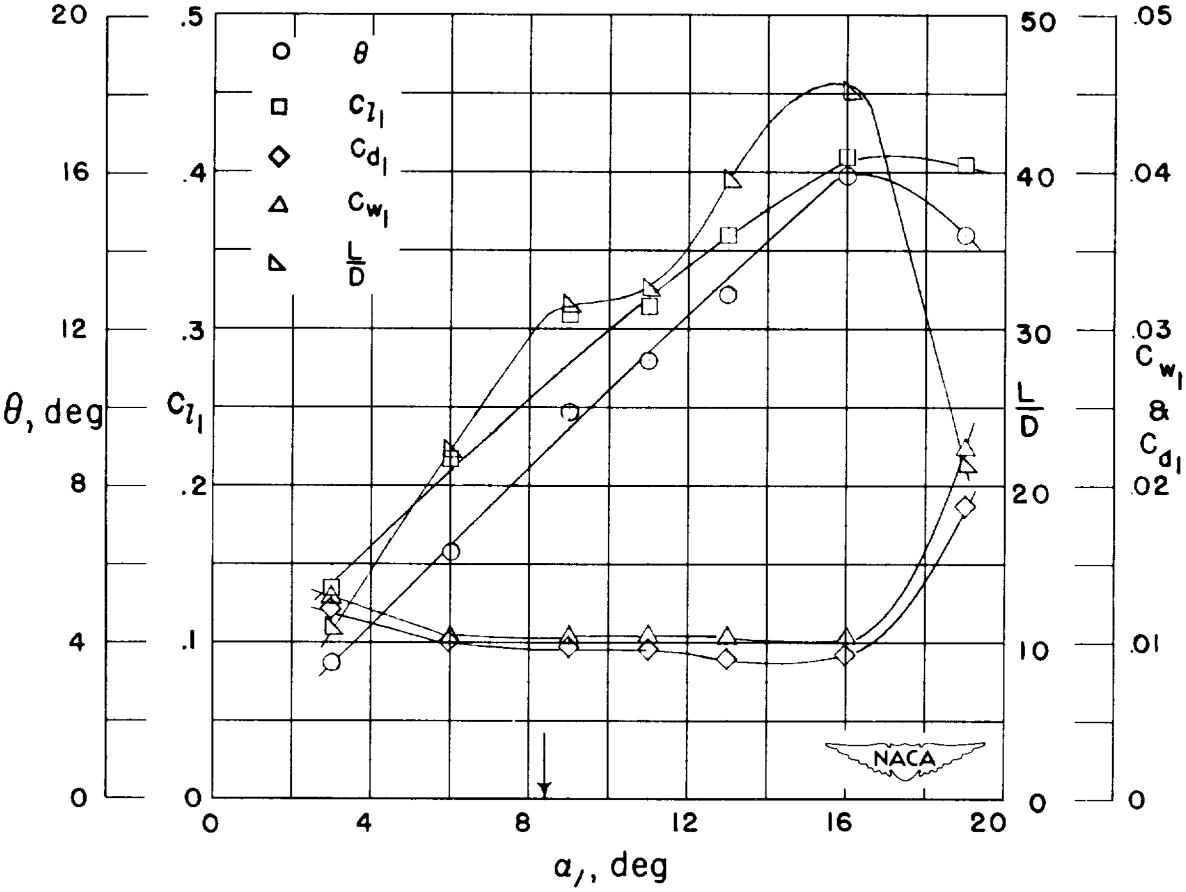

(g) Section characteristics; arrow shows design angle of attack.

Figure 64.- Concluded.

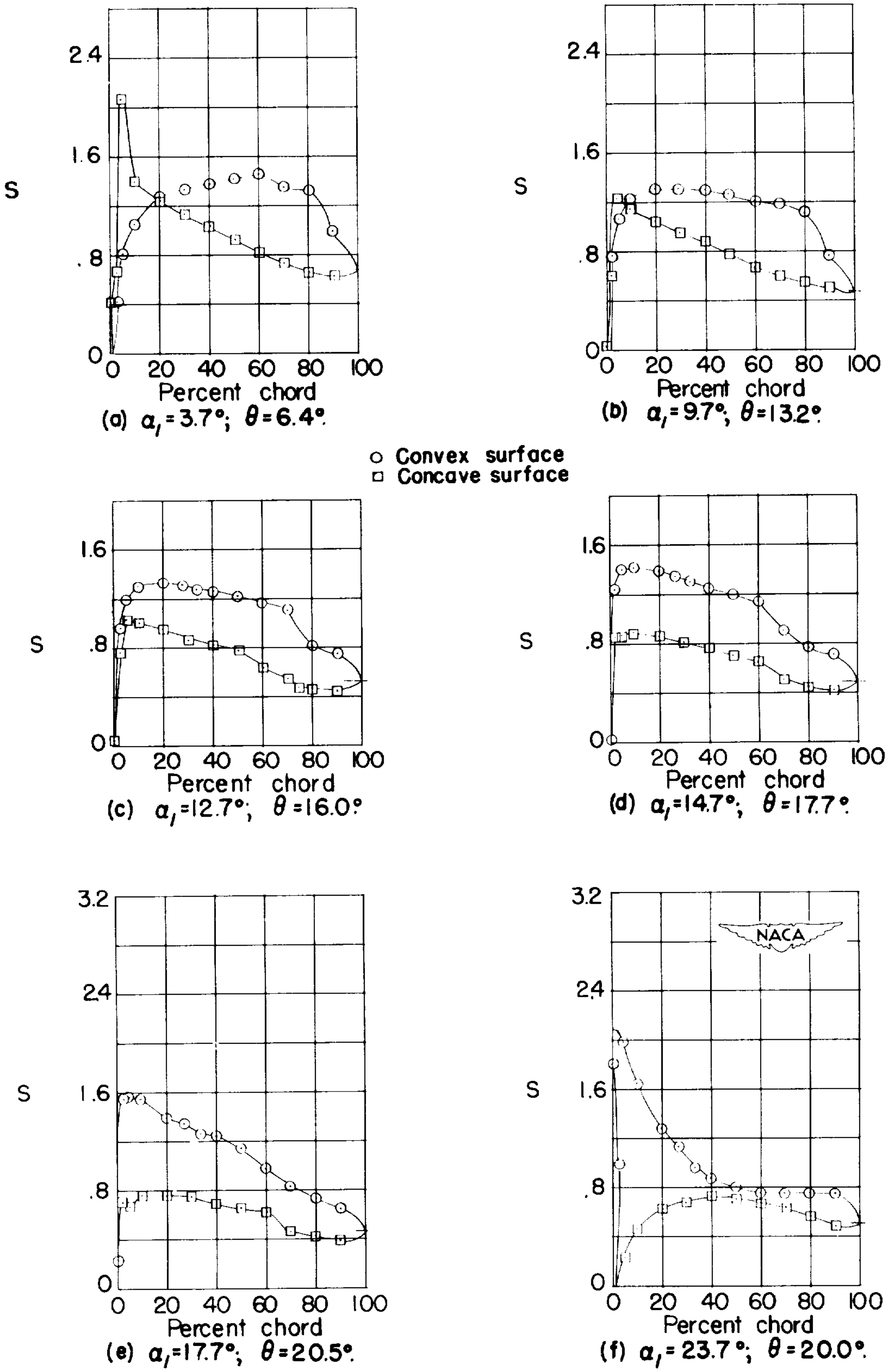

Figure 65.- Blade-surface pressure distributions and blade section characteristics for the cascade combination, $\beta_1 = 60^\circ$, $\sigma = 1.50$, and blade section, NACA 65-810.

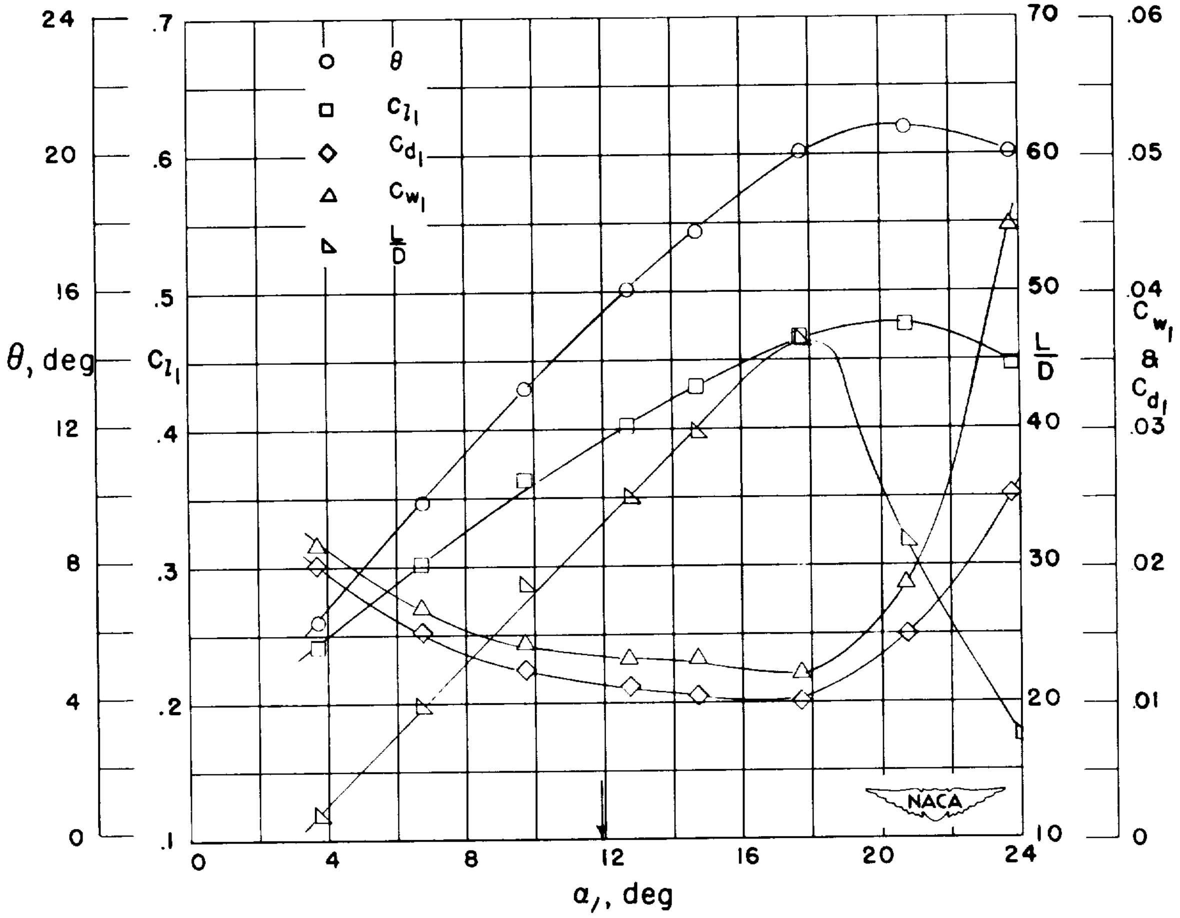

(g) Section characteristics; arrow shows design angle of attack.

Figure 65.- Concluded.

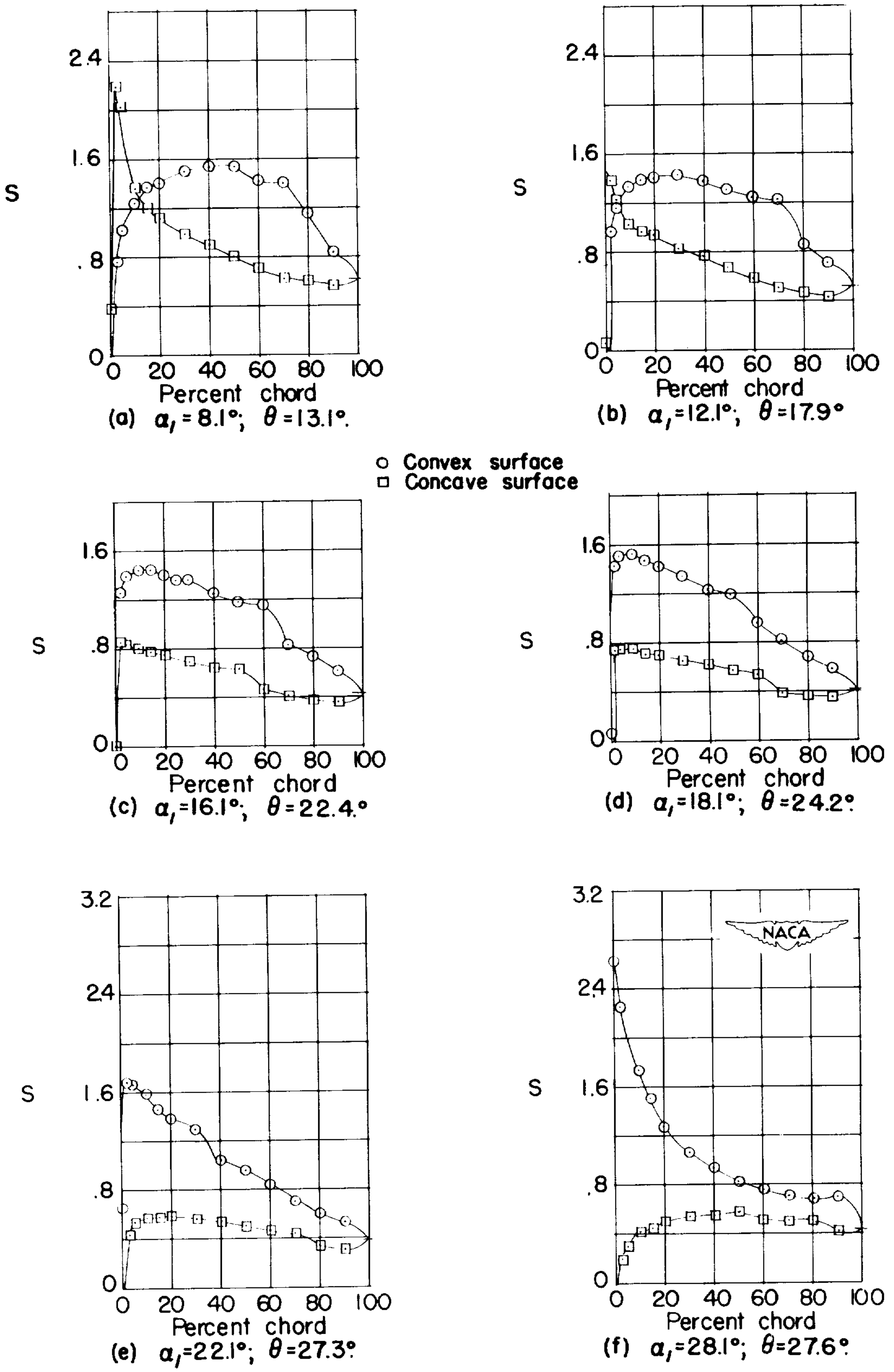

(a) $\alpha_1 = 8.1°$; $\theta = 13.1°$.

(b) $\alpha_1 = 12.1°$; $\theta = 17.9°$

(c) $\alpha_1 = 16.1°$; $\theta = 22.4°$

(d) $\alpha_1 = 18.1°$; $\theta = 24.2°$

(e) $\alpha_1 = 22.1°$; $\theta = 27.3°$

(f) $\alpha_1 = 28.1°$; $\theta = 27.6°$

Figure 66.- Blade-surface pressure distributions and blade section characteristics for the cascade combination, $\beta_1 = 60°$, $\sigma = 1.50$, and blade section, NACA 65-(12)10.

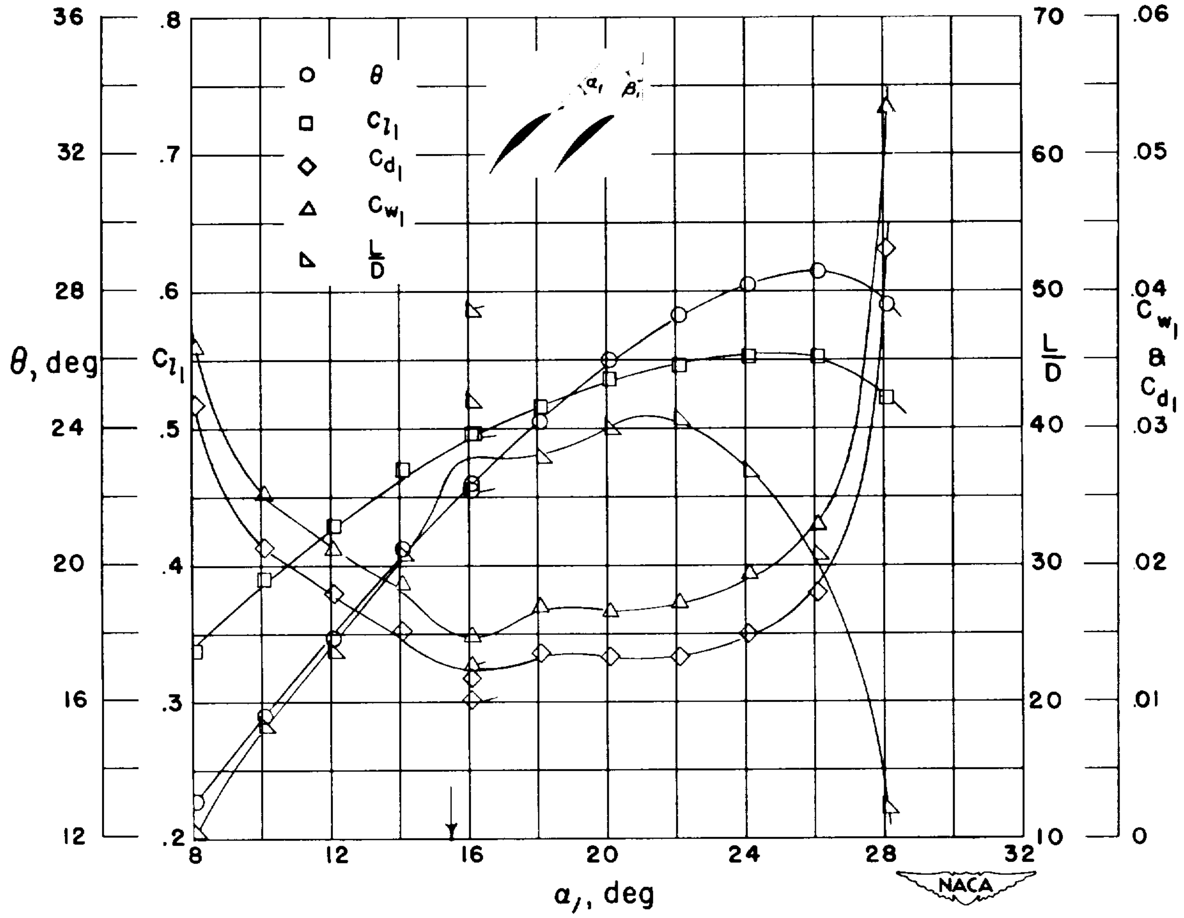

(g) Section characteristics; arrow shows design angle of attack; flagged symbol indicates leading-edge roughness.

Figure 66.- Concluded.

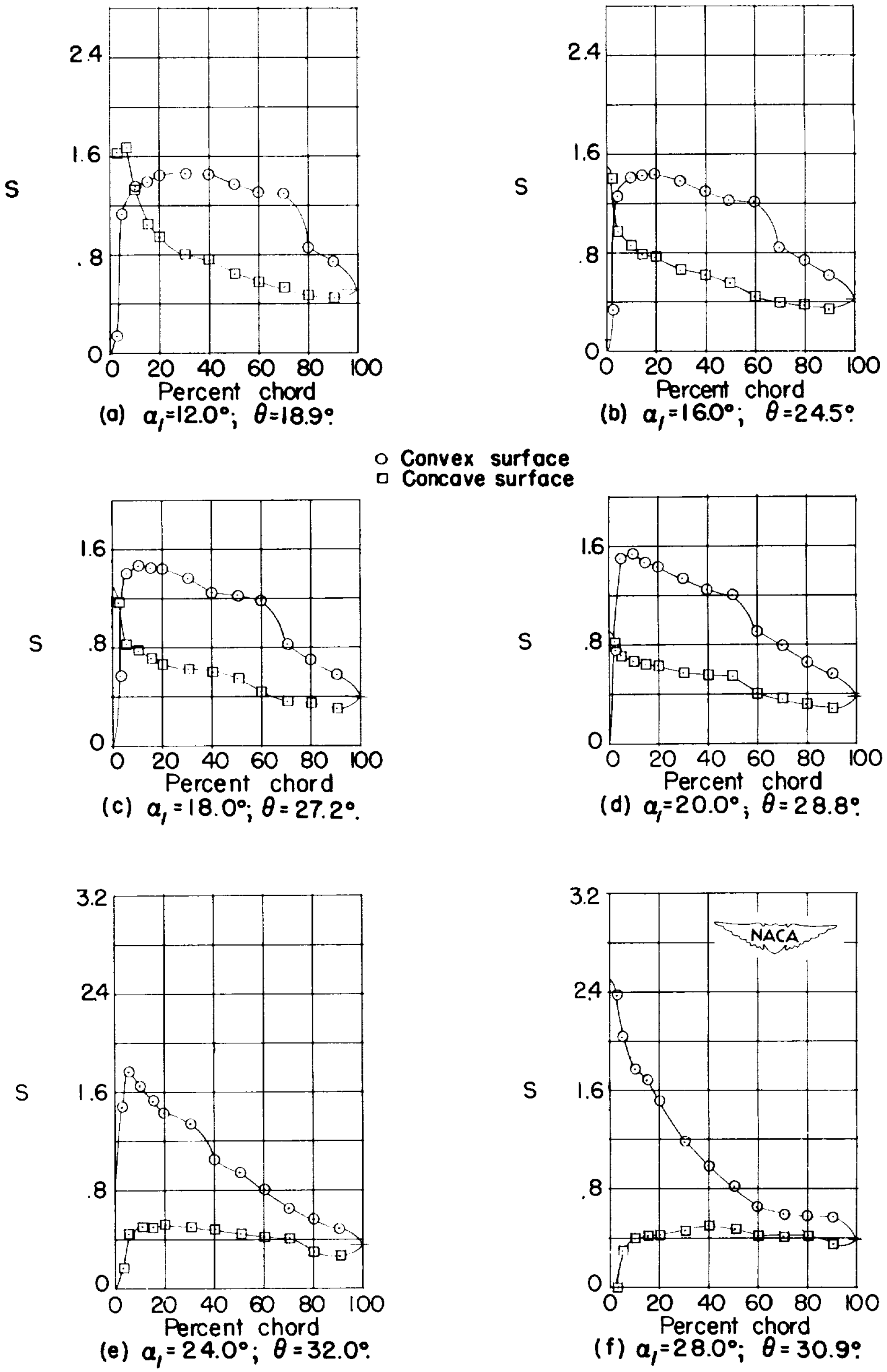

(a) $\alpha_i = 12.0°$; $\theta = 18.9°$.

(b) $\alpha_i = 16.0°$; $\theta = 24.5°$.

(c) $\alpha_i = 18.0°$; $\theta = 27.2°$.

(d) $\alpha_i = 20.0°$; $\theta = 28.8°$.

(e) $\alpha_i = 24.0°$; $\theta = 32.0°$.

(f) $\alpha_i = 28.0°$; $\theta = 30.9°$.

Figure 67.- Blade-surface pressure distributions and blade section characteristics for the cascade combination, $\beta_1 = 60^\circ$, $\sigma = 1.50$, and blade section, NACA 65-(15)10.

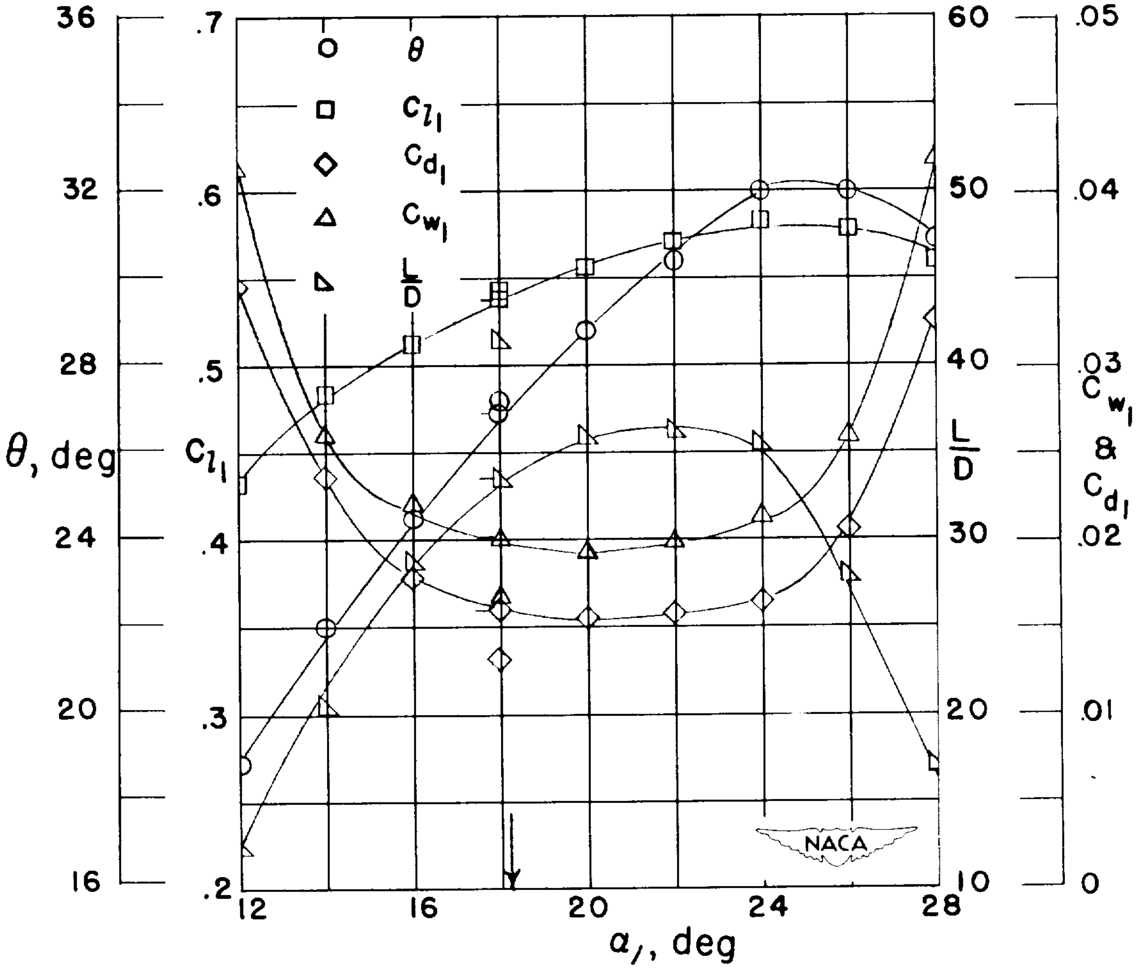

(g) Section characteristics; arrow shows design angle of attack; flagged symbol indicates leading-edge roughness.

Figure 67.- Concluded.

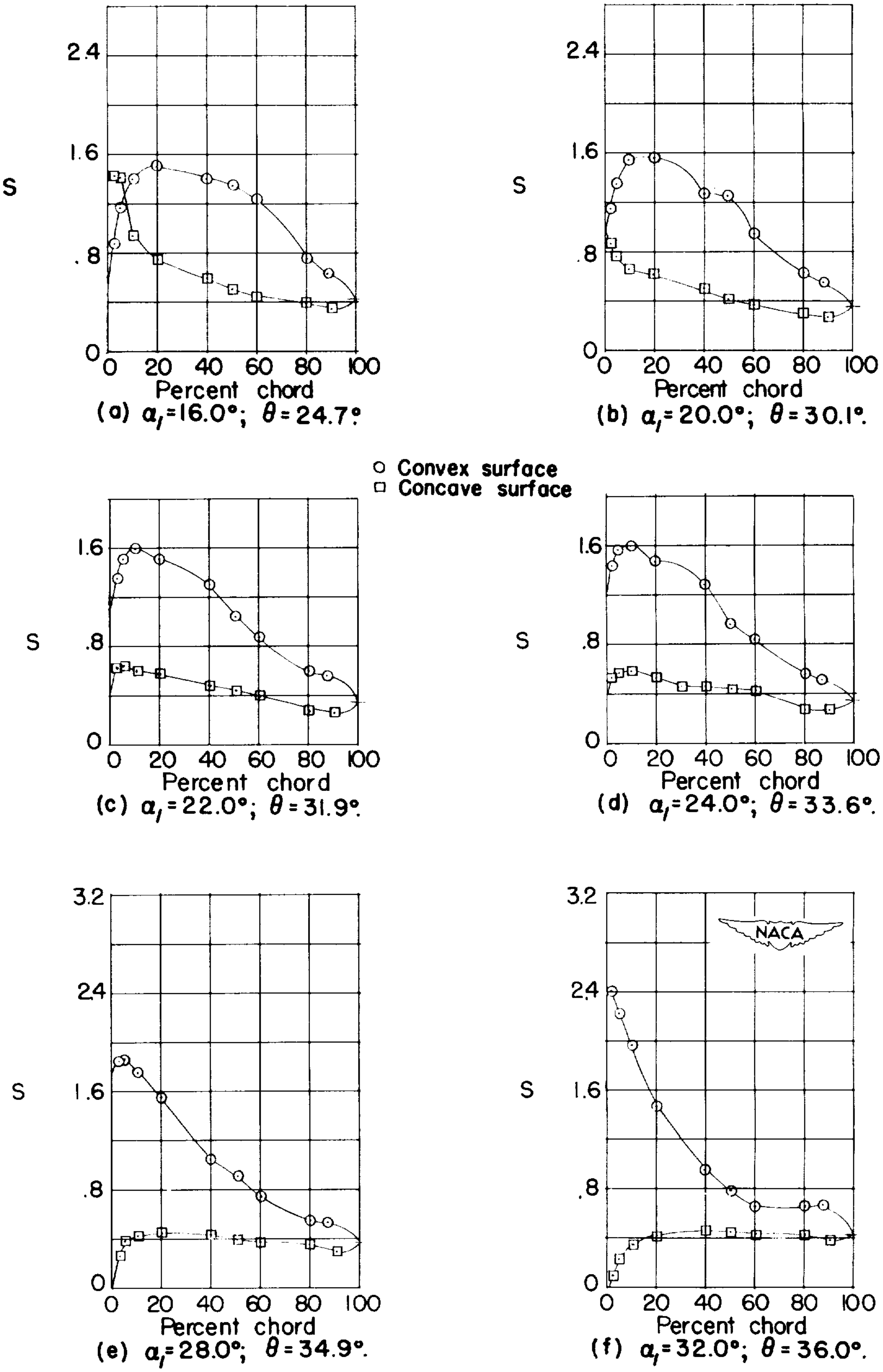

(a) $\alpha_l = 16.0°$; $\theta = 24.7°$.

(b) $\alpha_l = 20.0°$; $\theta = 30.1°$.

(c) $\alpha_l = 22.0°$; $\theta = 31.9°$.

(d) $\alpha_l = 24.0°$; $\theta = 33.6°$.

(e) $\alpha_l = 28.0°$; $\theta = 34.9°$.

(f) $\alpha_l = 32.0°$; $\theta = 36.0°$.

Figure 68.- Blade-surface pressure distributions and blade section characteristics for the cascade combination, $\beta_1 = 60^{\circ}$, $\sigma = 1.50$, and blade section, NACA 65-(18)10.

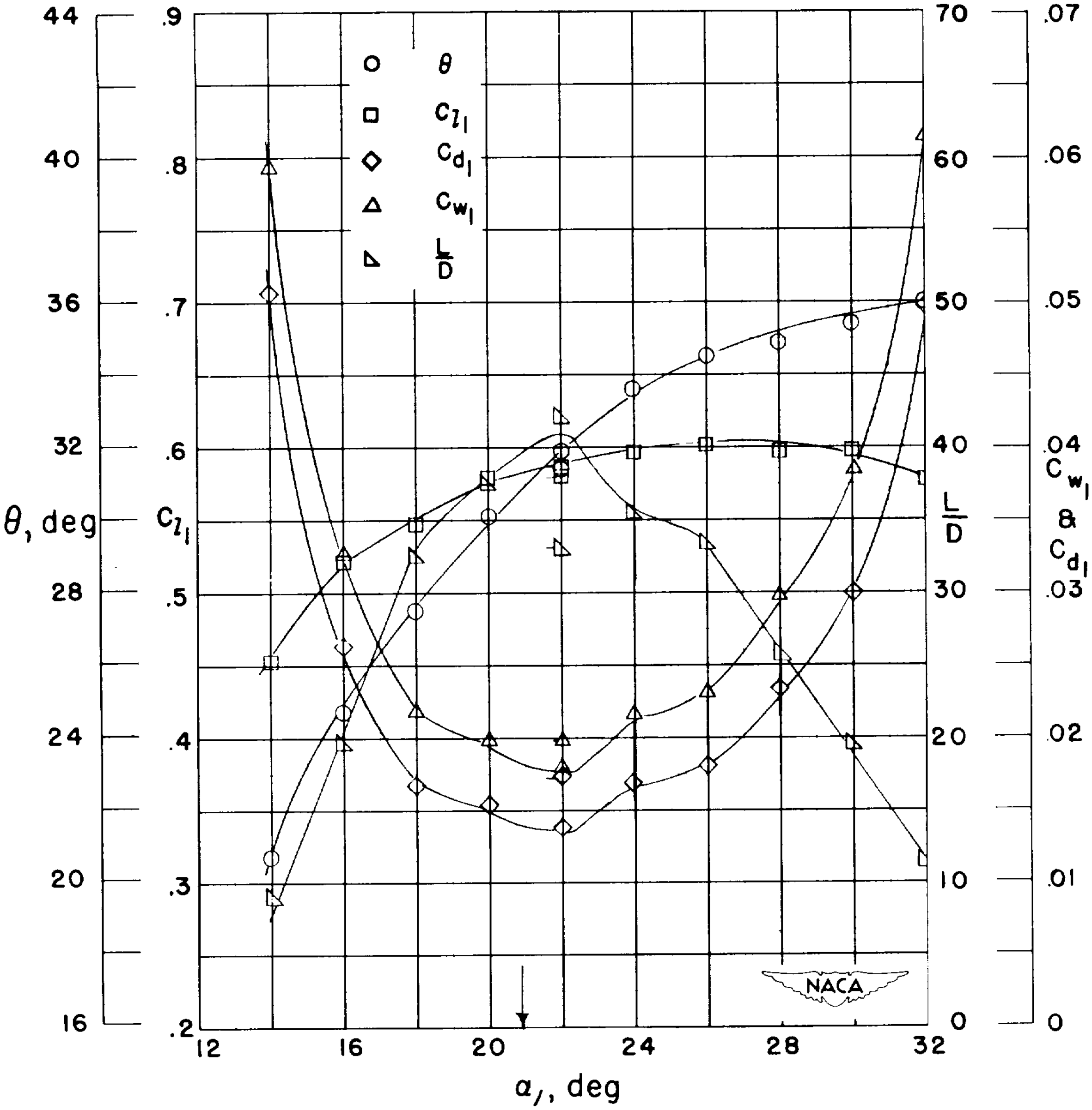

(g) Section characteristics; arrow shows design angle of attack; flagged symbol indicates leading-edge roughness.

Figure 68.- Concluded.

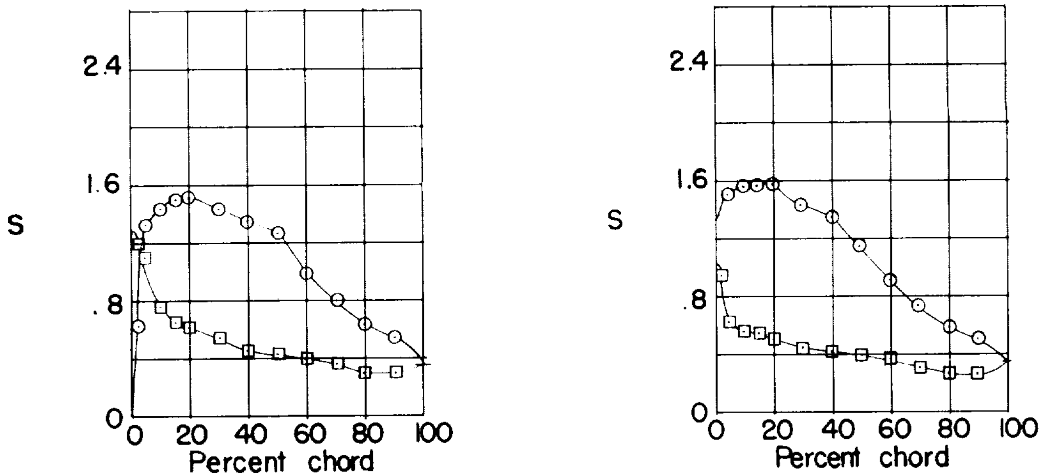

(a) α_l=19.0°; θ=29.8°. (b) α_l=22.0°; θ=32.2°

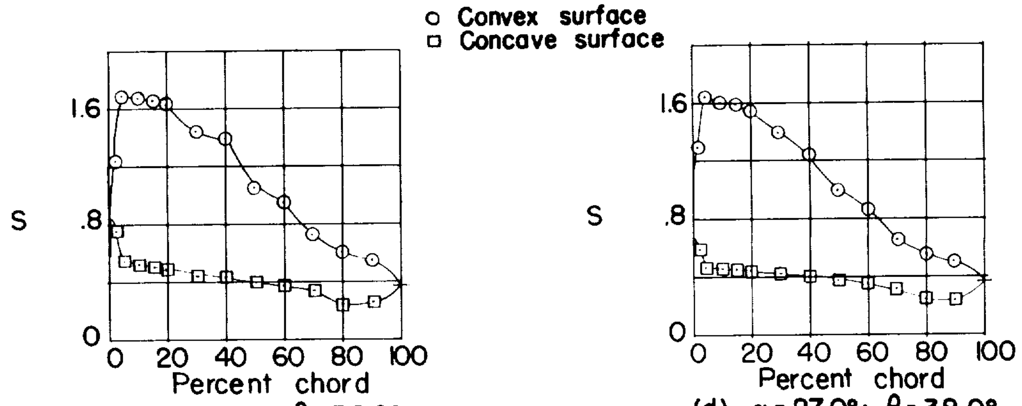

(c) α_l=25.0°; θ=36.0°. (d) α_l=27.0°; θ=38.0°.

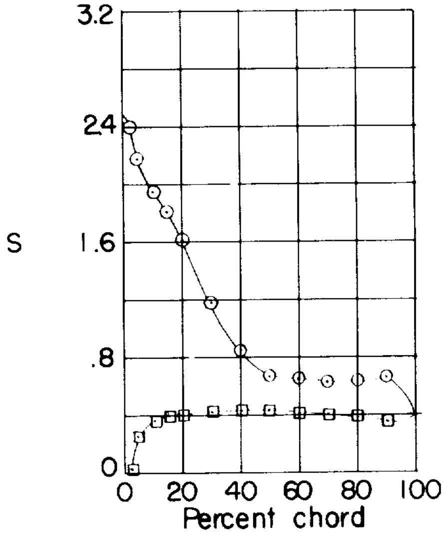

(e) α_l=30.0°; θ=38.1°

Figure 69.- Blade-surface pressure distributions and blade section characteristics for the cascade combination, β_1 = 60°, σ = 1.50, and blade section, NACA 65-(21)10.

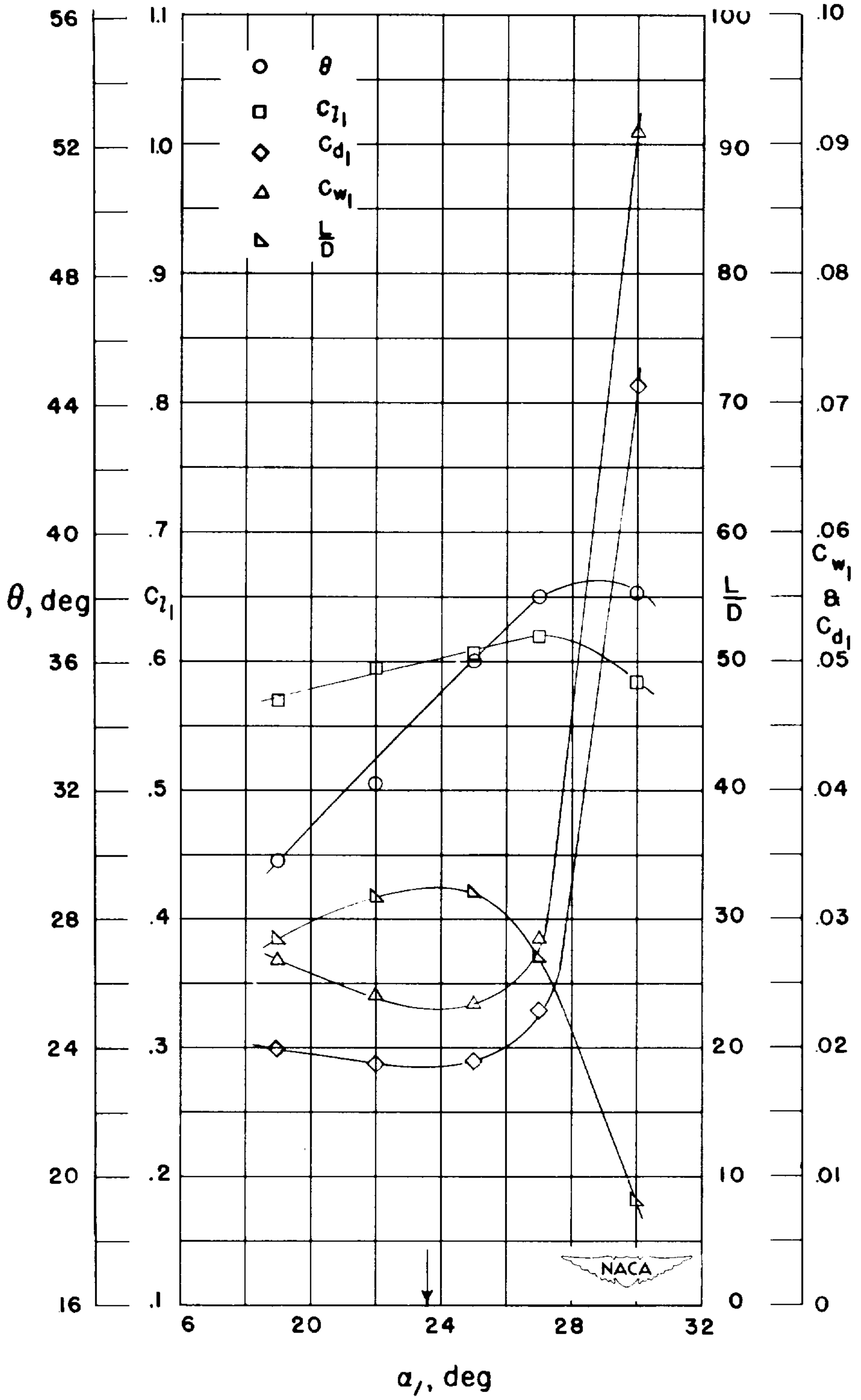

(f) Section characteristics; arrow shows design angle of attack.

Figure 69.- Concluded.

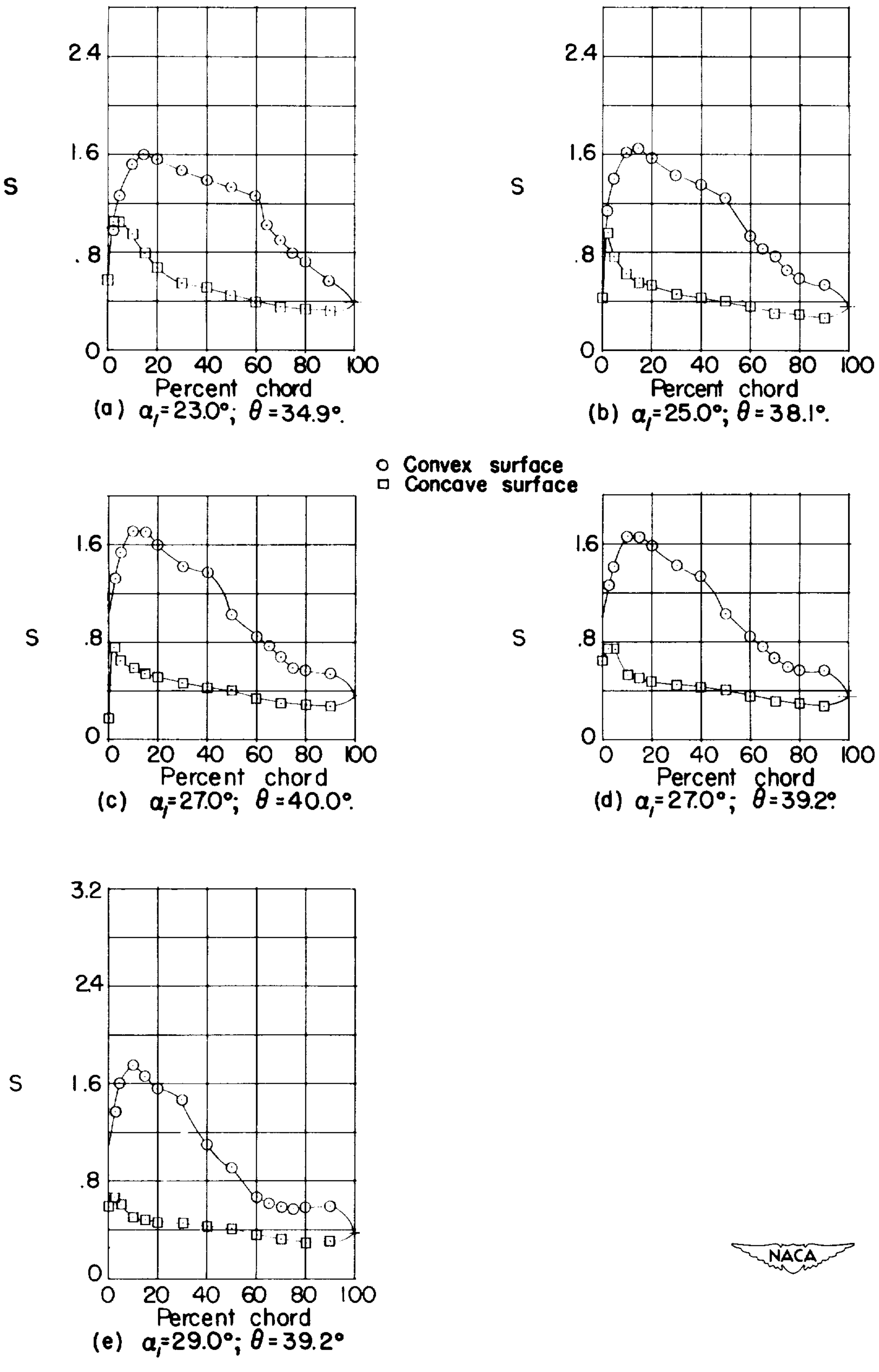

(a) α_l=23.0°; θ=34.9°.

(b) α_l=25.0°; θ=38.1°.

(c) α_l=27.0°; θ=40.0°.

(d) α_l=27.0°; θ=39.2°

(e) α_l=29.0°; θ=39.2°

Figure 70.- Blade-surface pressure distributions and blade section characteristics for the cascade combination, $\beta_1 = 60^\circ$, $\sigma = 1.50$, and blade section, NACA 65-(24)10.

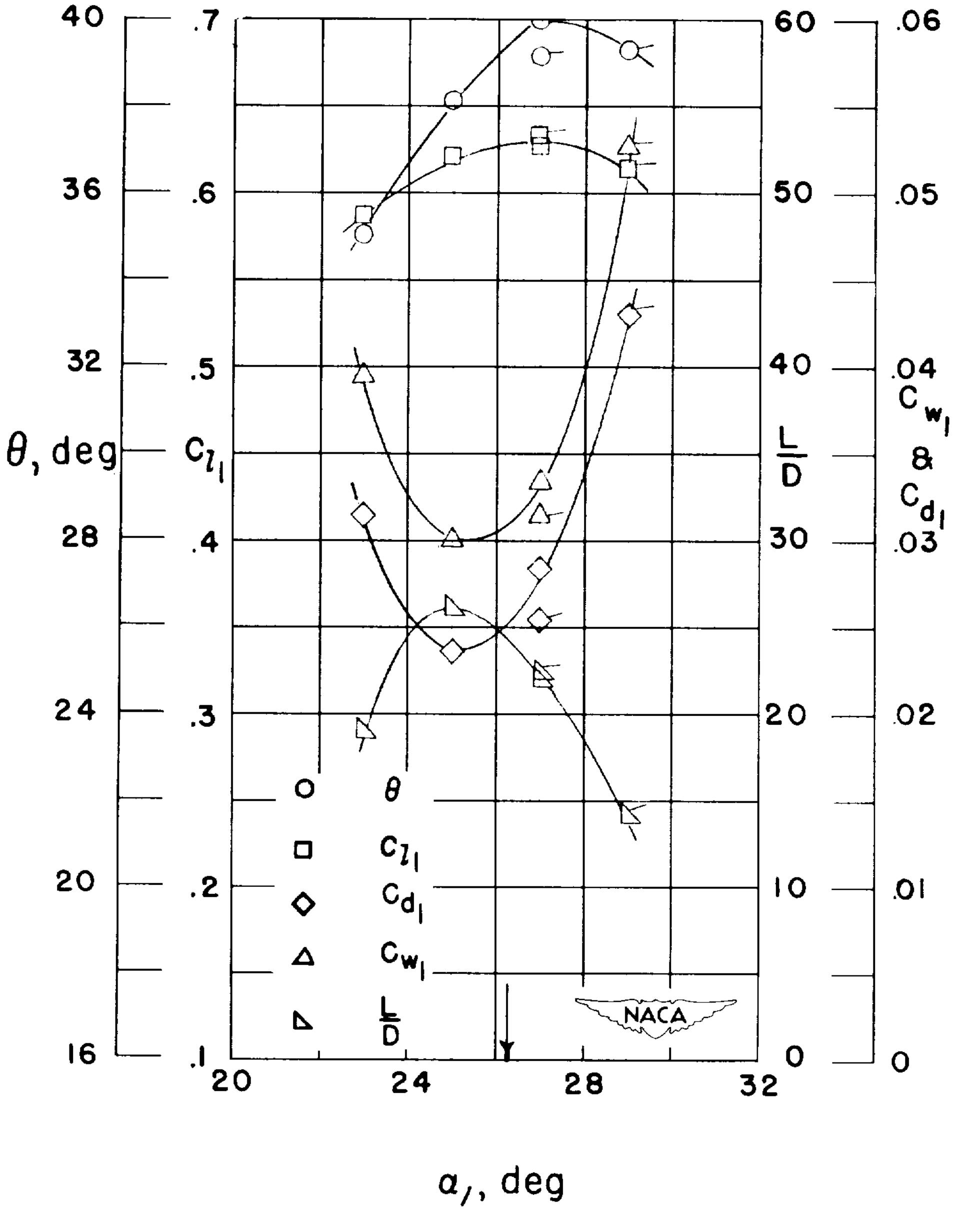

(f) Section characteristics; arrow shows design angle of attack; flagged symbol indicates leading-edge roughness.

Figure 70.- Concluded.

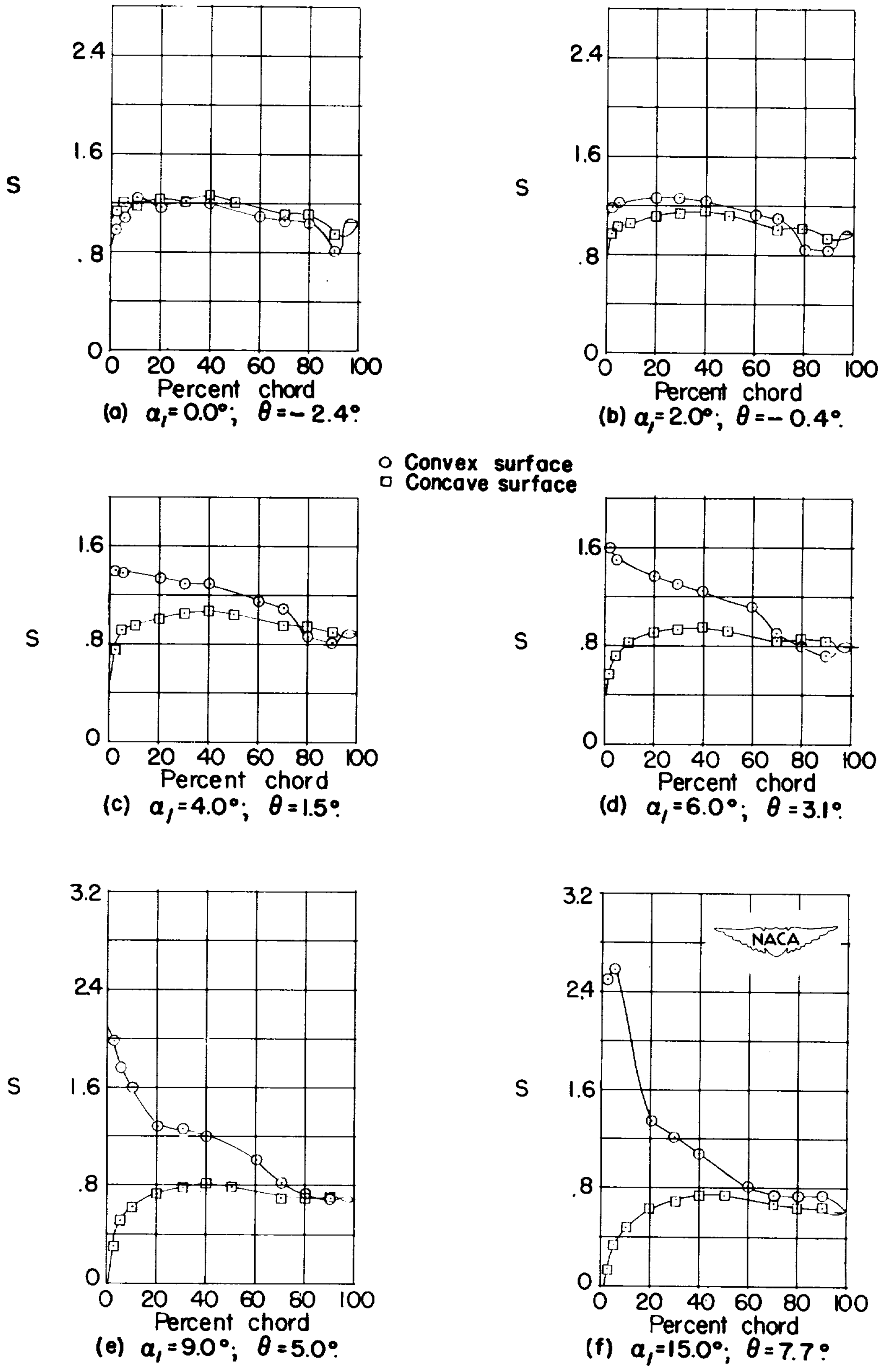

(a) $\alpha_1 = 0.0°$; $\theta = -2.4°$

(b) $\alpha_1 = 2.0°$; $\theta = -0.4°$

(c) $\alpha_1 = 4.0°$; $\theta = 1.5°$

(d) $\alpha_1 = 6.0°$; $\theta = 3.1°$

(e) $\alpha_1 = 9.0°$; $\theta = 5.0°$

(f) $\alpha_1 = 15.0°$; $\theta = 7.7°$

Figure 71.- Blade-surface pressure distributions and blade section characteristics for the cascade combination, $\beta_1 = 70^{\circ}$, $\sigma = 1.00$, and blade section, NACA 65-010.

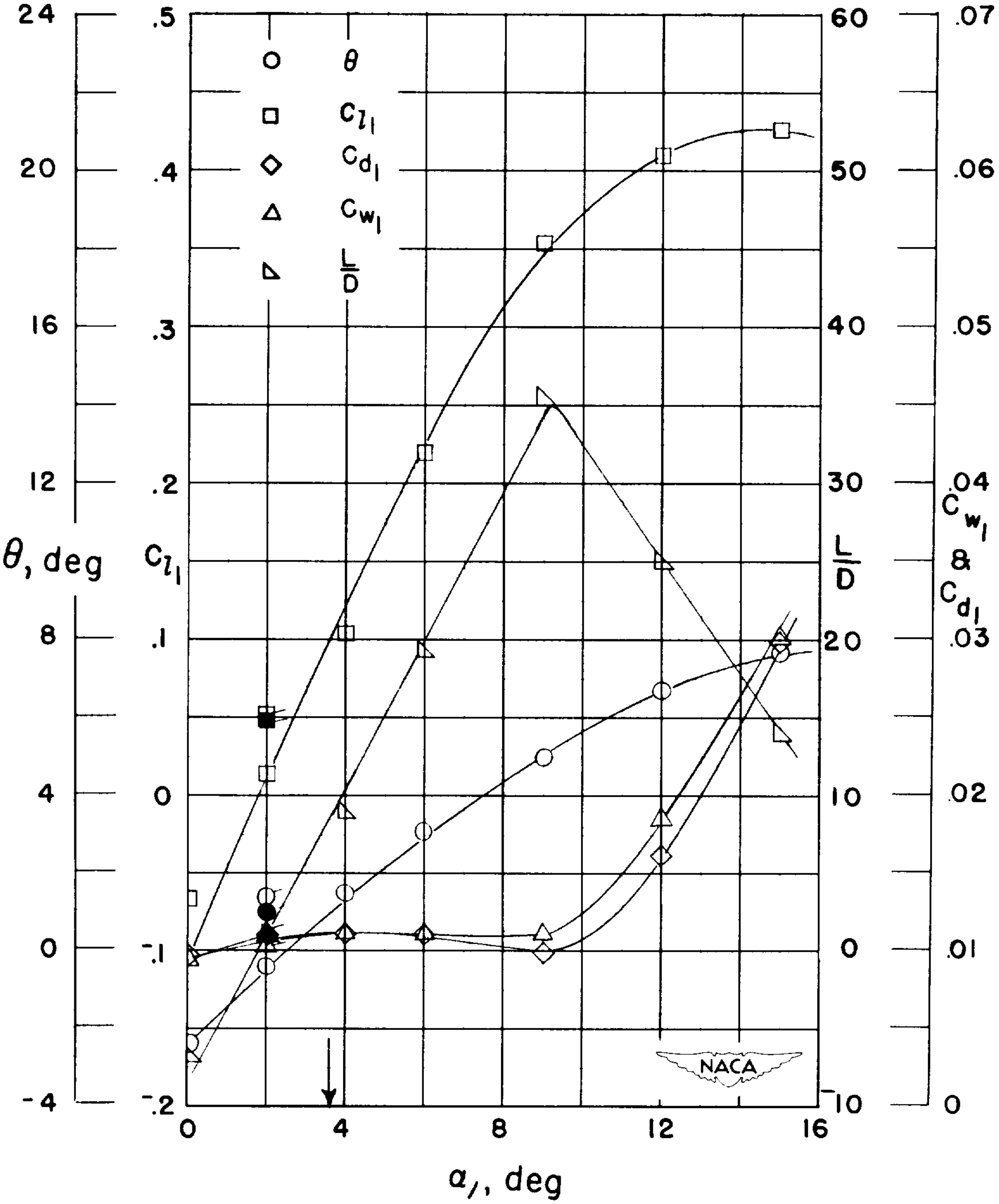

(g) Section characteristics; arrow shows design angle of attack; flagged symbol indicates leading-edge roughness; solid symbol indicates high Reynolds number.

Figure 71.- Concluded.

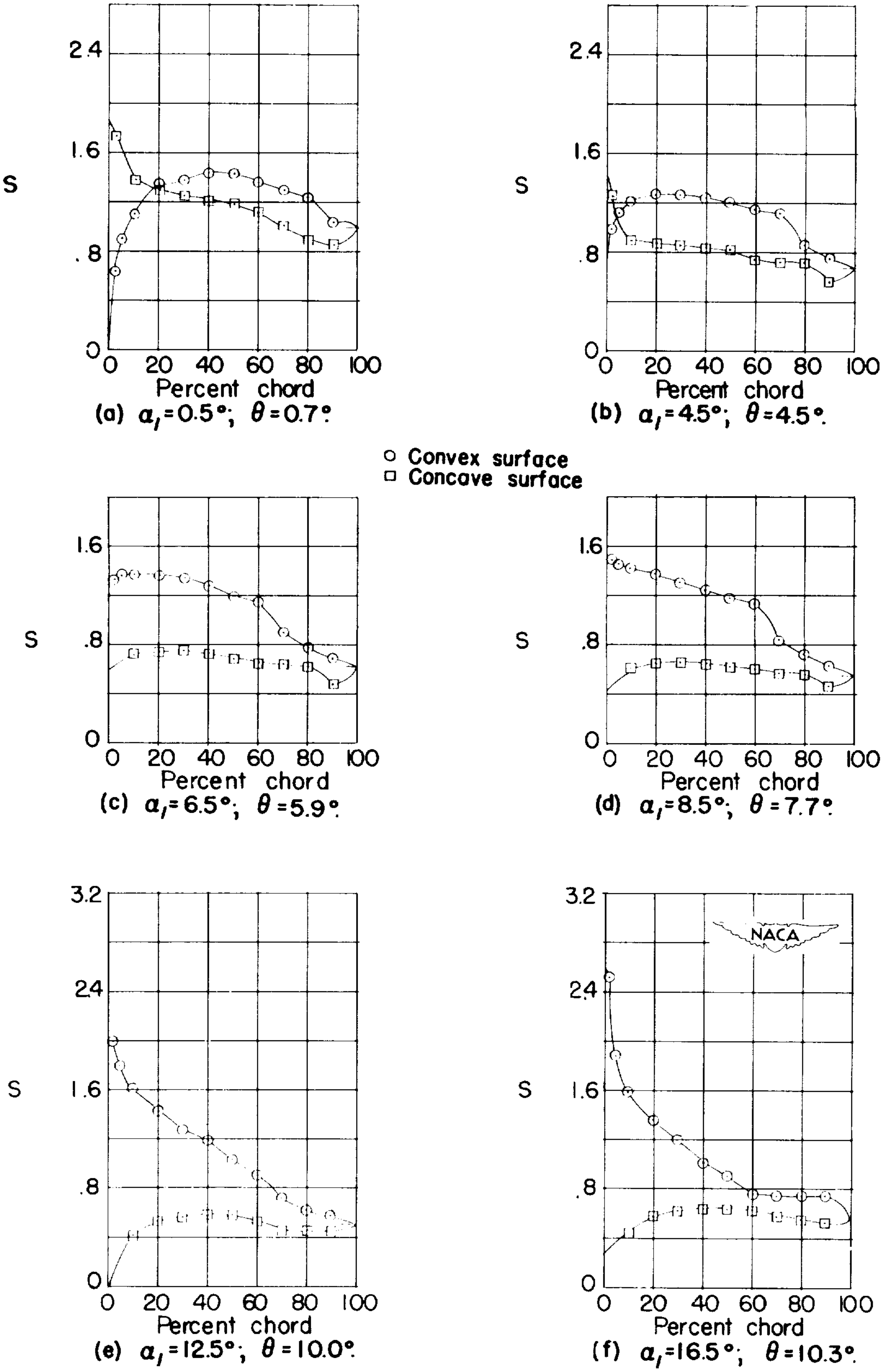

(a) $a_l = 0.5°$; $\theta = 0.7°$

(b) $a_l = 4.5°$; $\theta = 4.5°$

(c) $a_l = 6.5°$; $\theta = 5.9°$

(d) $a_l = 8.5°$; $\theta = 7.7°$

(e) $a_l = 12.5°$; $\theta = 10.0°$

(f) $a_l = 16.5°$; $\theta = 10.3°$

Figure 72.- Blade-surface pressure distributions and blade section characteristics for the cascade combination, $\beta_1 = 70°$, $\sigma = 1.00$, and blade section, NACA 65-410.

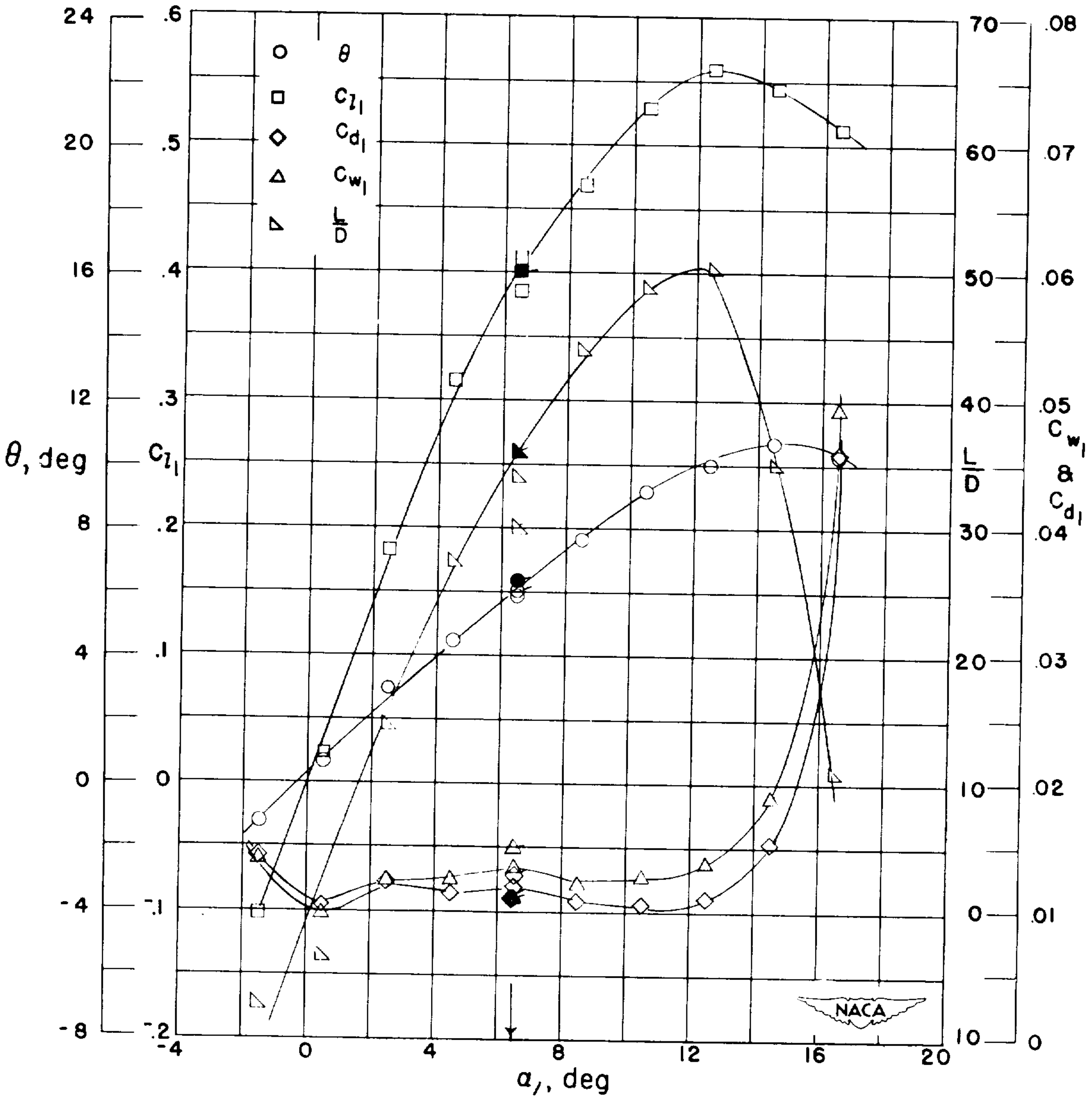

(g) Section characteristics; arrow shows design angle of attack; flagged symbol indicates leading-edge roughness; solid symbol indicates high Reynolds number.

Figure 72.- Concluded.

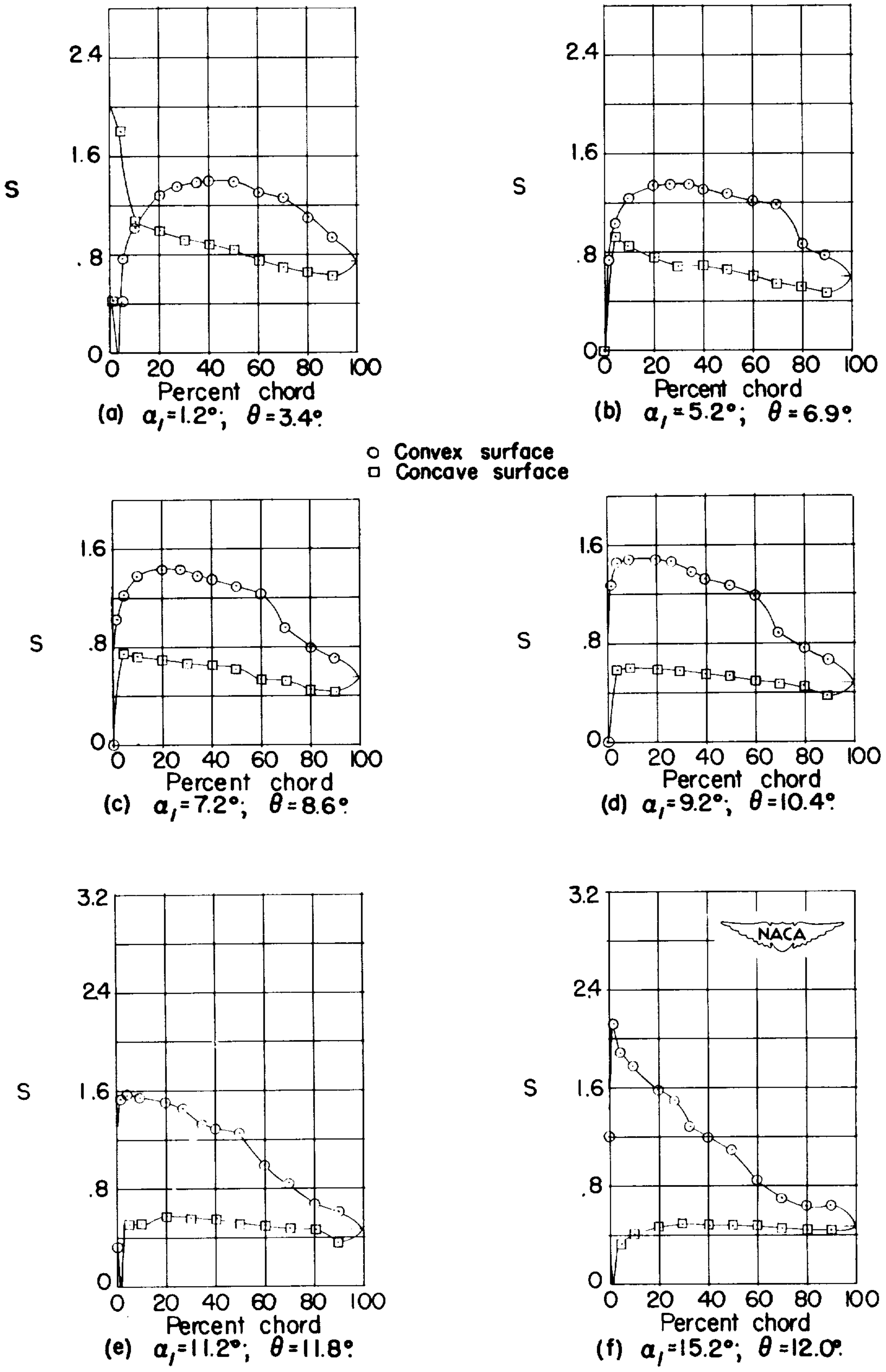

(a) $\alpha_l = 1.2°$; $\theta = 3.4°$

(b) $\alpha_l = 5.2°$; $\theta = 6.9°$

(c) $\alpha_l = 7.2°$; $\theta = 8.6°$

(d) $\alpha_l = 9.2°$; $\theta = 10.4°$

(e) $\alpha_l = 11.2°$; $\theta = 11.8°$

(f) $\alpha_l = 15.2°$; $\theta = 12.0°$

Figure 73.- Blade-surface pressure distributions and blade section characteristics for the cascade combination, $\beta_1 = 70°$, $\sigma = 1.00$, and blade section, NACA 65-810.

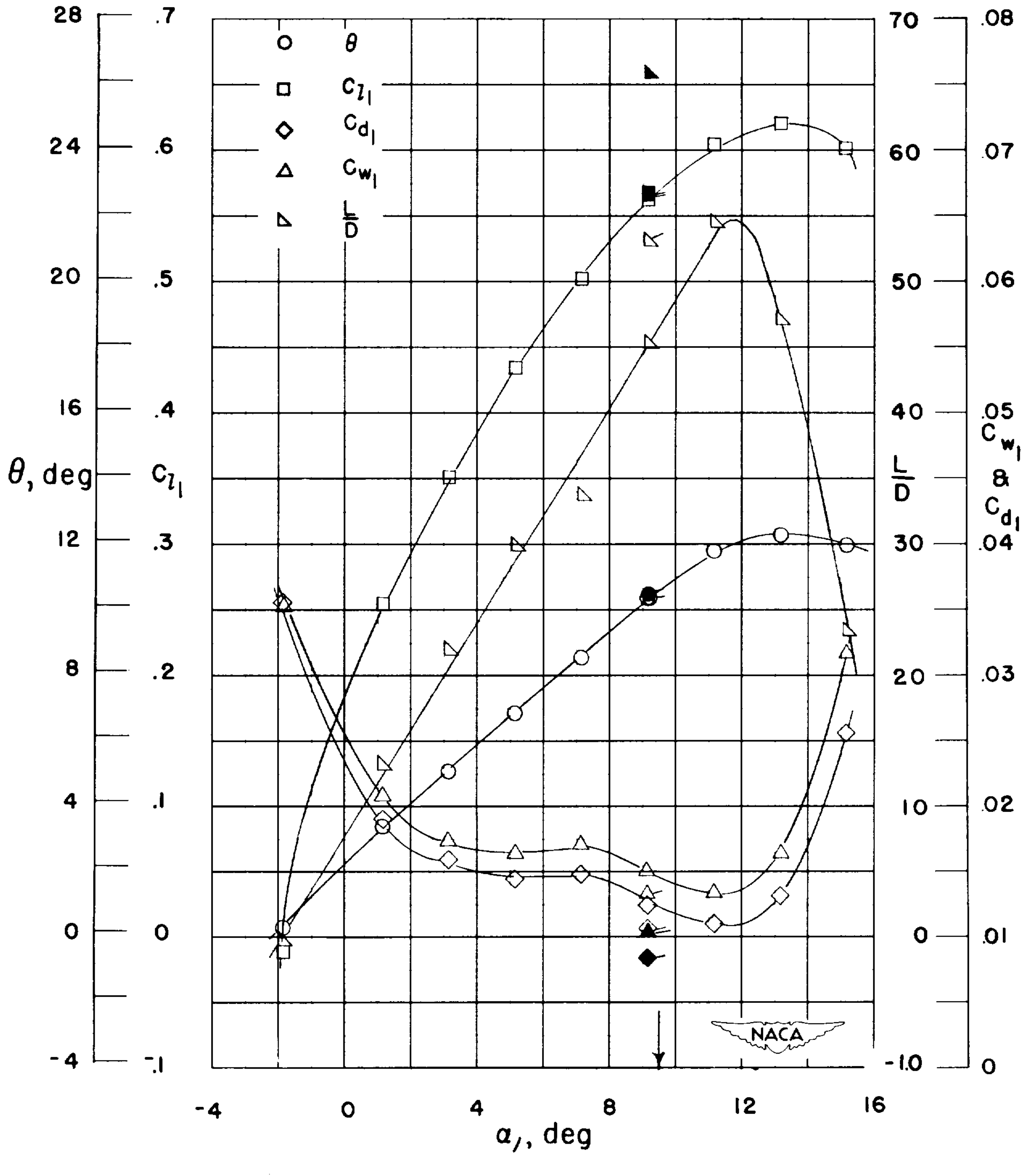

(g) Section characteristics; arrow shows design angle of attack; flagged symbol indicates leading-edge roughness; solid symbol indicates high Reynolds number.

Figure 73.- Concluded.

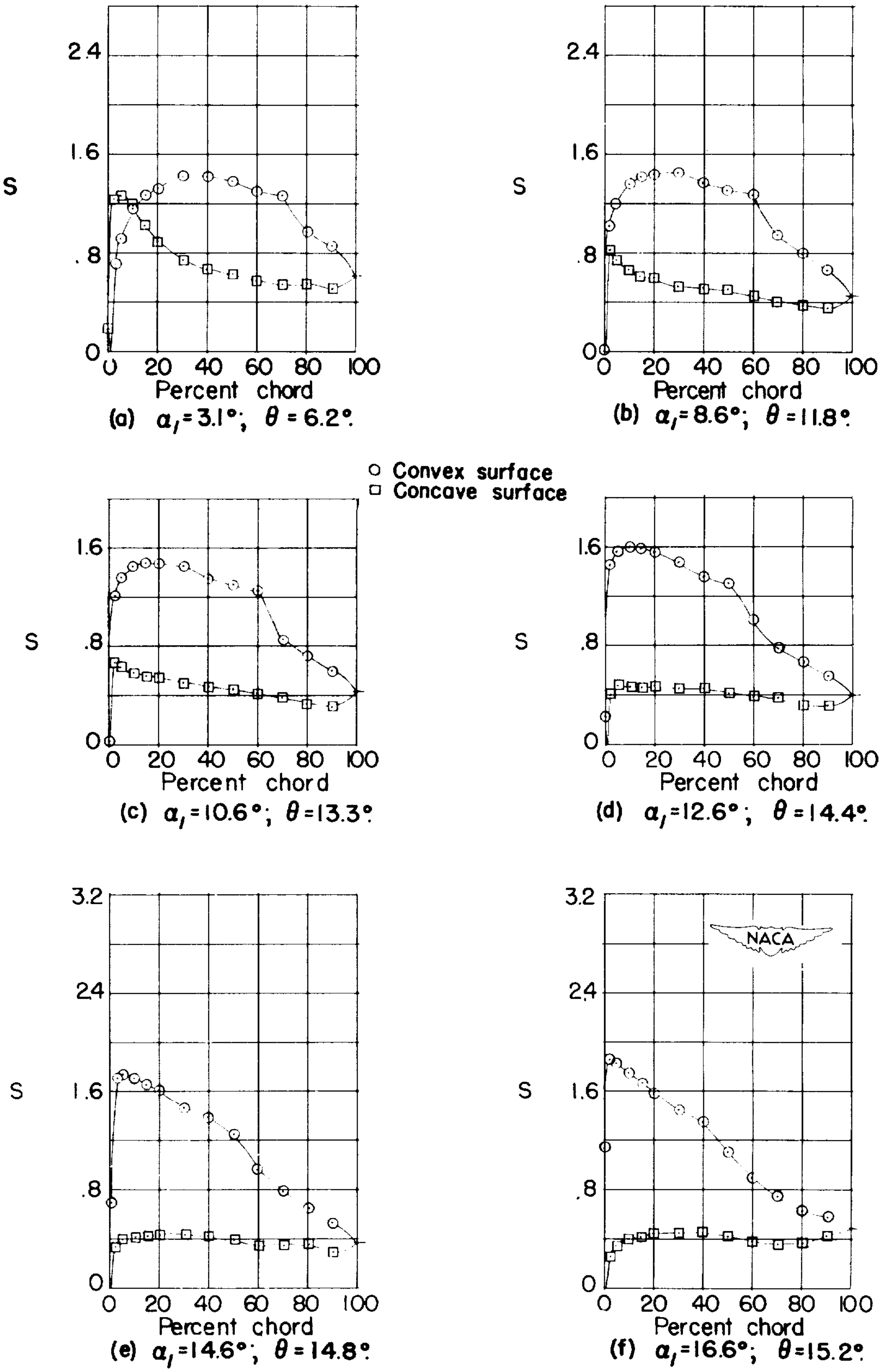

(a) α_l=3.1°; θ=6.2°.

(b) α_l=8.6°; θ=11.8°.

(c) α_l=10.6°; θ=13.3°.

(d) α_l=12.6°; θ=14.4°.

(e) α_l=14.6°; θ=14.8°.

(f) α_l=16.6°; θ=15.2°.

Figure 74.- Blade-surface pressure distributions and blade section characteristics for the cascade combination, β_1 = 70°, σ = 1.00, and blade section, NACA 65-(12)10.

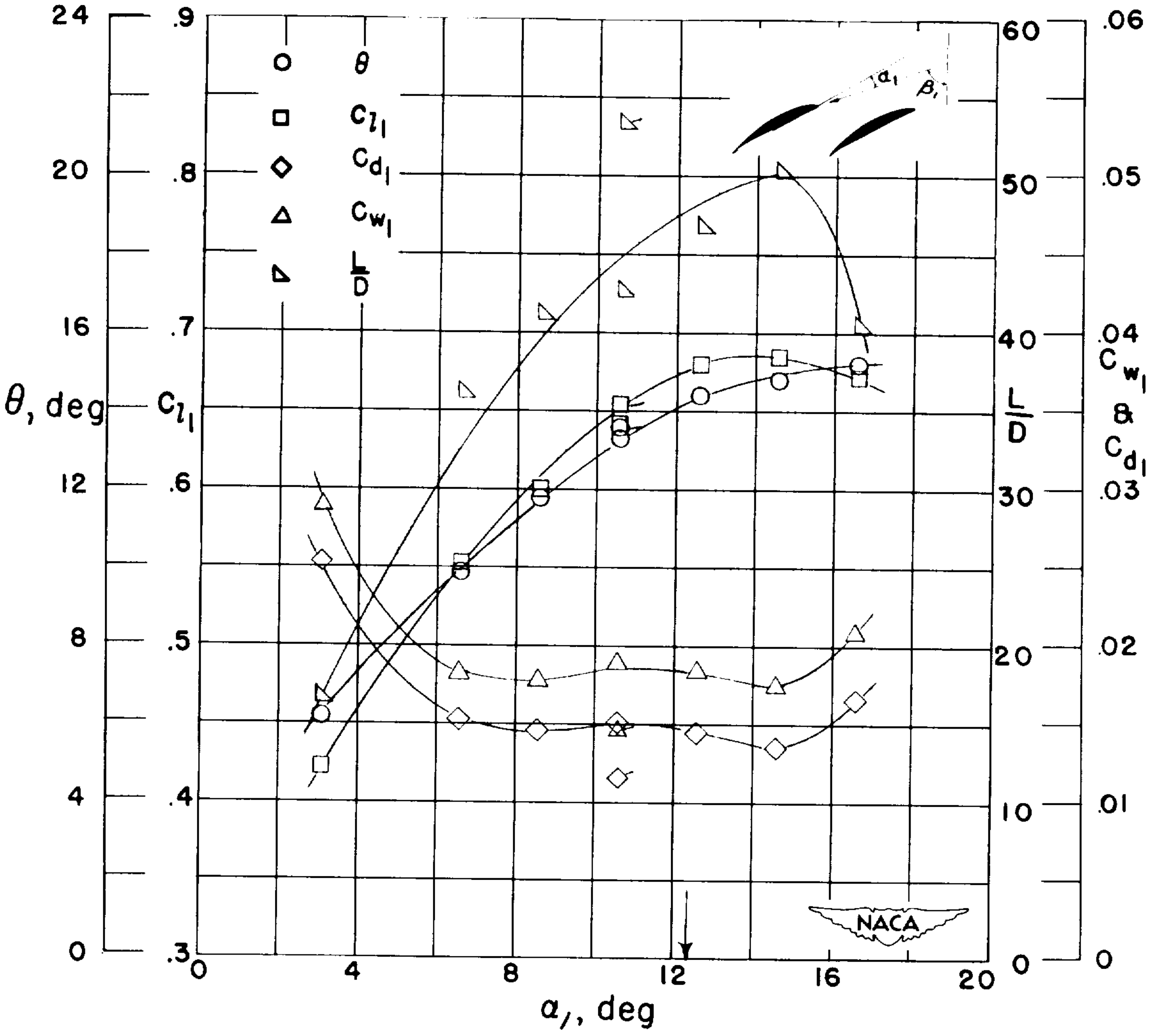

(g) Section characteristics; arrow shows design angle of attack; flagged symbol indicates leading-edge roughness.

Figure 74.- Concluded.

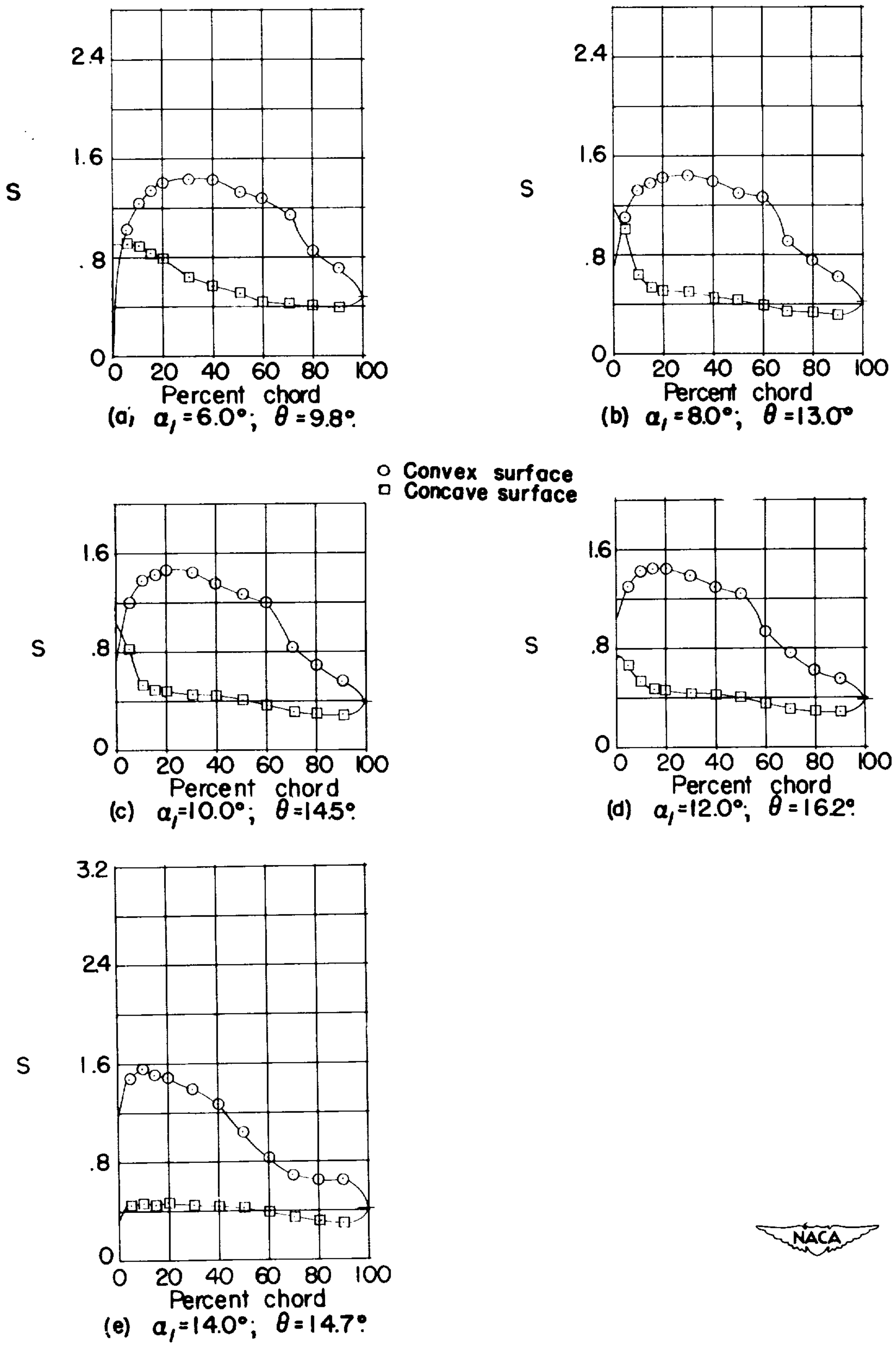

(a) $\alpha_1 = 6.0°$; $\theta = 9.8°$.

(b) $\alpha_1 = 8.0°$; $\theta = 13.0°$

(c) $\alpha_1 = 10.0°$; $\theta = 14.5°$.

(d) $\alpha_1 = 12.0°$; $\theta = 16.2°$

(e) $\alpha_1 = 14.0°$; $\theta = 14.7°$

Figure 75.- Blade-surface pressure distributions and blade section characteristics for the cascade combination, $\beta_1 = 70°$, $\sigma = 1.00$, and blade section, NACA 65-(15)10.

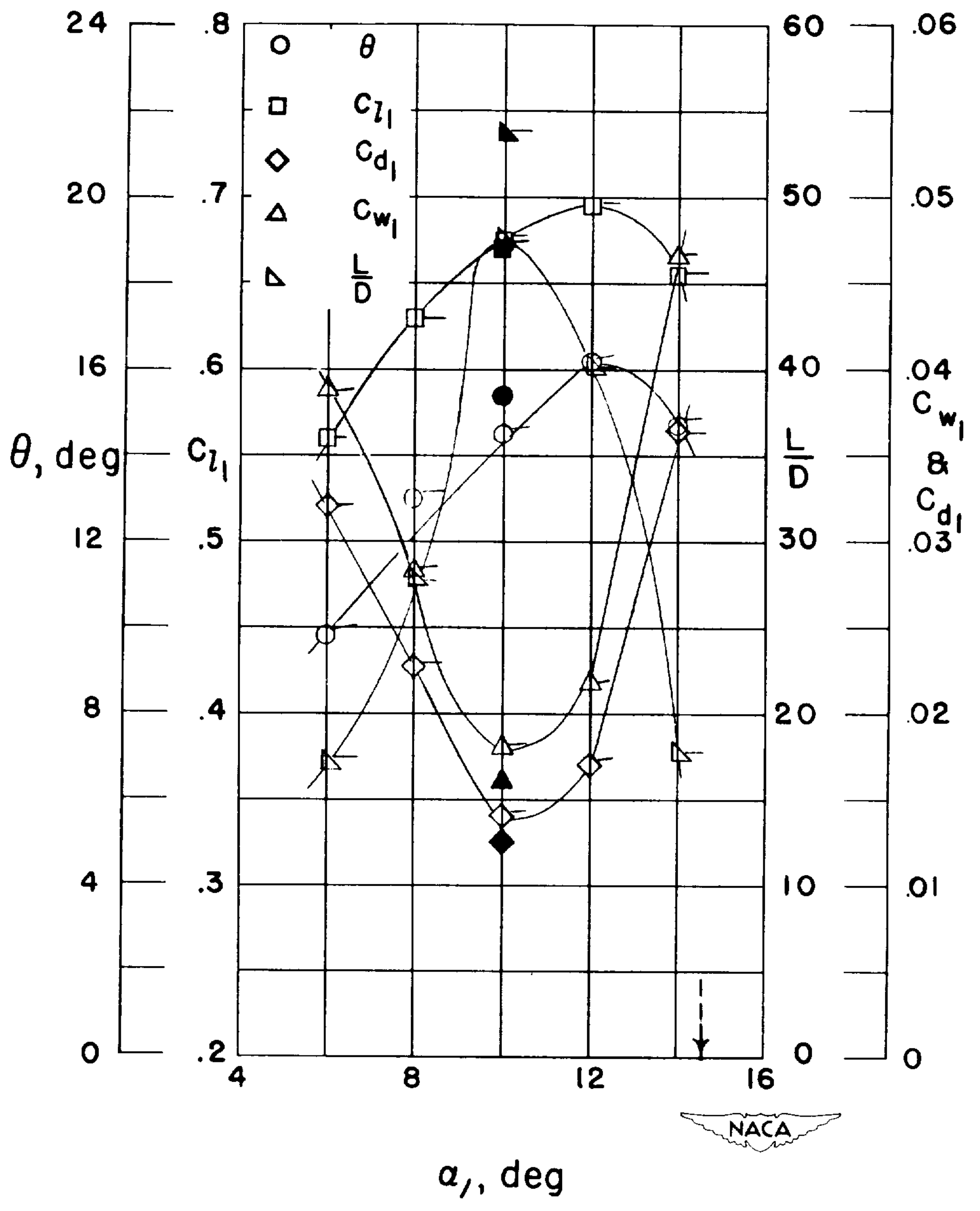

(f) Section characteristics; no design point was obtained; flagged symbol indicates leading-edge roughness; solid symbol indicates high Reynolds number.

Figure 75.- Concluded.

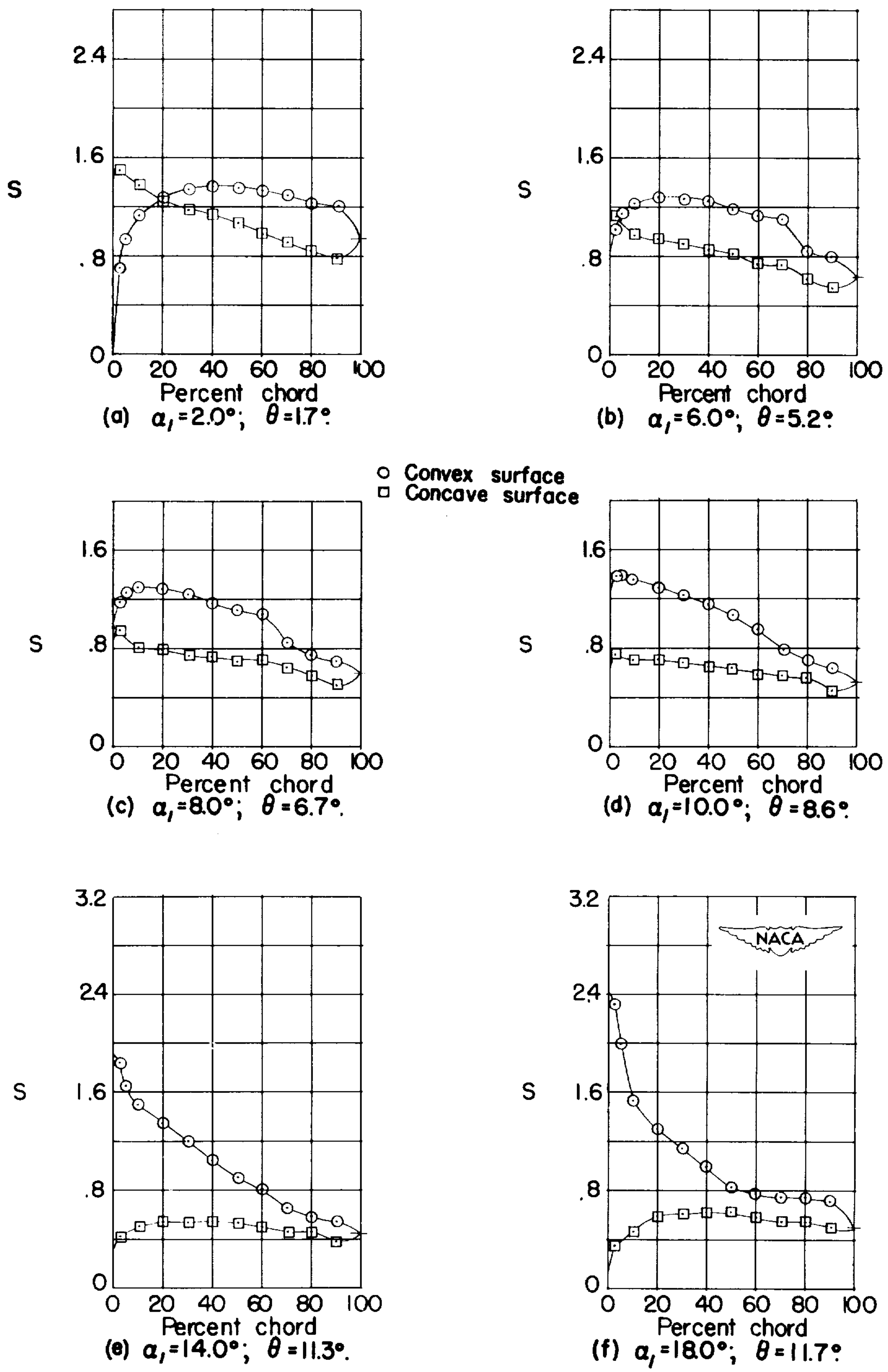

(a) $\alpha_1 = 2.0°$; $\theta = 1.7°$.

(b) $\alpha_1 = 6.0°$; $\theta = 5.2°$.

(c) $\alpha_1 = 8.0°$; $\theta = 6.7°$.

(d) $\alpha_1 = 10.0°$; $\theta = 8.6°$.

(e) $\alpha_1 = 14.0°$; $\theta = 11.3°$.

(f) $\alpha_1 = 18.0°$; $\theta = 11.7°$.

Figure 76.- Blade-surface pressure distributions and blade section characteristics for the cascade combination, $\beta_1 = 70^{\circ}$, $\sigma = 1.25$, and blade section, NACA 65-410.

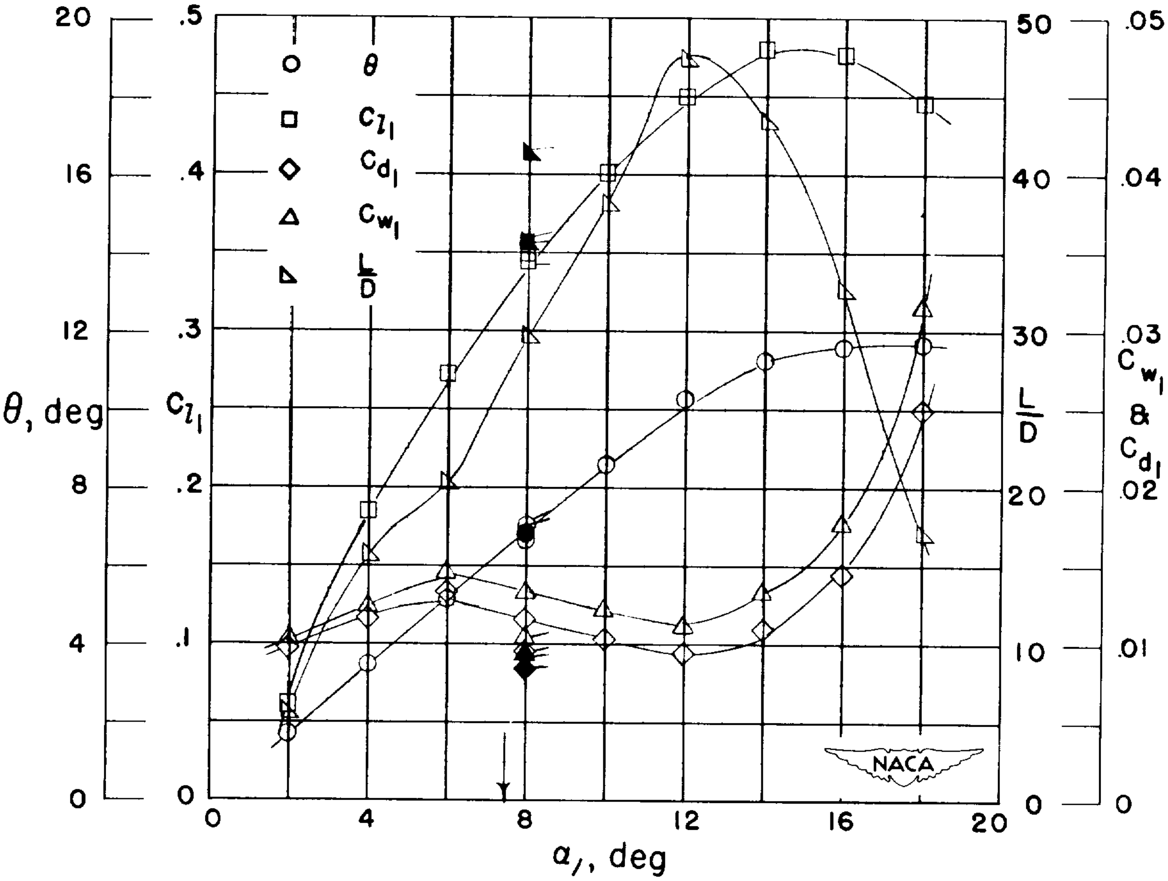

(g) Section characteristics; arrow shows design angle of attack; flagged symbol indicates leading-edge roughness; solid symbol indicates high Reynolds number.

Figure 76.- Concluded.

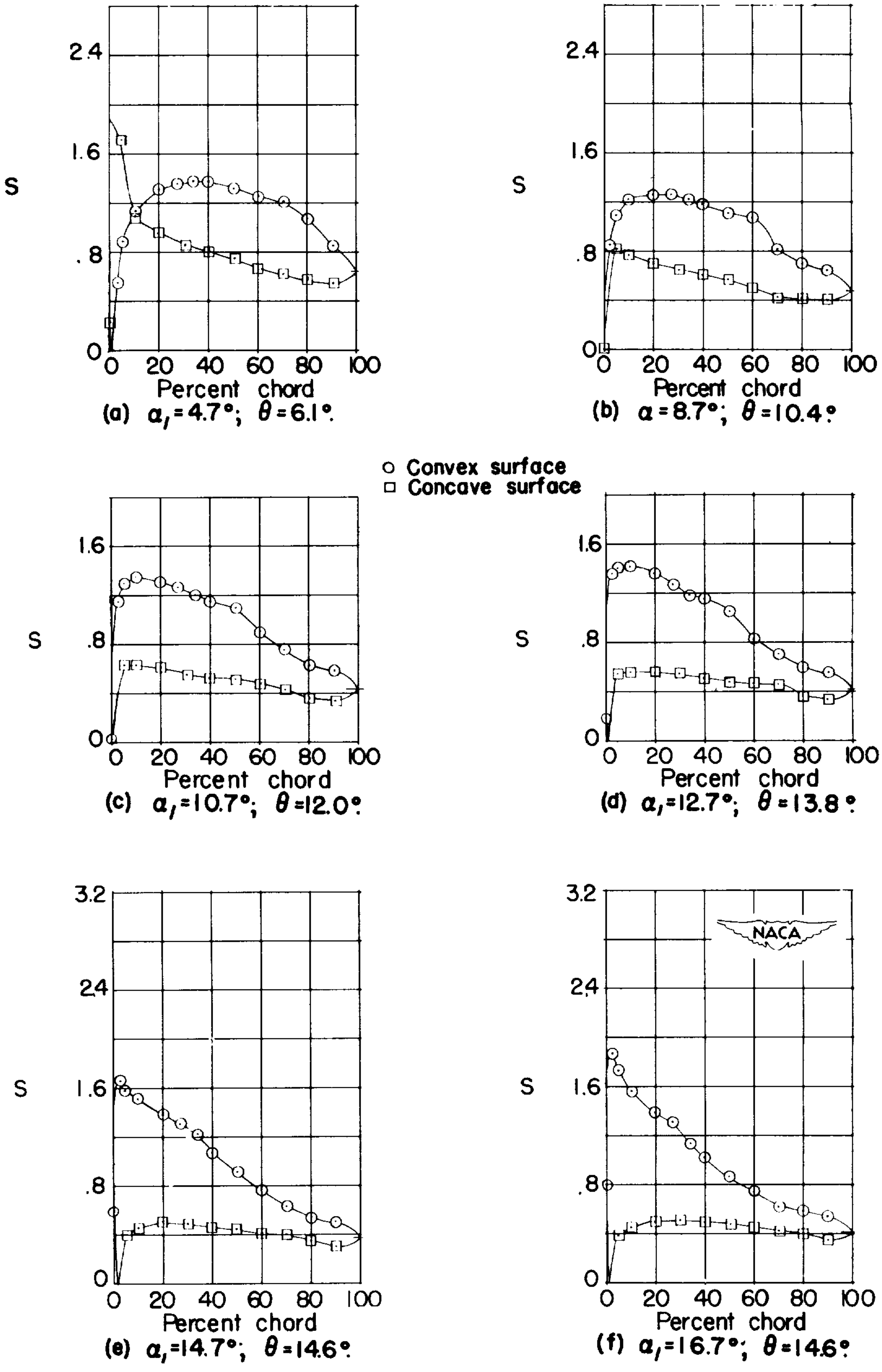

(a) $\alpha_1 = 4.7°$; $\theta = 6.1°$.

(b) $\alpha = 8.7°$; $\theta = 10.4°$

(c) $\alpha_1 = 10.7°$; $\theta = 12.0°$

(d) $\alpha_1 = 12.7°$; $\theta = 13.8°$

(e) $\alpha_1 = 14.7°$; $\theta = 14.6°$

(f) $\alpha_1 = 16.7°$; $\theta = 14.6°$

Figure 77.- Blade-surface pressure distributions and blade section characteristics for the cascade combination, $\beta_1 = 70°$, $\sigma = 1.25$, and blade section, NACA 65-810.

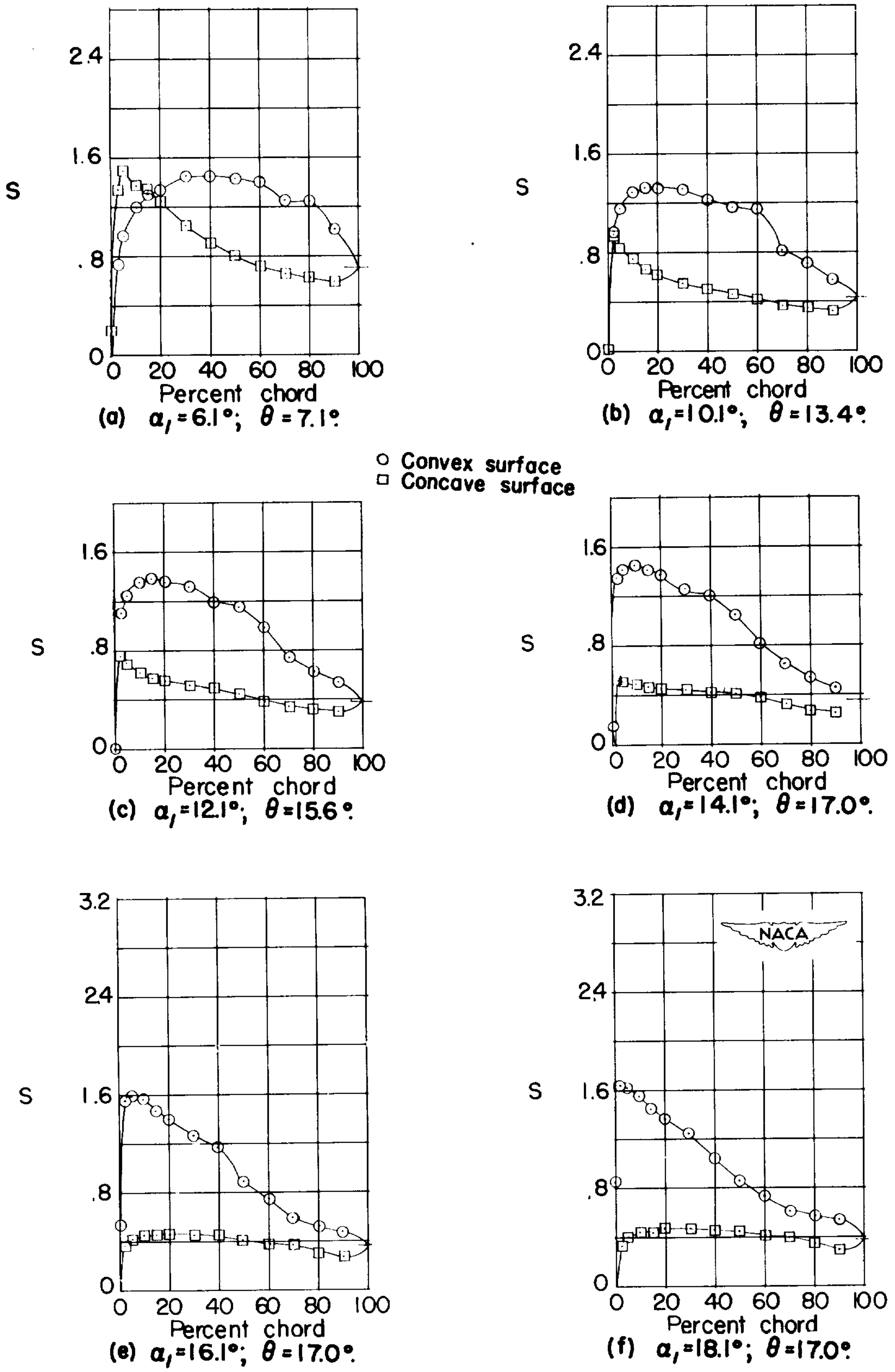

(a) $\alpha_1 = 6.1°$; $\theta = 7.1°$.

(b) $\alpha_1 = 10.1°$; $\theta = 13.4°$.

(c) $\alpha_1 = 12.1°$; $\theta = 15.6°$.

(d) $\alpha_1 = 14.1°$; $\theta = 17.0°$.

(e) $\alpha_1 = 16.1°$; $\theta = 17.0°$.

(f) $\alpha_1 = 18.1°$; $\theta = 17.0°$.

Figure 78.- Blade-surface pressure distributions and blade section characteristics for the cascade combination, $\beta_1 = 70^{\circ}$, $\sigma = 1.25$, and blade section, NACA 65-(12)10.

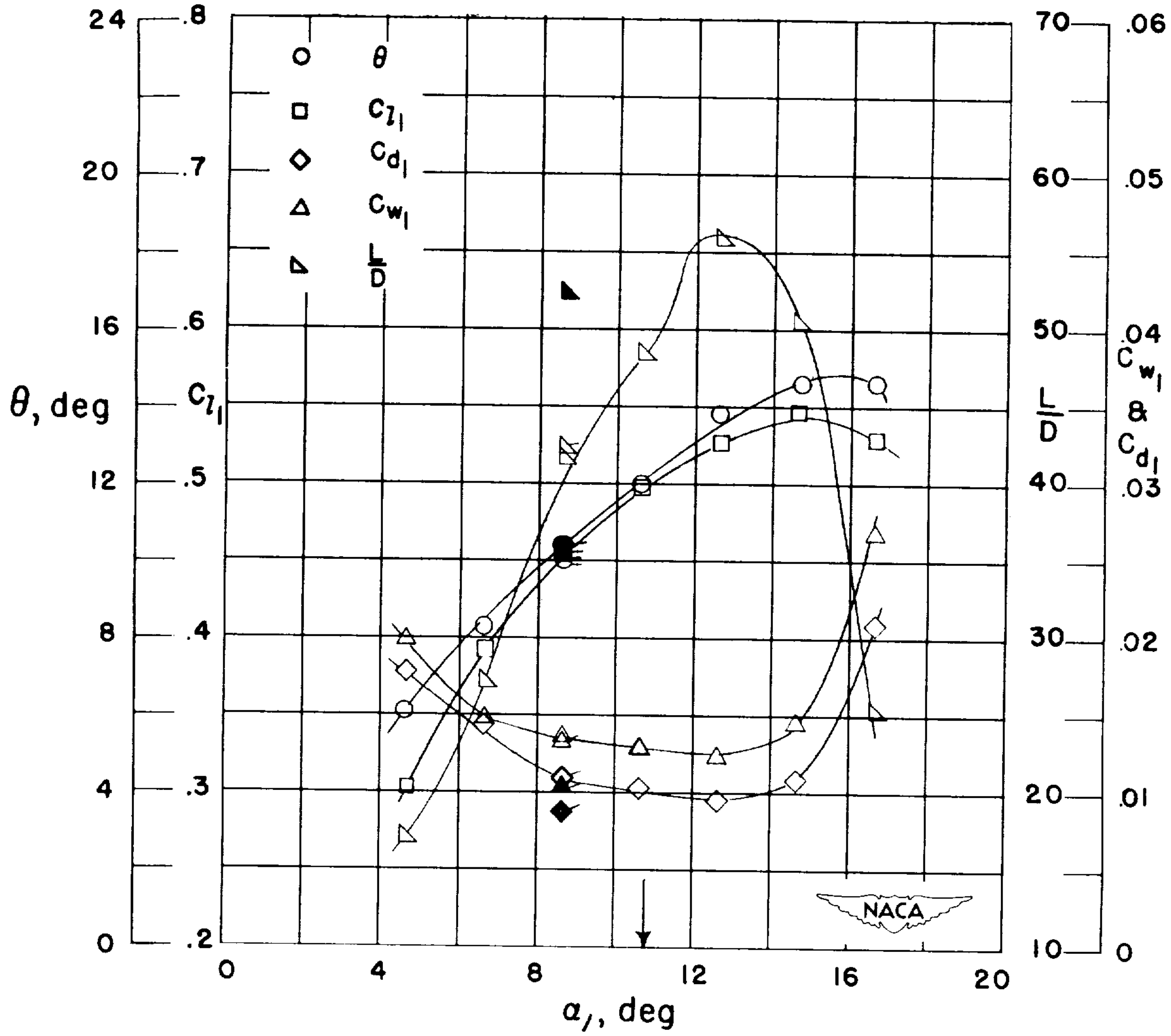

(g) Section characteristics; arrow shows design angle of attack; flagged symbol indicates leading-edge roughness; solid symbol indicates high Reynolds number.

Figure 77.- Concluded.

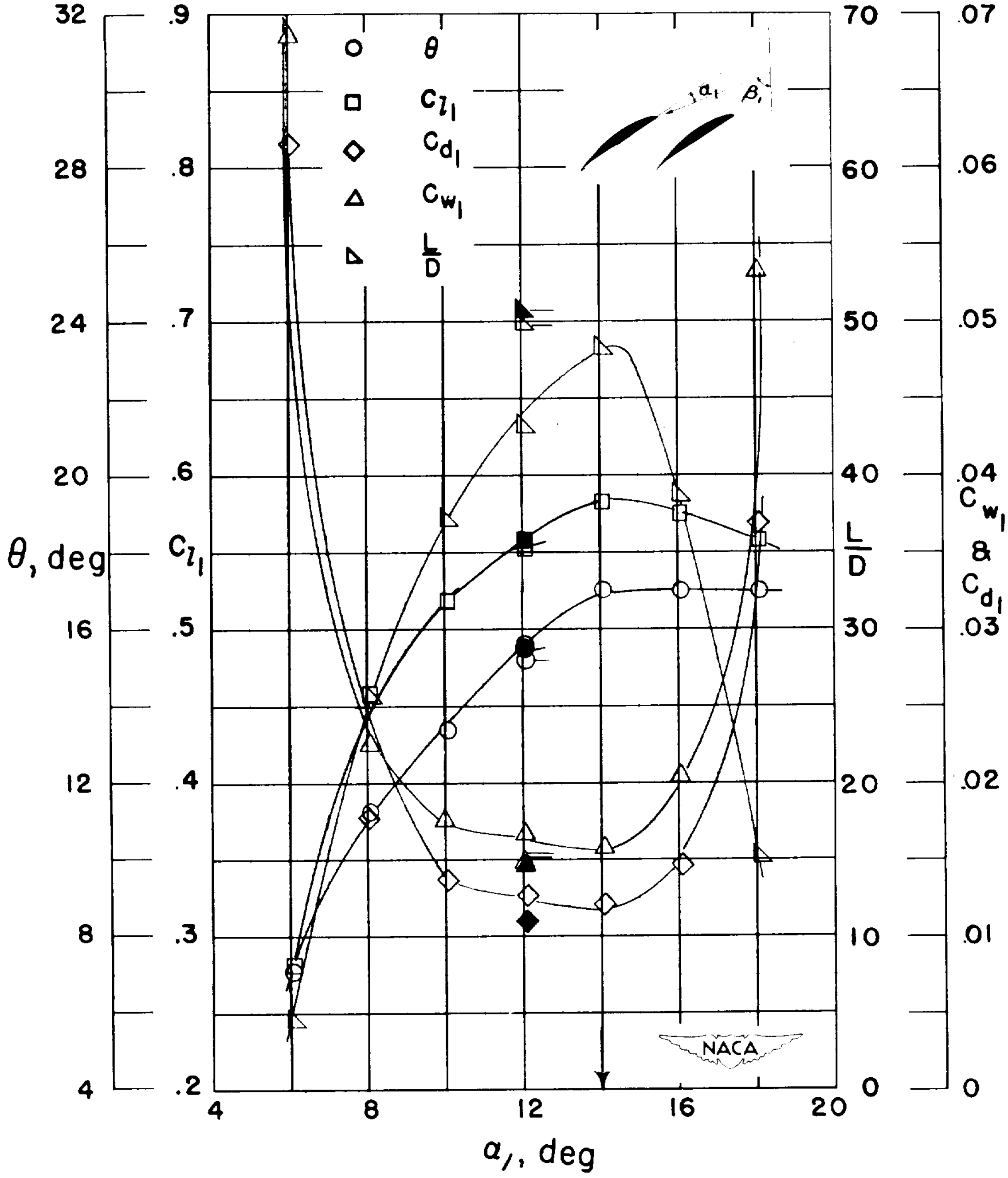

(g) Section characteristics; arrow shows design angle of attack; flagged symbol indicates leading-edge roughness; solid symbol indicates high Reynolds number.

Figure 78.- Concluded.

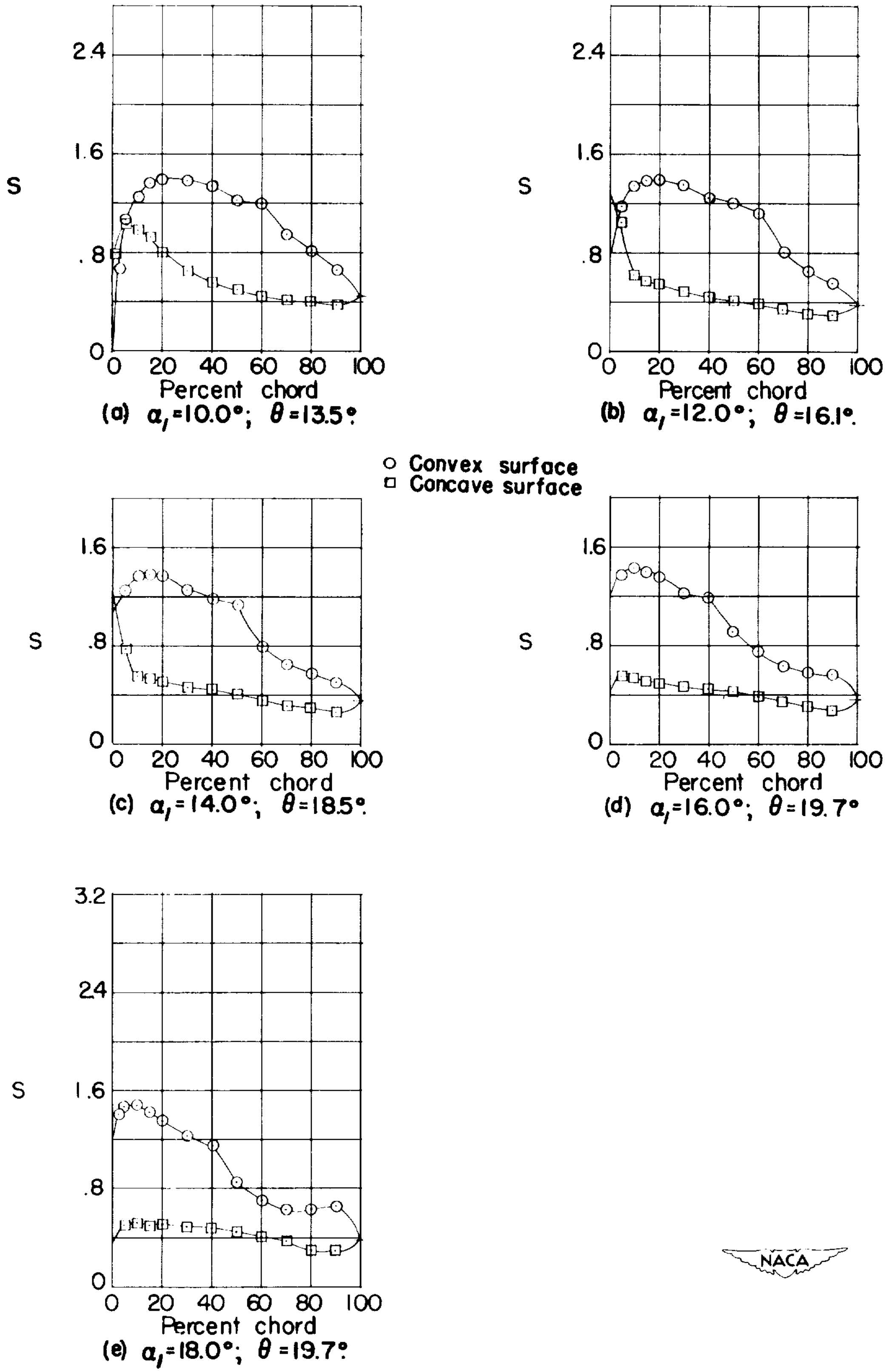

(a) $\alpha_1 = 10.0°$; $\theta = 13.5°$

(b) $\alpha_1 = 12.0°$; $\theta = 16.1°$

(c) $\alpha_1 = 14.0°$; $\theta = 18.5°$

(d) $\alpha_1 = 16.0°$; $\theta = 19.7°$

(e) $\alpha_1 = 18.0°$; $\theta = 19.7°$

Figure 79.- Blade-surface pressure distributions and blade section characteristics for the cascade combination, $\beta_1 = 70°$, $\sigma = 1.25$, and blade section, NACA 65-(15)10.

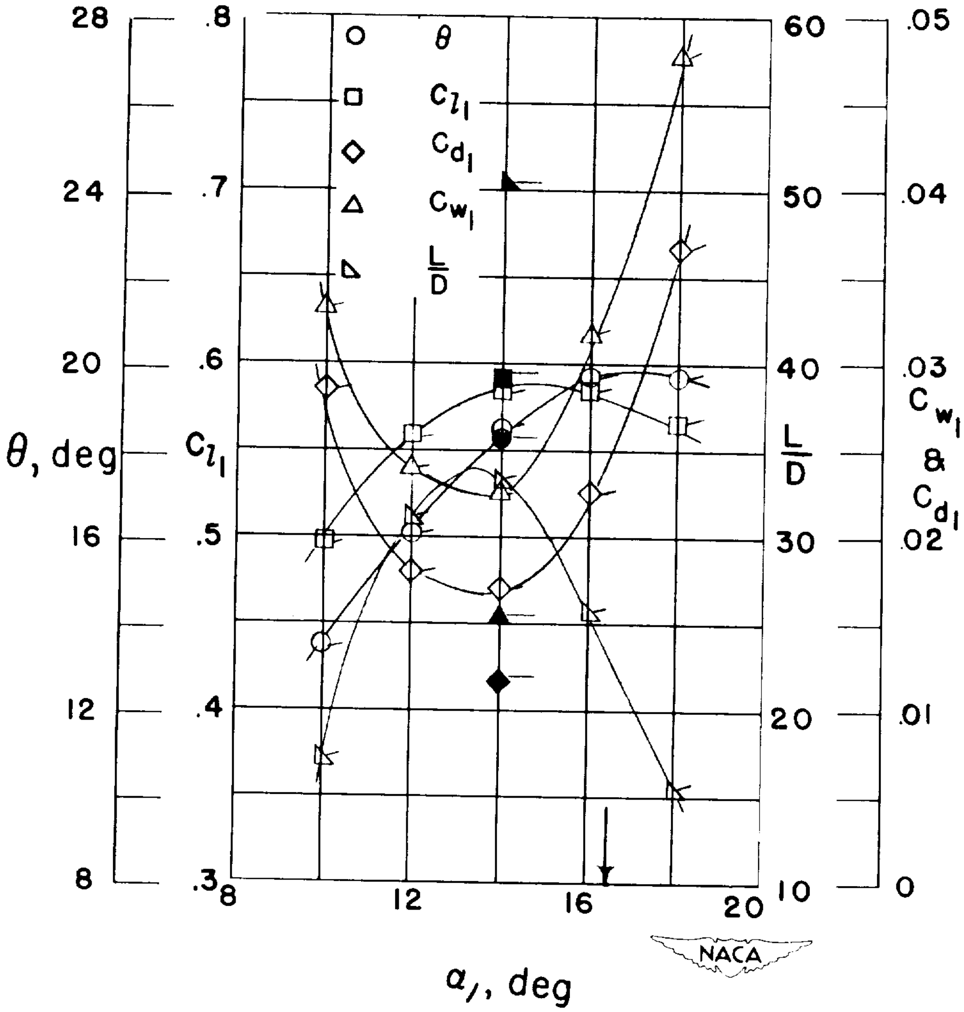

(f) Section characteristics; arrow shows design angle of attack; flagged symbol indicates leading-edge roughness; solid symbol indicates high Reynolds number.

Figure 79.- Concluded.

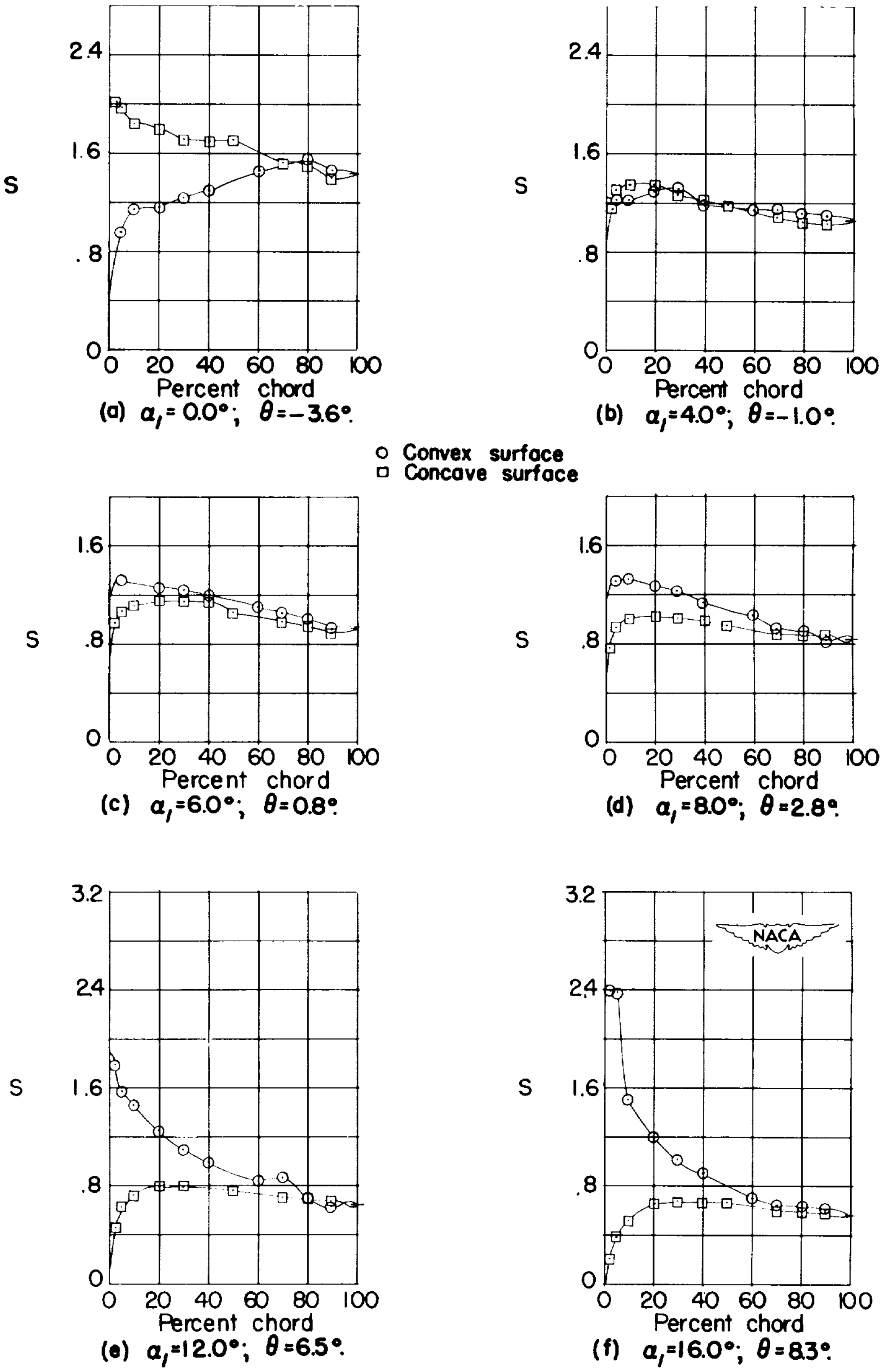

(a) $\alpha_l = 0.0°$; $\theta = -3.6°$.

(b) $\alpha_l = 4.0°$; $\theta = -1.0°$.

(c) $\alpha_l = 6.0°$; $\theta = 0.8°$.

(d) $\alpha_l = 8.0°$; $\theta = 2.8°$.

(e) $\alpha_l = 12.0°$; $\theta = 6.5°$.

(f) $\alpha_l = 16.0°$; $\theta = 8.3°$.

Figure 80.- Blade-surface pressure distributions and blade section characteristics for the cascade combination, $\beta_1 = 70°$, $\sigma = 1.50$, and blade section, NACA 65-010.

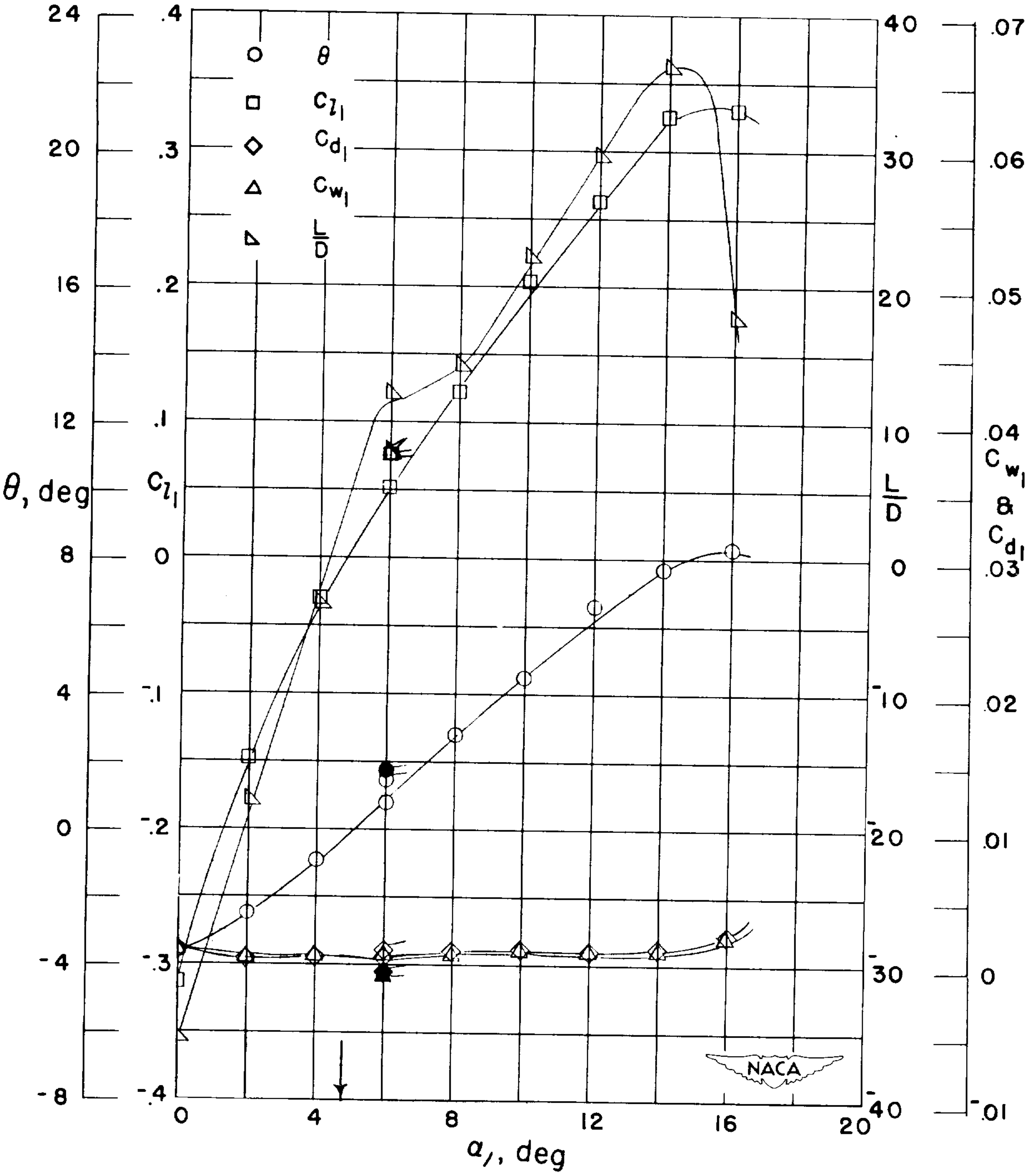

(g) Section characteristics; arrow shows design angle of attack; flagged symbol indicates leading-edge roughness; solid symbol indicates high Reynolds number.

Figure 80.- Concluded.

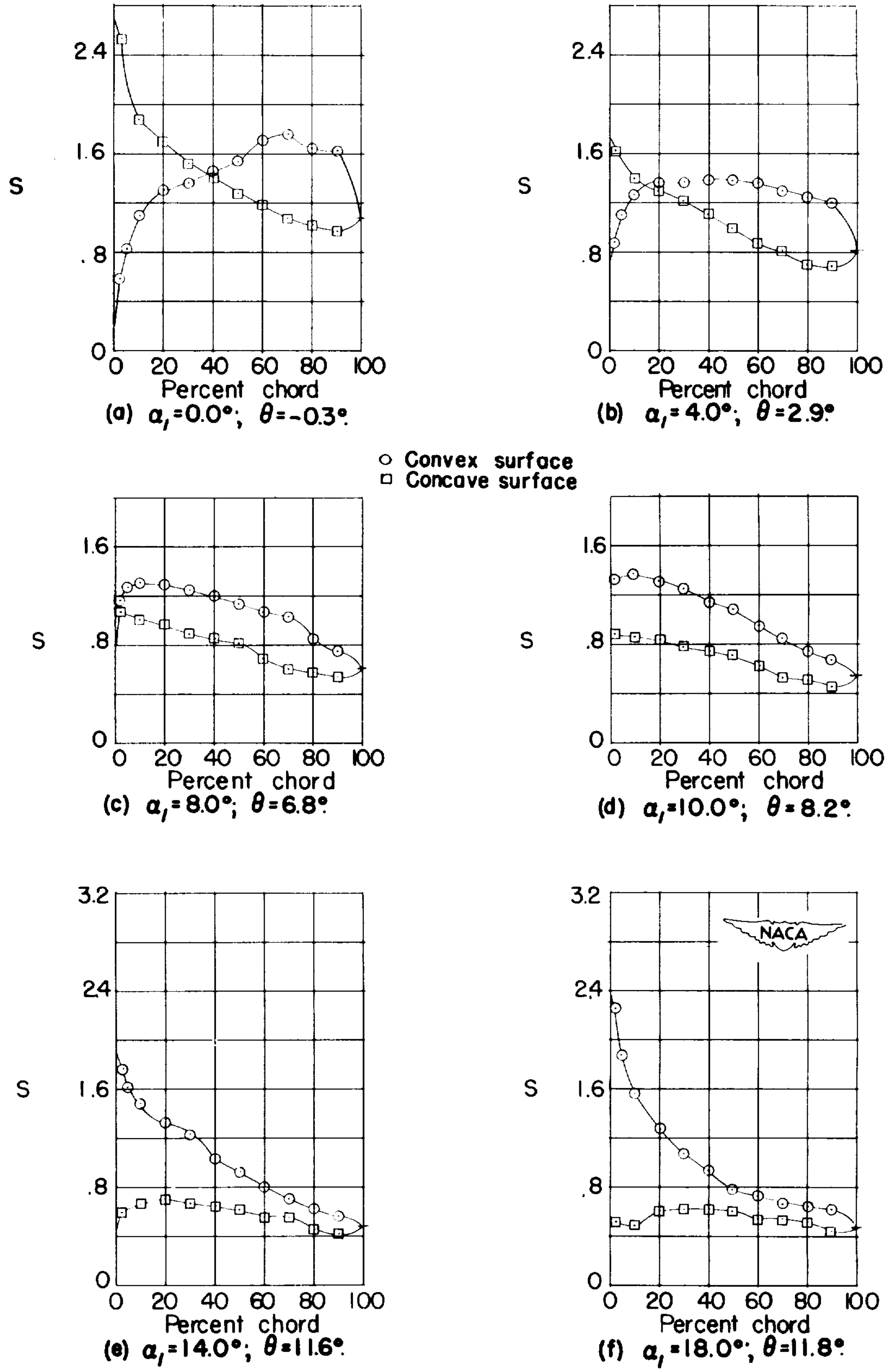

(a) $\alpha_l = 0.0°$; $\theta = -0.3°$.

(b) $\alpha_l = 4.0°$; $\theta = 2.9°$

(c) $\alpha_l = 8.0°$; $\theta = 6.8°$

(d) $\alpha_l = 10.0°$; $\theta = 8.2°$.

(e) $\alpha_l = 14.0°$; $\theta = 11.6°$.

(f) $\alpha_l = 18.0°$; $\theta = 11.8°$

Figure 81.- Blade-surface pressure distributions and blade section characteristics for the cascade combination, $\beta_1 = 70°$, $\sigma = 1.50$, and blade section, NACA 65-410.

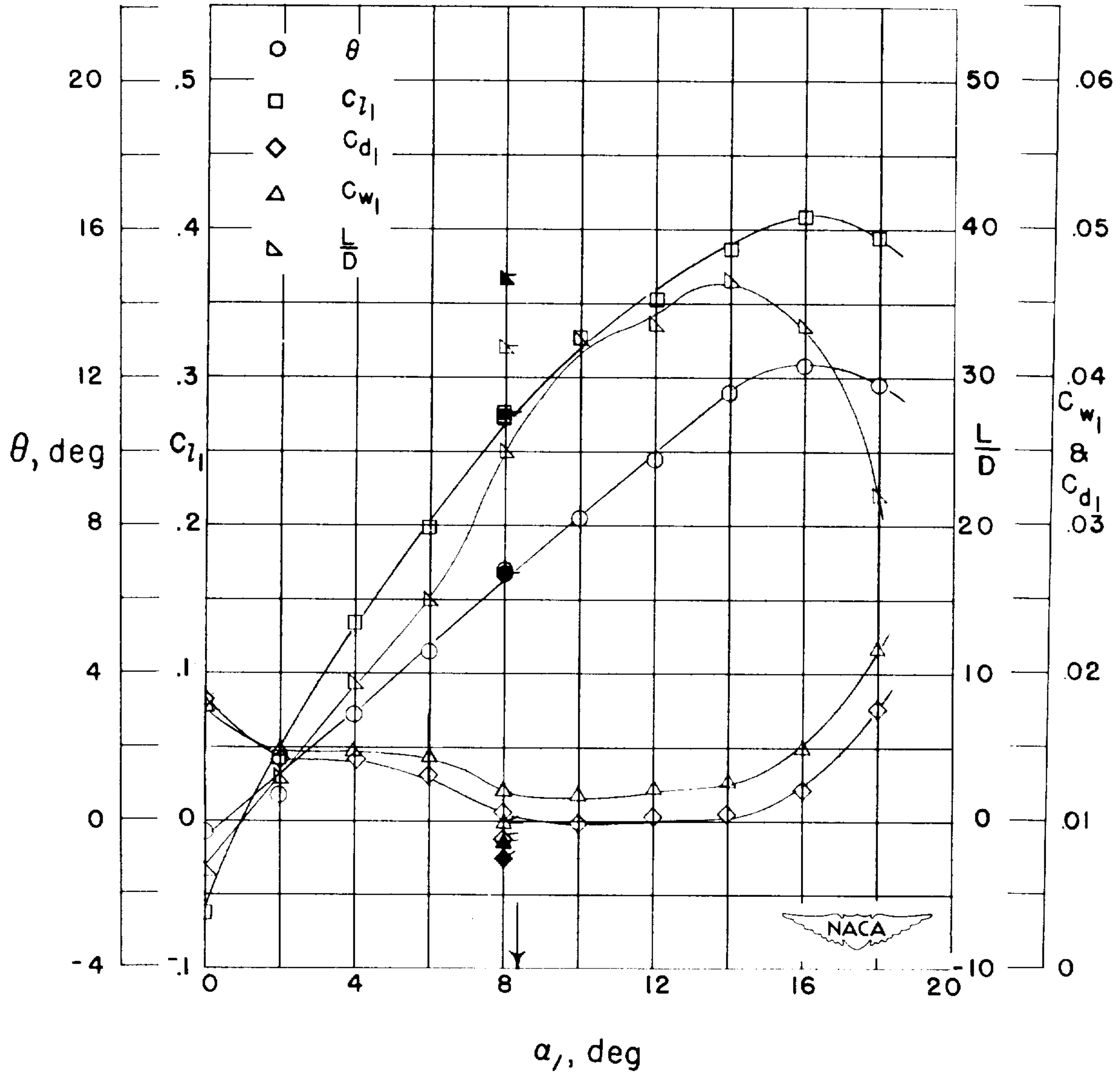

(g) Section characteristics; arrow shows design angle of attack; flagged symbol indicates leading-edge roughness; solid symbol indicates high Reynolds number.

Figure 81.- Concluded.

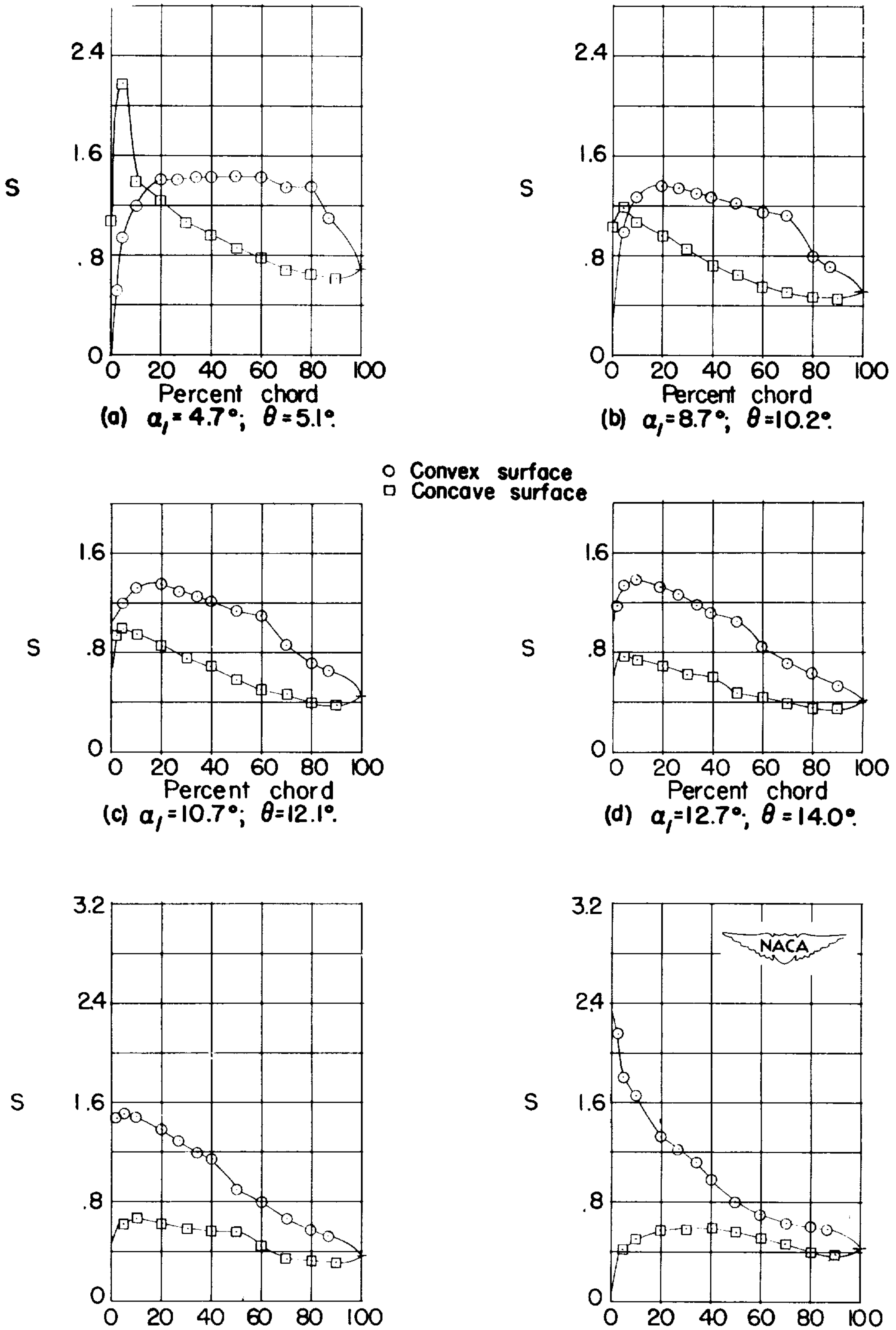

(a) $\alpha_l = 4.7^\circ$; $\theta = 5.1^\circ$.

(b) $\alpha_l = 8.7^\circ$; $\theta = 10.2^\circ$.

(c) $\alpha_l = 10.7^\circ$; $\theta = 12.1^\circ$.

(d) $\alpha_l = 12.7^\circ$; $\theta = 14.0^\circ$.

(e) $\alpha_l = 14.7^\circ$; $\theta = 15.7^\circ$

(f) $\alpha_l = 18.7^\circ$; $\theta = 17.4^\circ$.

Figure 82.- Blade-surface pressure distributions and blade section characteristics for the cascade combination, $\beta_1 = 70^\circ$, $\sigma = 1.50$, and blade section, NACA 65-810.

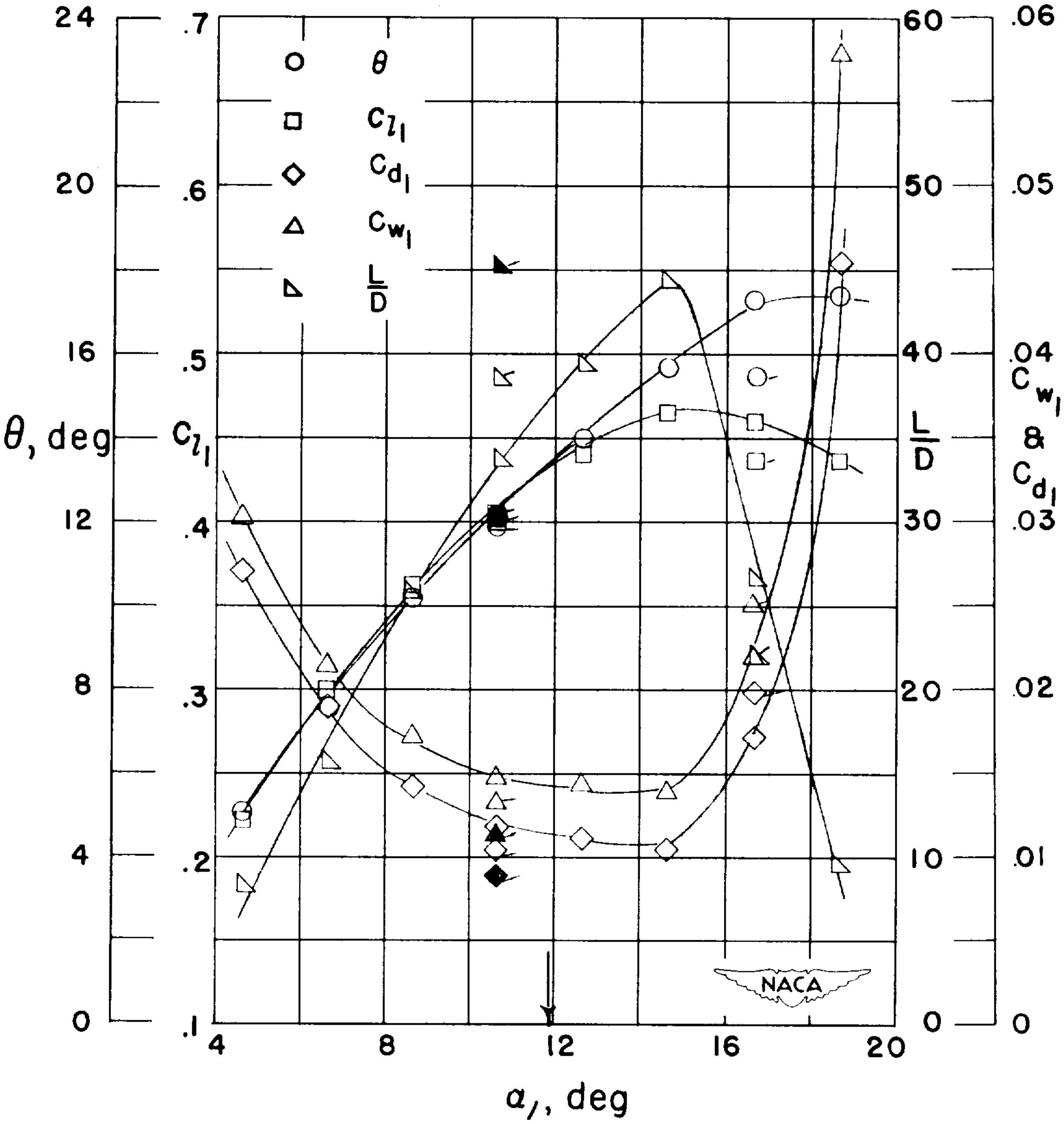

(g) Section characteristics; arrow shows design angle of attack; flagged symbol indicates leading-edge roughness; solid symbol indicates high Reynolds number.

Figure 82.- Concluded.

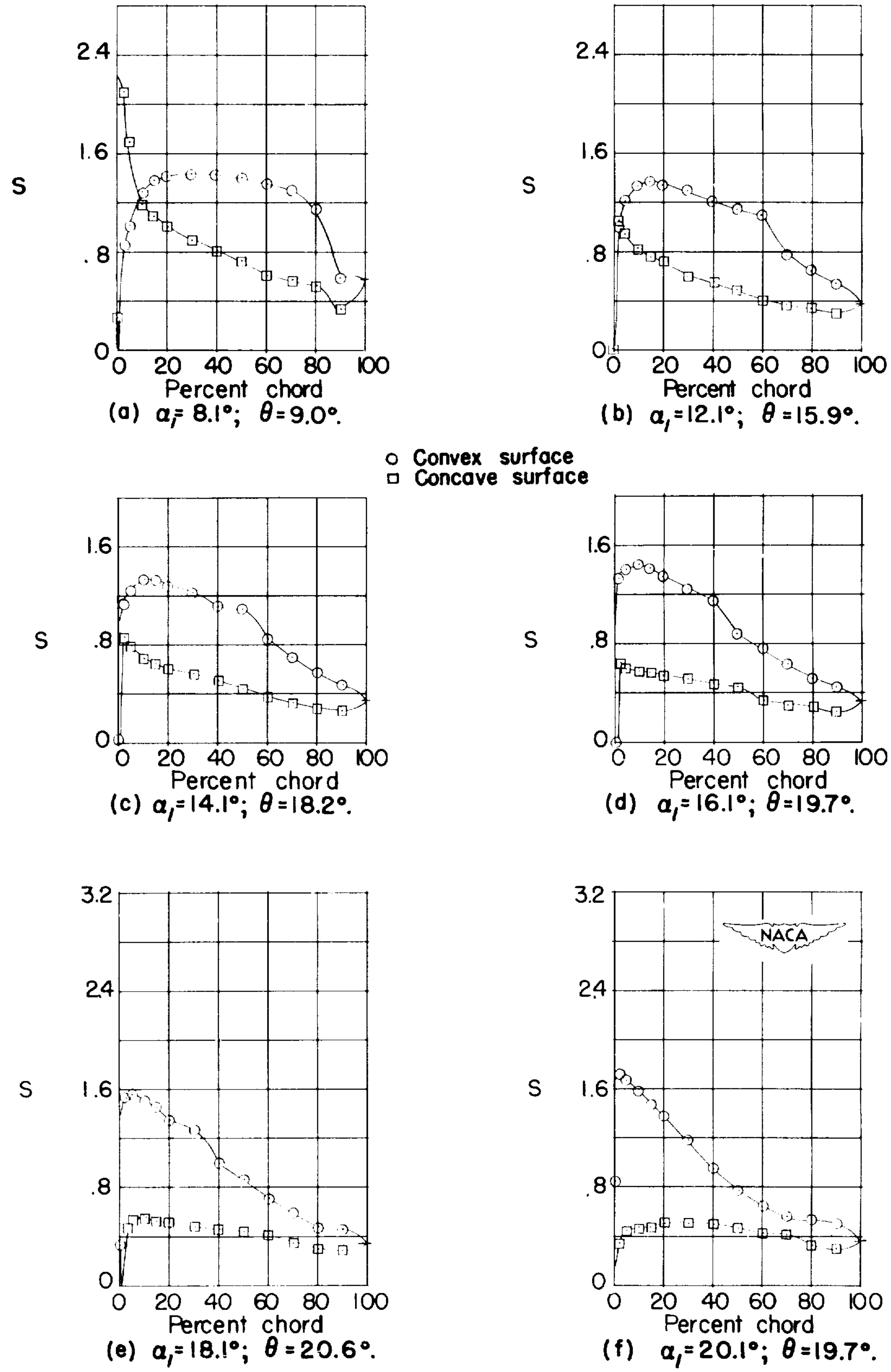

(a) $\alpha_l = 8.1°$; $\theta = 9.0°$.

(b) $\alpha_l = 12.1°$; $\theta = 15.9°$.

(c) $\alpha_l = 14.1°$; $\theta = 18.2°$.

(d) $\alpha_l = 16.1°$; $\theta = 19.7°$.

(e) $\alpha_l = 18.1°$; $\theta = 20.6°$.

(f) $\alpha_l = 20.1°$; $\theta = 19.7°$.

Figure 83.- Blade-surface pressure distributions and blade section characteristics for the cascade combination, $\beta_1 = 70^{\circ}$, $\sigma = 1.50$, and blade section, NACA 65-(12)10.

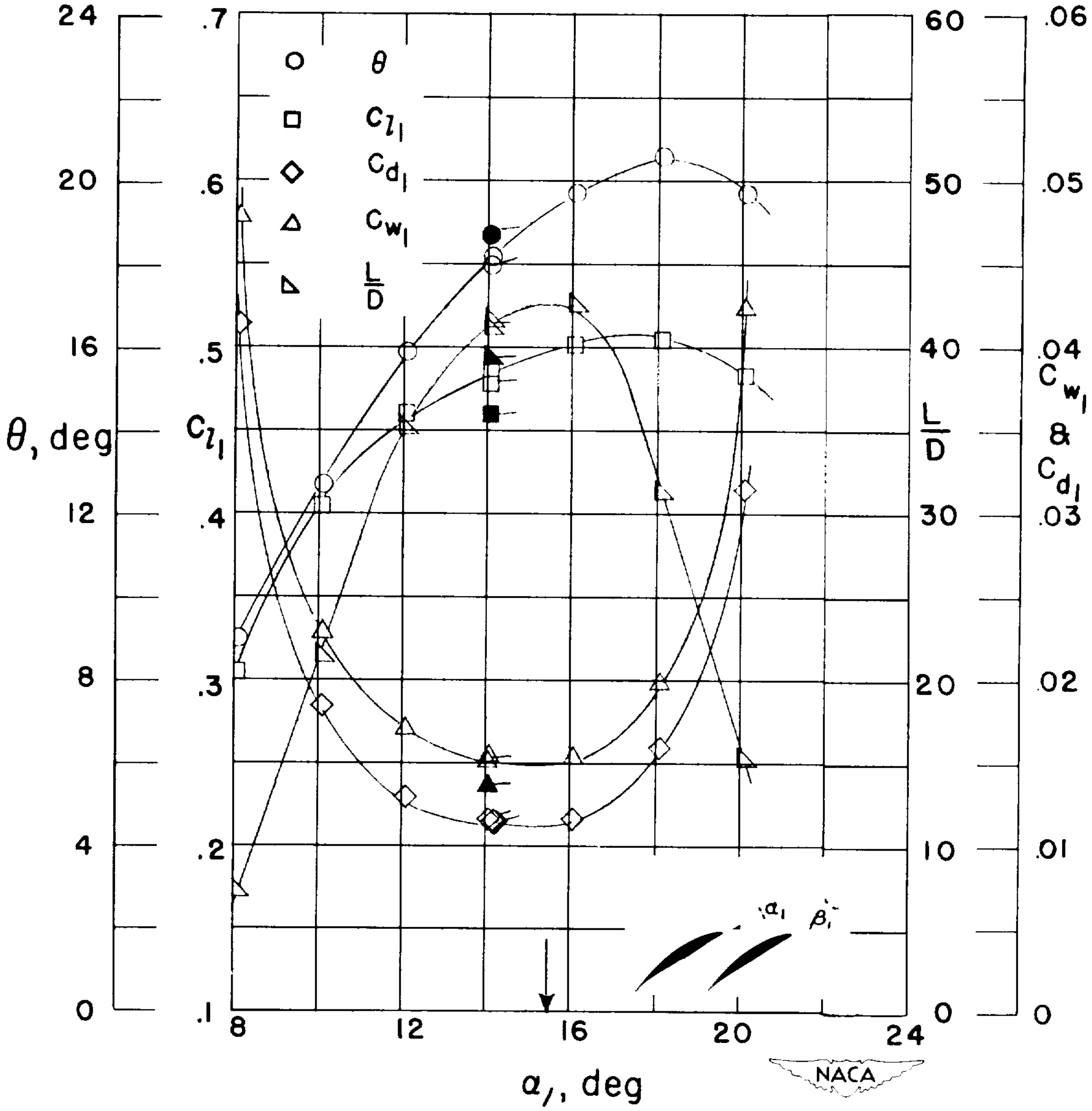

(g) Section characteristics; arrow shows design angle of attack; flagged symbol indicates leading-edge roughness; solid symbol indicates high Reynolds number.

Figure 83.- Concluded.

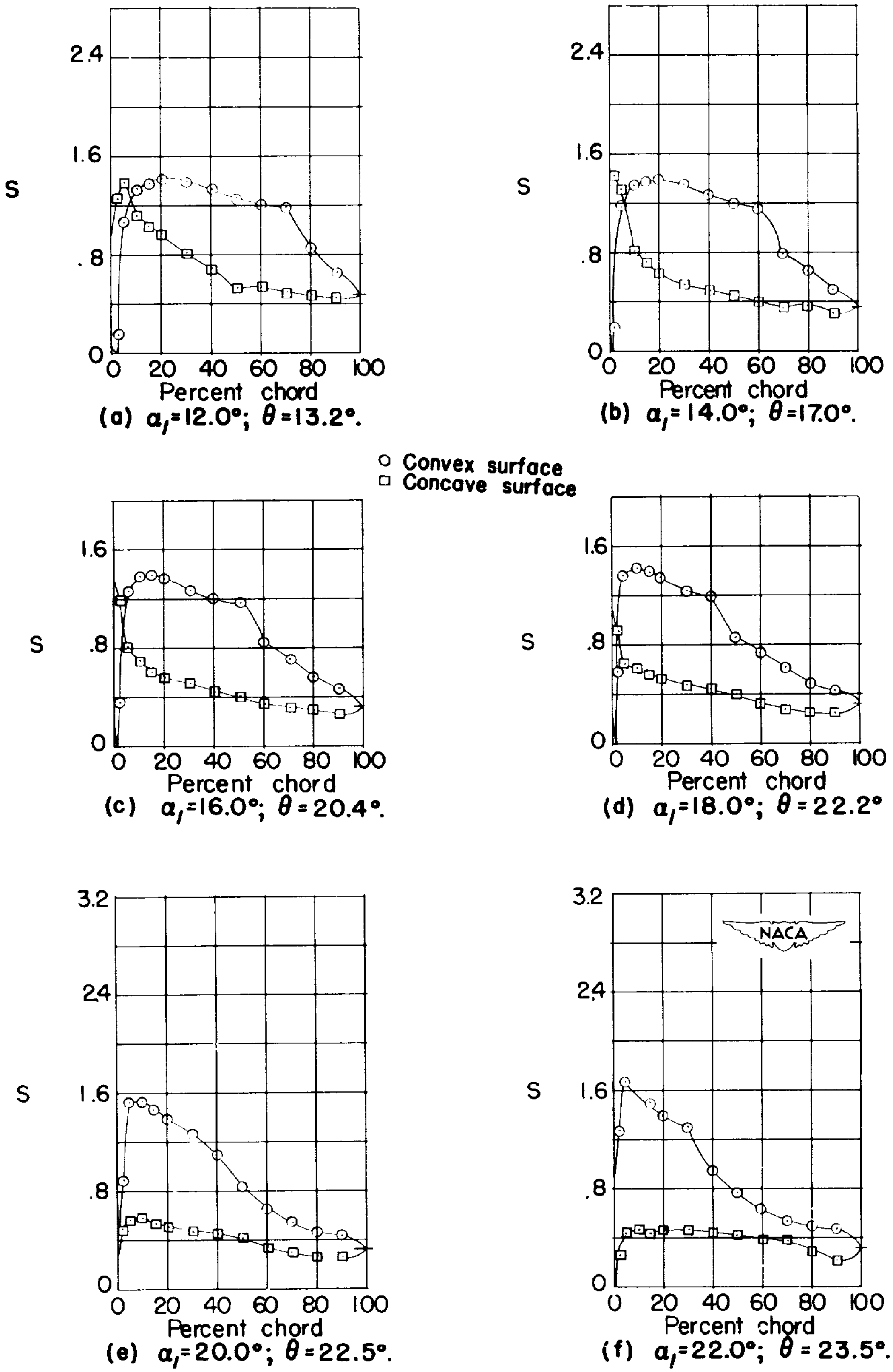

(a) $a_l = 12.0°$; $\theta = 13.2°$.

(b) $a_l = 14.0°$; $\theta = 17.0°$.

(c) $a_l = 16.0°$; $\theta = 20.4°$.

(d) $a_l = 18.0°$; $\theta = 22.2°$

(e) $a_l = 20.0°$; $\theta = 22.5°$.

(f) $a_l = 22.0°$; $\theta = 23.5°$.

Figure 84.- Blade-surface pressure distributions and blade section characteristics for the cascade combination, $\beta_1 = 70°$, $\sigma = 1.50$, and blade section, NACA 65-(15)10.

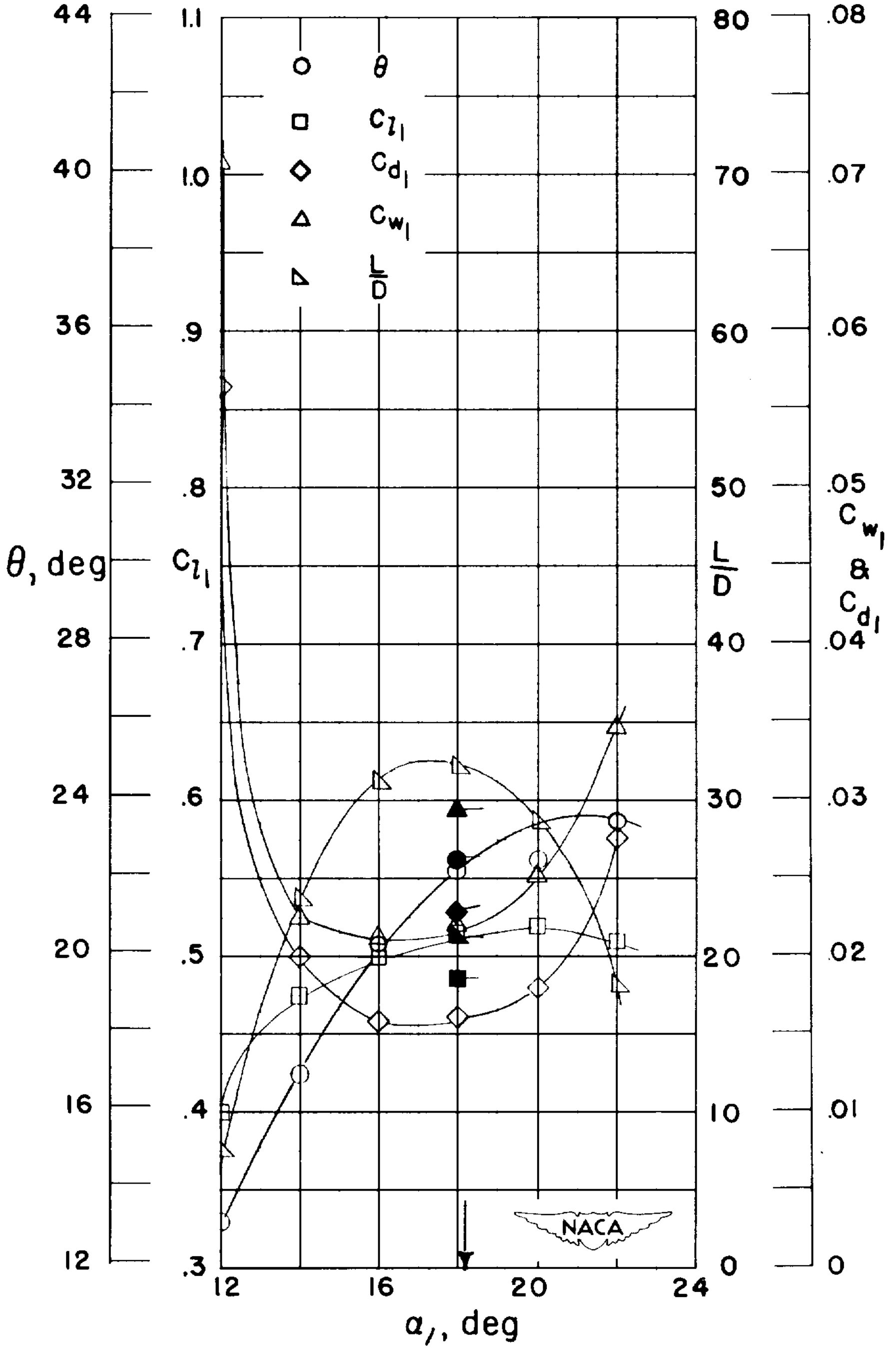

(g) Section characteristics; arrow shows design angle of attack; flagged symbol indicates leading-edge roughness; solid symbol indicates high Reynolds number.

Figure 84.- Concluded.

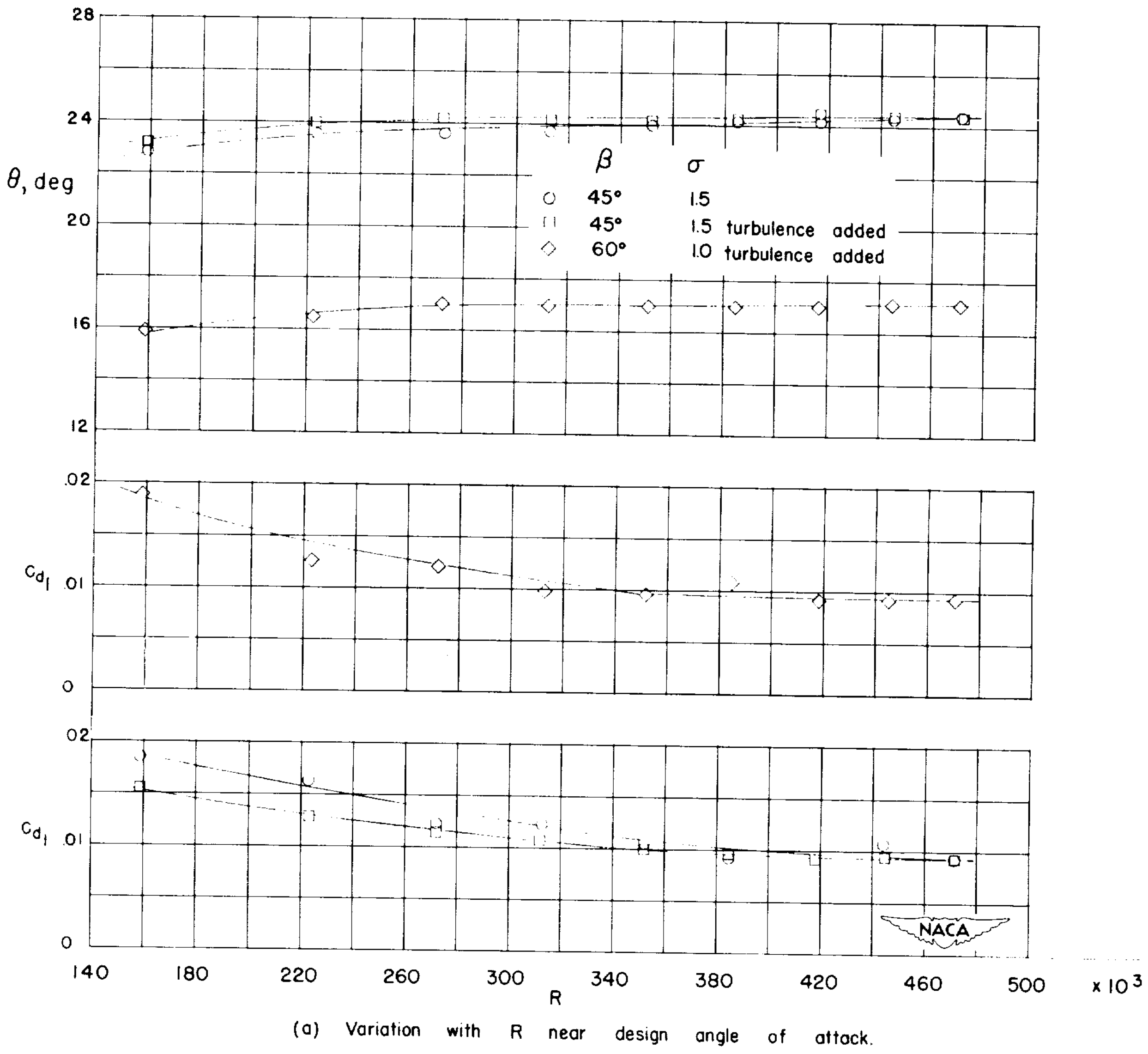

(a) Variation with R near design angle of attack.

Figure 85.- Effect of Reynolds number on turning angle and drag coefficient of the NACA 65-(12)10 blade section for typical cascade combinations.

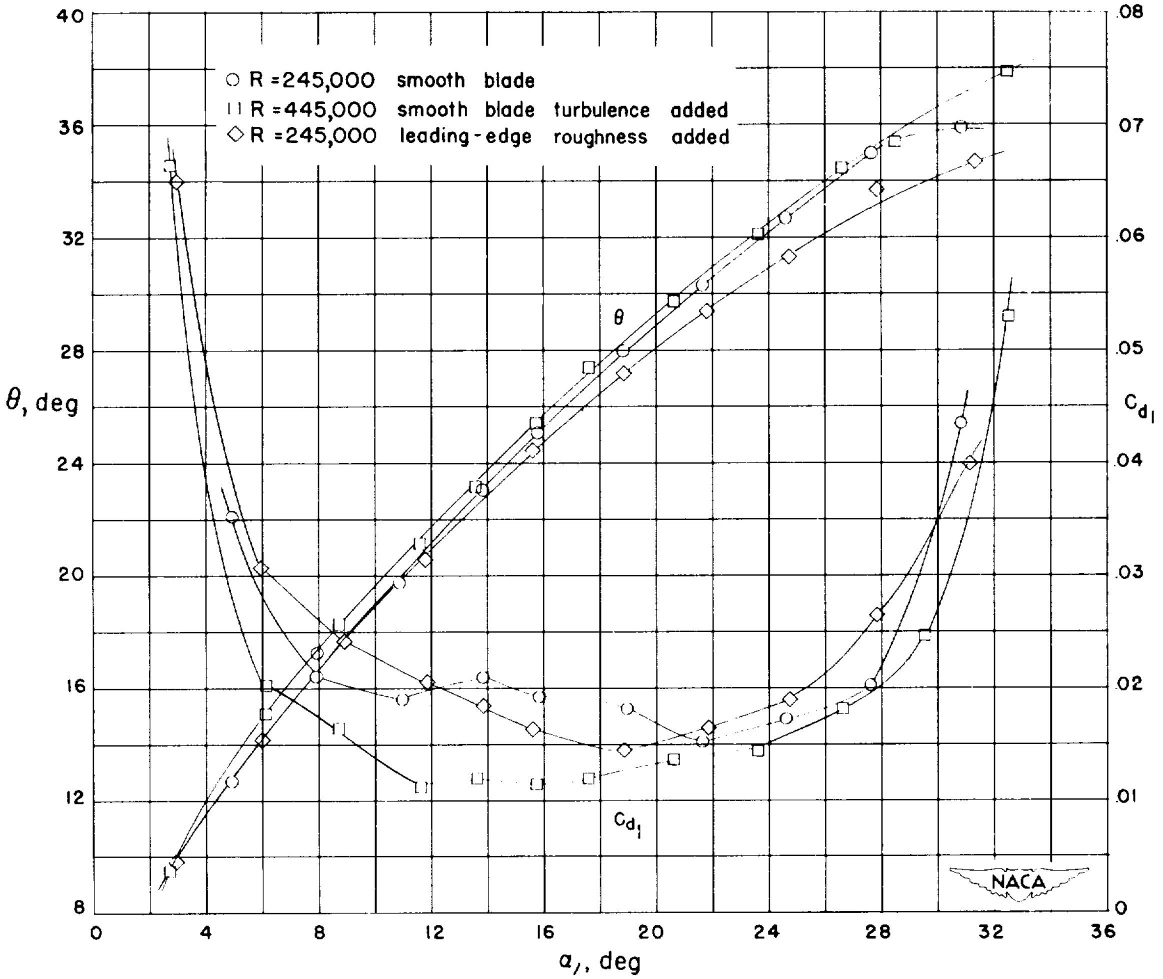

(b) Comparison for the angle-of-attack range for $\beta = 45°$, $\sigma = 1.5$.

Figure 85.- Continued.

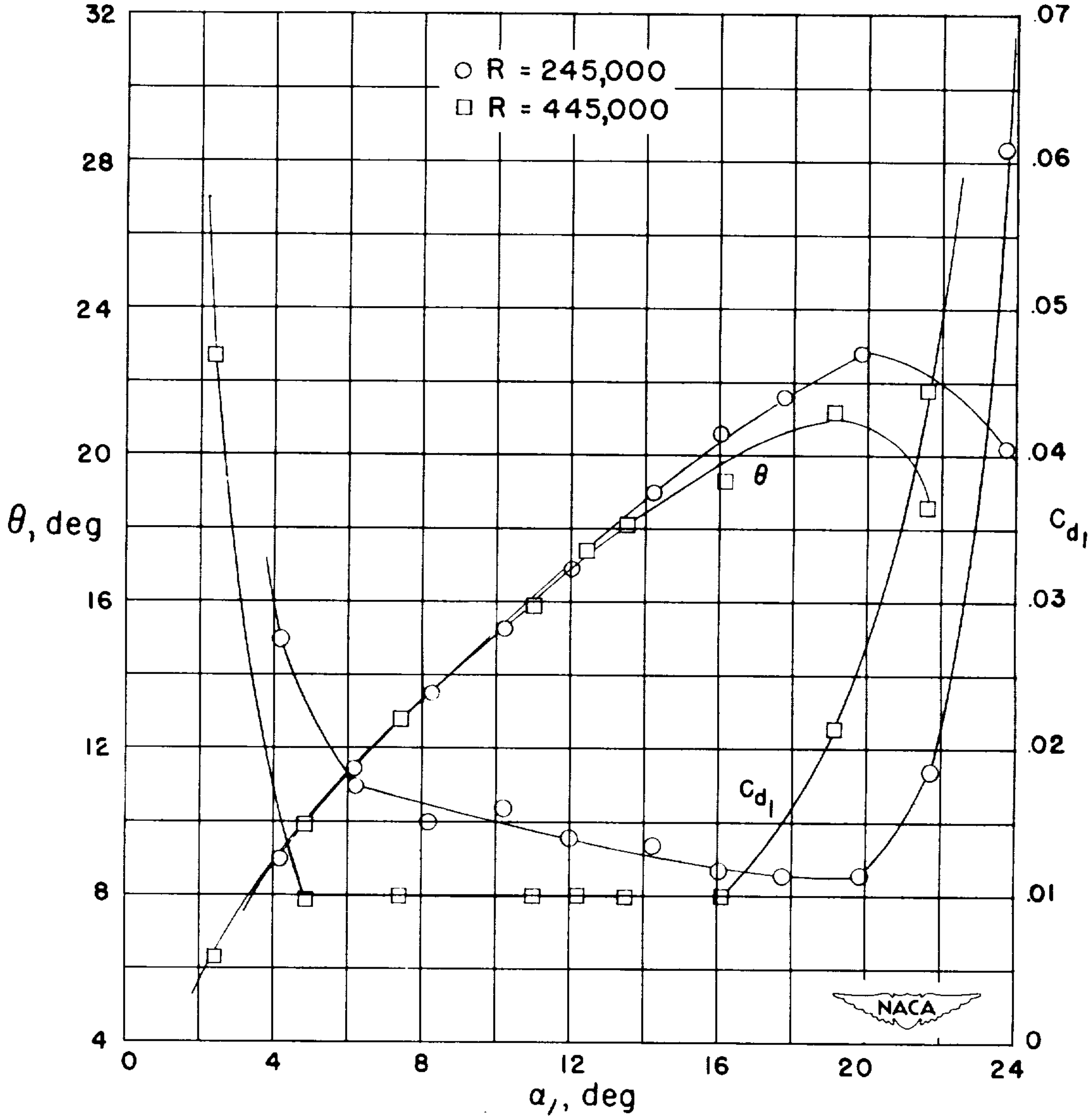

(c) Comparison for the angle-of-attack range for $\beta = 60°$, $\sigma = 1.0$ smooth blade.

Figure 85.- Concluded.

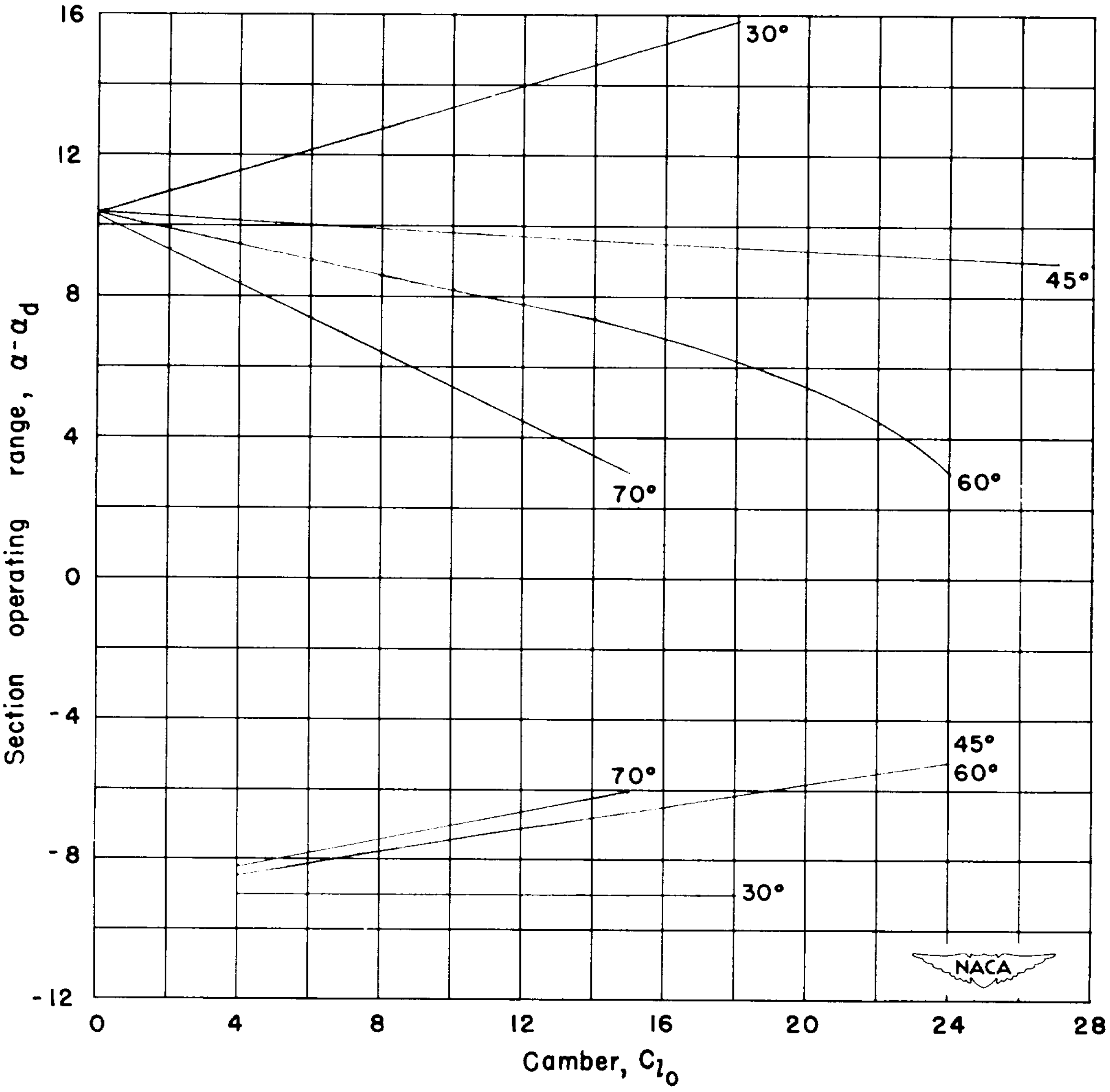

Figure 86.- Variation of estimated operating angle-of-attack range with camber for the inlet angles tested.

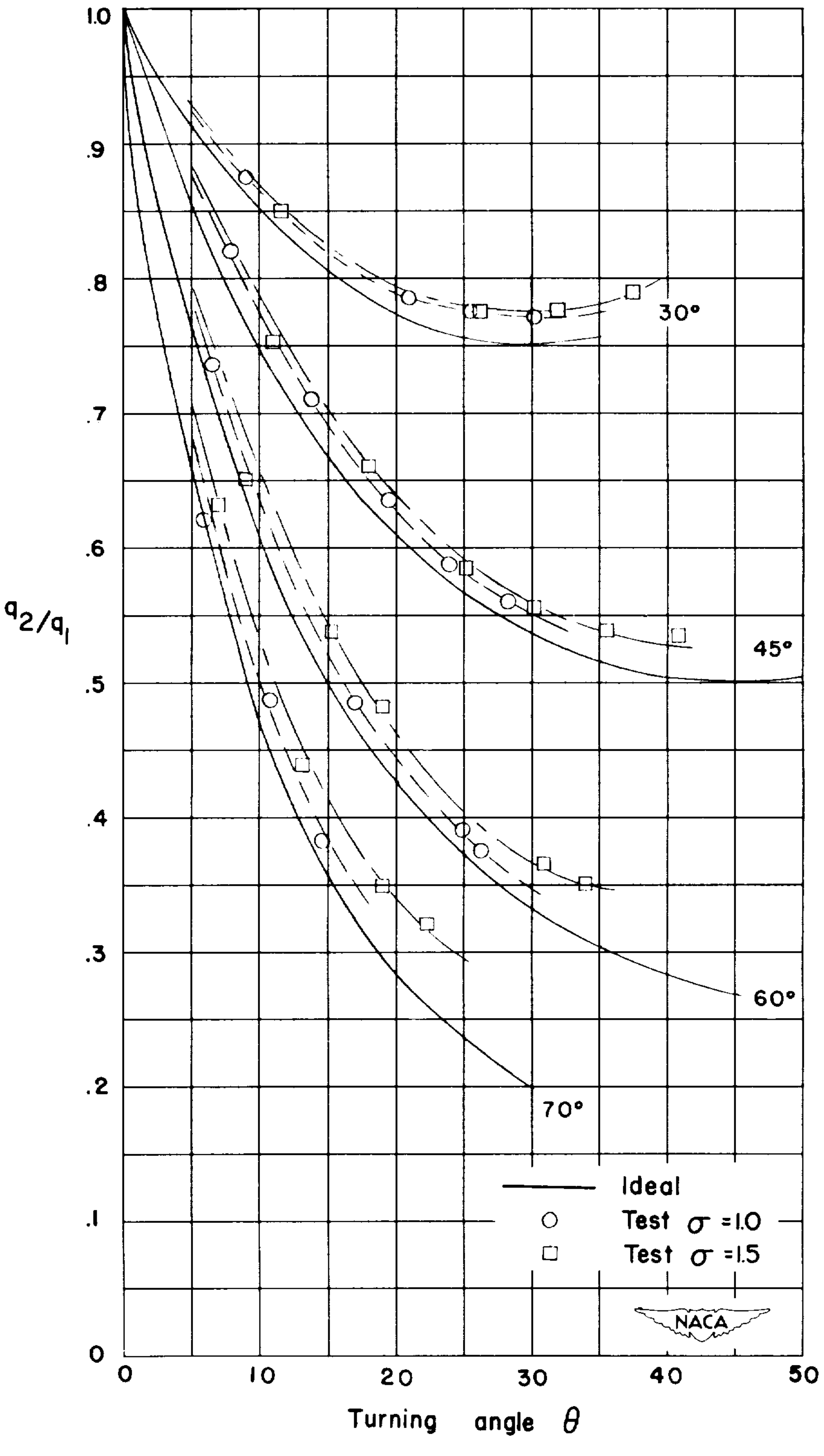

Figure 87.- Variation of ideal and test dynamic-pressure ratio across the cascade.

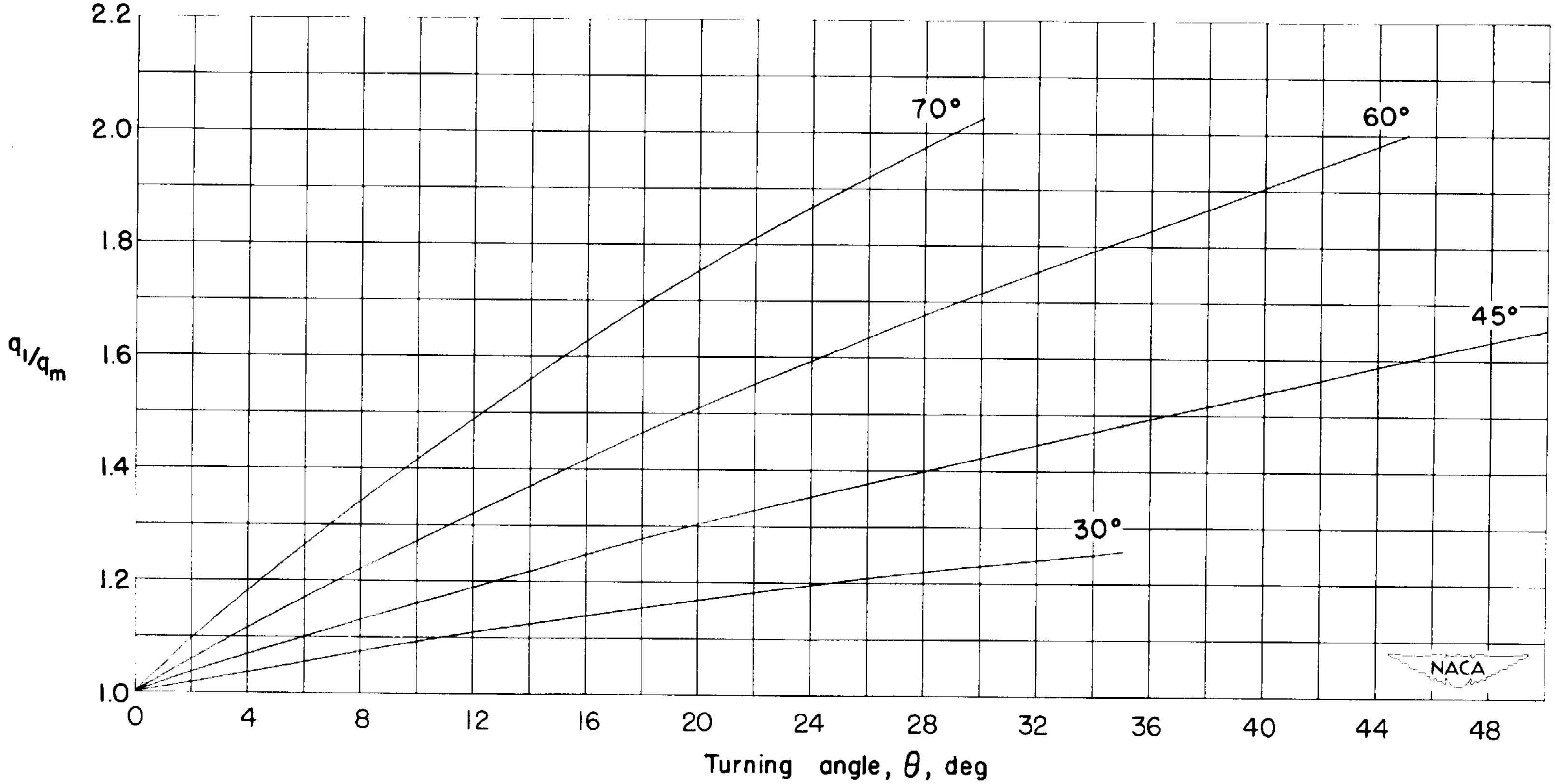

Figure 88.- Conversion chart showing the relation between entering and mean dynamic pressure as a function of turning angle and inlet angle.

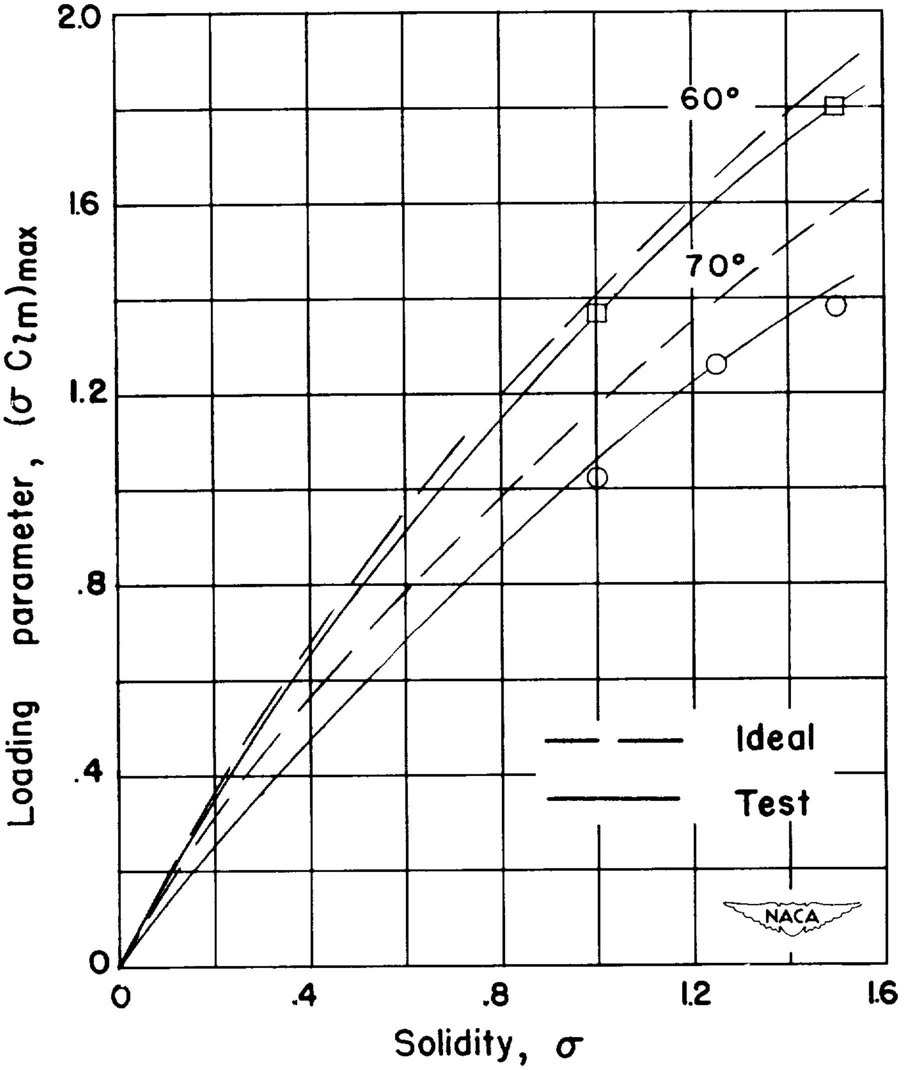

Figure 89.- Variation of the limit loading parameter, $(\sigma C_{l_m})_{max}$ with solidity for inlet angles of 60° and 70°.

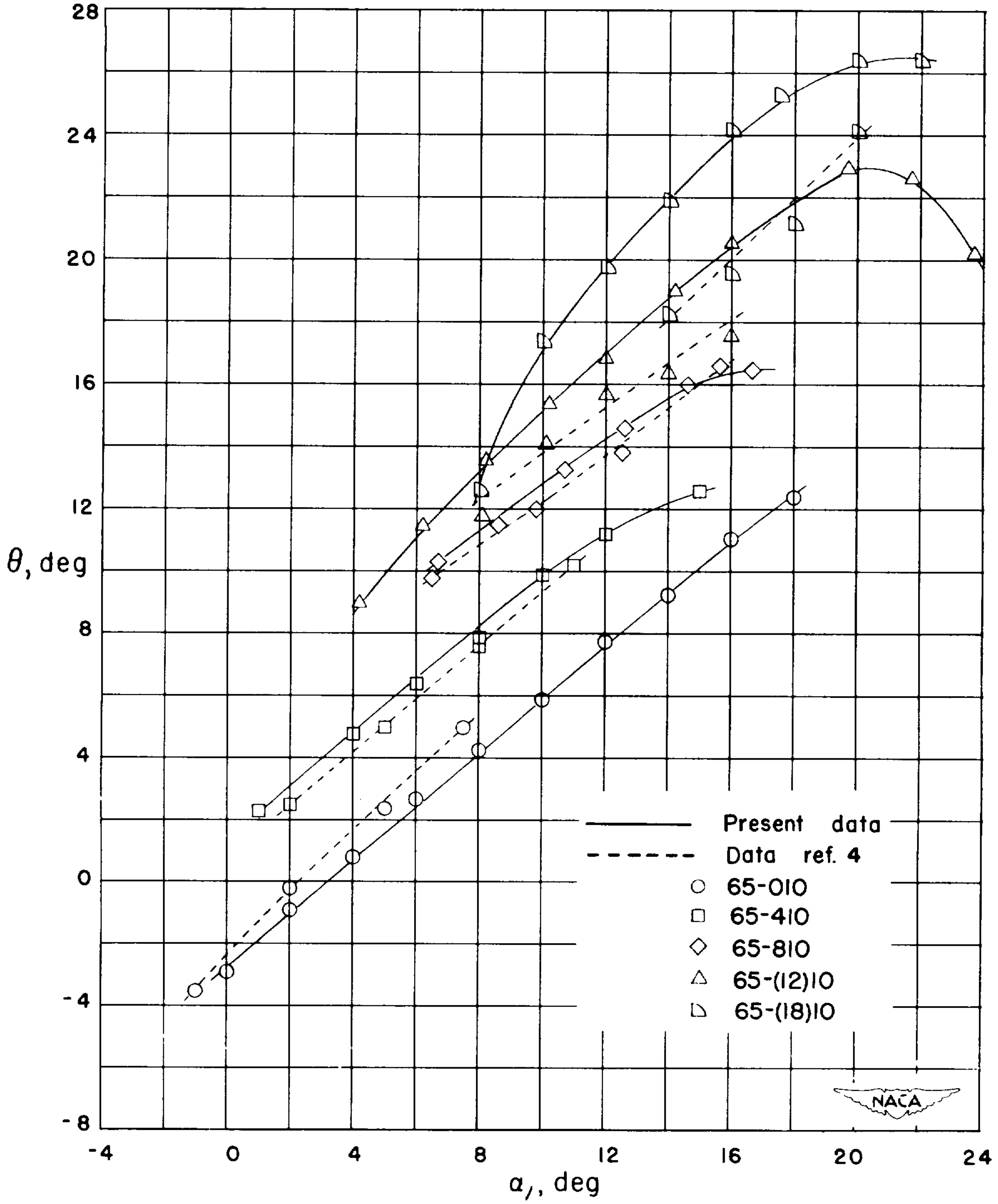

Figure 90.- Comparison of relationships between turning angle and angle of attack for the present porous-wall cascade results with those for the solid-wall cascade of reference 4 for a typical combination, $\beta_1 = 60^\circ$, $\sigma = 1.00$.

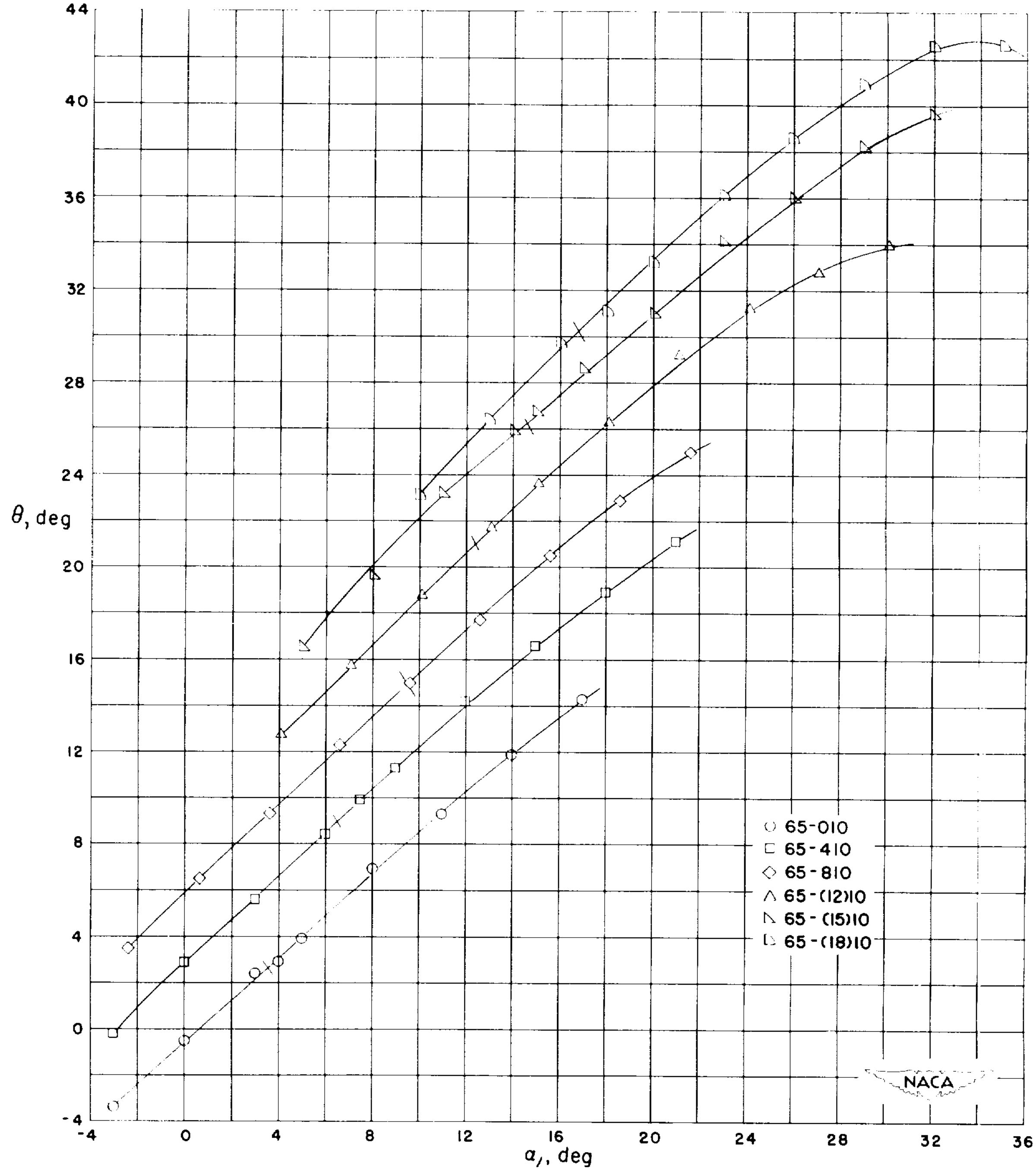

Figure 91.- Summary of relationship between turning angle θ and angle of attack α for the blade sections tested at $\beta_1 = 30^\circ$, $\sigma = 1.00$. Short bars across curves indicate design points.

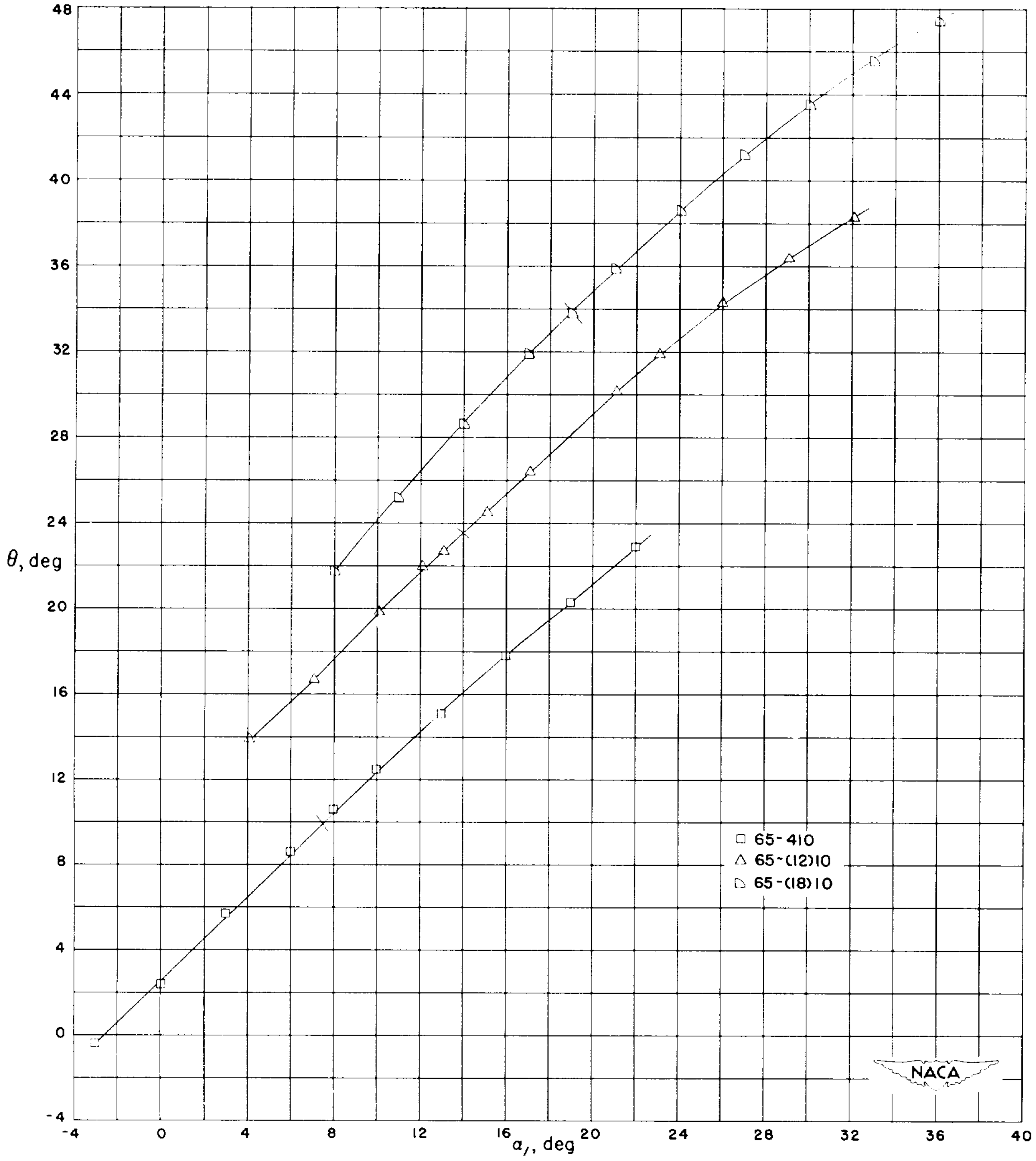

Figure 92.- Summary of relationship between turning angle θ and angle of attack α for the blade sections tested at $\beta_1 = 30^\circ$, $\sigma = 1.25$. Short bars across curves indicate design points.

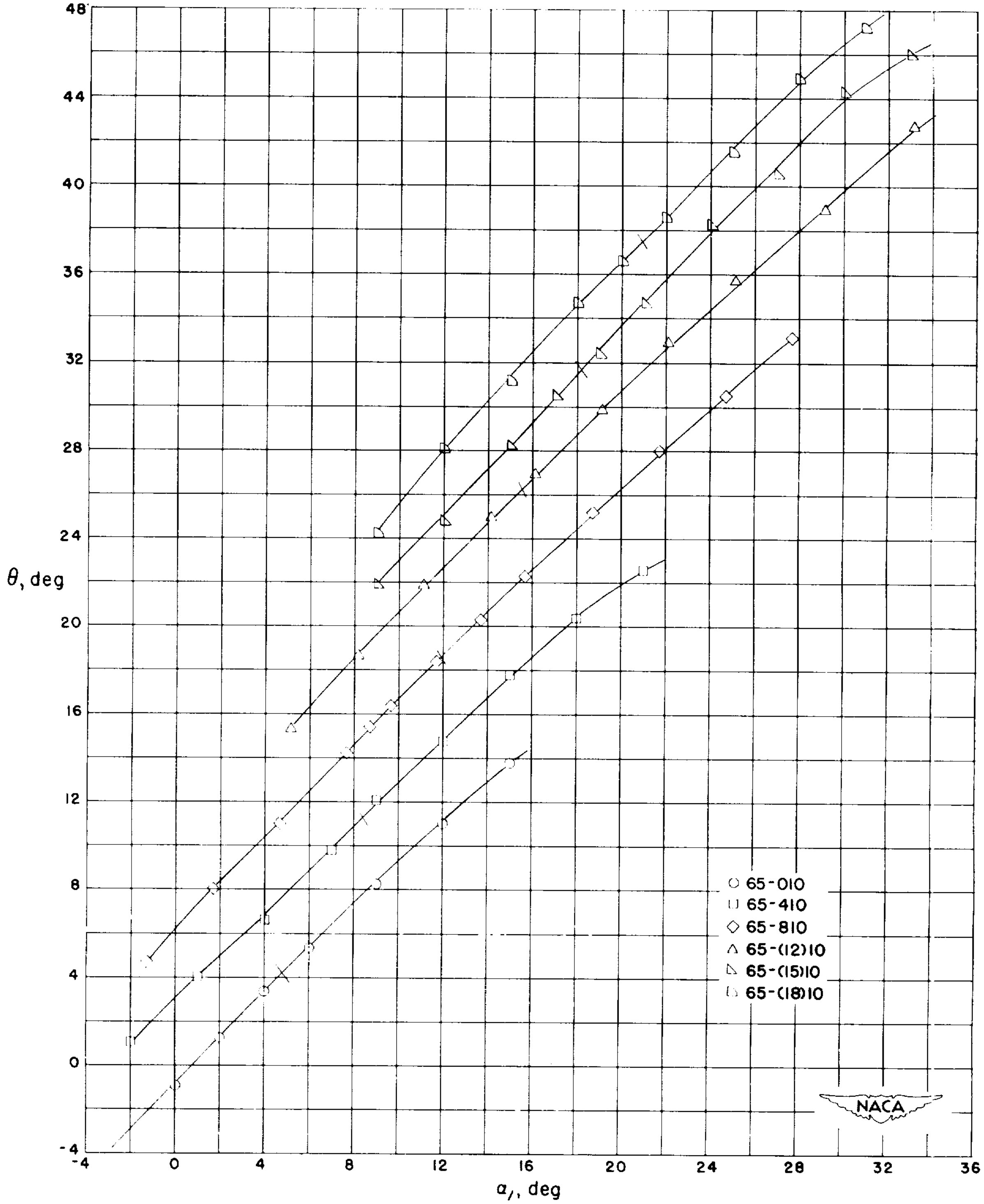

Figure 93.- Summary of relationship between turning angle θ and angle of attack α for the blade sections tested at $\beta_1 = 30^\circ$, $\sigma = 1.50$. Short bars across curves indicate design points.

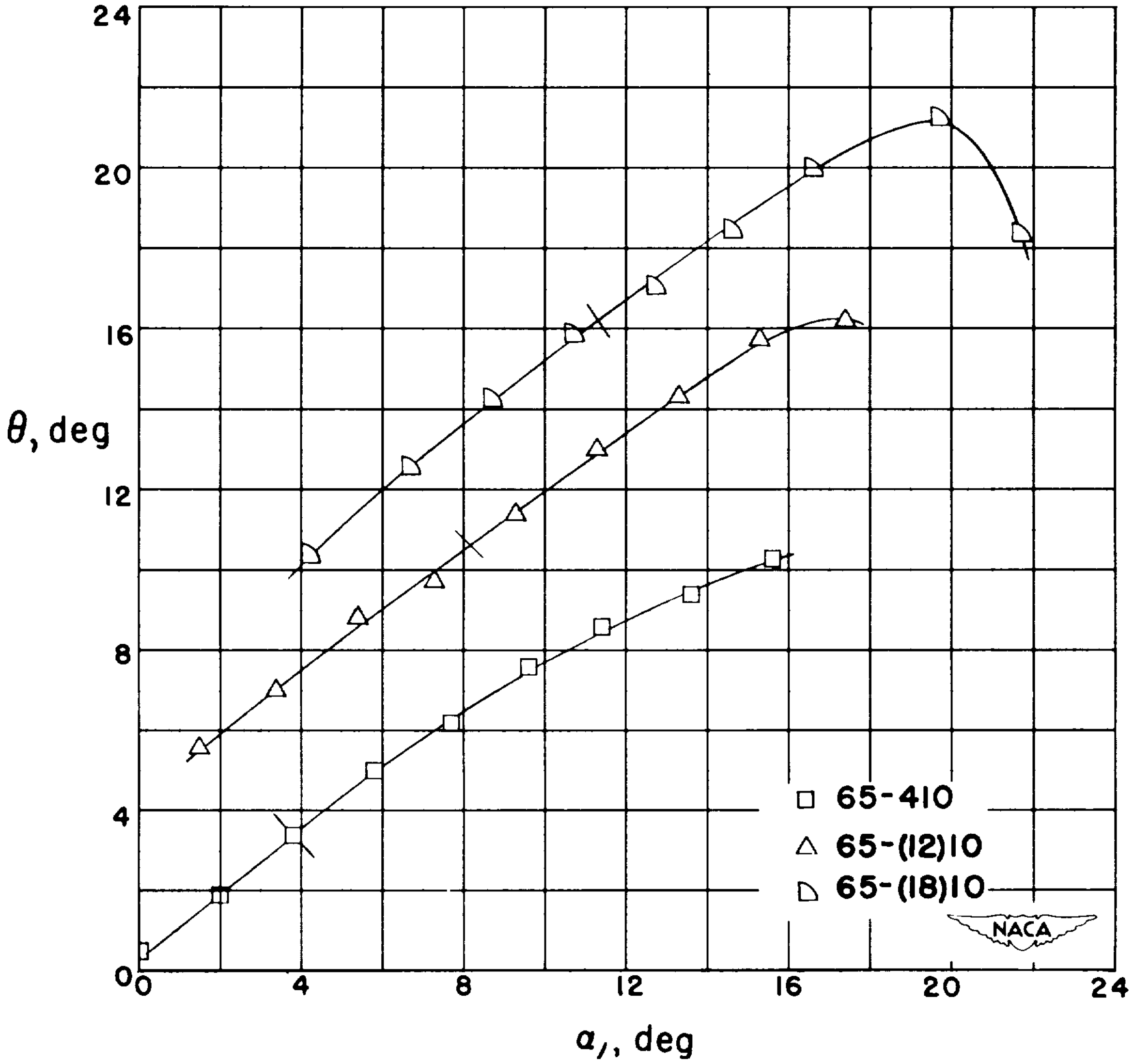

Figure 94.- Summary of relationship between turning angle θ and angle of attack α for the blade sections tested at $\beta_1 = 45^\circ$, $\sigma = 0.50$. Short bars across curves indicate design points.

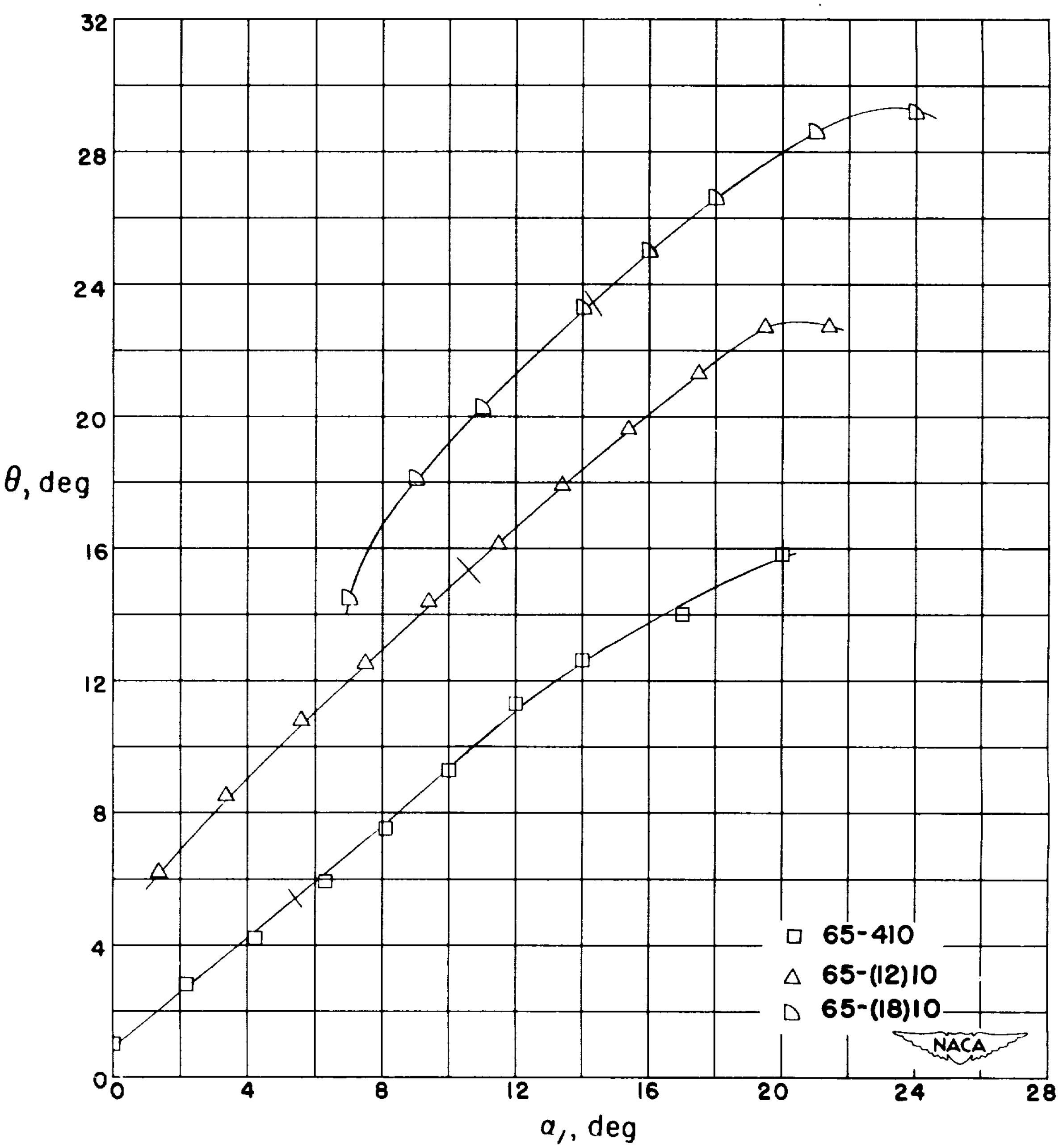

Figure 95.- Summary of relationship between turning angle θ and angle of attack α for the blade sections tested at $\beta_1 = 45^\circ$, $\sigma = 0.75$. Short bars across curves indicate design points.

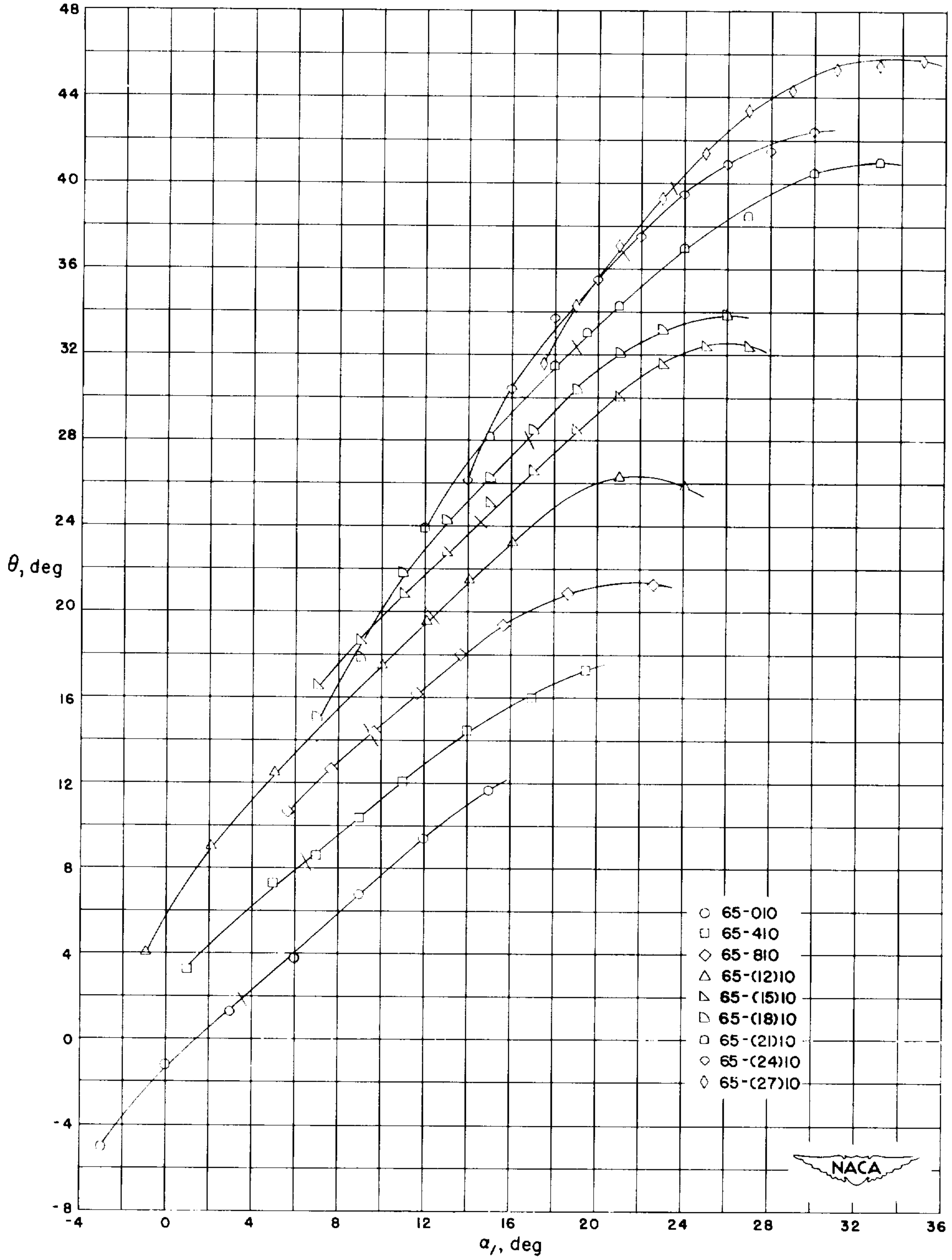

Figure 96.- Summary of relationship between turning angle θ and angle of attack α for the blade sections tested at $\beta_1 = 45^\circ$, $\sigma = 1.00$. Short bars across curves indicate design points.

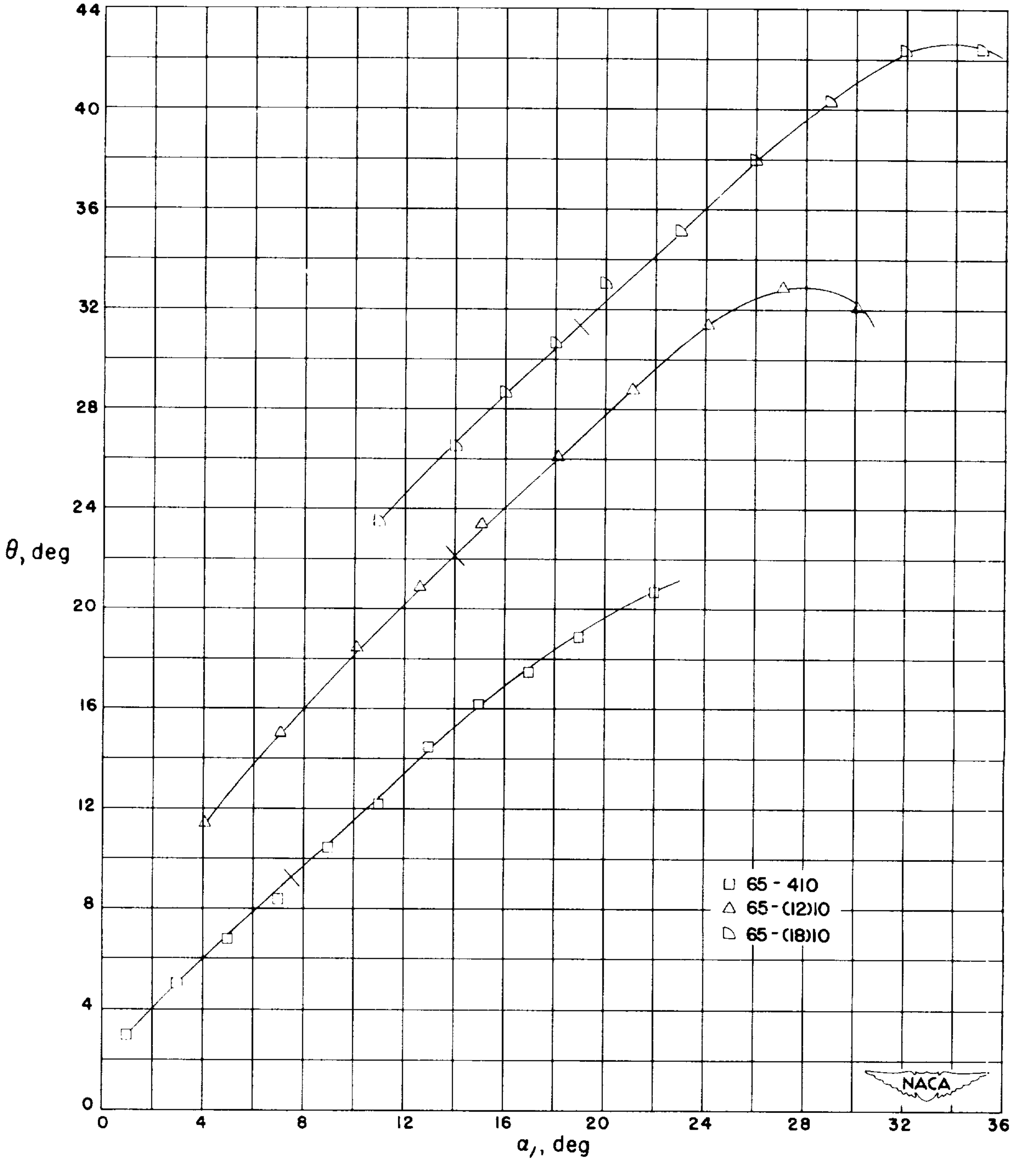

Figure 97.- Summary of relationship between turning angle θ and angle of attack α for the blade sections tested at $\beta_1 = 45^\circ$, $\sigma = 1.25$. Short bars across curves indicate design points.

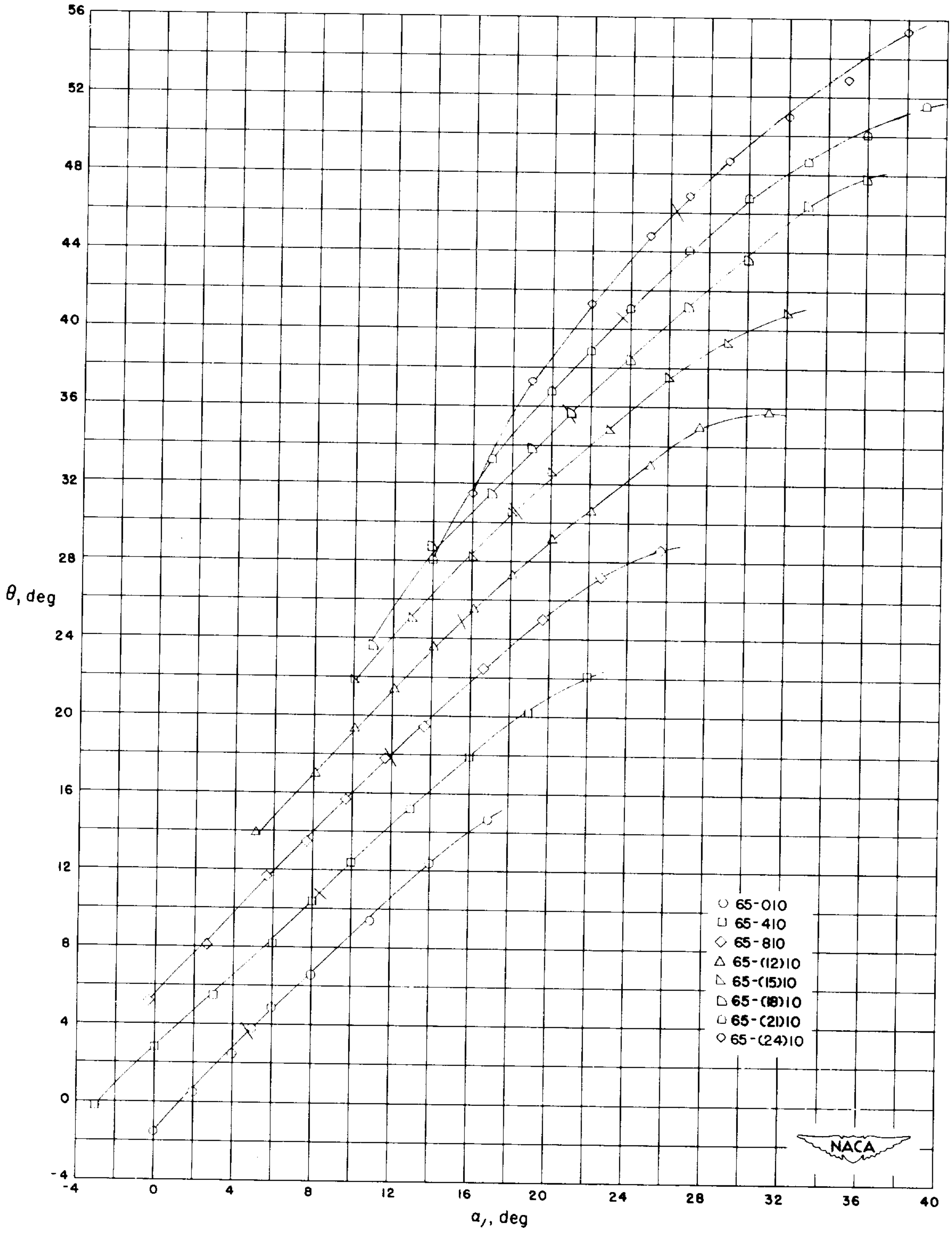

Figure 98.- Summary of relationship between turning angle θ and angle of attack α for the blade sections tested at $\beta_1 = 45^{\circ}$, $\sigma = 1.50$. Short bars across curves indicate design points.

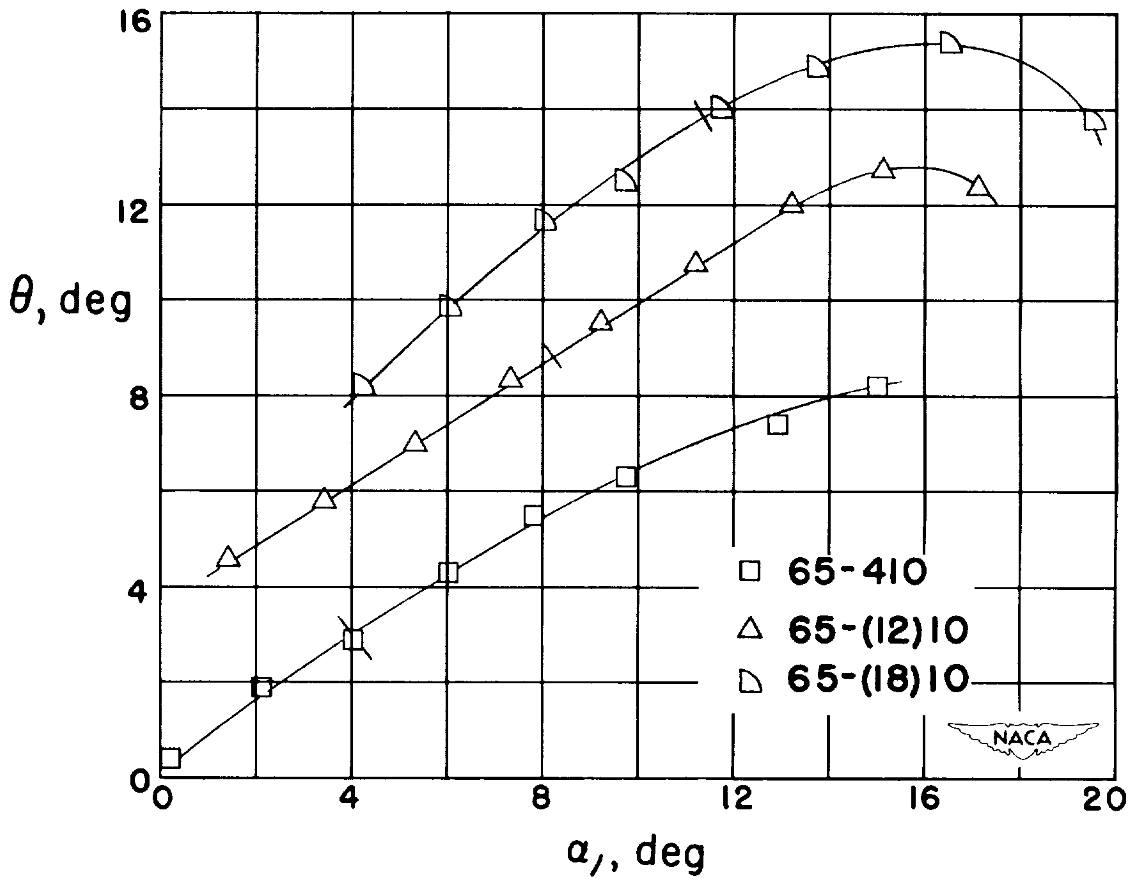

Figure 99.- Summary of relationship between turning angle θ and angle of attack α for the blade sections tested at $\beta_1 = 60^\circ$, $\sigma = 0.50$. Short bars across curves indicate design points.

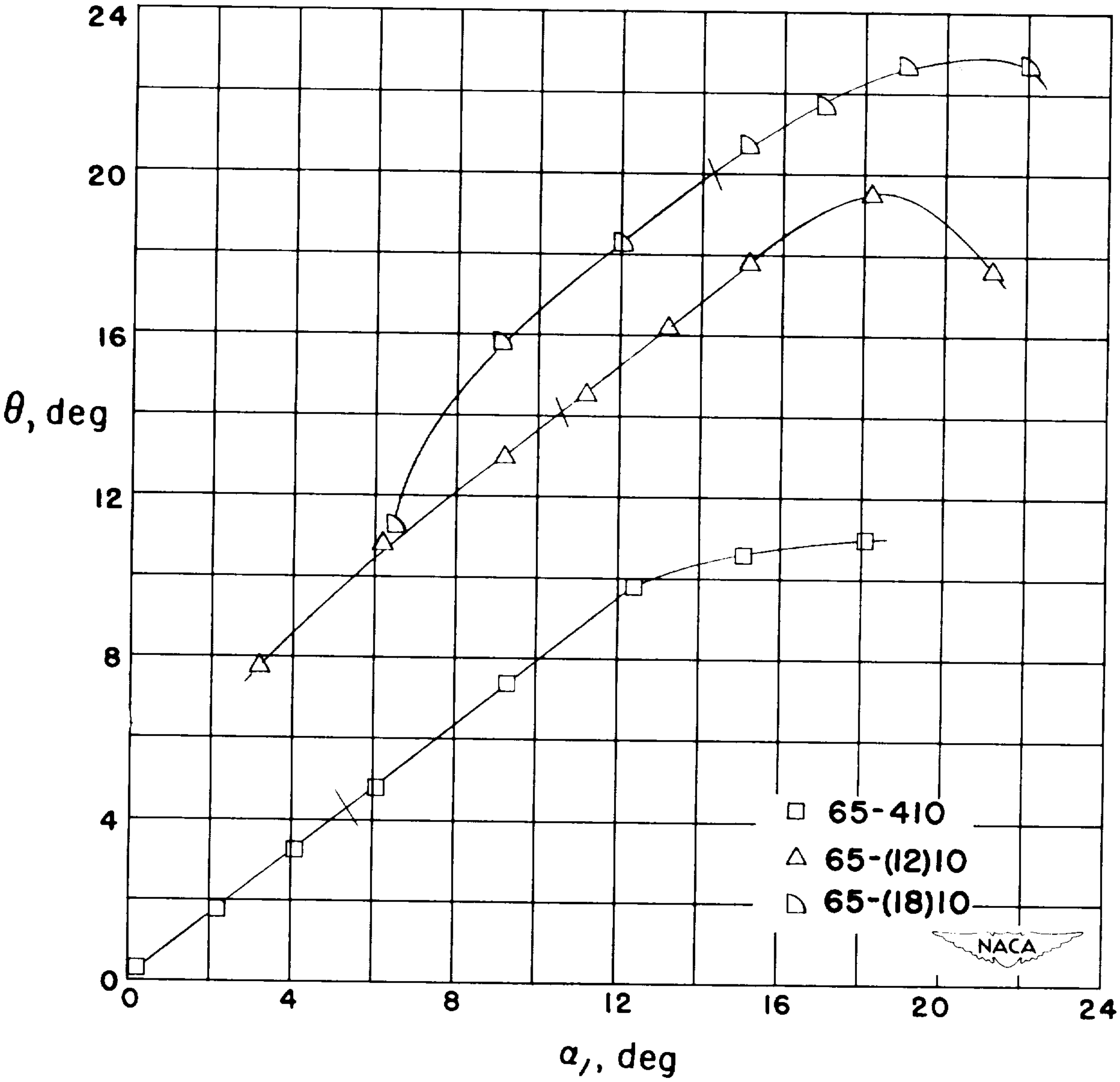

Figure 100.- Summary of relationship between turning angle θ and angle of attack α for the blade sections tested at $\beta_1 = 60^\circ$, $\sigma = 0.75$. Short bars across curves indicate design points.

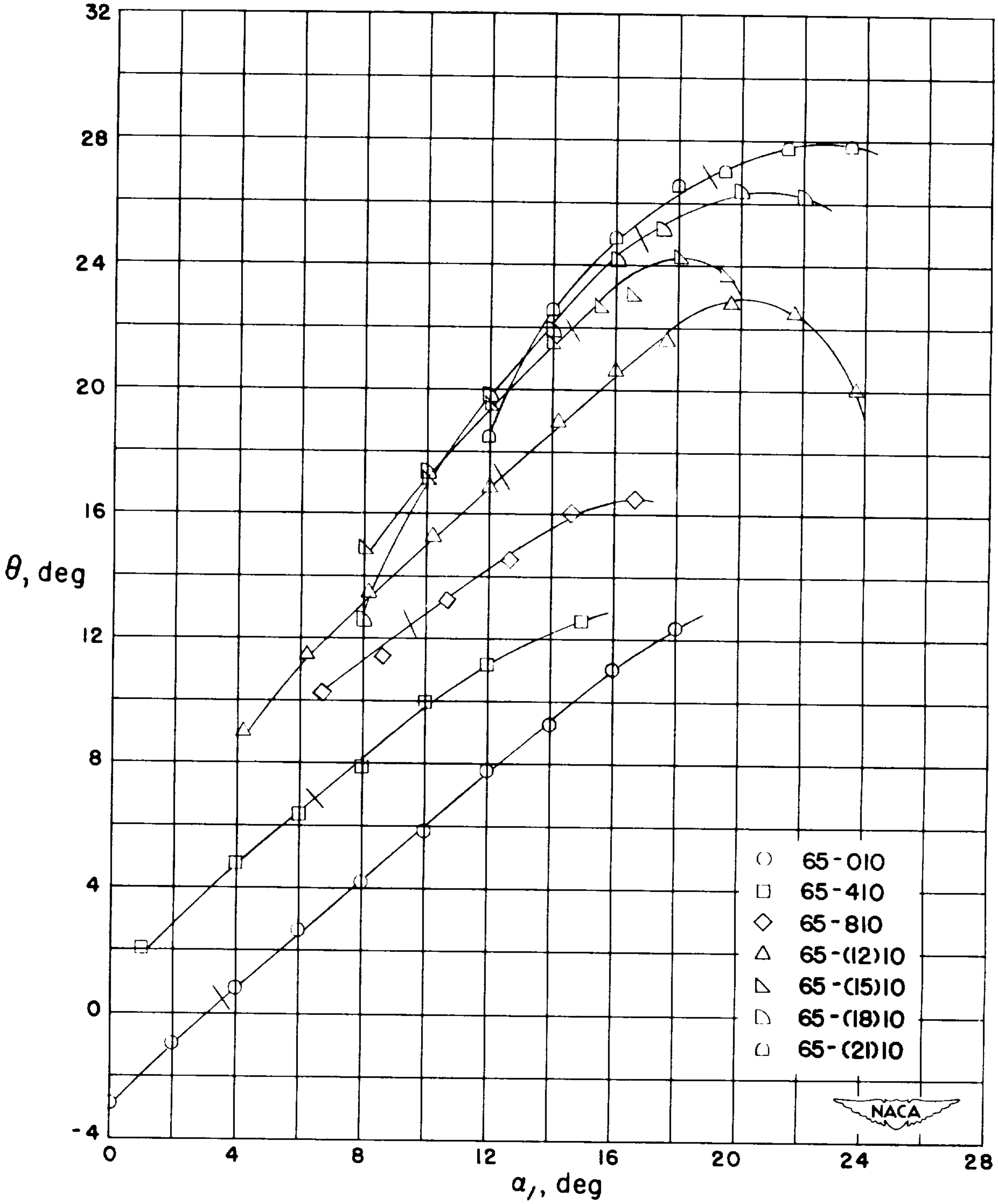

Figure 101.- Summary of relationship between turning angle θ and angle of attack α for the blade sections tested at $\beta_1 = 60^\circ$, $\sigma = 1.00$. Short bars across curves indicate design points.

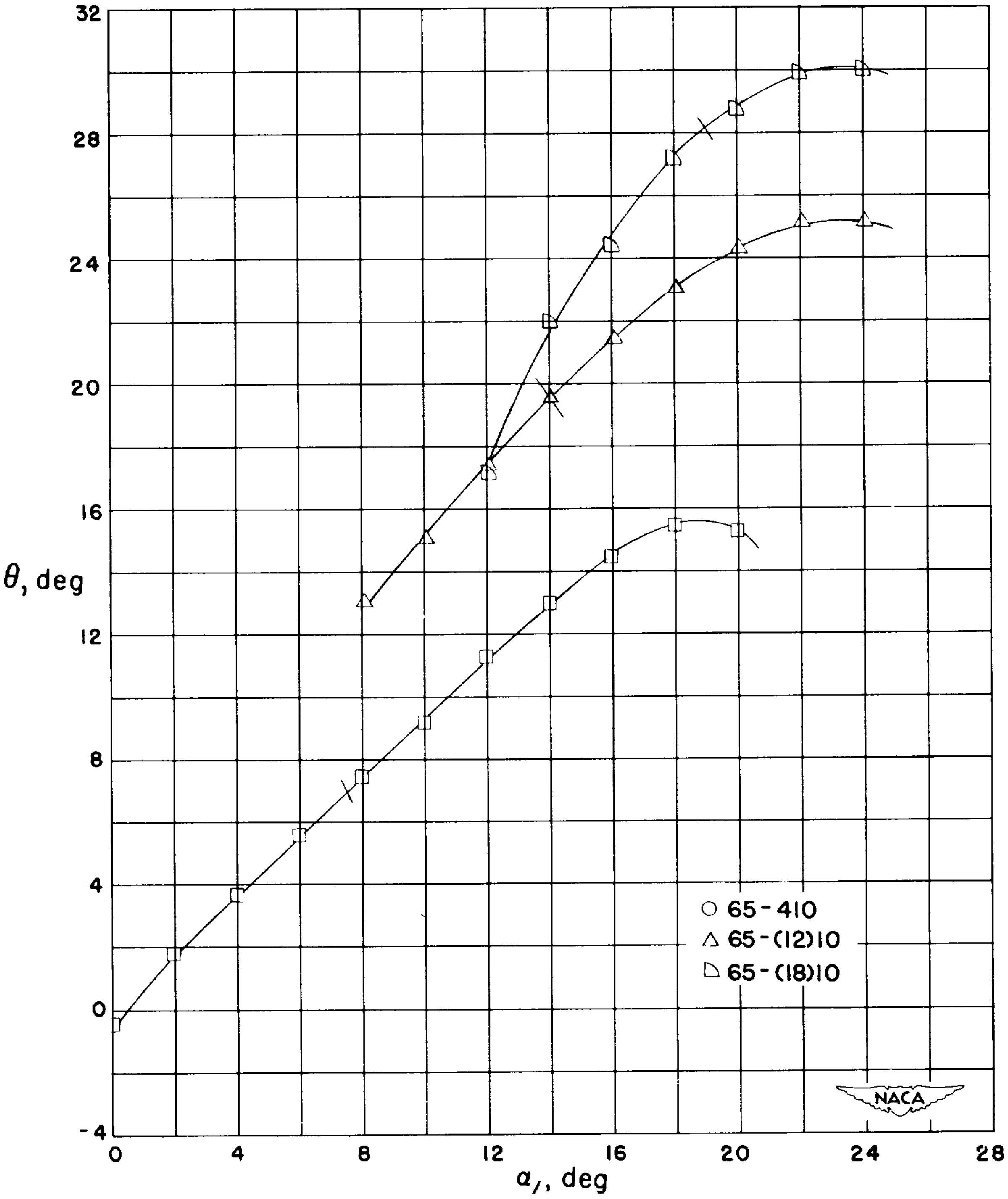

Figure 102.- Summary of relationship between turning angle θ and angle of attack α for the blade sections tested at $\beta_1 = 60^\circ$, $\sigma = 1.25$. Short bars across curves indicate design points.

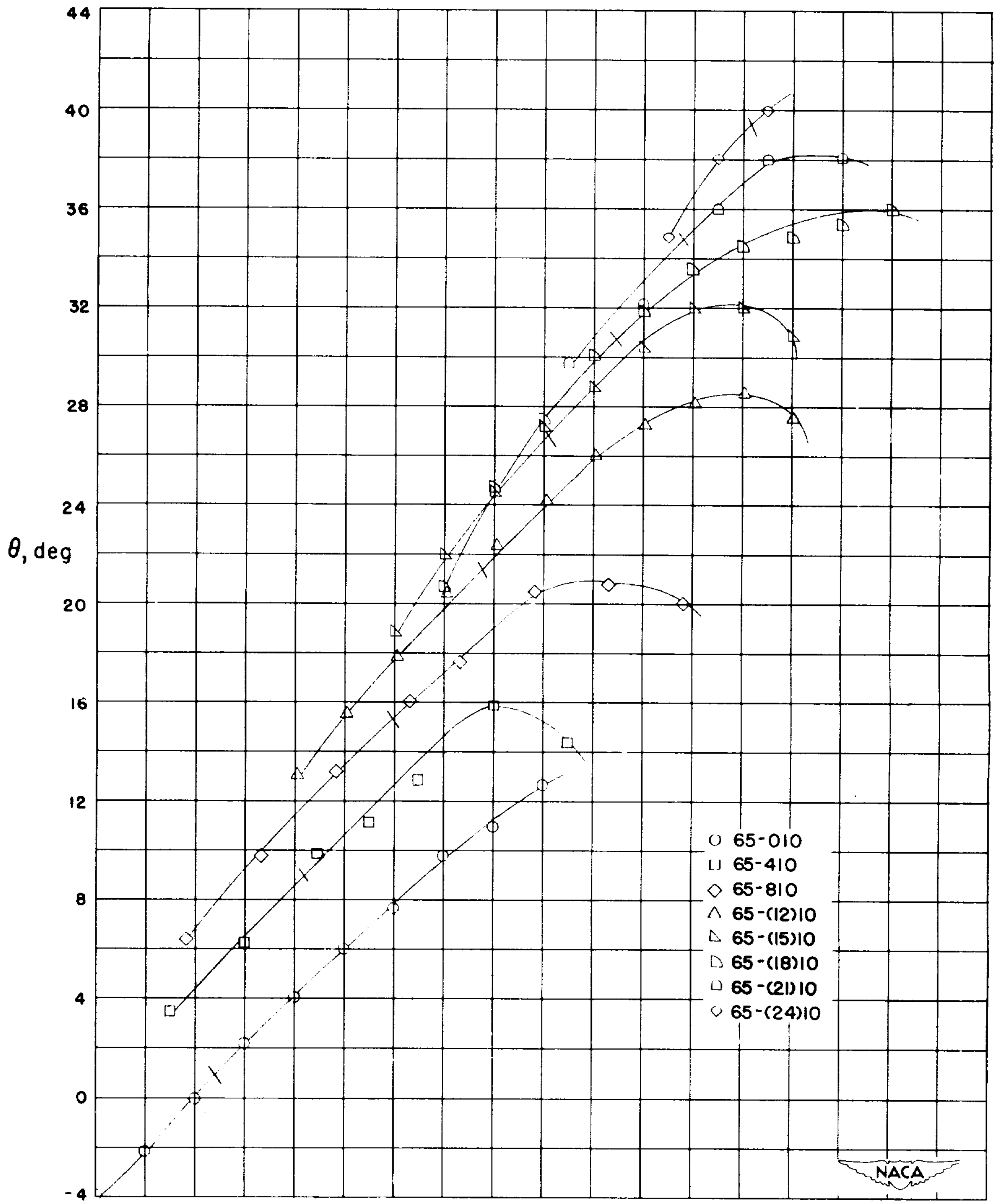

Figure 103.- Summary of relationship between turning angle θ and angle of attack α for the blade sections tested at $\beta_1 = 60^\circ$, $\sigma = 1.50$. Short bars across curves indicate design points.

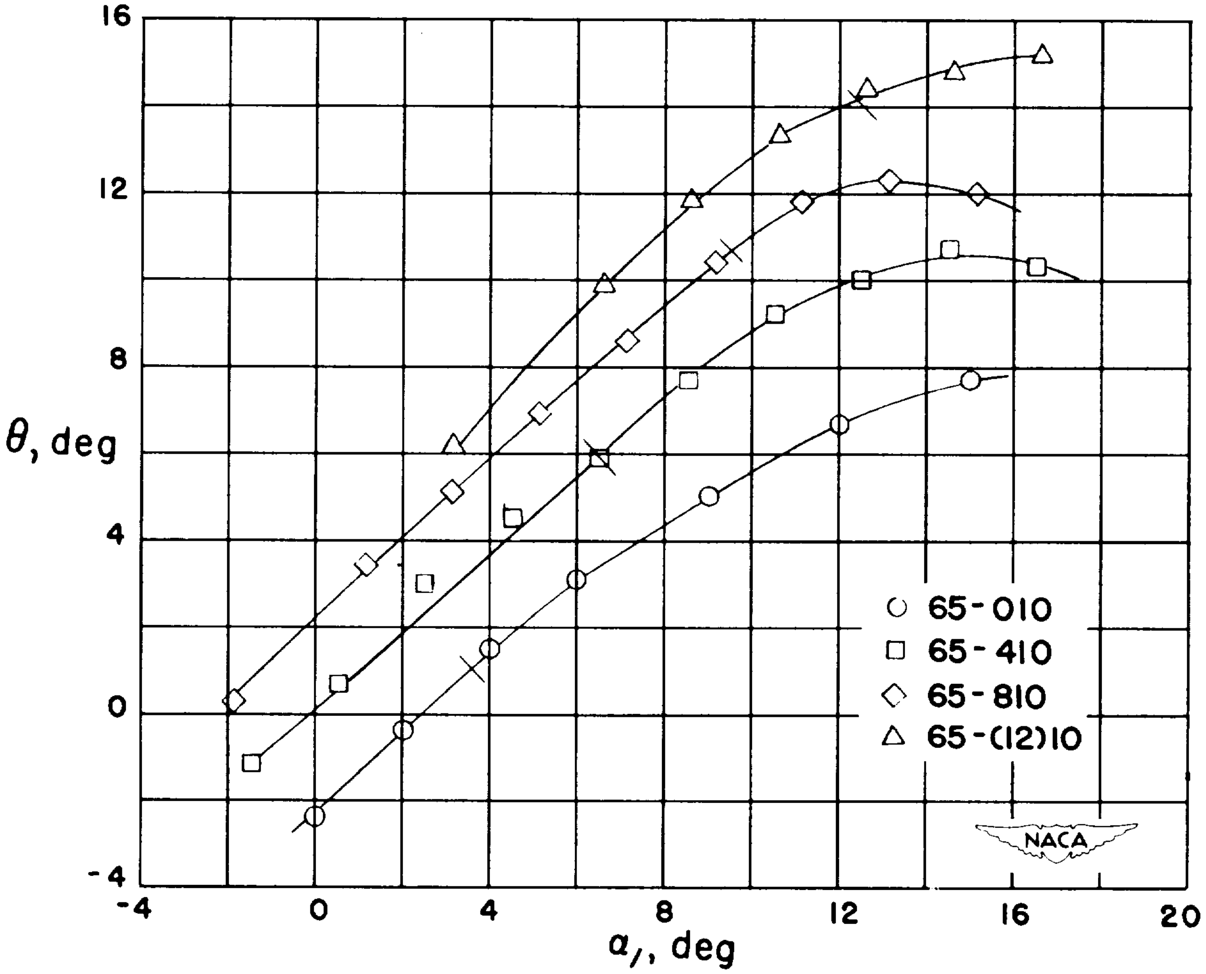

Figure 104.- Summary of relationship between turning angle θ and angle of attack α for the blade sections tested at $\beta_1 = 70^\circ$, $\sigma = 1.00$. Short bars across curves indicate design points.

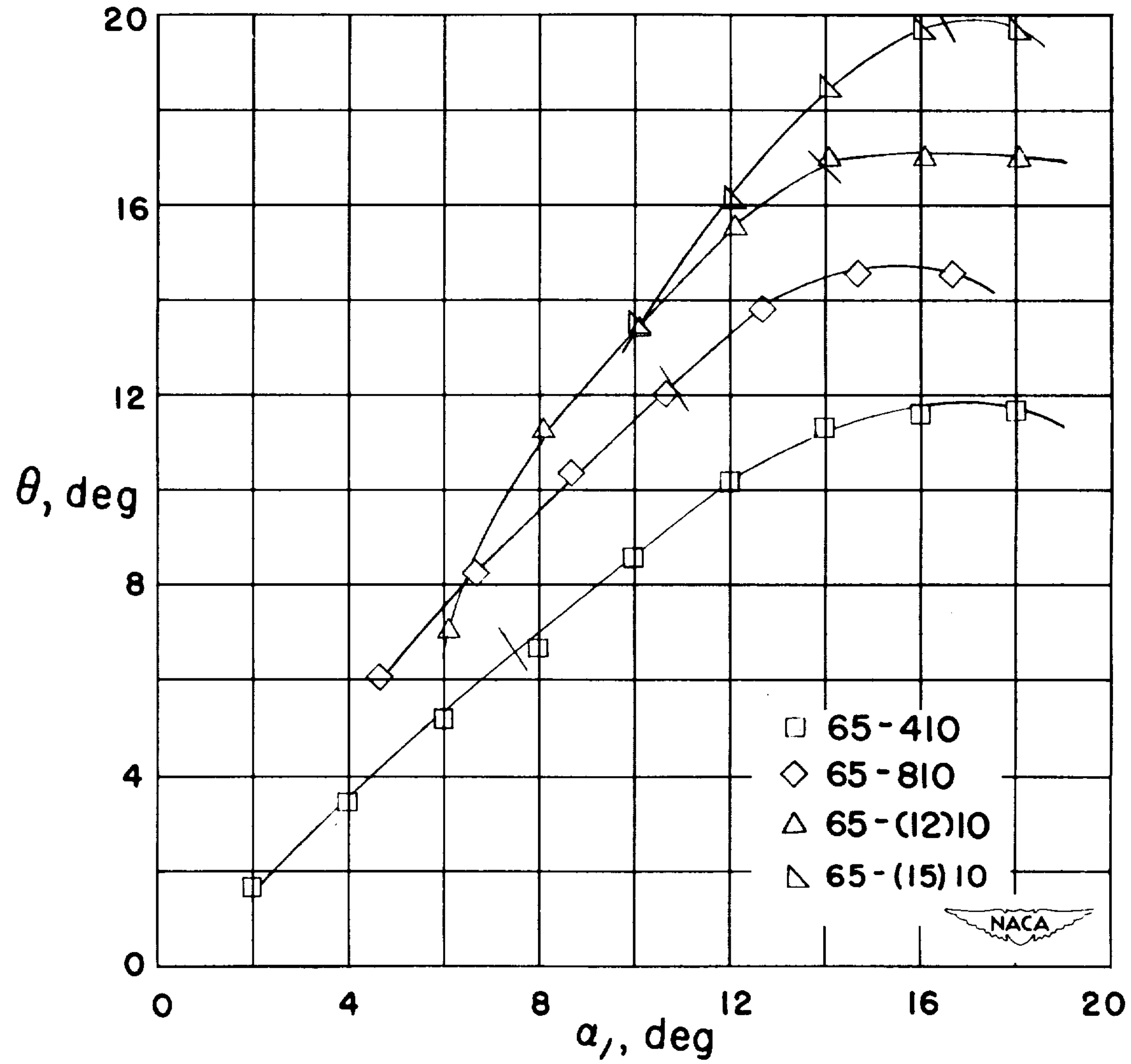

Figure 105.- Summary of relationship between turning angle θ and angle of attack α for the blade sections tested at $\beta_1 = 70^\circ$, $\sigma = 1.25$. Short bars across curves indicate design points.

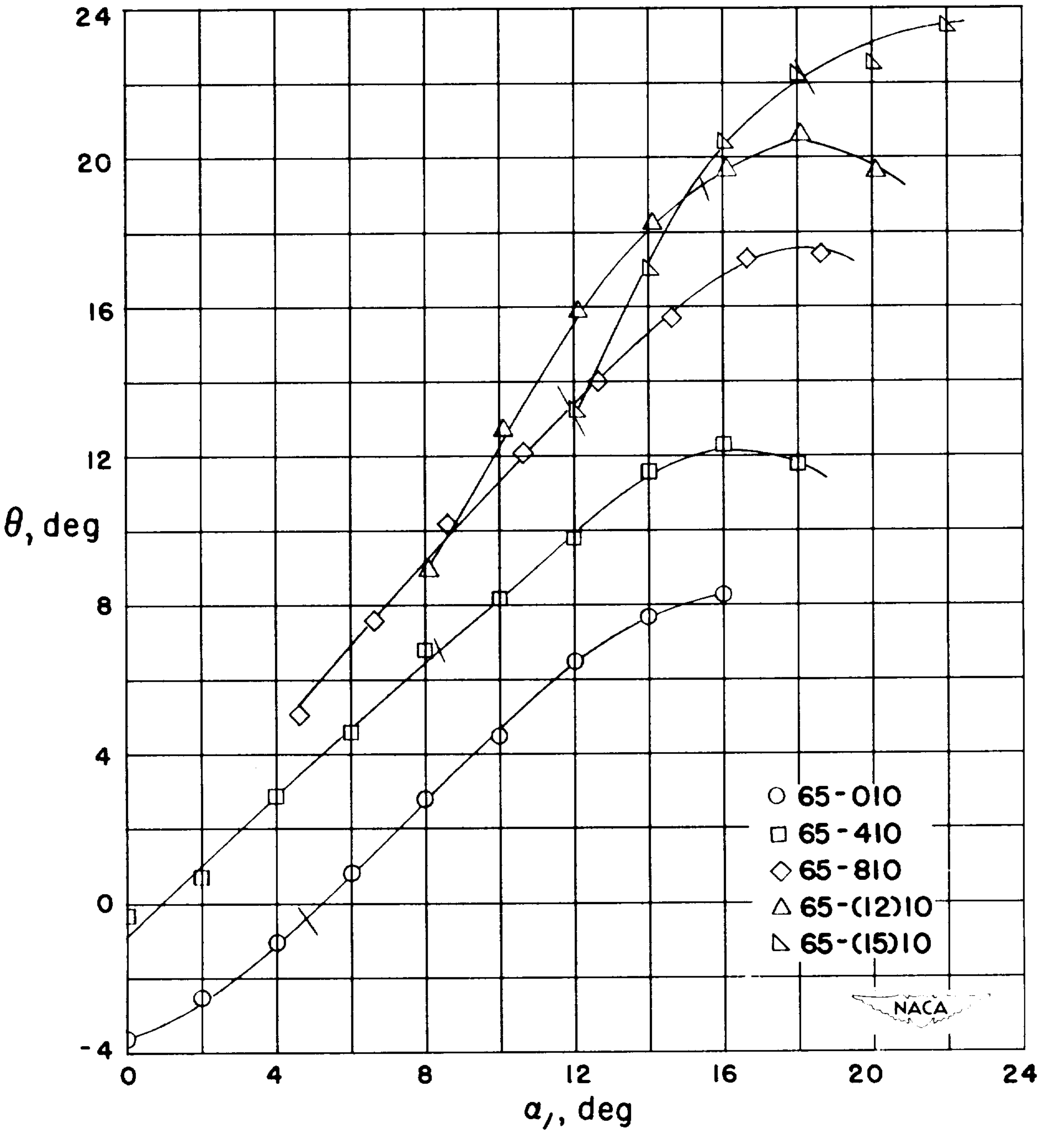

Figure 106.- Summary of relationship between turning angle θ and angle of attack α for the blade sections tested at $\beta_1 = 70^\circ$, $\sigma = 1.50$. Short bars across curves indicate design points.

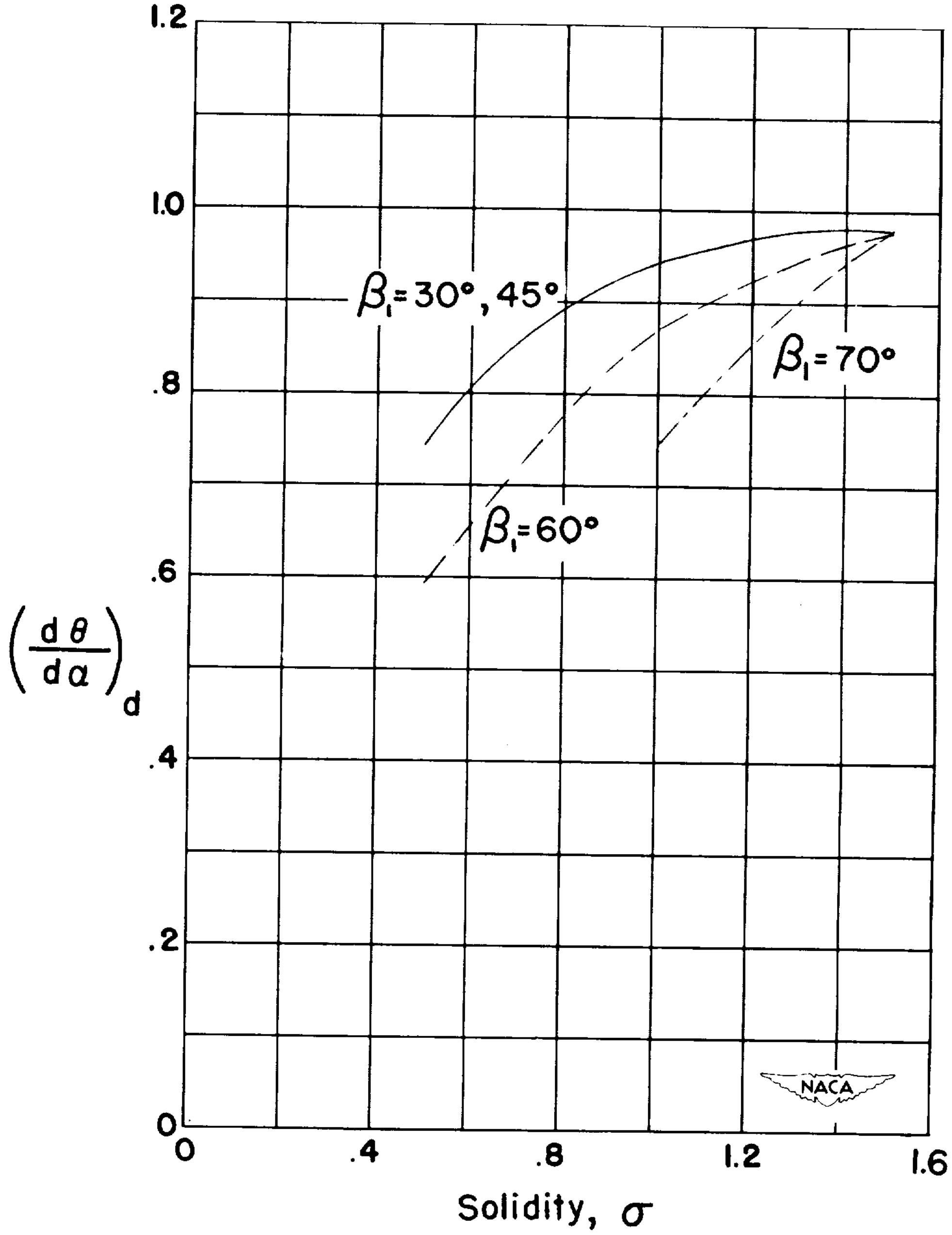

Figure 107.- Variation of turning-angle, angle-of-attack slope at design with solidity and inlet angle. The slopes are averages for the moderate camber range.

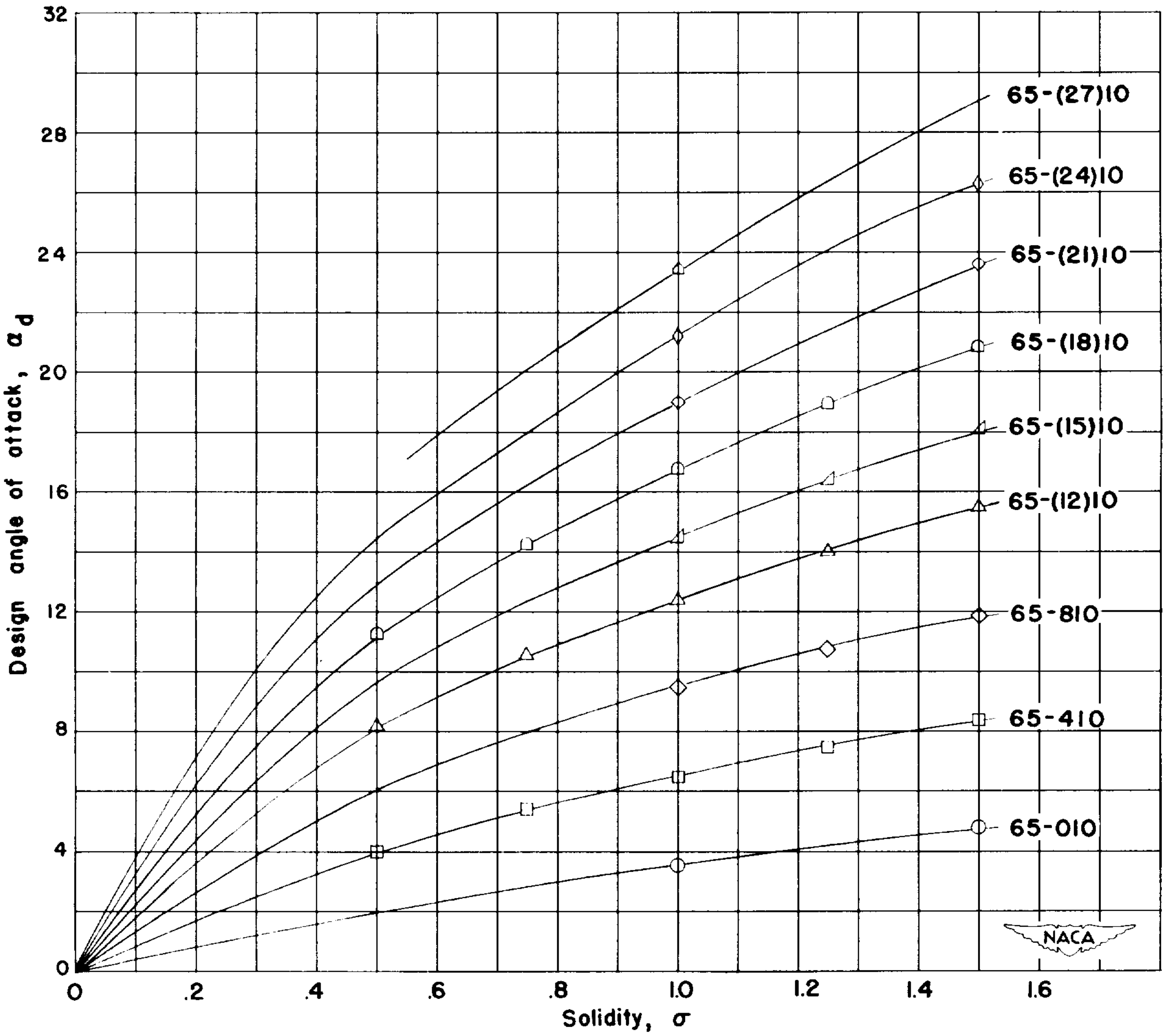

Figure 108.- Variation of design angle of attack with solidity for the sections tested.

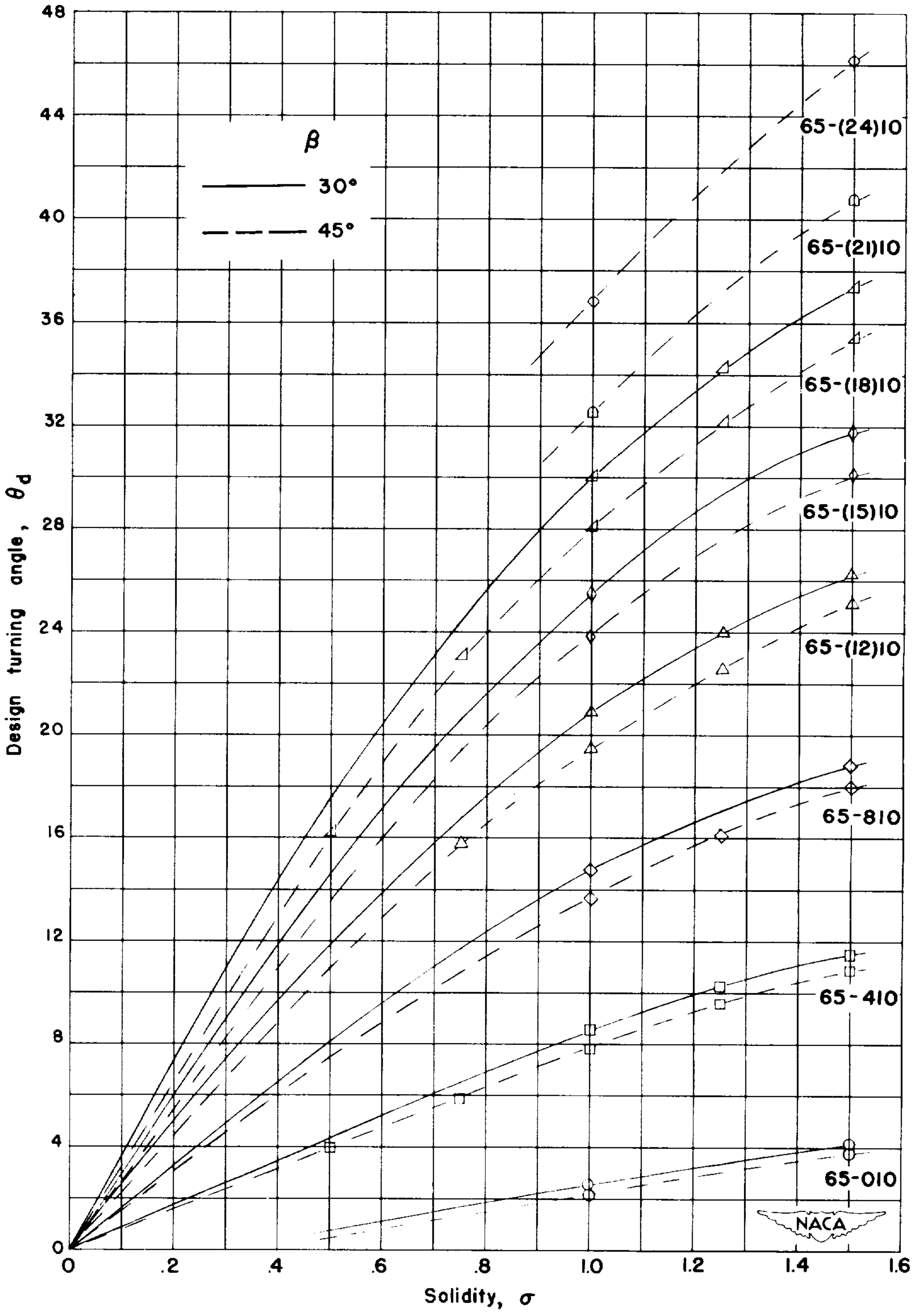

(a) Inlet angles of 30° and 45°

Figure 109.- Variation of design turning angle with solidity and inlet angle for the sections tested.

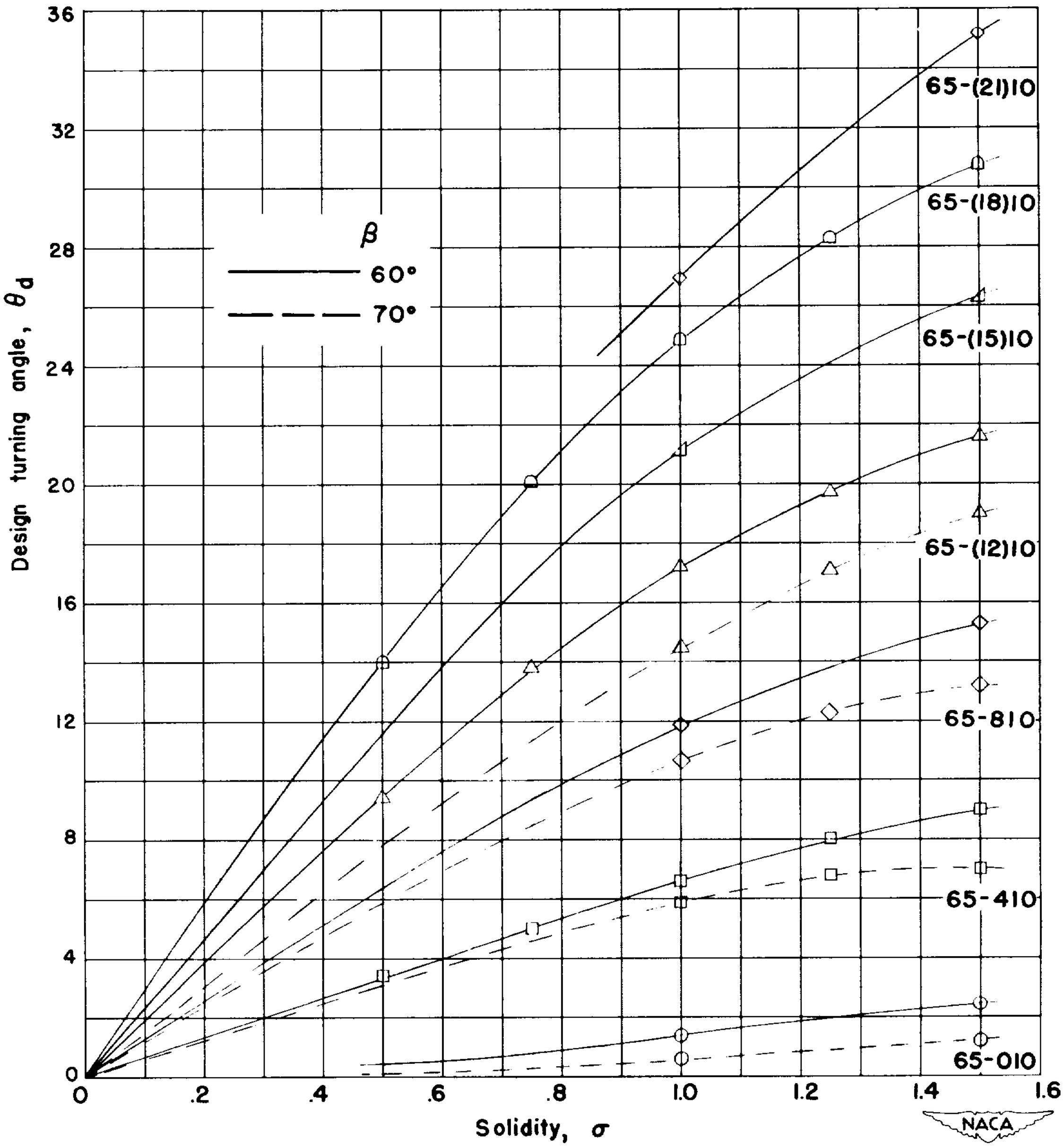

(b) Inlet angles of 60° and 70°

Figure 109.- Concluded.

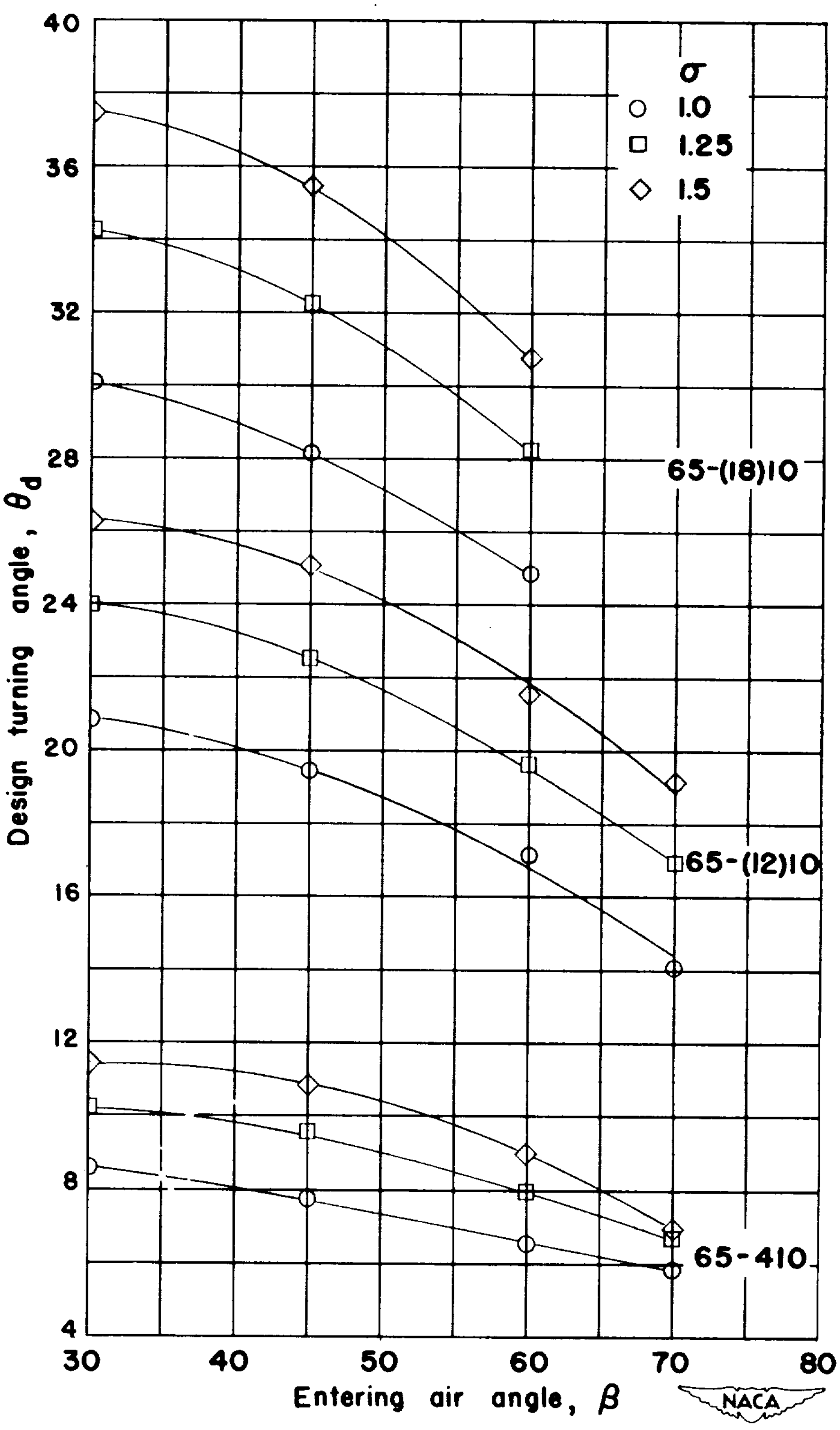

Figure 110.- Variation of design turning angle with inlet angle and solidity for typical sections.

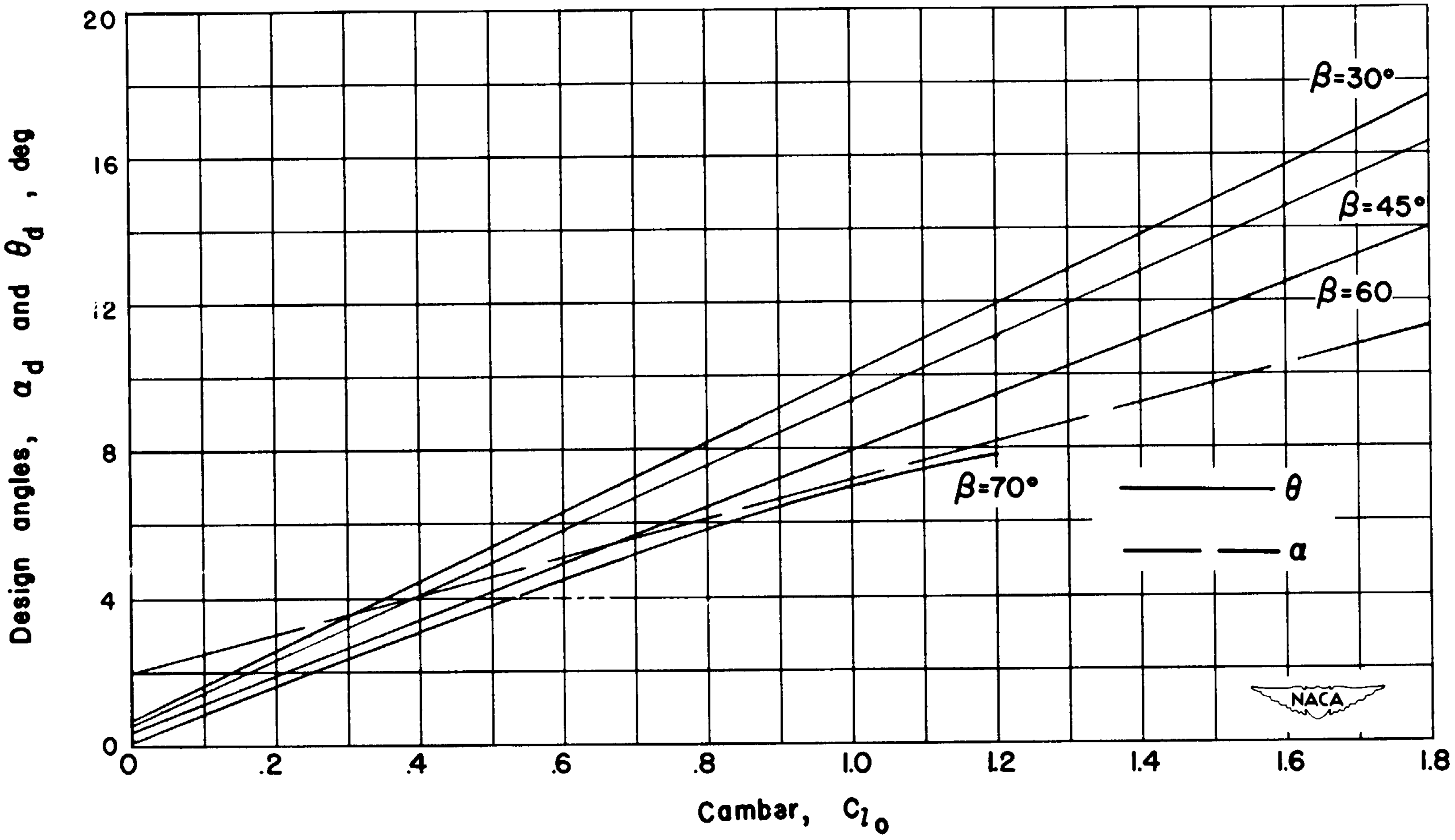

(a) Solidity of 0.50

Figure 111.- Variation of design turning angle and design angle of attack with camber and inlet angle.

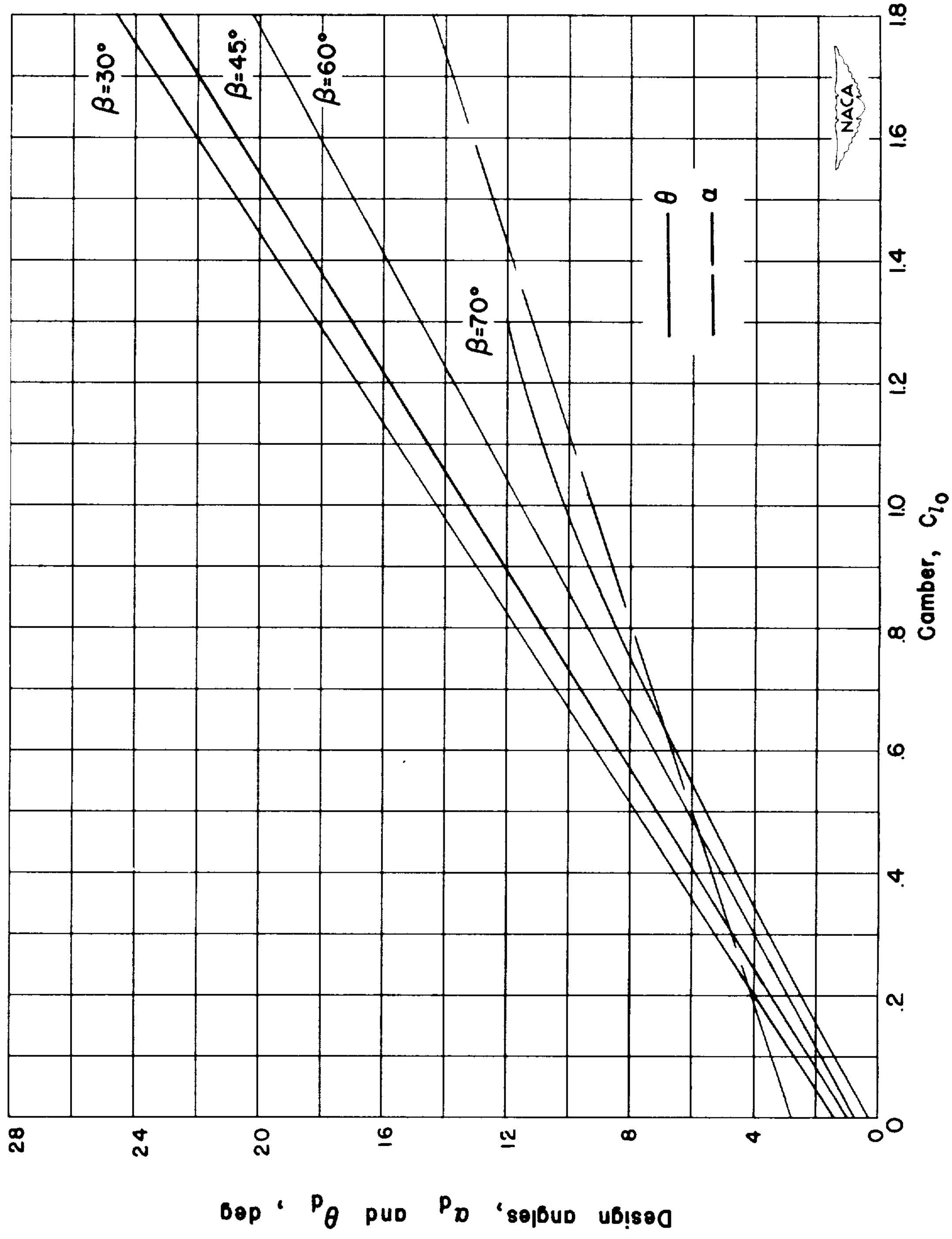

(b) Solidity of 0.75

Figure 111.- Continued.

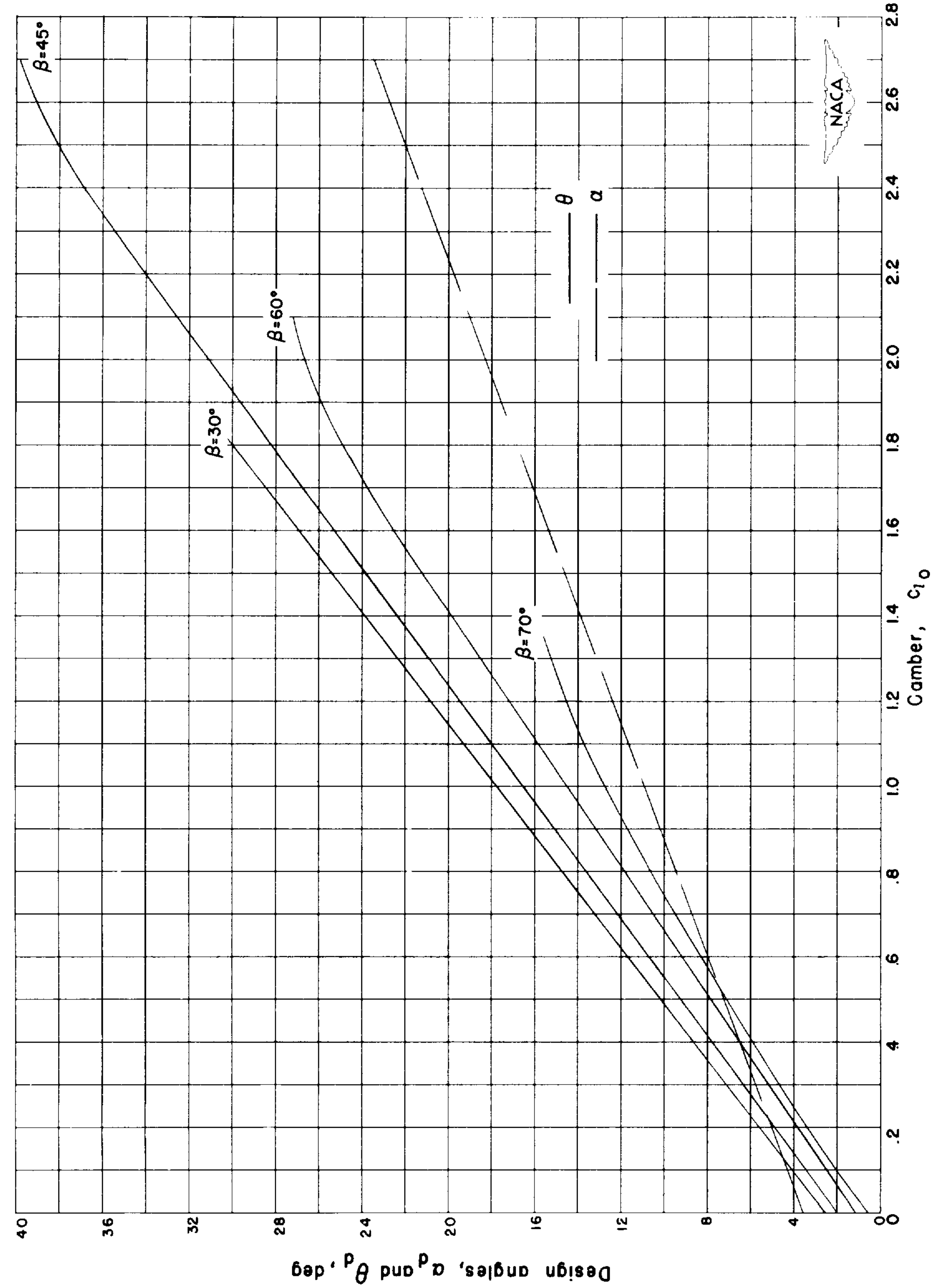

(c) Solidity of 1.00

Figure 111.- Continued.

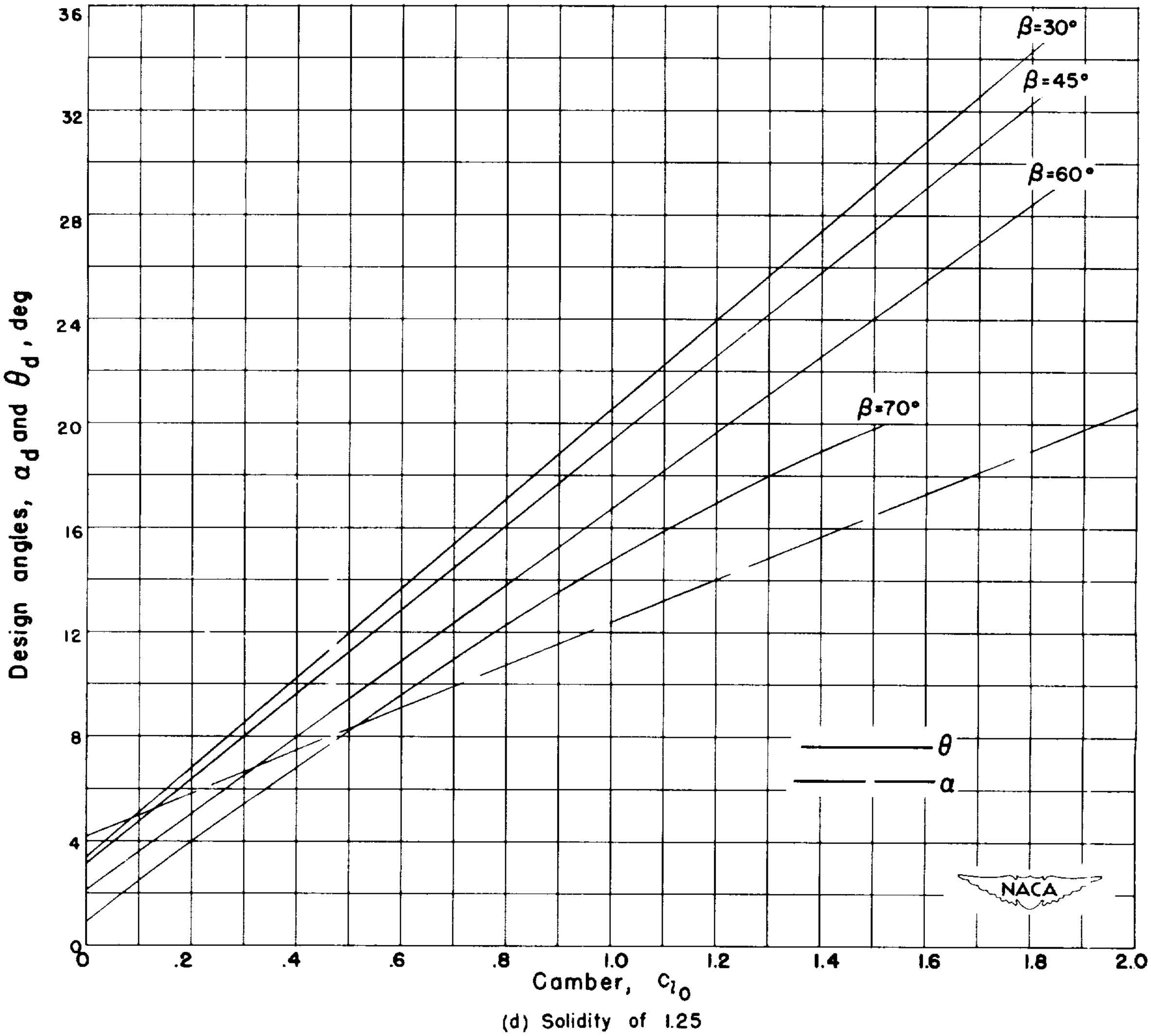

(d) Solidity of 1.25

Figure 111.- Continued.

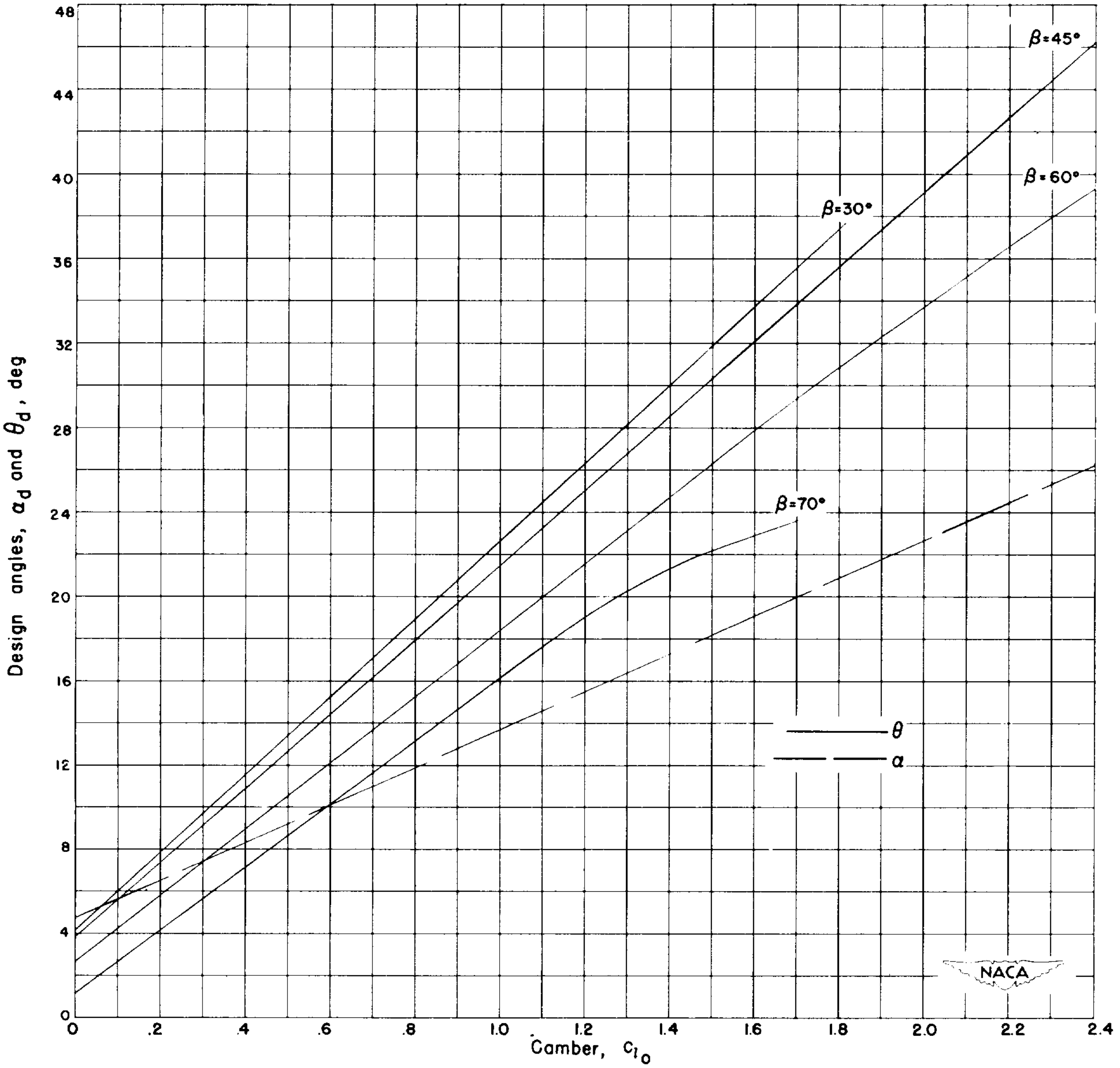

(e) Solidity of 1.50

Figure 111.- Concluded.

NACA - Langley Field, Va.